Digital Image Elasto-Tomography: Mechanical Property Reconstruction from Surface Measured Displacement Data

Ashton Peters

A thesis presented for the degree of
Doctor of Philosophy
in
Mechanical Engineering
at the
University of Canterbury,
Christchurch, New Zealand.

July 2007

This thesis is dedicated to the memory of Madge Peters (1918–2003), and all other New Zealanders whose lives have been affected by breast cancer. May the perseverance of researchers throughout the world yield a cure that will render our work unnecessary.

Acknowledgments

The research presented in this thesis would not have been possible, or as enjoyable as I have found it, without the assistance of a number of individuals, who I will attempt to acknowledge in this short note of appreciation.

It was my supervisor, Dr. Eli Van Houten, who first proposed that I extend my university studies to work on the DIET project. Eli, I thoroughly appreciate the many hours you have spent with me brainstorming ideas, debugging computer code, or discussing strategies when I was stuck at one of the countless obstacles encountered during the past three years. I have enjoyed your friendly, easy-going, and patient nature, and I consider myself very fortunate to have a supervisor who I also consider to be a friend. I also owe a significant thanks to my associate supervisor, Prof. Geoff Chase, whose experience and helpful assistance when writing and reviewing material for publication, and thoughts on my research from an independent perspective, have been most appreciated. I look forward to working with both of you in the future.

The DIET project has been, and continues to be, a team effort that involves a number of students and staff. I would like to acknowledge the assistance of all those who have contributed over the past few years, including (but not limited to): Jérôme Rouzé, Arnaud Milsant, Stefan Wortmann, Fabrice Jandet, Edouard Ravni, Crispin Berg, Anthony Hii, Shig Kinoshita, Richard Brown, Hans Uwe-Berger, Rodney Elliott, Mark Staiger, Kevin Stobbs, and Chris Hann. Thanks also to my fellow research students in the Center for Bioengineering for contributing to the sense of community we share, and to Prof. Tim David for creating a work environment where the overall 'feel' is determined by research students, and not by administrators.

To my family, including those in New Plymouth, Hamilton, Christchurch and Timaru, thank you for you words of encouragement, and for the various forms of support you have given me, particularly during the writing of this thesis, which at one point seemed an insurmountable task. Finally, to Alison, you are both family and my best friend, and I thank you for all the love and encouragement you have given me. After more than three years of additional study, I am finally a salaried employee (hooray!), and I look forward to spending the rest of my life with you.

Contents

List of Figures

List of Tables

Nomenclature

Acronyms

BEM	Boundary element methods
BLAS	Basic linear algebra sub-programs
CO	Combinatorial optimization
CCD	Charge-coupled device
DCIS	Ductal carcinoma *in situ*
DIET	Digital image elasto-tomography
EIT	Electrical impedance tomography
DMA	Dynamic mechanical analysis
FE	Finite element
GA	Genetic algorithm
LAPACK	Linear algebra package
LVDT	Linear velocity displacement transducer
MRE	Magnetic resonance elastography
MRI	Magnetic resonance imaging
PVC	Polyvinyl chloride
SA	Simulated annealing
TDLU	Terminal duct lobular unit
TNM	Tumor, lymph node, metastasis breast cancer classification system
USB	Universal serial bus

Roman Symbols

C	Stiffness contrast parameter
$\hat{C}$	Stiffness contrast corresponding to global minimum error
C_1	Stiffness contrast using a corroborative approach
C_2	Stiffness contrast using a contradictive approach
C_+	Stiffness contrast parameter providing the closest match to experimental data

E	Young's modulus
$\hat{E}$	Young's modulus corresponding to global motion error
E_+	Young's modulus providing the closest match to experimental data
E^*	Complex elastic modulus
E'	Storage modulus
E'_s	Soft material storage modulus
E'_h	Hard material storage modulus
E''	Loss modulus
$\bar{E}'$	Mean reconstructed storage modulus
G	Combinatorial optimization gene
$\tilde{G}$	Gene following mating and mutation
G_+	Combinatorial optimization gene providing the closest match to experimental data
H	Hessian matrix
J	Jacobian matrix
M	Number of generations in combinatorial optimization
$\mathbf{n^e}$	Surface element normal vector
$\mathbf{n^n}$	Surface node normal vector
N_G	Number of genes in combinatorial optimization
P	Interface position parameter
$\hat{P}$	Interface position corresponding to global minimum error
P_s	Interface position for stacked geometry
P_c	Interface position for concentric geometry
P_h	Inclusion vertical position for spherical geometry
P_d	Inclusion diameter for spherical geometry
P_+	interface position parameter providing the closest match to experimental data
$\bar{\mathbf{P}}$	Reference point position across all image frames
$\mathbf{P}_\Delta$	Reference point motion path centroid
R	Residual term
$\mathbf{u}$	Complex-valued displacement amplitude
$\mathbf{u_R}$	Real component of displacement amplitude
$\mathbf{u_I}$	Imaginary component of displacement amplitude
$\tilde{\mathbf{u}}$	Real-valued displacement amplitude
$\bar{\mathbf{u}}(t)$	Time-varying displacement
$\mathbf{u^m}$	Measured displacement amplitude
$\mathbf{u^c}$	FE-simulated displacement amplitude

Greek Symbols

Γ	Motion path error
γ	Hessian matrix regularization term

δ	Gradient descent step size parameter
ϵ	Mechanical strain
ζ	Damping ratio
θ	Parameter combination
$\hat{\theta}$	Parameter combination corresponding to global minimum error
ν	Poisson's ratio
Π_{mate}	Mating probability
Π_{mutate}	Mutation probability
${}_{SA}\Pi$	Simulated annealing probability
ρ	Material density
σ	Mechanical stress
Σ^2	Variance of reconstructed solutions
$\sigma_{E'}$	Standard deviation of reconstructed storage modulus
ϕ	Linear basis function
φ	Phase
Ψ_1	2-parameter simulated reconstruction success metric
Ψ_2	3-parameter phantom reconstruction success metric
Ω	Non-linear squared error function
Ω_1	Undamped phantom surface motion error
Ω_2	Undamped/damped phantom surface motion error
Ω_3	Damped phantom surface motion error
Ω_4	Undamped simulated surface motion error
$\hat{\Omega}$	Global minimum surface motion error
Ω_+	Motion error corresponding to the best-matching gene
ω	Radial frequency

Abstract

Interest in elastographic techniques for soft tissue imaging has grown as relevant research continues to indicate a correlation between tissue histology and mechanical stiffness. Digital Image Elasto-Tomography (DIET) presents a novel method for identifying cancerous lesions via a three-dimensional image of elastic properties. Stiffness reconstruction with DIET takes steady-state motion captured with a digital camera array as the input to an elastic property reconstruction algorithm, where finite element methods allow simulation of phantom motion at a range of internal stiffness distributions. The low cost and high image contrast achievable with a DIET system may be particularly suited to breast cancer screening, where traditional modalities such as mammography have issues with limited sensitivity and patient discomfort. Proof of concept studies performed on simulated data sets confirmed the potential of the DIET technique, leading to the development of an experimental apparatus for surface motion capture from a range of soft tissue approximating phantoms. Error studies performed on experimental data from these phantoms using a limited number of shape and modulus parameters indicated that accurate measurements of surface motion provide sufficient information to identify a stiffness distribution in both homogeneous and heterogeneous cases. The elastic reconstruction performed on simulated and experimental data considered both deterministic and stochastic algorithms, with a combination of the two approaches found to give the most accurate results, for a realistic increase in computational cost. The reconstruction algorithm developed has the ability to successfully resolve a hard spherical inclusion within a soft phantom, and in addition demonstrated promise in reconstructing the correct stiffness distribution when no inclusion is present.

Chapter 1

Introduction and Background

Cancer is one of the most significant public health issues in the world, with one in four deaths in the United States currently directly attributable to the disease. Amongst all forms of cancers diagnosed in the female population, breast cancer is the most common, with new cases in 2007 expected to represent a total of 26% of all female cancer diagnoses. Although deaths from cancer of the lung and bronchus surpassed breast cancer fatalities among American women in 1987, breast cancer remains the second highest cause of female cancer death in the United States, with over 100 American women per day currently dying from the disease [1].

The most recent statistics available from New Zealand indicate that breast cancer is proportionally at least as significant an issue as in the United States. The 2,235 breast cancer cases registered in New Zealand in 1999 represented a total of 28% of all female cancer registrations, the highest proportion of any cancer among New Zealand women. Significantly, and in contrast to American statistics, breast cancer is the leading cause of cancer death for New Zealand females, with a fatality/case ratio of 29% [2]. A related study of cancer mortality covering the 18,990 female breast cancer registrations in New Zealand in the period 1994–2003 concluded that the majority of breast cancers were diagnosed at a localized stage, where survival rates are at their highest [3]. The increase in survival rate associated with early detection provides significant motivation for screening programmes that are designed to detect breast cancer at the earliest possible stage.

1.1 Basic Cancer Biology

Cancer initiates when cells within the body multiply at an abnormally high rate. These groups of cells often form a hard, palpable mass, generically referred to as a tumor, although other forms of cancer, such as leukemia, do not manifest in this manner. The spread of cancerous cells beyond a localized area of the body is known as metastasis.

The majority of cancer fatalities are a result of this metastatic spread to critical organ systems, where malignant cells replace and inhibit the function of cells critical for healthy organ function.

The biological mechanisms underlying cell transformation from healthy to cancerous are thought to be linked to changes in cell DNA, though the exact process is not well understood. Hanahan and Weinberg proposed that cancerous cells acquire an important set of functional capabilities that govern their transformation into malignant cancers [4]. These capabilities are shown in Figure 1.1, and summarized in the following.

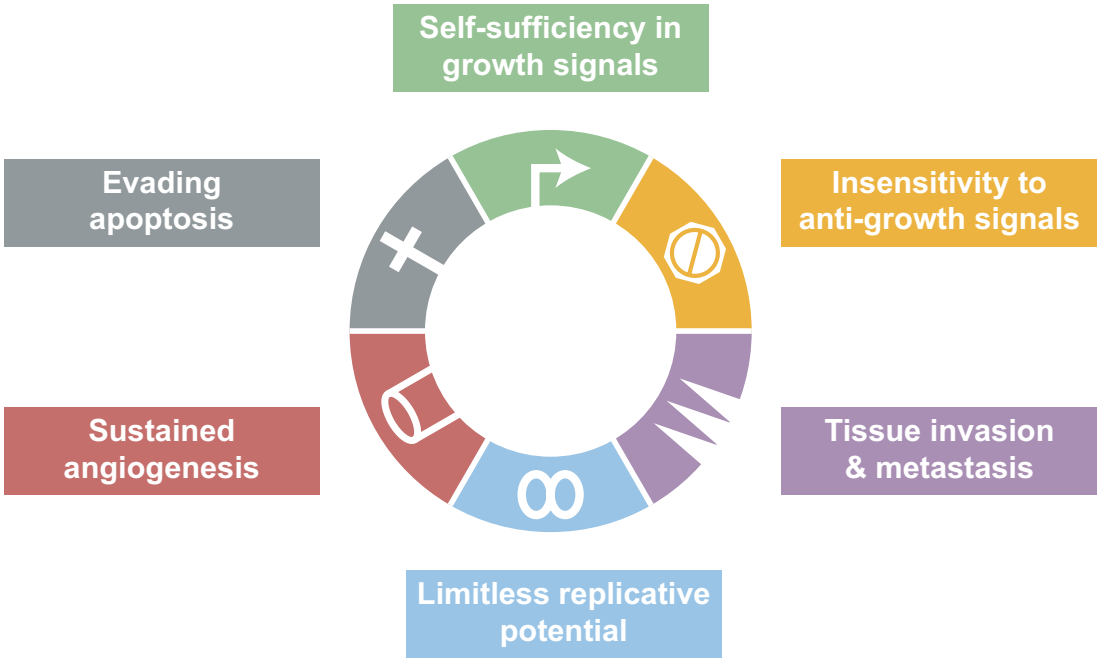

Figure 1.1 The acquired capabilities that differentiate cancerous and healthy cells [4].

The natural process of cell division and growth is controlled by stimulatory signals provided by the body. It is believed that cancerous cells are able to multiply at rates far greater than healthy cells due to an apparent self-sufficiency in growth signals [4]. This reduced dependence on external growth stimulation allows cancerous tissue to expand rapidly and without reference to the mechanisms that usually ensure regulated cell development. In addition to a reduced dependence on external stimulation for growth and division, cancerous cells appear to have decreased sensitivity to the biological anti-growth signals that are intended to keep the division and growth of normal cells within healthy limits.

An additional factor leading to unchecked cancerous cell expansion is a lack of response to apoptosis, or programmed cell death. After receiving an appropriate trigger, the attrition of healthy cells is a key mechanism in maintaining a healthy balance of

cell types within tissue. While the scientific understanding of the exact mechanisms behind cell apoptosis is limited, it has been hypothesized that cancer cells are able to ignore apoptosis signals and live beyond a regular cellular lifespan [4].

The first three acquired capabilities of cancer cells – growth signal autonomy, insensitivity to anti-growth signals, and resistance to apoptosis – allow the growth mechanism of cancers to be de-coupled from the cellular signals in their environment. In theory, this independence from cellular control mechanisms allows a limitless multiplication of cancer cells within the body. It is this unconstrained multiplication, where cancerous cells are able to invade large areas of healthy tissue, that can cause major disruption to the functional systems within the body.

For cells to survive and perform their biological function, they must lie in close proximity to blood vessels that provide essential nutrients and oxygen. Within healthy human tissue, the ability to create new blood vessels, termed angiogenesis, is highly regulated. This angiogenesis regulation ensures that the growth of abnormal lesions is limited by the inability of the lesion to create a supporting vasculature. To sustain the growth of macroscopic tumors, an intrinsic form of angiogenesis within cancerous tissue is required, and has been observed in a range of human cancers.

Finally, it is the acquired ability of cancer to metastasize, or move around the body, that is a key point of difference between cancerous and healthy cells. The exact processes controlling this cellular migration are of critical importance to the development of cancer treatments, but are complicated and not well understood. Survival rates for almost all types of cancer drop considerably once metastasis has occurred, as the ability to treat the disease locally, via methods such as radiation therapy, is removed, and systemic treatments generalized to the entire body, such as chemotherapy, become a requirement.

1.2 Breast Cancer

The adult female breast, shown in Figure 1.2, is a modified skin gland, comprised of several different types of tissue. Between 15–20 glandular lobes form an approximately conical projection from the chest wall, with the apex at the nipple. Included in this region are lactiferous, or milk producing, ducts that open independently at the surface of the nipple. These ducts form a complicated branching structure within the breast, ending in Terminal Duct Lobular Units (TDLUs). Surrounding the central glandular region of the breast is a layer of subcutaneous fat. The amount and distribution of this fatty tissue can vary considerably, as can the appearance and position of the interface with the underlying glandular structures. Both glandular and fatty elements of the breast are held together by a connective network of fibrous tissue, known as mammary, or Cooper's, ligaments. Over time, these ligaments weaken and elongate, causing breast

tissue to sag as age increases. The observed decrease in breast tissue density with age occurs as the breakdown of fibrous connective tissue means fat provides an increased proportion of the total breast mass [5, 6].

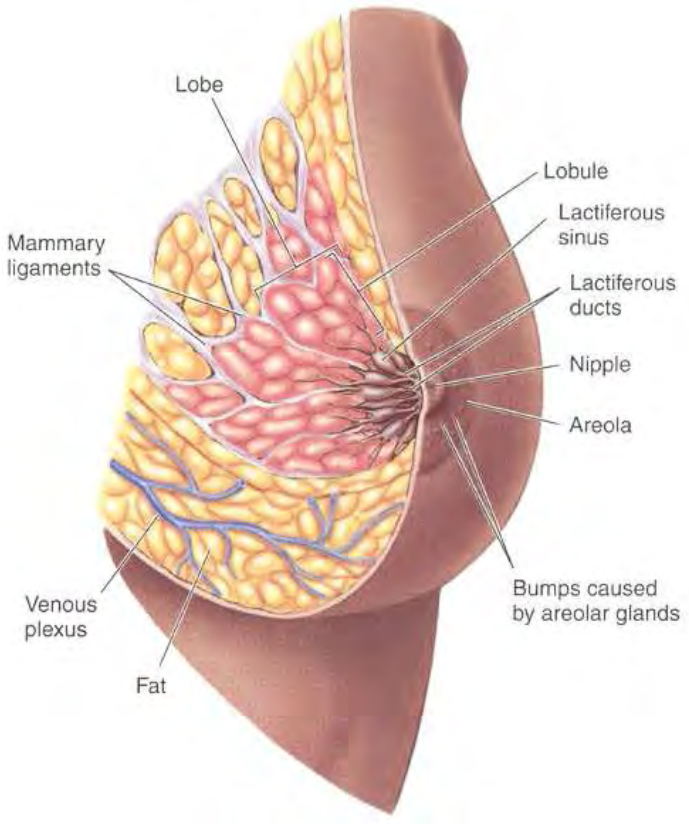

Figure 1.2 Anatomy of the female breast [6].

The majority of lesions within the breast are believed to form within the TDLU, with over 70% of breast cancers found at or near the interface between the glandular structures and fatty tissue within the breast. Most breast cancers begin with an increase in the number of cells within a localized area of the duct system, known as hyperplasia. In many cases, this rapid cell multiplication becomes atypical and, if cancerous cells are involved, is termed ductal carcinoma *in situ* (DCIS). Figure 1.3 shows a microscopic view of a DCIS tissue specimen [7]. Cancers within the breast that initially present as DCIS are estimated to represent 40% of all cancers detected via mammography [8].

The transition from localized to an invasive carcinoma occurs when cancer cells break out from the ductal system into adjacent ducts, or other areas of the breast and chest wall. As with a number of other types of cancer, *in situ* breast cancer, and even invasive cancer contained within the breast, is not necessarily fatal. It is the metastatic spread of the disease to other vital bodily systems, such as the lungs, liver, or bowel, that ultimately cause death.

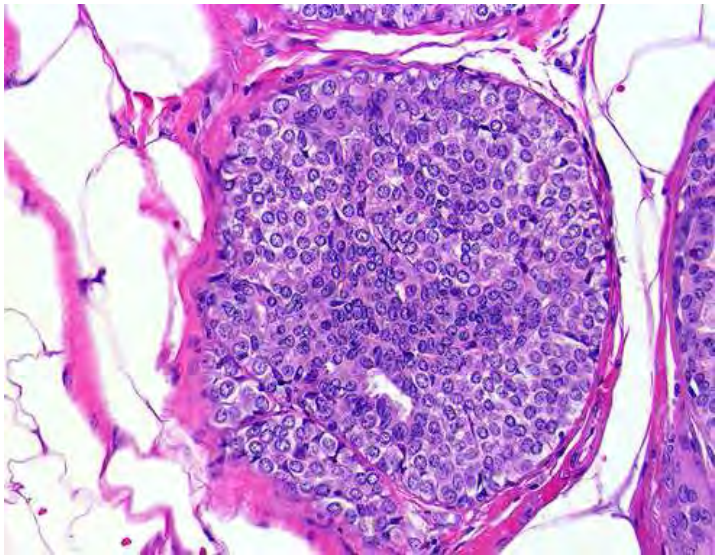

Figure 1.3 A stained pathological specimen from ductal carcinoma *in situ* [7].

Following detection, the diagnosis of breast cancer is categorized based on the size of the tumor, its invasiveness, and the involvement of other parts of the body. The standard classification system for breast cancer is provided by the American Joint Committee on Cancer, where the letters T, N and M are used to describe the tumor size, underarm lymph node involvement, and metastasis state respectively [9]. The range of classifications for each category in the TNM system is given in Table 1.1.

Alongside the TNM system, breast cancer is often given a stage classification in the range 0–IV, providing a more straightforward method of conveying the current severity of the disease. The stage number for a particular case is determined by the combination of TNM values. DCIS, where the cancer cells have not spread to the surrounding breast tissue, is referred to as Stage 0 breast cancer. Stage I describes a situation where the tumor has expanded past the TDLU, is smaller than 2 cm, and has not spread to the lymph nodes or other distant locations. Stage II covers tumors that are small and have not spread into the lymph nodes, or larger tumors that are contained within the breast. Tumors that are mid-sized and have spread to internal sites within the breast and/or lymph nodes are classified as Stage III. If the cancer has metastasized and is present in other organs, regardless of the size of any tumor, it is regarded as Stage IV, where the disease is often terminal. The relative five year survival rate for women with Stage IV breast cancer is less than 20%, compared with over 95% for localized cases in Stages 0–II [3]. Determining the staging of breast cancer is a process that can involve a range of procedures, including x-ray mammography, ultrasound, Magnetic Resonance Imaging (MRI), and tissue biopsy via either needle aspiration or surgery.

Treatment options for women diagnosed with breast cancer are varied, although the majority of cases involve surgery of some form. A lumpectomy involves the surgical

Table 1.1 The 2002 American Joint Committee on Cancer TNM system for breast cancer classification [9].

Category	Identifier and Description	
Tumor	TX	Primary tumor cannot be assessed.
	T0	No evidence of primary tumor.
	Tis	Pure carcinoma in situ.
	T1	Tumor 2 cm or less in greatest dimension.
	T2	Tumor more than 2 cm but not more than 5 cm in greatest dimension.
	T3	Tumor more than 5 cm in greatest dimension.
	T4	Tumor of any size growing into the chest wall or skin.
Lymph Nodes	NX	Regional lymph nodes cannot be assessed.
	N0	Cancer has not spread to regional lymph nodes.
	N1	Cancer has spread to 1–3 lymph nodes under the arm.
	N2	Cancer has spread to 4–9 lymph nodes under the arm.
	N3	Cancer has spread to more than 10 lymph nodes under the arm, or also involves lymph nodes in other areas.
Metastasis	MX	Presence of metastasis cannot be assessed.
	M0	No evidence of metastasis.
	M1	Metastasis is present.

removal of a specific area of breast tissue known to contain cancerous cells, and is usually performed on women with localized breast cancers such as DCIS. This surgery is breast conserving, and is accompanied in most cases with a period of radiotherapy to ensure the destruction of all cancer cells in the affected region of the breast. For women with more advanced cancer, including those with multiple regions of localized cancer within a single breast, a lumpectomy may not be the most appropriate option. In these cases, as a simple mastectomy, involving removal of the entire breast, is performed. This procedure may also include the removal of some or all of the lymph nodes from the underarm region, in a procedure known as a modified radical mastectomy [10].

Systemic treatment options are often used in addition to surgery in an attempt to kill cancer cells that may have spread beyond the breast into other areas of the body, even if there is no direct evidence of such spread. For women with breast cancers that contain estrogen receptors, hormone therapy can be used to limit the growth of the tumor by blocking the supply of estrogen to the affected region. Chemotherapy involves the oral or intravenous application of cancer fighting drugs, and is often used in combination with hormone therapy. Recent advances in genome research have led to the

increased popularity of gene therapy in the treatment of breast cancer. Gene therapy involves using targeted drugs to combat the growth of specific types of breast cancer using the body's natural defence mechanisms. The side effects of systemic treatments can be wide and varied, and are often controlled with the use of additional drugs.

1.3 Breast Cancer Screening

Breast cancer screening aims to reduce cancer mortality by detecting the disease at the earliest possible stage. The intent is not to prevent breast cancer, but to reduce the risk of dying from the disease. Screening programs involve widespread testing of the general population, or at-risk groups, to identify individual cases that warrant further investigation. Such programs require significant funding and resources, often sourced from central or local government, to encourage target population compliance.

The use of breast self examination is widespread for detecting the presence of suspicions lesions at an early stage [11]. This technique relies on the underlying mechanical properties of breast tissue, where tumors often present as a discrete mass significantly stiffer than the surrounding tissue [12]. However, such an examination is only able to provide a qualitative assessment of tissue properties, limiting its usefulness for further diagnosis of tissue histology. In addition, a number of studies have challenged the effectiveness of the breast self exam as a useful tool for reducing the occurrence and fatality rates of advanced stage breast cancer [13–15].

Twelve countries have currently implemented systematic breast cancer screening programs [16]. The program in the United States has grown considerably in both size and participation level over the past two decades, with the proportion of American women over the age of 40 who have had a mammogram in the previous two years rising from 29% in 1987 to over 70% in 2000. The American Cancer Society aims to have 90% of all women over the age of 40 in a screening program by 2008 [17].

In New Zealand, the first trials of government-funded breast cancer screening using mammography were performed in 1991. Following this initial trial, a nationwide breast cancer screening program was announced in 1995. BreastScreen Aotearoa was officially launched in December 1998, and currently offers a free biennial mammogram to all women aged between 45 and 69 with no previous history of cancer [18, 19].

The majority of literature supports the conclusion that screening for breast cancer using mammography reduces mortality rates by detecting small tumors that would not be identified by manual palpation. This early detection allows swift treatment while the disease is still at a localized stage. A large study performed by Tabar *et al.* found a 44% reduction in breast cancer mortality in the 40–69 age group after screening was introduced for Swedish women in 1978 [20]. The majority of this reduction in deaths was attributed to breast cancer screening. Seven other major trials have all

indicated that screening with mammography leads to a 20–30% reduction in breast cancer mortality [16]. Though these trials have been critiqued by Olsen *et al.* [21], who contended that none were of a high-quality, the weight of clinical evidence suggests systematic breast cancer screening can save lives if performed correctly and accurately.

Two important metrics when assessing a cancer screening program are sensitivity and specificity. Sensitivity refers to the proportion of the population with breast cancer who will have a positive test using the screening modality. High sensitivity is desirable for a screening modality in order to correctly identify those individuals who currently have breast cancer. Specificity is a complimentary term that refers to the proportion of people without cancer who test negative using the screening modality [22]. Sensitivity is more important than specificity in a widespread screening program, as false positive results can be compensated for by follow-up diagnosis. However, an ideal screening method combines high sensitivity and high specificity, reducing false-positives, which can have a negative psychological impact on the patient, and false-negatives, which lead to increased patient mortality [16].

1.3.1 Mammography

Mammography is currently the most widespread clinical breast imaging method for both screening and diagnostic purposes, and is currently regarded as the gold standard for breast cancer screening [22]. The image contrast in a film mammogram is based on the difference in propagation of x-rays through breast tissues. Various tissue properties such as thickness, density and atomic composition alter the attenuation of the x-rays, where areas on the resulting film that have had high x-ray attenuation appear lighter [5].

Standard mammographic procedure, shown in Figure 1.4(a) for a craniocaudal mammogram, involves placing the breast between an x-ray source and a detector. The breast is then compressed between paddles before the image is exposed. Compression helps to even out the thickness of the breast over the image area, reducing the exposure difference between the periphery and the center of the breast. Additionally, compression reduces blur due to patient motion, and allows tissue close to the chest wall to be drawn onto the projector. A standard screening mammogram involves both a craniocaudal view in the horizontal plane, and mediolateral oblique view in the vertical plane. Both images are shown for a healthy breast in Figures 1.4(b)-(c). The use of two views allows examination of the internal structure of the breast from multiple perspectives, reducing the chance of a false negative result. Following x-ray image development, a radiologist examines the films and determines whether further diagnosis is required.

The interpretation of a mammogram requires skill, experience, and sound clinical systems to reduce the incidence of false negative cases. A radiologist will often be required to interpret screen-film mammograms in large batches, often with as little as one minute available to analyze each image. With a low proportion of mammograms

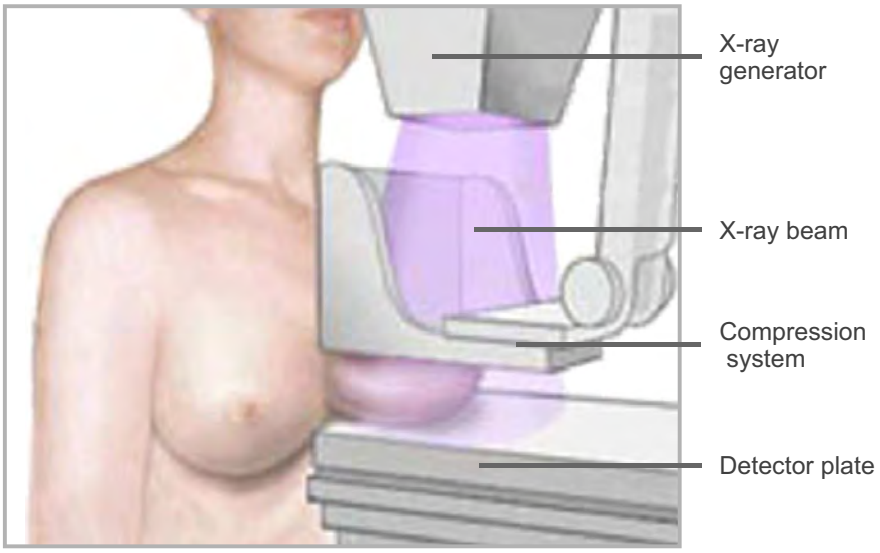

(a) Equipment and patient positioning for a craniocaudal mammogram.

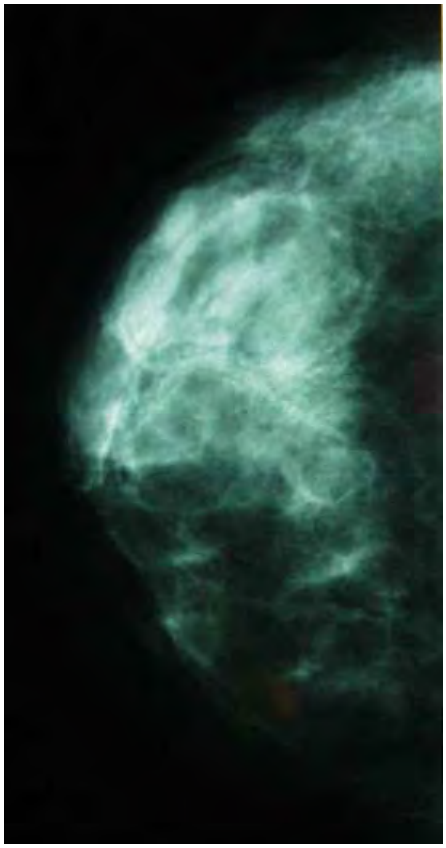

(b) Craniocaudal projection.

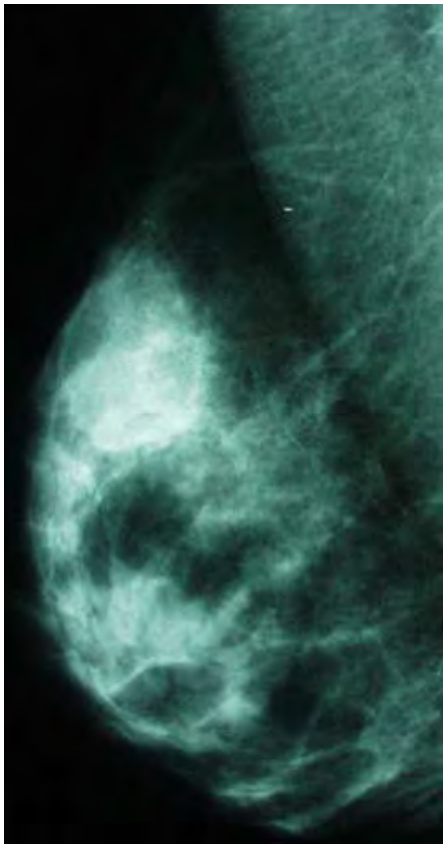

(c) Mediolateral oblique projection.

Figure 1.4 The equipment used and resulting images from a screening mammogram [23, 24].

having radiological abnormalities, fatigue or lack of attention introduces significant potential for human error [16, 25].

Kriege *et al.* reported that the sensitivity and specificity of screening mammography is 33% and 95% respectively, and that the sensitivity of mammographic breast screening is less than ideal [26]. A separate study performed using professionals accredited by the American College of Radiology indicated a variation of at least 11% in the ability of a radiologist to discriminate between a mammograms from women with and without breast cancer [27]. An Italian study by Ciatto *et al.* reported that double-reading of screening mammograms, where each image is interpreted by multiple radiologists, significantly reduced the incidence rate of false-negatives [28].

The low contrast of the mammographic image creates issues when identifying abnormalities, particularly in young women, where high breast tissue density has been linked to a decrease in the effectiveness of mammography [29]. When the x-ray attenuation of the surrounding tissue is largely the same as a tumor, and there are no noticeable calcifications, it is possible for a tumor to be invisible in a mammogram. This lack of image contrast accounts for 30–50% of all false-negative results [5].

Computer-aided detection and the use of digital mammography is becoming more widespread as part of an effort to increase the sensitivity of mammography. Such systems use computers to process images from digital mammography and automatically identify suspicious regions [22]. Other techniques such as computer aided thickness correction have been used to enhance the periphery of the mammographic image [30].

A significant reason for non-compliance with mammography screening programs is the expected and/or experienced discomfort associated with breast compression. The pain and discomfort experienced by women undergoing mammography has been investigated by several studies, yet is not well understood [31]. Using a visual analogue scale, Ashgari *et al.* found that 92% of patients reported a mammogram as being painful, a similar result to the 88% of painful mammography experiences reported by Kashikar-Zuck *et al.* [32, 33]. In general terms, patients report pain during mammography at a low to moderate level, although the pain levels experienced show high variability. The cause of this variation in discomfort is not conclusively understood. Kashikar-Zuck *et al.* found no significant relationship between breast density and pain levels, a conclusion that conflicts with the findings of Kornguth *et al.*, who observed a connection between breast density and discomfort [34]. Although the percentage of women that reported severe pain levels during mammography is low, a number of patients indicated they would not have further mammography due to the pain they experienced. In addition to reduced compliance among women who have experienced discomfort while having a mammogram, the perceived discomfort amongst those women who have not enrolled in a screening program can be a significant barrier to widespread participation.

1.3.2 Alternative Breast Imaging Modalities

MRI uses powerful magnetic fields to create images of the human body by measuring the absorption and emission of radio frequency waves. When applied to soft tissue, MRI can be used to generate highly detailed images of the internal structure of the breast. MRI signal strength, and therefore image contrast, is determined by the density of hydrogen protons within the imaged tissue and their response to rapidly changing radio waves and magnetic fields. The image contrast of MRI systems can be significantly enhanced using a range of chemicals ingested or injected prior to the scan [35, 36]. An example of the equipment used for breast MRI and the type of image that can be obtained from such a system is shown in Figure 1.5 [37, 38].

(a) Patient positioning for breast MRI, where the breasts hang pendant beneath the patient.

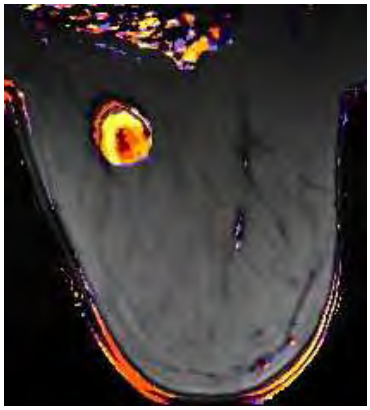

(b) A contrast-enhanced, color corrected breast MRI scan clearly indicating a tumor.

Figure 1.5 MRI patient positioning, and an MRI image produced with a contrast-enhancing agent [37, 38].

While not as prevalent as mammography, MRI has seen limited application as a breast cancer screening modality. A large study in the Netherlands concluded that breast cancer screening with MRI was more sensitive for at risk women than mammography [26]. However, MRI was also found to have a lower specificity, indicating that screening using MRI alone would lead to a much higher recall rate for false-positives. Further evidence supporting the use of MRI for breast cancer screening was presented by Warner *et al.*, who concluded that breast MRI may be superior to mammography for detecting small breast cancers in women at high risk [39]. However, the high cost of MRI hardware and the difficulty in producing clear and consistent images has prevented its adoption in widespread screening programs [40].

Medical imaging with ultrasound involves the use of high frequency acoustic signals to form an image of subsurface tissue structure. Ultrasonic waves introduced using a hand-held scanner are reflected at discontinuities within the tissue, such as the interface between different tissue types. Precise measurement of these reflected waves allows

an image representing the internal tissue structure to be calculated and displayed. Figure 1.6 shows an example of a clinical ultrasound examination, where the resulting sonogram shows a large breast mass [41].

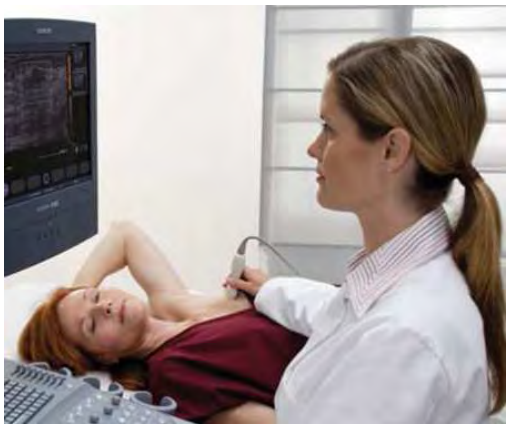

(a) Technician performing a breast ultrasound exam.

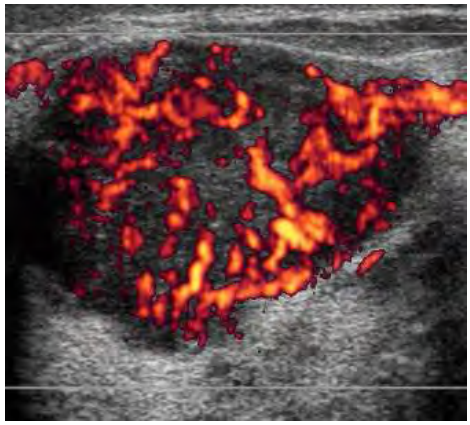

(b) A color-enhanced ultrasound image showing a large breast mass.

Figure 1.6 Diagnostic ultrasound of the breast [41].

Ultrasound is not currently approved in the United States for widespread screening in women with no previous history of breast cancer. However, it is often used as a diagnostic tool in a follow-up examination if abnormalities are detected using mammography. In these scenarios, ultrasound has proven useful as a tool for identifying the possible malignancy of a detected mass [42]. Limitations of ultrasound systems include a low spatial resolution and a limited ability to detect microcalcifications, which are often an early warning sign of breast cancer [22].

The effect of breast tumors on the temperature of overlying skin was first identified in the 1950s, when declassified military technology was adapted to produce accurate thermal images of the human body [43]. Thermal imaging techniques measure the infrared emissions from human skin, where the emitted signals have a wavelength of approximately 5–15 μm. Using sensitive thermal imaging cameras and a carefully controlled laboratory environment, accurately calibrated thermograms of the chest region can be obtained, with examples shown in Figure 1.7. Early research in breast thermography relied on entirely subjective image analysis, leading to large variations in the effectiveness of such systems across a range of studies. The use of computers to assist with image capture and processing in modern breast thermography has significantly improved the accuracy of these systems.

Thermographic breast images are graded according to a thermobiological classification on a scale from TH1 (normal) through TH5 (highly abnormal), where the abnormal surface temperature distribution in Figure 1.7(b) is indicative of a subsurface breast lesion. The use of breast thermography in conjunction with mammography

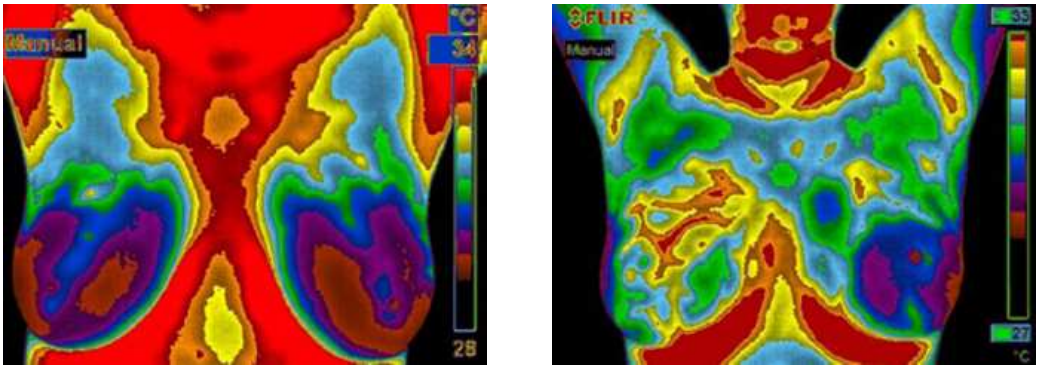

(a) A TH1 (normal) thermogram image.

(b) A thermogram showing a severe abnormality (TH5) in the patient's right breast.

Figure 1.7 Healthy and abnormal images from breast thermography [44].

is widespread, with both systems providing physicians with complimentary information [44].

Electrical Impedance Tomography (EIT) is a novel breast imaging system that uses low level electrical currents to create images of internal breast structure. EIT systems are based on the observed correlation between tissue pathology and electrical properties, where malignant breast tumors have shown lower electrical impedance than healthy tissue [45]. Cherepenin *et al.* developed a three dimensional EIT system that had potential to be used for breast cancer detection [46]. A similar system developed at Dartmouth College is shown in Figure 1.8, and has been successfully used to identify subsurface breast abnormalities [47]. Breast imaging using microwaves is a similar area of research based on experimental data that indicate cancerous tissue has a lower dielectric permittivity than healthy breast tissue [48, 49]. Both EIT and microwave systems for breast imaging have shown promising initial results, but are yet to undergo widespread clinical trials.

1.4 Elastography

Despite the questionable effectiveness of manual palpation, the mechanical property contrast measured by breast self examination has inspired a range of research into the accurate quantification of soft tissue elastic properties. One of the first significant studies in quantitative analysis of soft tissue mechanical properties was performed by Ophir *et al.*, who defined the term *elastography* when referring to measurement of the elastic properties of biological tissues. The resulting image, where tissue stiffness is visualized in a two-dimensional plane through a specimen, is termed an *elastogram*.

Using an ultrasound scanner and cross-correlation techniques, elastographic evaluation was performed on a range of foam phantoms, and a block of porcine tissue,

(a) EIT imaging hardware, where the patient's breast is surrounded by electrodes within the circular opening.

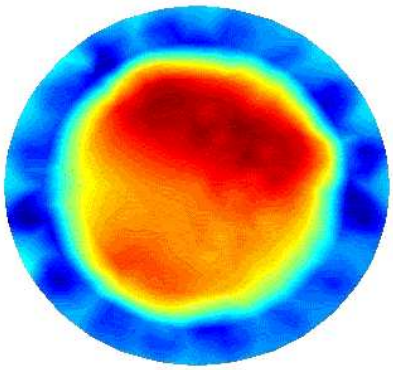

(b) Coronal image through the breast showing absolute permittivity values. A malignant tumor is visible in the upper right quadrant.

Figure 1.8 A prototype EIT system, and the resulting image of electrical properties [47].

shown in Figure 1.9(a). The sonogram resulting from an ultrasound scan of the tissue was converted to an image of elastic modulus based on the correlation between sets of images taken before and after a small sample compression. Although the resulting elastogram, shown in Figure 1.9(b), has a low spatial resolution, the striated nature of the tissue is apparent, with bands of soft fatty tissue identified as light horizontal lines. The promising results from this and other similar studies demonstrated that quantitative assessment of tissue elasticity was possible, and that the elastograms produced using an ultrasound system had potential uses in a wide range of applications, including diagnostic medical imaging [50, 51].

(a) Porcine tissue sample, with visible striations of fat and muscle.

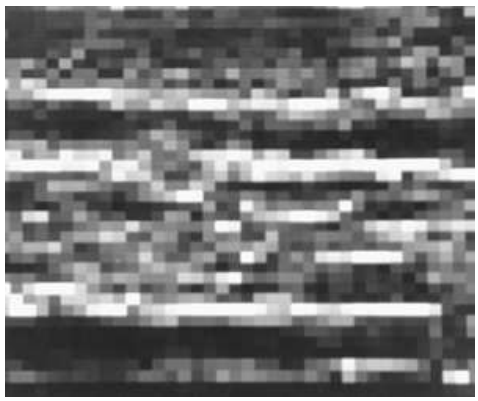

(b) The corresponding tissue elastogram, where bright pixels represent regions with a lower elastic modulus.

Figure 1.9 A tissue sample and elastogram from early research using ultrasound for elastography [50].

1.4.1 Mechanical Properties of Soft Tissue

Mechanical property measurement of *in vivo* or *ex vivo* human soft tissue is a challenging field, with only a limited number of studies able to provide quantitative results using traditional mechanical testing techniques. Biological soft tissue has features common to both solid and liquid materials, making accurate characterization a difficult process largely dependent on the assumptions about mechanical behavior made when performing testing. These assumptions regularly include treating the material as an elastic, homogeneous, isotropic solid that is close to, or completely, incompressible, allowing the stiffness of samples to be expressed as a single modulus value, where Young's Modulus, E, is commonly used.

Sarvazyan *et al.* provide a summary of early research in soft tissue elastography, presenting both collated and experimentally generated mechanical testing results from a range of human tissue types, including soft tissue and cartilage [52, 53]. The elastic modulus results show large variation across the range of tissue types, and within each tissue type, indicating the large experimental uncertainties often associated with testing biological samples. However, an observed contrast in elastic modulus between healthy and cancerous tissue of 1–2 orders of magnitude was postulated as the basis of an imaging modality that could have particular relevance to breast and prostate tissue.

Krouskop *et al.* developed a mechanical testing system using a hydraulic servo apparatus that allowed compressive viscoelastic mechanical testing of small tissue samples using a sinusoidally displaced indenter [54]. A total of 142 breast tissue samples were tested at room temperature soon after excision in a surgical environment. These samples represented a range of healthy fatty, glandular, and fibrous breast tissue, as well as both intraductal and infiltrating ductal carcinoma. All samples were tested at pre-compression values of 5% and 20%. For actuation frequencies between 0.1–4 Hz, breast tissue was found to be only slightly viscoelastic, with modulus values not strongly dependent on actuation frequency. When actuated at 1 Hz, fatty breast tissue showed only small variations in elastic modulus over a large strain range, with elastic modulus values of approximately 20 kPa. Results from glandular and fibrous breast tissue samples indicated that both types were significantly stiffer than fatty tissue. Glandular tissue modulus values were in the range 28–66 kPa, while fibrous breast tissue was measured at between 96–244 kPa. Modulus values for glandular and fibrous breast tissue displayed a high dependence on the amount of sample pre-compression, indicating a non-linear elastic response to loading. A significant result of this study was the consistently high measured elastic modulus values for cancerous tissue, with contrast values up to 700% when compared to healthy fat and glandular tissue.

Wellman *et al.* developed a portable punch indenter system that allowed tissue samples to be tested in the operating room immediately following excision [55]. A total of 68 samples representing eight different types of breast and cancerous tissue were

statically tested to a strain of approximately 0.15. Fatty and glandular tissues were found to have an approximately linear stress-strain relationship, with elastic modulus values in the range 5–90 kPa at strain values less than 0.1. Carcinoma and other benign lesions displayed non-linear elastic behavior, with a 500–1200% contrast observed between carcinoma and fatty breast tissue. This study provides further evidence of a significant correlation between tissue histology and observed stiffness.

Mechanical testing of excised tissue traditionally requires relatively large, homogeneous samples that are challenging to obtain in a surgical environment. The difficulty in obtaining consistent samples was addressed by Samani *et al.*, who developed a testing system designed to compensate for biological tissue sample limitations, such as small size, irregular shape, and inhomogeneity [56]. Small blocks of unconstrained excised tissue were indented in a quasi-static manner using a computer controlled loading apparatus, with the resulting force measurements recorded. An approximate Young's Modulus value was obtained from force-displacement data using a conversion factor based on sample geometry and calculated using a finite element (FE) model. Tissue modulus values were observed to be non-linear over the small strains applied, with Young's Modulus values for fatty and fibroglandular breast tissues of approximately 2 kPa. In comparison, high grade ductal carcinoma had measured Young's Modulus values of approximately 12 kPa, a modulus contrast of approximately 600% when compared to healthy breast tissue.

Subsequent refinement of the mechanical testing system developed by Samani *et al.* allowed a more accurate characterization of tumor stiffness using larger tissue samples containing intact tumors. This modified system was verified against small synthetic samples of known stiffness [57]. A comprehensive study of 169 breast tissue samples was performed using slightly different experimental setups for healthy tissue samples and those containing tumors, based on the different sample geometries. The mechanical testing results again indicated similar Young's Modulus values for fatty and fibroglandular breast tissue at low strains, with both tissue types having observed modulus values of approximately 3.5 kPa. Statistical analysis indicated that there was a significant difference in stiffness between a range of breast cancers and healthy tissue, with Young's Modulus values for high grade invasive ductal carcinoma more than 10 times greater than healthy tissue. Breast fibroadenoma, which are usually benign, were found to have stiffness values between those of healthy tissue and carcinoma. This result indicates the potential of accurate stiffness characterization to differentiate between benign and cancerous lesions within the breast. Such characterization could improve the specificity of elastographic imaging modalities by reducing the occurrence of false positive results [58].

While experimentally tested soft tissue modulus values show large variations depending on a range of factors specific to each testing methodology, a clear distinction is apparent between healthy and cancerous breast tissue. This observed elastic contrast

has encouraged the development of a range of techniques that aim to determine the distribution of elastic properties throughout the breast. A number of these approaches are based on existing medical imaging modalities, where a modified application of the hardware and/or software allows the generation of elasticity images that can assist in determining tissue pathology.

1.4.2 Ultrasound Elastography

In addition to traditional clinical use, ultrasound technology has been implemented as an elastographic breast imaging tool. Displacement of the breast during an ultrasound scan allows the tissue displacement response to be expressed as a strain image. Early research in ultrasound elastography used ultrasound scanning machines to measure the mechanical response of both phantoms and soft tissue to harmonic actuation. By assuming constant material stress throughout the material, the recorded strain information was converted directly into a description of elastic modulus using basic Hookean theory. Results from these studies indicated that ultrasound elastography had significant potential to detect abnormal lesions within breast, prostate and liver tissue based solely on tissue stiffness [59–62].

Recent results have clearly demonstrated the potential of ultrasound elastography in diagnostic clinical medicine. Barr *et al.* developed a freehand ultrasound elastography technique that was applied in conjunction with conventional ultrasound analysis [63]. This method used the relative size of suspicious lesions in sonograms and elasticity images as an indicator of tissue pathology. As shown in Figure 1.10, cancerous tumors with high stiffness contrast to the surrounding tissue appeared significantly larger in the elastographic image.

A study performed on 80 patients with a total of 123 previously identified breast lesions indicated this technique had a sensitivity of 100%, with all 17 malignant tumors positively identified. A 99% specificity was also achieved, with 105 of 106 benign lesions correctly identified based on their smaller appearance in the resulting elastographic image. While ultrasound elastography studies such as these have shown significant promise in diagnostic imaging, their widespread application in a breast cancer screening program is limited by a number of factors, including a lack of off-axis resolution and geometric repeatability.

The strain-based approach to ultrasound elastography relies on the assumption of constant material stress in order to generate an elastic property image. Model-based elastography is an alternative technique where stress values can vary across the domain of interest, requiring the solution of an inverse problem to determine the elastic property distribution [64]. Recent results have indicated that these forms of inverse problems are ill-posed, meaning more than one exact mathematical solution to the problem exists [65, 66]. However, studies in both transient and steady state

(a) A conventional ultrasound image, where an invasive ductal carcinoma appears as a dark region.

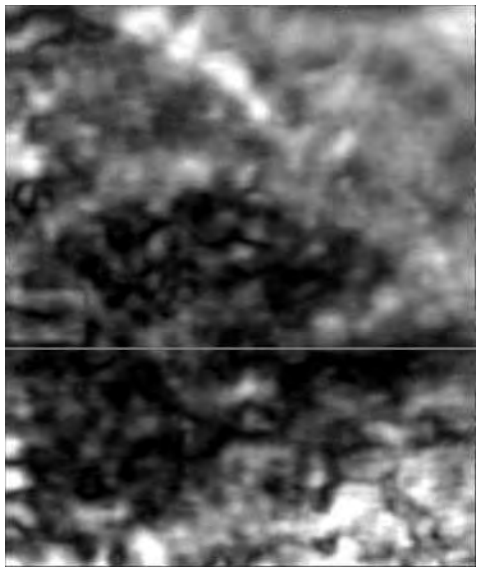

(b) The corresponding elasticity image, where the lesion appears significantly larger.

Figure 1.10 Modern diagnostic ultrasound elastography of a biopsy-proven breast cancer [63].

model-based ultrasound elastography have yielded comparable results to the strain-based approach, indicating that the mathematical challenge of non-uniqueness can be overcome with careful choice of inverse algorithm [67–69].

1.4.3 Magnetic Resonance Elastography

In addition to the static images obtained in traditional medical diagnosis, MRI has the ability to detect three dimensional motion within a displaced sample. Plewes *et al.* used MRI to obtain quasi-static strain images from the breasts of volunteers, and used these images to determine the bio-mechanical properties of previously-detected lesions [70]. Muthupillai *et al.* demonstrated a technique where an oscillating magnetic gradient could be used to measure tissue amplitude when harmonically perturbed [71]. Strain-based property estimation has been used to calculate measurements of tissue modulus from the mechanical wavelength or velocity of the propagating shear waves in breast tissue [72].

Van Houten *et al.* developed a harmonic Magnetic Resonance Elastography (MRE) system for breast imaging [73, 74]. In combination with a sub-zone based inversion algorithm, this system was able to reconstruct elastic property distribution of both phantoms and *in vivo* breast tissue, with results from a breast with an high stiffness inclusion shown in Figure 1.11. The mechanical properties reconstructed in this study compared well with values from independent mechanical testing. Development of this

sub-zone approach using phantoms indicated that the system was capable of detecting inclusions as small as 5 mm using a model-based elastic inversion algorithm [75, 76].

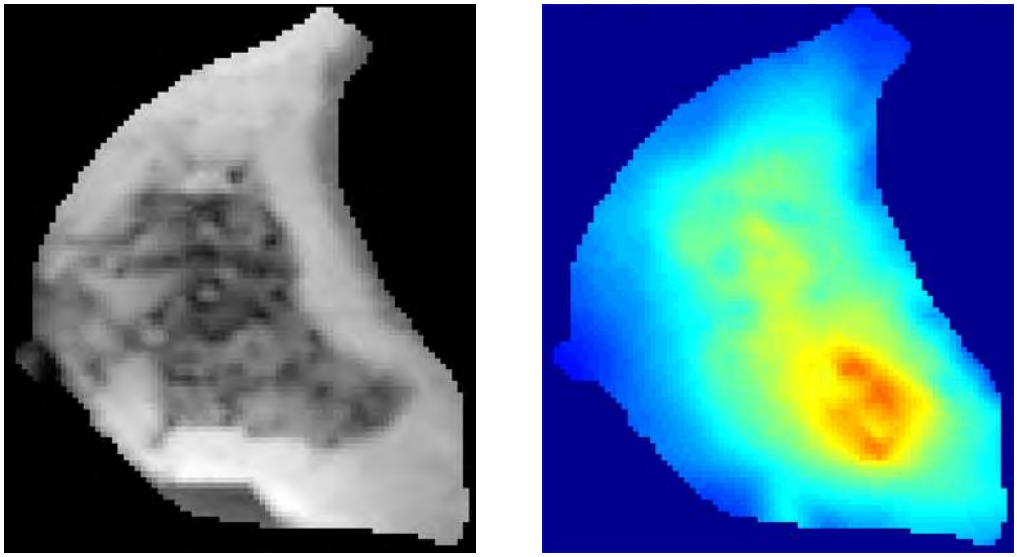

(a) MR detected displacement image.

(b) The reconstructed elastic modulus distribution, where a fibroadenoma is visible in the lower right quadrant of the image.

Figure 1.11 Displacement and stiffness images from a MRE system [74].

1.4.4 Novel Elastographic Techniques

Several novel methods for elastographic tissue imaging are currently in development. Kirkpatrick developed an optical elastography technique for measuring strain values in biological tissue [77, 78]. This system used a CCD camera to capture the harmonic motion of samples of chicken skeletal muscle. The observed change in speckle patterns between subsequent images was used to calculate strain field data that could be used to infer mechanical properties. While not currently intended for breast elastography, such a system may has relevance for the measurement of strains as part of a surface measurement based elastographic system.

Model-based computer-aided registration of breast images produced using traditional imaging modalities has shown potential for breast elastography. Rothney *et al.* used a FE model with assumed elastic properties to displace images previously obtained with a breast MRI system [79]. Using a range of image similarity metrics to compare the original and displaced images, reconstruction of tumor location was demonstrated, including situations with multiple inclusions. Barbone *et al.* have reported results from a similar system, where an ultrasound scanner was used to generate images from an experimental phantom, and image registration used to identify the presence of an interior inclusion [80].

Recent work by Liu *et al.* has indicated the feasibility of elastographic property reconstruction from a set of boundary measurements [81]. Such a system differs from ultrasound or MRI-based elastography techniques in the limited amount of data available for elastic property reconstruction. Using an optimization-based reconstruction algorithm, measurements of force and displacement at external and internal boundaries within a simulated phantom model were used to reconstruct elastic properties. A single static displacement mode was used for an isotropic elastic property reconstruction, while anisotropic reconstruction required data from a combination of multiple independent loading modes. While this method is currently limited to idealized simulated data, the promising results indicate that elastographic reconstruction is possible using only a small subset of the large data sets used for full-volume based reconstruction techniques.

Alongside developments in data acquisition and registration, research into reconstruction algorithms for solving the elastic inverse problem is ongoing. While many of these algorithms are based on traditional approaches to non-linear reconstruction such as gradient-descent methods, there is increasing interest in the use of stochastic methods for solving the large, highly non-linear problems often found in elastography. The stochastic approach to non-linear optimization is summarized in the following section, with particular focus on developments in soft tissue elastography.

1.5 Stochastic Optimization in Elastography

A stochastic process is one where the changes between consecutive states of a system contain an element of randomness, and cannot be exactly predicted. Such systems differ from deterministic processes, where subsequent system states can be predicted using known information about the current and previous configurations. Stochastic optimization algorithms include an element of random behavior in an attempt to overcome limitations in traditional algorithms, such as a heavy reliance on starting conditions.

Combinatorial Optimization (CO) is a form of stochastic algorithm that combines a set of possible solutions, termed a *population*, in a semi-random manner. CO aims to minimize the value of an objective function, often represented by an error term. Genetic Algorithms (GAs) are a form of CO that perform population combination in a manner similar to the naturally occurring process of genetic evolution. The overall 'fitness' of the population increases over time, as strong solutions with a low error value are retained across generations, while weak solutions are more likely to be eliminated. Subsequent generations are created by combining the 'genetic material' of solutions within the population in a manner similar to reproduction in the animal world.

In many GAs it is necessary that parameters for optimization are converted into a standard form using a genetic encoding process. This encoding allows the optimization

of several independent parameters with different units. Incorporating the naturally occurring phenomena of genetic mutation into the reconstruction algorithm further increases the diversity of solutions by introducing controlled, random variation to the population [82–86].

Annealing is a metallurgical process involving several stages of controlled temperature variation that allows the microstructure of a material to reach a minimum energy state. Kirkpatrick *et al.* first reported the application of annealing theory to problems in CO in the early 1980s, describing a strategy where CO solutions that decreased the overall system 'energy' were increasingly preferred over time [87]. Allowing a limited number of solutions that increased the system energy provided possible additional pathways to a global minimum error state. One interesting conclusion from this work was the limited aspects of artificial intelligence observed in such algorithms when applied to the common 'travelling salesman' optimization problem [88].

Applications of CO in the field of elastic property reconstruction are limited, although increasing in popularity as more powerful computer systems become mainstream. Matsuoka *et al.* used a GA in combination with FE methods to solve for the mechanical properties and internal structure of composite materials [89]. Here, the inverse algorithm optimized the internal structure of a composite to obtain a desired Young's Modulus value. Olmi *et al.* performed a preliminary investigation into the use of a GA for image reconstruction in EIT [90]. Here, a numerical model was used to simulate the electrical properties of a simple geometry containing a high resistivity inclusion. The GA used in this study to perform image reconstruction was found to have significantly higher computational cost than more traditional Newton-Raphson methods, though this increase was offset by a clear improvement in reconstructed solution accuracy. Advances in computer processing were seen as a pathway to the possible implementation of such optimization techniques in realtime EIT systems.

The use of stochastic techniques in soft tissue elastography is a new and emerging field. Zhang *et al.* developed a theoretical framework for the application of a GA to problems in soft tissue elastography [91]. To ensure numerical stability, this method constrained solutions using an assumed *a priori* property distribution. Simulating displacements with a synthetic numerical model, stochastic methods were found to give consistently accurate results for the elastographic reconstruction problem. Khalil *et al.* developed a combined GA and FE approach to solve for elasticity values in vascular soft tissue [92]. This study lumped material parameters into discrete regions in order to simplify the genetic encoding process, and used a numerical model to simulate displacements in a 2D model. Successful elastic property reconstructions were performed on both homogeneous and heterogeneous models with multiple inclusions in the presence of noise.

1.6 Digital Image Elasto-Tomography

Digital Image Elasto-Tomography (DIET) is a novel technique intended to detect and identify areas of high tissue stiffness within the breast, where cancerous lesions can be identified due to their high elastic modulus values. Utilizing digital imaging sensors, image processing algorithms, and computer reconstruction techniques, DIET aims to generate a three dimensional representation of elastic properties throughout the breast volume. The system is targeted at providing an inexpensive, comfortable screening test, where the associated hardware is compact enough to make portable screening units a reality. The three-dimensional nature of the resulting elastogram should allow accurate image registration between subsequent scans, assisting in tracking changes in internal breast structure over time. The DIET system can be split into several key stages, summarized in Figure 1.12. While the final configuration will integrate all stages into a single unit, each step in the process has a degree of independence that allows limited development in isolation from associated aspects of the system.

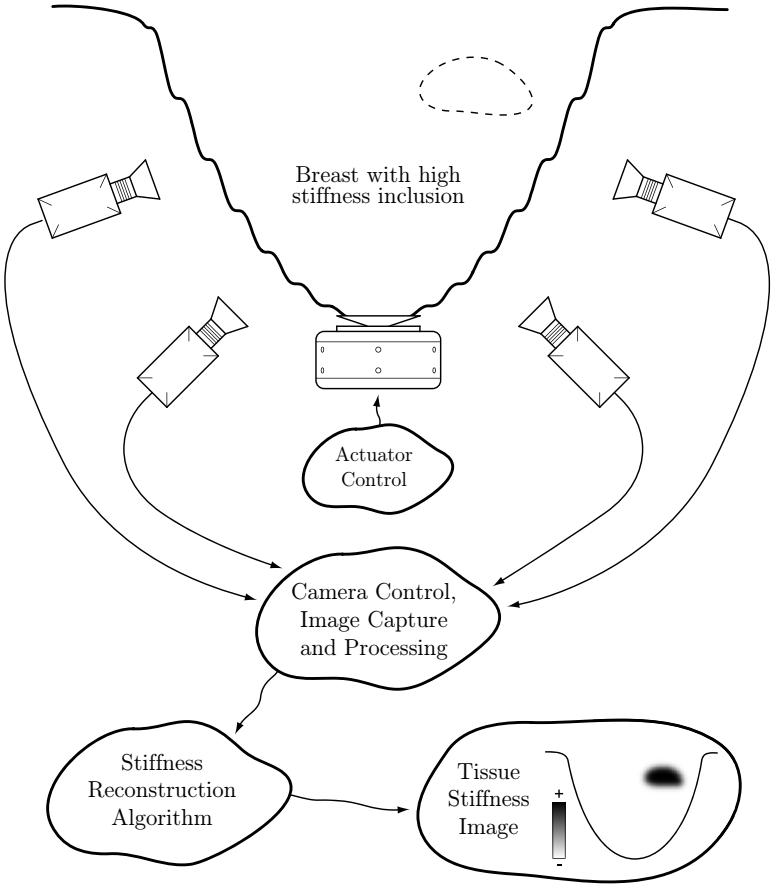

Figure 1.12 Key components in the DIET system.

Mechanical breast actuation is used to induce a steady state, harmonic motion throughout the patient's breast volume. It is currently envisaged that the patient

lies prone on a table with the examined breast hanging in the pendant position, and actuated vertically from below by a small actuator placed against the surface of the breast. Accurate control of the breast actuator allows a precise sinusoidal displacement to be applied at a known frequency and amplitude. Once the motion throughout the breast volume has reached a steady-state, imaging of the breast surface can commence.

The steady-state motion pattern at the surface of the breast is captured using a digital imaging sensor array surrounding the breast surface. Calibration performed prior to breast imaging allows a set of camera-specific parameters to be generated for each sensor, describing the three dimensional position and orientation of each camera with respect to a global origin. Strobe lighting allows consecutive images of the steady-state surface motion to be captured at a lower frequency than the actuation, eliminating the requirement for an expensive, high speed motion capture setup. Stereo imaging techniques are used to convert the consecutive two-dimensional images from all cameras into a three-dimensional vector description of the breast surface motion, where displacements are measured at a set of reference points on the breast surface.

The final stage in the DIET process is a reconstruction that converts the surface motion provided by the image capture system into a three dimensional description of breast tissue stiffness. Here, a non-linear reconstruction algorithm is used in conjunction with a FE model, and minimizes the motion error between observed and computer-simulated breast surface displacement fields. The output from this reconstruction algorithm is a full-volume description of elastic breast properties. This stiffness image should clearly indicate suspicious areas based on their high property contrast with healthy tissue.

1.7 From Proof of Concept to Phantom Elastography

This thesis outlines the progressive steps taken from the theoretical concept of surface based mechanical property reconstruction through to the current implementation of the DIET system hardware. Chapter 2 describes an initial proof of concept trial performed to evaluate the DIET approach to stiffness reconstruction. This experiment involved a basic simulation study that used FE methods to simulate breast model displacement, with stiffness reconstruction performed using inverse algorithms based on previous research in MRE. This study confirmed the feasibility of surface-based property reconstruction, and identified several issues relevant to the experimental implementation of DIET.

The phantoms and equipment used for experimental trials of the DIET system are described in Chapter 3. The details of phantom development, including the progression from simple homogeneous phantoms to more realistic geometries containing high stiffness regions, are considered. The actuation and motion capture system used for experimental data collection is described,along with a brief consideration of the pho-

togrammetry required for three-dimensional point tracking. The iterative refinement of the experimental system over time is discussed in approximately chronological order, where improvements in phantom preparation and experimental hardware were made across the collection of multiple phantom data sets.

Chapter 4 describes an investigation into the experimental surface motions obtained from the tissue-approximating phantoms. These experiments consider the correlation between FE-simulated motion and the motion captured from the experimental phantoms. The sensitivity of surface motion error metric values to variations in phantom material properties is investigated, with the results providing useful information when considering the design of a DIET stiffness reconstruction algorithm. In addition, this chapter details the refinement of the FE model used for motion simulation across the motion studies performed.

The reconstruction algorithms developed to solve the elastic inverse problem are described in Chapter 5. Initial results are presented using traditional deterministic non-linear reconstruction techniques, where the advantages and limitations of such methods when applied to the DIET problem are considered. The development and implementation of a novel phantom stiffness reconstruction algorithm is described, where techniques from stochastic optimization theory are combined with traditional methods to form a hybrid reconstruction algorithm. Results from both simulated and experimentally obtained phantom data sets are presented, and show the improvement in reconstruction accuracy with the refinement of the reconstruction algorithm. A consideration of the computational costs associated with the range of reconstruction algorithms investigated is also provided.

Finally, Chapters 6 and 7 provide a summary of the major findings of the thesis, and an outline the areas of system improvement requiring focus in the future. Further research in these areas will allow more accurate phantom stiffness reconstruction using the DIET system, with an eventual aim towards a limited clinical trial on human subjects. The implementation of the DIET system in such a trial will present a number of significant challenges, but will also represent a major milestone for the project.

Chapter 2

Proof of Concept Studies

The DIET system was originally envisaged as an extension to previous research in MRE, where positive results from both phantom studies and *in vivo* testing have provided solid evidence that motion data sets can be used to determine the elastic properties within a volume of soft material, specifically breast tissue. Using carefully controlled MRI hardware and image processing algorithms, full volume data sets were realized, with three dimensional information about displacement available at voxel resolution [73, 75].

The initial successes of MRE as an elastographic modality were tempered by the requirement of full volume data sets for successful reconstruction. The DIET concept was conceived as a method of enabling volumetric stiffness reconstruction using only surface motion data, hence avoiding the need for costly MRI equipment to obtain data sets. The reduced input data set for DIET reconstruction leads to a challenging inverse problem, where local minima are expected to play a significant role in the performance of any reconstruction algorithm. The work presented in this chapter represents the first studies in DIET, where reconstruction techniques and algorithms for MRE are modified and applied to data sets comprising only surface motion. This study was intended as a proof of concept for an elastographic imaging system based entirely on surface motion data.

2.1 Data Simulation

The lack of previous work in DIET meant that no experimental apparatus existed for measuring surface displacement data from soft phantoms or *in vivo* tissue. Thus, the proof of concept study was undertaken with data simulated using the FE method. FE techniques allow simulation of harmonic displacements from three dimensional models, using standard mathematical techniques, outlined in Appendix A. Sampling from the surface motions calculated by FE analysis provides the data required for a DIET re-

construction. Gaussian random noise was added to the simulated surface data sets to account for inaccuracies in any feasible experimental measurement system.

To provide a reasonable estimation of the geometry involved, a computer model was developed of approximately the same size as a female breast. The absence of commercial meshing software at this stage required that the model was meshed using crude mesh generation code not originally intended for use with the geometry in question. Computational limitations placed an upper limit on the number of nodes in the mesh, based on the memory required to perform the necessary matrix inversions in the FE code. This limitation meant that the initial breast model used was a quarter-hemisphere, with radius 50 mm. Meshing this computer model with linear tetrahedral elements gave a total of approximately 2,700 nodes, where the meshed model geometry is shown in Figure 2.1.

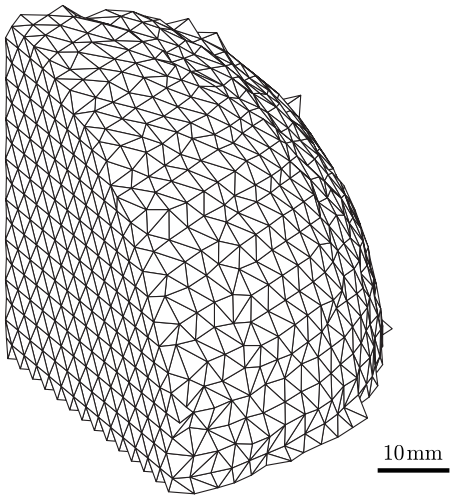

Figure 2.1 The FE mesh used for computer model simulation in the three-region proof of concept study.

An attempt was made to approximate the heterogeneous nature of a human breast by dividing the basic model into two regions with different elastic modulus values. A basic representation of breast physiology divides the volume into an inner region of fibroglandular tissue, with a layer of fatty tissue closer to the skin. However, to give a reasonable approximation to published values, the fibroglandular and fatty tissues were assigned Young's Modulus values of $E = 35\,\text{kPa}$ and $E = 22\,\text{kPa}$ respectively [54]. The outermost 20 mm of the base breast model volume was categorized as fatty tissue, with the remainder having the higher fibroglandular modulus value. Poisson's ratio, ν, and density, ρ, were set at 0.49 and $1{,}000\,\text{kg/m}^3$ respectively, approximating the near-incompressibility of soft tissue due to its high water content [70, 93, 94]. Validation of the compressible material model used for FE simulation was required to confirm that simulations near $\nu = 0.5$ did not introduce significant numerical inaccuracy. This

validation was performed against simulations using an incompressible material model, with details included in Appendix A.

A range of high stiffness inclusions were modelled using the basic FE mesh, with a total of 27 separate models representing a combination of three inclusion locations, sizes, and stiffness contrasts to the surrounding tissue. Variation of inclusion sizes and positions allowed the sensitivity of the reconstruction method to be investigated. All inclusions were spherical, with centers 15, 25 and 35 mm from the breast surface. These positions represent shallow, middle, and deep inclusion locations. Inclusion diameters were 5, 10 and 15 mm, representing small, medium and large inclusions. Figure 2.2 shows the range of internal geometries used for computer simulation. The stiffness contrast values chosen for the inclusion were relative to the fibroglandular model region, and were chosen to represent a range of inclusion stiffness values around those obtained in relevant clinical testing [54, 56]. Contrast values of 5x, 10x and 100x gave inclusion modulus values of 174 kPa, 348 kPa and 3,480 kPa respectively.

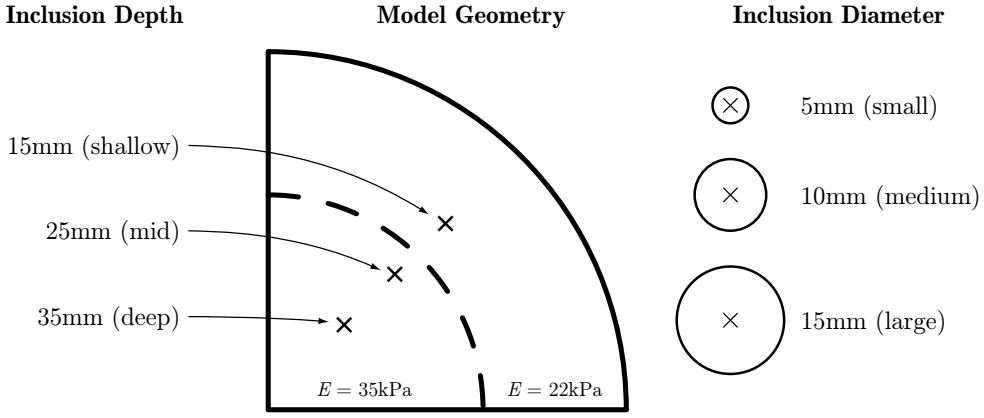

Figure 2.2 The geometry used to generate simulated data sets in the three-region study.

The FE code used to simulate model motion was written in Fortran 77, and assumes an undamped, linear elastic material model, in line with previous work in MRE [74]. Stiffness values within the mesh were assigned nodally based on the three dimensional position of the node with respect to the stiffness distribution being simulated. The boundary conditions applied during FE simulation were an approximation to a possible clinical implementation of a DIET system, where harmonic vertical displacement was applied over a small semi-circular area at the highest point of the model. An actuation frequency of 100 Hz was chosen as it led to mechanical waves with a wavelength of approximately 30 mm, allowing the motion to be clearly defined on the model surface. The amplitude of actuation was 10 mm. The bottom face of the model had displacement constrained to zero in all directions, representing a rough approximation of the chest wall attachment. The quarter-hemisphere model used in the initial study required additional boundary conditions to constrain the model in a symmetric manner, ensuring

realistic displacements. These additional boundary conditions were applied at the two vertical internal faces of the model, and prescribed no in-plane forces or normal displacement.

The output from FE simulation is a full vector of steady-state motion amplitudes for each orthogonal motion component, x, y and z, at every node within the model. The simulated motion observed at the surface of the mesh for a selection of the cases simulated is shown in Figure 2.3. Here, the large amplitudes observed are directly proportional to the amplitude of actuation for the linear elastic model assumed. Therefore, clinically unrealistic displacements in the simulated data could be reduced with a reduction in the actuation amplitude. Thirty two randomly selected nodes on the outer surface of the model were used as reference points, simulating the measurement of motion data at points on the surface of the breast only. An assumed value for experimental measurement error was added to all reference point displacements during motion processing. This noise was normally distributed about the mean surface displacement amplitude, with a standard deviation of 5% of the average scale of motion. The resulting simulated data set comprised 96 orthogonal displacement measurements for each of the 27 scenarios simulated.

2.2 Three Region Reconstruction

The reduced number of known displacement values used as input to the reconstruction algorithm requires a corresponding reduction in the number of reconstructed parameters. Reconstruction of a modulus value at all 2,700 nodes within the model using only 96 known displacement values presents a highly ill-posed problem with little chance of success, particularly given the noise added to the input data. The number of reconstructed parameters for the inverse problem was reduced by dividing the FE model into regions of constant modulus value. These regions were based on the internal geometry configuration used for forward FE simulation, resulting in a total of three independent stiffness values, one each for the fibroglandular, fatty, and inclusion regions of the model.

Dividing the domain into fixed regions would be highly impractical in a real life application due to the necessary *a priori* knowledge of internal tissue structure. However, it was considered appropriate for the initial study, where the success of the method regardless of significant assumptions was unknown. The large reduction in parameter space for the inverse problem also reduced computational cost, allowing rapid simulation at this early stage.

The inverse elastic reconstruction algorithm used in the three-region study was based on the gradient descent method, and comprised Fortran 77 code developed from algorithms already in use for MRE data [74, 94]. Here, the reconstruction aimed to

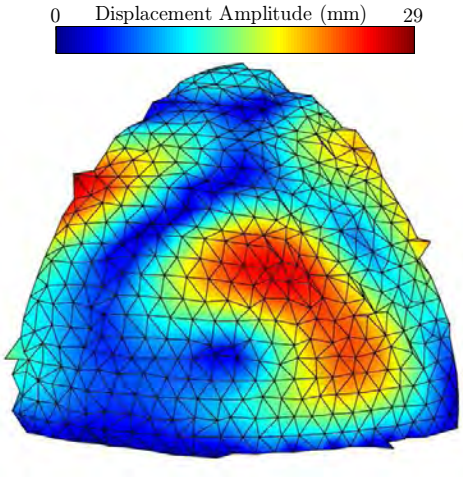

(a) Shallow, 5 mm diameter, 5x contrast.

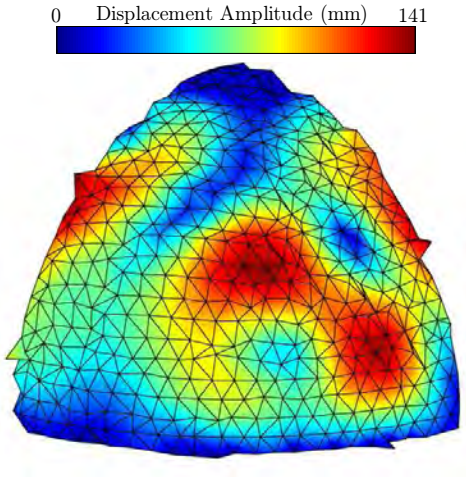

(b) Middle, 10 mm diameter, 10x contrast.

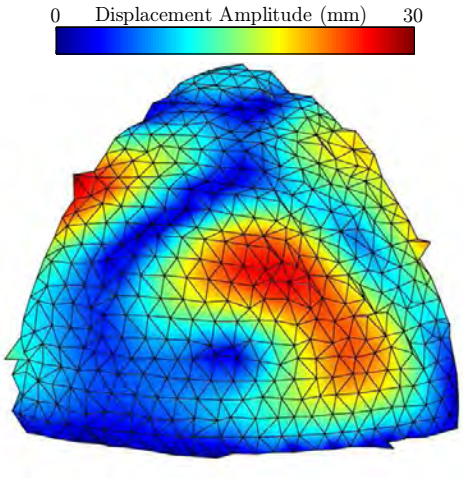

(c) Deep, 5 mm diameter, 100x contrast.

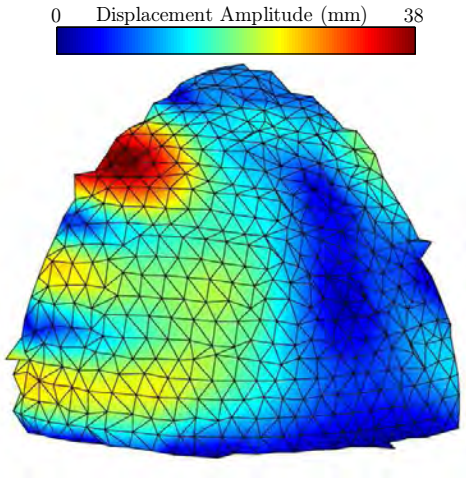

(d) Deep, 15 mm diameter, 100x contrast.

Figure 2.3 Surface displacement amplitudes for four of the inclusion scenarios simulated in the three-region study.

minimize an error term representing the difference between the displacements simulated at the target stiffness distribution and those simulated using the current values for the three stiffness parameters. The initial Young's Modulus guess for all three model regions was 24 kPa, chosen as an approximation to the mean nodal stiffness value across the entire model. Reconstructions on each simulated scenario were run to 300 iterations, regardless of algorithm convergence. Each iteration required approximately 90 seconds to complete on a Linux workstation with a 1.4 GHz CPU.

Figure 2.4 shows the convergence of the reconstruction algorithm for a selection of simulated scenarios. Figures 2.4(a) and 2.4(d) indicate a failed reconstruction, where the inclusion stiffness is reconstructed as softer than the surrounding regions. Figures 2.4(b)-(c) represent reconstructions considered successful, where the modulus value for the inclusion is correctly identified as greater than the surrounding material. In addition to successful and unsuccessful reconstructions, cases where the fatty or glandular modulus values are reconstructed at unrealistic values were considered inconclusive. The lack of convergence observed in a large number of scenarios was not of significant concern due to the unsophisticated gradient descent reconstruction algorithm used.

Figure 2.5 is a summary of the reconstruction result obtained in all 27 scenarios tested in the three-region study. The success rate of the algorithm is nearly constant across the full range of inclusion stiffness contrasts. Of particular significance is the algorithm's identification of a stiff inclusion in all the deep, low-contrast cases simulated. These are situations that present a significant challenge to conventional screening and diagnosis modalities. The algorithm has limited success with cases where the inclusion is large, even though these would initially appear to be the easiest cases to reconstruct. In addition, the algorithm was found to be very sensitive to the initial parameter stiffness guess, and it appeared that in a number of the large inclusion cases that using the same initial guess of 24 kPa was no longer suitable, as it led to convergence at an incorrect solution representing a local error minimum.

The reconstructed results from the initial proof of concept study indicated that a surface motion based reconstruction algorithm had the potential to successfully identify a high stiffness inclusion given only a selection of surface displacement data. However, significant issues were raised that required further investigation. Prevalent among these concerns was the tendency of the inversion algorithm to converge to solutions that only represented a local error minimum, and not the global optimum parameter values. Issues with mesh resolution and accuracy were likely causes for the unrealistically large simulated displacements observed, most probably as a result of resonance within the model. These issues indicated that a further study would be of benefit, using a refined FE mesh, and a more realistic approach to the reconstruction of internal stiffness that did not rely on prior knowledge of the internal model geometry.

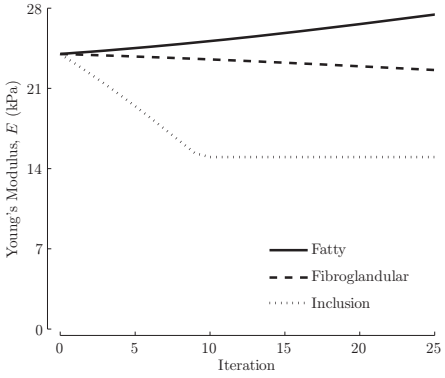

(a) Shallow, 5 mm diameter, 5x contrast.

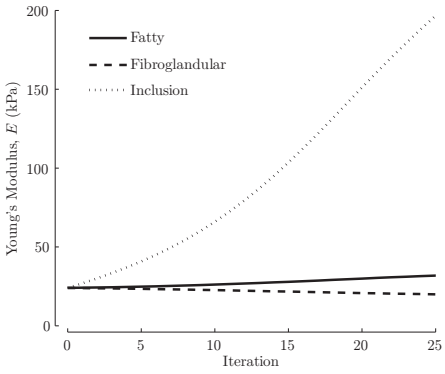

(b) Middle, 10 mm diameter, 10x contrast.

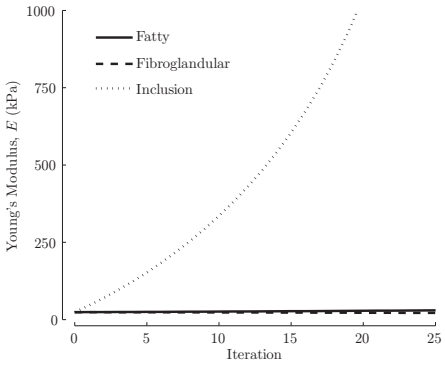

(c) Deep, 5 mm diameter, 100x contrast.

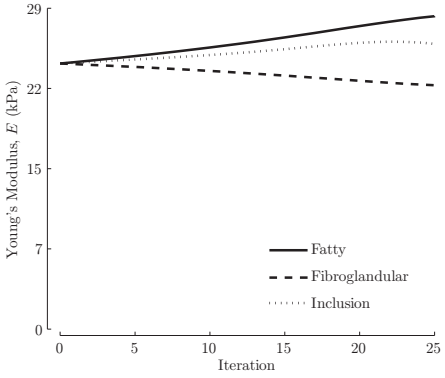

(d) Deep, 15 mm diameter, 100x contrast.

Figure 2.4 Convergence of the three-region reconstruction algorithm for a selection of inclusion scenarios, where the target modulus values for the fibroglandular and fatty regions were $E = 35\,\text{kPa}$ and $E = 22\,\text{kPa}$ respectively.

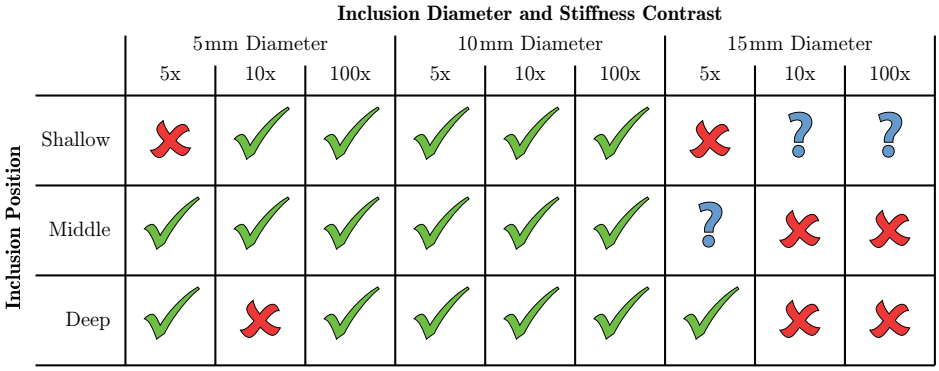

Figure 2.5 A summary of the reconstruction results from the three-region study, showing successful, unsuccessful and inconclusive reconstructions.

2.3 Dual-Mesh Reconstruction

A significant limitation of the initial three-parameter reconstruction study was the required *a priori* knowledge of the model's internal structure when formulating the inverse problem. Because the three parameters described in Section 2.2 were based on known model physiology, the reconstruction algorithm had no way of indicating an inclusion in a more generalized case, where internal structure was not known. As this general case is the intended target of the DIET system, a second phase of work was undertaken that aimed to allow a more sophisticated stiffness reconstruction through the use of an increased number of reconstructed parameters. This additional study also allowed issues concerning mesh resolution and accuracy to be addressed.

The availability of a commercial FE meshing software package and an increased computational capacity at the time of this study allowed creation of a significantly refined FE mesh, shown in Figure 2.6. The mesh contained approximately 8,700 nodes, with the more advanced meshing software able to produce significantly smoother external surfaces. Here, the external model geometry remained the same as that described in Section 2.2.

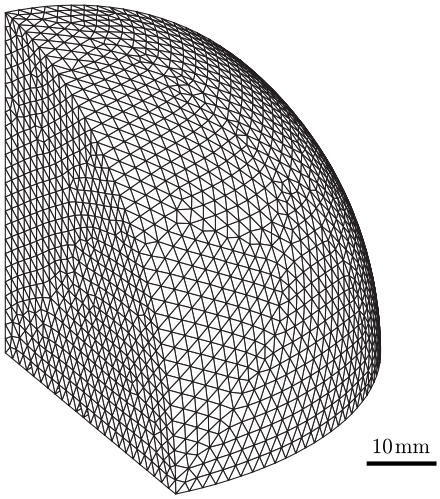

Figure 2.6 The fine mesh used for FE displacement simulation during dual-mesh reconstructions.

A single inclusion scenario was modelled for this experiment, where a 10 mm diameter spherical inclusion was located 30 mm from the surface of the model. The target material properties for the 'healthy' regions were the same as the initial study, with an inner fibroglandular stiffness of $E = 35\,\text{kPa}$, and an outer fatty region where $E = 22\,\text{kPa}$. The inclusion stiffness was set at $E = 175\,\text{kPa}$, representing a stiffness contrast of approximately seven times the surrounding material.

Boundary conditions applied to the mesh were the same as those described for the three-region study, with actuation amplitude limited to 1 mm in an attempt to avoid the unrealistically large surface displacements observed with the previous mesh. Surface displacement amplitudes resulting from FE simulation of the model at 100 Hz are shown in Figure 2.7. Here, the symmetric appearance of the motion field indicates the mesh is sufficiently refined to avoid significant numerical errors.

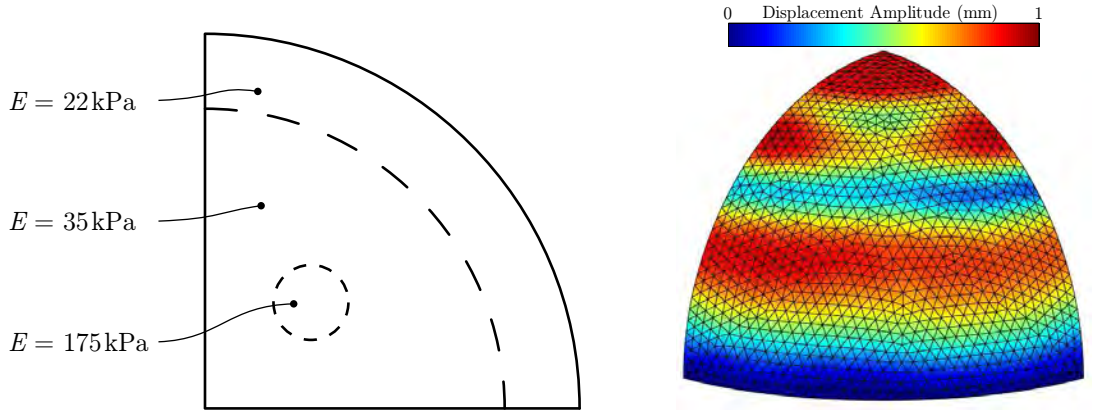

(a) The target stiffness distribution along a plane passing through the center of the inclusion.

(b) Simulated surface displacement at the target stiffness distribution when actuated at 100 Hz.

Figure 2.7 The stiffness distribution and surface motion from the target model in the dual-mesh study.

Increasing the number of reconstructed parameters for this study required a corresponding increase in the number of surface displacement values used in the inverse problem in order to maintain the posedness of the reconstruction. Promising advances in the concurrent development of the DIET motion tracking system indicated that a high point resolution on the breast surface was possible [95], allowing all 980 nodes on the exterior surface of the mesh to be considered as reference points for motion measurement. Normally distributed noise was again applied to the simulated motion values, with a standard deviation of 10% of the mean surface motion amplitude value.

The desire for an increased number of parameters in the reconstruction problem led to the development of a dual-mesh scheme for reconstruction of the model stiffness distribution. Here, the displacements were discretized on a fine mesh to ensure accurate capture of the model physics, while the elastic property distribution was supported on a coarse mesh, which allowed for gradual stiffness variation while maintaining a reasonable match between the number of measurements and the number of unknowns. The conversion from a stiffness distribution supported on this coarse mesh to the fine mesh was performed by interpolation, where the value of the stiffness at each fine node was the linear interpolation of the coarse node stiffness values surrounding it. This

interpolation method required that the coarse mesh elements completely enclosed all fine mesh nodes to prevent numerical errors.

A two dimensional example of a dual mesh scheme is shown in Figure 2.8, where the material property distribution is interpolated from the coarse (black) nodes to the fine (red) mesh used for FE simulation. Using a coarse mesh scheme gave the inverse problem the flexibility to reconstruct a range of internal stiffness distributions. Here, a variable number of coarse mesh points can increase or decrease the spatial resolution of the reconstructed solution.

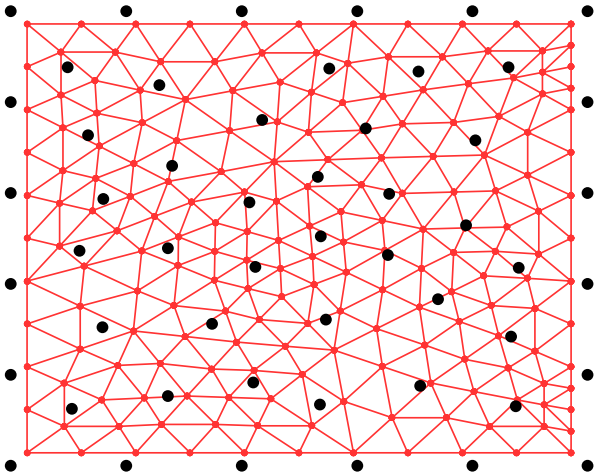

Figure 2.8 A two-dimensional representation of a dual mesh scheme, where displacements are calculated using the fine mesh (red), and material properties are described at the coarse nodes (black).

Reconstructions were performed using a range of coarse meshes varying from 20 nodes through to over 800. The gradient, or Jacobian, matrix calculation routine within the gradient descent algorithm was modified to account for the added interpolation required for the dual mesh scheme. Figure 2.9 shows the best results obtained from the dual mesh reconstruction study. Results from the vast majority of reconstructions failed to correctly localize the hard inclusion, although many were able to detect the presence of a high stiffness region. These results indicated that local minima were severely hampering the reconstruction performance as the number of reconstructed parameters was increased.

2.4 Summary

The first proof of concept studies in DIET applied modified theory and computational algorithms from MRE to the surface motion based reconstruction problem. Initial results from the three region simulation and reconstruction study indicated that reconstruction of a simplified internal modulus distribution was possible using the DIET

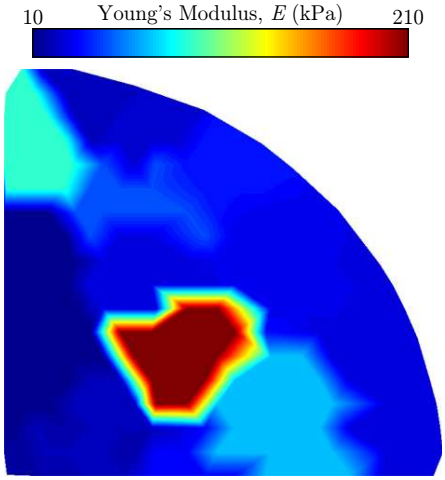

(a) Coarse material property mesh with 20 nodes.

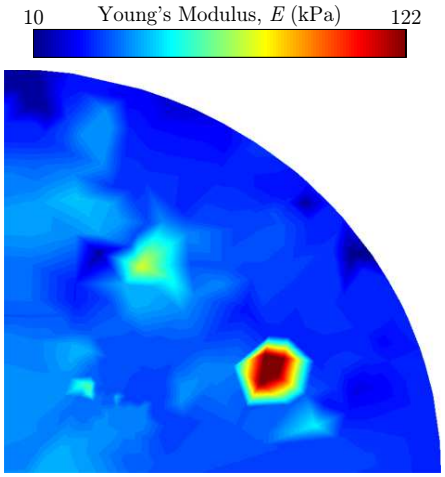

(b) Coarse material property mesh with 839 nodes.

Figure 2.9 The best reconstructed stiffness distributions achieved during the dual-mesh reconstruction study, where the image plane passes through the center of the target inclusion position.

method. Limitations in the accuracy and flexibility of both the forward FE model and the reconstructive approach led to a dual mesh study with an increased number of reconstructed parameters. Although the dual mesh study also contained promising results, the majority of reconstruction attempts failed to reconstruct the correct target modulus distribution. Analysis of the reconstruction algorithm code confirmed it was performing as intended, indicating that the limitations of the approach had more to do with the forward FE model, and the relationship between internal stiffness distribution and observed surface displacements.

Difficulties in analyzing the limited success of the reconstruction algorithms led to a decision to shift focus to soft phantom based studies. Such studies would allow more thorough evaluate the overall DIET system in a controlled experimental environment. Concurrent research had reached a point where an experimental actuation and motion system was ready for testing [96]. This research provided the hardware and software required to extend the evaluation of the DIET concept into experimental phantom studies.

Chapter 3

Experimental Methods

An important step in the development of any soft tissue imaging modality is a testing phase using tissue approximating phantoms. In such testing, experimental data collection and processing can occur in a controlled environment, allowing detailed system analysis prior to attempting *ex vivo* or *in vivo* testing. The first experimental studies using the DIET system were performed on data obtained from a series of cylindrical phantoms.

This chapter describes the methodology behind the selection of suitable phantom materials, and the creation of the phantoms. Also detailed is the experimental system developed for phantom actuation and motion capture, including the algorithms that allow comparison of measured data with FE-simulated displacement fields. Developments in the major facets of the experimental method are presented chronologically, detailing the improvements in experimental technique over the collection of a number of experimental data sets.

3.1 Phantom Preparation

Previous soft tissue imaging research has been supported by the use of tissue approximating phantoms created from a range of both natural and artificial materials, including gelatine and agar based gels, and polymer materials [53, 97]. Experimental data collection for the DIET system utilized two distinct classes of phantom material. The first experimental efforts used gelatine based phantoms. An investigation of alternative materials led to soft silicone gels being used for subsequent experiments.

A cylindrical phantom geometry was chosen to provide a simple shape for mold manufacture using commonly available hardware components. In addition, when actuated along the major axis, the cylindrical shape was expected to provide a symmetric mechanical deformation pattern on the phantom surface. This symmetry would allow

for a simplified camera system that had been developed to capture surface deformation from only a small area of the phantom surface.

3.1.1 Gelatine Phantoms

Gelatine is a translucent solid manufactured primarily from collagen, a connective tissue found in animals. Raw materials for gelatine manufacture are sourced primarily from animal processing plants, and include skin, cartilage and bone [98]. After pre-treatment to sanitize and stabilize the raw material, gelatine is extracted in a multi-stage process using hot water. Filters and separators in a purification stage separate gelatine from any fat and other fibres remaining in the mixture. The resulting material is a soft gel containing hydrolyzed collagen. Drying, grinding, sifting and blending this gel produces small granules suitable for transport and storage, shown in Figure 3.1.

Figure 3.1 Granules of processed gelatine, a raw ingredient in the first experimental phantoms.

A gelatine-based hydrogel was chosen for the initial phantom experiments because of its linear elastic behavior and similar mechanical properties to soft human tissue [97]. In addition, it is commonly used in testing medical imaging modalities [76, 97, 99]. The major steps in the manufacturing process for the gelatine phantoms used in this research are outlined below:

1. Distilled water was heated to 70 °C and mixed with 37% 2-Propanol. The addition of Propanol altered the sound speed in the finished phantom. While this property was not imperative for the DIET system, as the testing did not involve ultrasound, the addition of Propanol ensured the compression wave speed was similar to that of soft tissue.

2. A small amount of titanium dioxide (TiO_2) powder was added to the hot liquid mixture. This gave the final phantom a white color, ensuring the surface motion was easily measured during actuation.

3. Granulated 20A grade gelatine was slowly added to the water mixture until completely dissolved. The mixture was stirred for at least ten minutes to ensure complete dissolution of the gelatine granules. The final stiffness of the phantom was determined by the amount of gelatine added at this stage.

4. After waiting for the temperature of the mixture to decrease to approximately 40 °C, a small amount of Formaldehyde was added to initiate the cross-linking process. Continued stirring ensured the Formaldehyde was evenly distributed throughout the mixture.

5. The warm liquid was poured from the mixing vessel into a mold, and left for 24 hours at room temperature, to allow the cross-linking process to complete and form a congealed solid. After setting, the resulting phantom was removed from the mold and stored in an airtight container, to prolong its shelf life.

Experiments with gelatine composition and manufacturing methods resulted in two different types of gelatine being used to create phantoms, with ingredients listed in Table 3.1. A 'soft' gelatine was created using 20 g of gelatine granules, with 40 g of raw gelatine used for a second, 'hard', gelatine material.

Table 3.1 The ingredients used to make to make the two types of gelatine used for phantom experiments.

	Identifier	
Ingredient	**Soft**	**Hard**
Distilled Water	300 ml	300 ml
2-Propanol	25 ml	25 ml
TiO_2	0.1 g	0.1 g
Gelatine	20 g	40 g
Formaldehyde	3 ml	3 ml

The high water content of the gelatine material made the phantoms highly susceptible to the environment in which they were left to set. Qualitative examination of gelatine phantoms created using a range of mold designs indicated that exposure to air when setting had a negative impact on the resulting phantom. Areas of the gelatine exposed during setting were found to have partially dehydrated and hardened after exposure to a room temperature environment. This sensitivity required careful mold design to ensure minimal exposure to the air while the gelatine set.

The final mold design used for gelatine phantom preparation is shown in Figure 3.2. The mold's circular top and bottom (1) were cut from 15 mm thick plastic sheet. A thin sheet of clear acetate film (2) wrapped around the end caps formed the cylindrical mold wall. Using clear sheet allowed the inside of the mold to be visible when filling with liquid gelatine. Fastening the acetate sheet to the end caps with double sided tape created a watertight seal that prevented gelatine leakage.

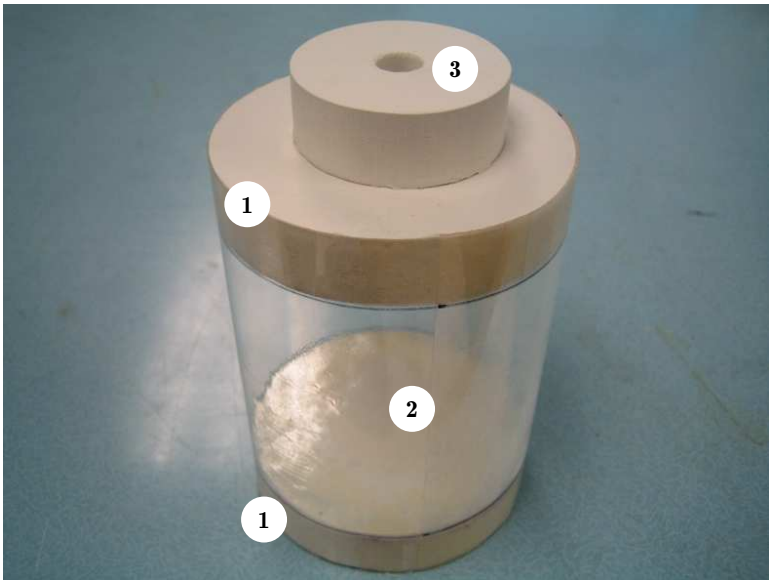

Figure 3.2 The cylindrical mold developed for gelatine phantom preparation, with end caps (1), clear sidewalls (2), and pouring 'chimney' (3) indicated.

The top of the mold was extended using a second plastic disc (3), with a small circular hole drilled through both layers. This 'chimney' functioned as an opening through which the liquid gelatine mixture was poured into the mold. In addition, filling the mold to the top face indicated by (3) prevented gelatine shrinkage during the setting process from leaving a depression in the top of the final phantom. All mold components were given a thin coating of a mold release spray before assembly to assist the phantom de-molding process.

After setting for twenty-four hours, the mold was carefully removed from around the phantom. Any gelatine in the chimney was removed using a scalpel. Two of the many test phantoms created during the mold development process are shown in Figure 3.3.

Two homogeneous phantoms created from gelatine were used for experimental motion capture. The first phantom was made using the soft gelatine ingredients listed in Table 3.1. After results had been obtained from this phantom, and experimental techniques advanced, a subsequent phantom was created using the hard gelatine recipe.

Figure 3.3 Two gelatine phantoms created during the mold development process.

Both phantoms had a number of reference points added to their exterior surface using an oil-based permanent marker prior to experimental motion capture.

Several significant limitations with the gelatine material were observed during manufacturing and qualitative evaluation of the gelatine phantoms. The use of highly toxic Formaldehyde to initiate cross-linking within the gelatine mixture required that parts of the manufacturing process were performed within a fume hood, while wearing protective equipment. In addition, to avoid any potential health risk, the gelatine phantoms were only handled while wearing latex gloves.

Phantom desiccation was observed to be a significant problem after de-molding, where the majority of the phantom surface was exposed to air. Dehydration of the phantom surface had the potential to alter the material properties of the gelatine, with the exposed surface hardening as the moisture content decreased. In addition to a complicated, airtight mold, phantom dehydration limited mechanical testing and surface motion capture to a time window of between one and two days after phantom manufacture.

The high temperature required for manufacture posed difficulties when considering heterogeneous gelatine phantoms. When the DIET system was sufficiently advanced, the natural progression from simple homogeneous phantoms would be to heterogeneous models with distinct hard and soft regions. However, tests performed indicated that any existing, set, gelatine in a mold began to melt when it came into contact with additional warm liquid gelatine, making it difficult to determine the appearance and location of the interface position between the hard and soft regions.

3.1.2 Silicone Phantoms

Silicone is a form of synthetic elastomer made from a cross-linked polymer reinforced with silica, and available in many forms, from liquid to solid [100]. Room Temperature Vulcanizing (RTV) soft silicone gel was identified as a suitable phantom material, having several advantages when compared with the gelatine previously used:

- Silicone gels were available in food grade standards, indicating many types were non-toxic, and completely safe to handle.
- The silicone manufacturing process was extremely simple and rapid, requiring only a mixture of two constituent parts.
- The manufacturing process could be performed entirely at room temperature.
- Achieving a range of phantom colors was possible using intrinsic pigments.
- The cured silicone gel was stable in air, resilient, and had an indefinite shelf life, allowing phantoms to be repeatedly tested over a period of time with no significant changes in material properties.
- The availability of silicone gels with a range of hardness values meant that creating heterogeneous phantoms from both hard and soft silicone would not present significant difficulties.
- The raw materials for silicone manufacture were affordable, and could be purchased in the small quantities required.

The silicone gel used for phantom manufacture was sourced from an American supplier to the prosthetic and special effects industry (Factor II Inc.). Dialogue with sales consultants identified two types of silicone likely to be suitable for approximating both soft and hard tissue, designated A-341 and LSR-05 respectively. Both products were Platinum catalyzed RTV-2 silicone gels, indicating a two part mixture that would cure in total confinement if required. Material Safety Data Sheets (MSDS) for both A-341 and LSR-05 silicones are included as Appendix B. The manufacturing process for both soft and hard silicone materials involved the same major steps:

1. Silicone components Part A and B were weighed according to manufacture-specified ratios into a plastic mixing container.
2. A small amount of intrinsic pigment was added to give the desired final phantom color.
3. Ingredients were thoroughly mixed by hand to ensure uniform distribution of silicone components and pigment.

4. The mixing container was placed into a small venturi vacuum chamber, shown in Figure 3.4, where a light vacuum was applied for 10–15 minutes. This stage removed any entrained air bubbles from the mixture.

5. The final silicone mixture was poured into a mold, and left to set at room temperature for 6–12 hours.

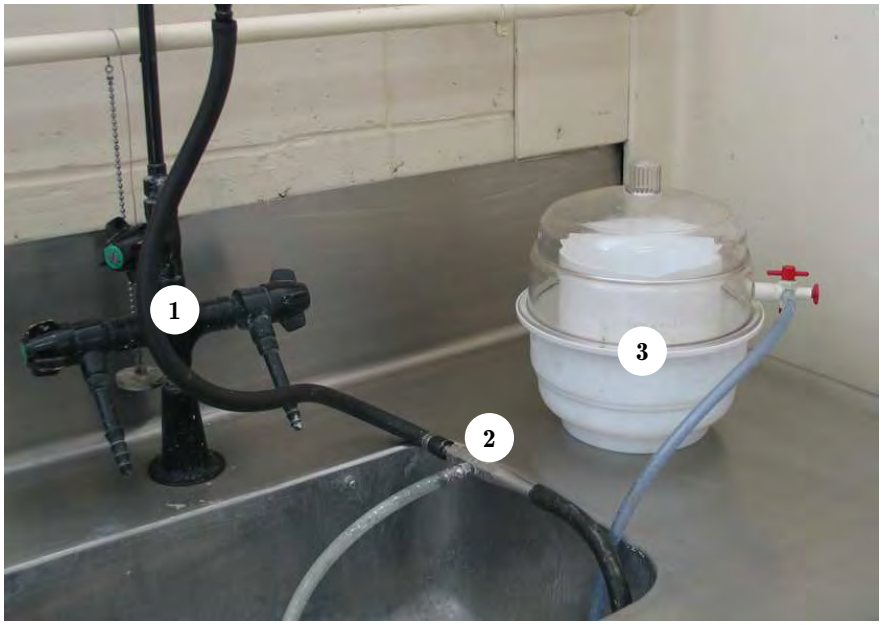

Figure 3.4 The venturi vacuum setup used to remove air from the silicone mixture, where the water supply (1), venturi (2), and chamber (3) are indicated.

Experimentation with both A-341 and LSR-05 indicated that minor variations in the ratio of Part A to Part B for each type of silicone had no significant effect on the stiffness of the resulting material. Hence, silicone stiffness was controlled using a combination of A-341 silicone and LSR-05 silicone, where the final stiffness was determined by the ratio of the two types. Combining the two silicones did not have an adverse effect on the resulting material as both types were chemically similar. The weight percentages of each type of silicone used to create the final 'soft' and 'hard' silicone materials are listed in Table 3.2.

The straightforward silicone manufacturing process meant that the cylindrical mold developed for gelatine phantoms in Section 3.1.1 could be simplified for silicone phantom manufacture. This final silicone mold developed is shown in Figure 3.5. The vertical sides of the mold (1) were created from 80 mm nominal diameter PVC pipe, providing an accurate circular cross-section and straight sides. This pipe section was split longitudinally into two pieces, allowing easy disassembly. A shallow groove machined around the inside of the pipe indicated a phantom height of 75 mm.

Table 3.2 The weight percentage composition of the two types of silicone used for phantom preparation.

	Identifier	
Ingredient	**Soft**	**Hard**
A-341 Part A	90%	36%
A-341 Part B	10%	4%
LSR-05 Part A	-	30%
LSR-05 Part B	-	30%

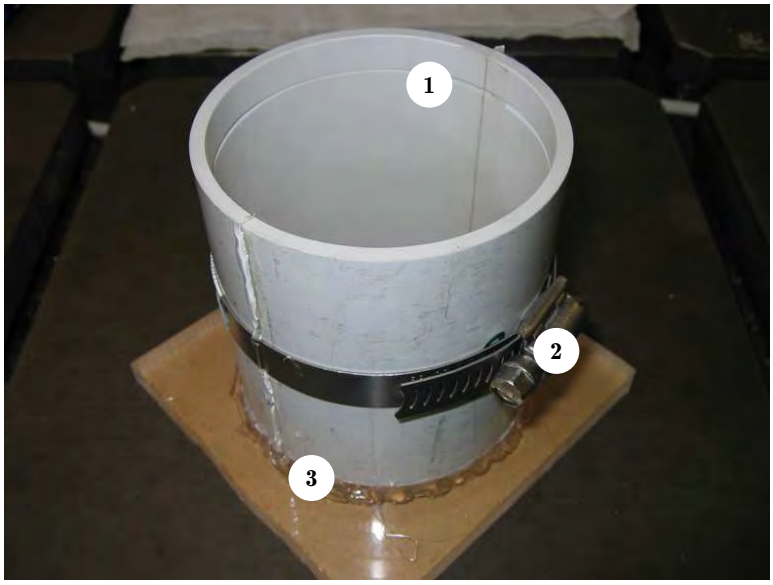

Figure 3.5 The mold used to cast silicone phantoms, with mold wall (1), clamping screw (2), and fastening glue (3) indicated.

To ensure the mold was watertight, a pipe clamp (2) was used to secure the sides of the mold together, and sticky tape was used to seal the internal seams. Hot glue was used liberally (3) to attach the pipe to a clean, flat plastic base plate. The watertightness of the mold was checked by filling with water prior to silicone casting. A lubricating silicone spray was applied to the interior surface of the mold before introducing the liquid silicone to assist the de-molding process. After curing, the phantoms were removed by disassembling the mold and gently prising the silicone material free. The phantoms were then stored at room temperature in a box to prevent accidental damage.

A total of five cylindrical phantoms were created using the soft and hard silicone materials identified in Table 3.2. The first two phantoms were homogeneous, with

one made entirely from soft silicone, and another from hard silicone. A further two heterogeneous phantoms were subsequently created for more advanced DIET system testing. A 'stacked' phantom was created with a layer of hard silicone beneath a layer of soft silicone, while a 'concentric' phantom contained a cylindrical core of hard silicone surrounded by soft silicone. The first four silicone phantoms created for experimental motion capture are shown in Figure 3.6. The reference points visible on the surface of these phantoms were created from small pieces of paper and glitter. The final silicone phantom created comprised a hard sphere within a soft cylinder, and is discussed in more detail in Chapter 5.

3.2 Material Testing

Independent knowledge of material properties is important for verification of an elastographic imaging system. In the experimental work with the DIET system, measured mechanical property values provided approximate material property values that were used to validate reconstructed results. This section describes the static and dynamic mechanical testing attempted on both gelatine and silicone phantom materials. All mechanical testing was performed using a Dynamic Mechanical Analysis (DMA) machine (Pyris Diamond DMA, Perkin Elmer Instruments), shown in Figure 3.7. The highly pliable nature of the phantom materials ruled out tensile material testing, meaning compressive testing was used for all mechanical measurements.

Mechanical testing samples were created from small batches of gelatine and silicone produced using the same method as the materials used for phantom manufacture. All samples were tested at room temperature approximately 24–48 hours after preparation. Gelatine samples were prepared using a sharp hollow cylindrical cutter of approximately 10 mm diameter to take cylindrical core samples from a block of gelatine. The extracted gelatine cylinder was then cut into 3–5 mm lengths with parallel ends using a razor blade, producing the small compression samples required. This technique ensured that the gelatine samples did not come from material exposed to the air when setting, avoiding the issue of surface dehydration described in Section 3.1.1. A mold for silicone mechanical testing samples was created by drilling 10 mm diameter holes in a 6 mm thick plastic sheet. Sealing the bottom of each hole and casting small amounts of liquid silicone created small, highly regular, cylindrical compression samples.

Material density estimates were made by weighing the homogeneous phantoms using digital scales. Measurements of the gelatine phantoms indicated a material density between 1000–1100 $\mathrm{kg/m^3}$. The measured density of the soft and hard silicone materials was $\sim$975 $\mathrm{kg/m^3}$ and $\sim$1045 $\mathrm{kg/m^3}$ respectively. All density calculations were performed assuming the phantoms had perfectly cylindrical geometry.

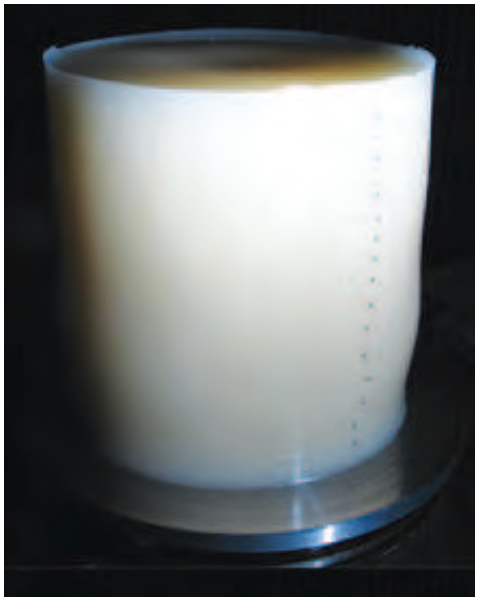

(a) 'Soft' homogeneous phantom.

(b) 'Hard' homogeneous phantom.

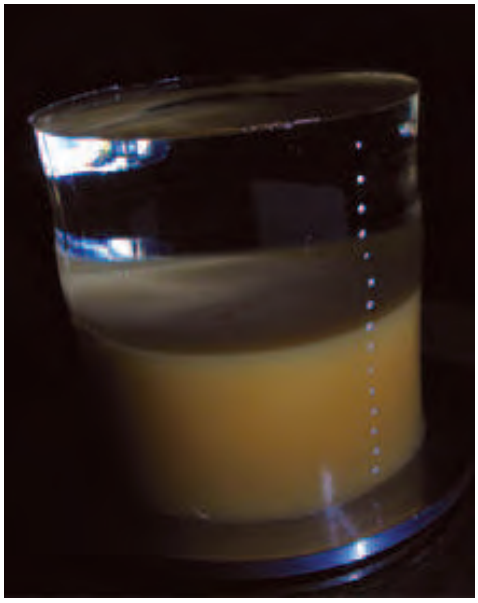

(c) 'Stacked' heterogeneous phantom.

(d) 'Concentric' heterogeneous phantom.

Figure 3.6 The four silicone phantoms used for experimental motion capture.

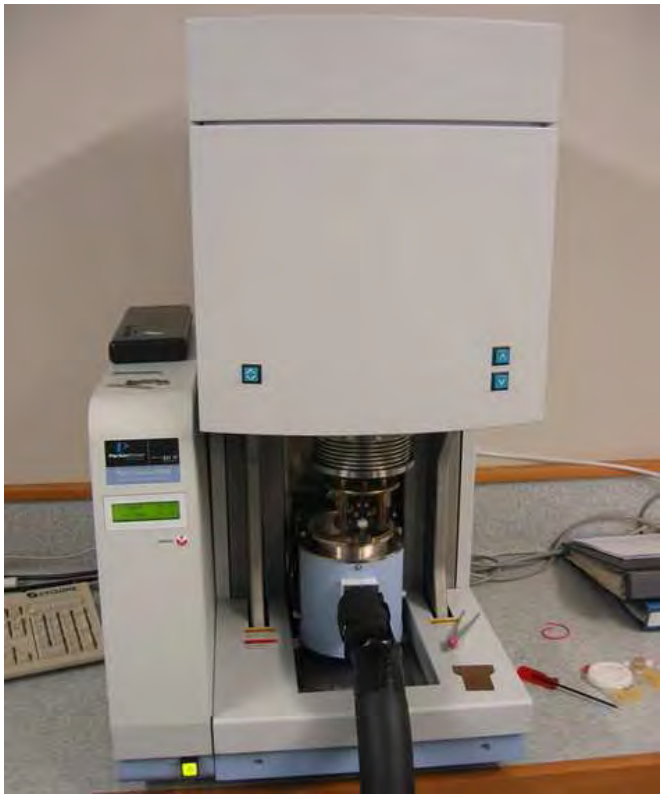

Figure 3.7 The Pyris Diamond DMA machine used for mechanical testing of phantom materials.

Static compressive tests were performed at room temperature on a range of samples from both gelatine and silicone materials to a strain of approximately 0.1. A low strain rate of 100 μm/min was used to approximate a static loading scenario. Stress-strain plots from static testing of both gelatine and silicone samples are shown in Figure 3.8.

The stress-strain relationship observed for both gelatine and silicone materials indicated an approximately linear elastic material behavior over the strain range tested. The apparent non-linearity at low strain for the hard silicone sample in Figure 3.8(b) is the result of incomplete contact between the upper testing platen and the top of the sample, meaning it was not completely constrained until a strain of approximately 0.02. The two small discontinuities in the hard silicone loading path are due to small amounts of slip, where the sample end faces moved slightly against the testing platens. Approximate Young's Modulus values, E, were calculated for all samples using Hooke's Law, where E is the gradient of the stress-strain plots in Figure 3.8:

$$E = \frac{\sigma}{\epsilon}. \tag{3.1}$$

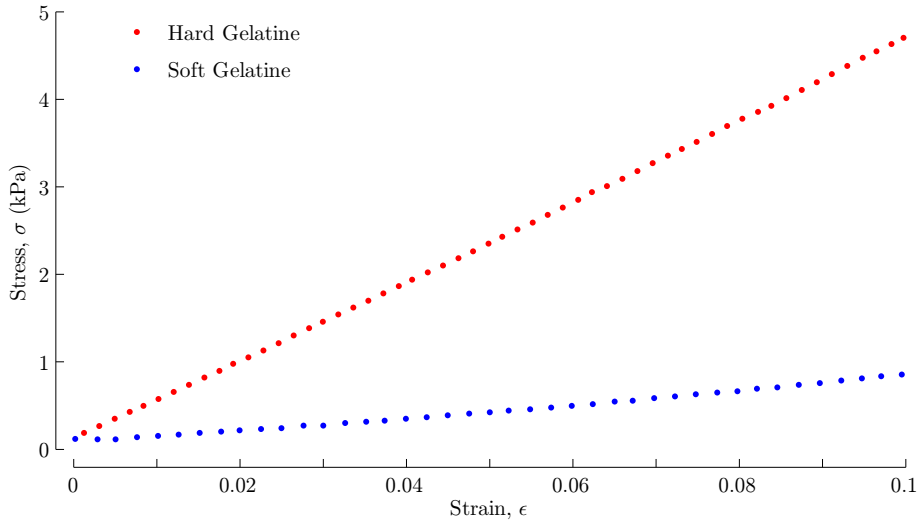

(a) Gelatine stress-strain plots.

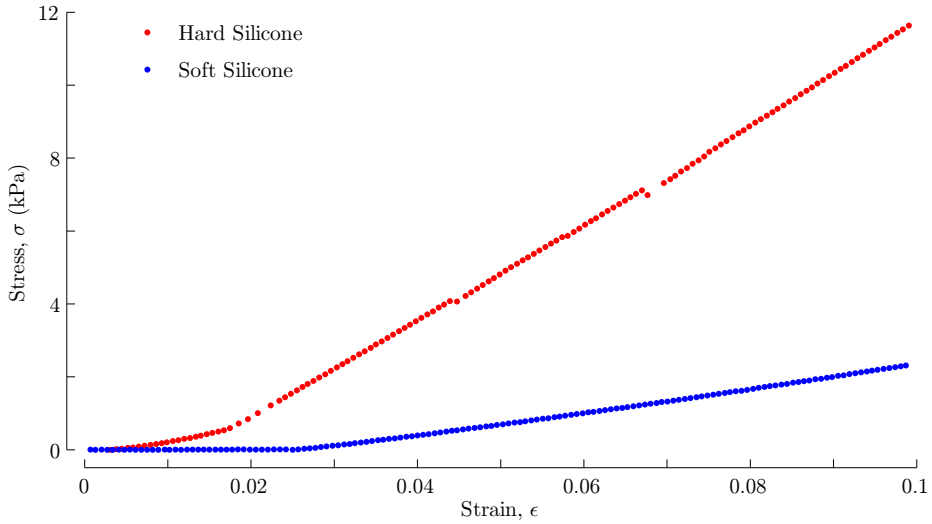

(b) Silicone stress-strain plots.

Figure 3.8 Static testing results from the gelatine and silicone materials used for phantom manufacture.

The calculated Young's Modulus values for the four phantom materials tested are given in Table 3.3.

Table 3.3 Young's Modulus values obtained from static testing of phantom materials.

Material	E
Soft Gelatine	9 kPa
Hard Gelatine	26 kPa
Soft Silicone	32 kPa
Hard Silicone	135 kPa

During static testing it was observed that there was little or no slip between the material sample and the testing platens. This type of boundary condition gives a non-uniform strain distribution within the sample, meaning Young's Modulus values calculated using Equation 3.1 may be overestimated. A stiffness correction factor can be calculated via FE simulation of the static testing scenario both with and without a no-slip condition at the boundaries. These additional simulations indicated that the measured static modulus was overestimated by up to 10%, depending on the material's Poisson's ratio.

Assessing soft material viscoelastic parameters at relatively high frequencies is a challenging task, meaning *ex vivo* and *in vivo* tissue testing has focused on static modulus values as a point of comparison between healthy and cancerous tissue [58, 73]. Because the modulus values of the phantom materials tested were at the lower limit of the DMA's capabilities, the results of dynamic material testing were highly variable, and considered unreliable.

3.3 Actuation and Motion Capture

Experimental motion capture from soft phantoms requires the development of a phantom actuation and motion capture system. The individual components within the experimental DIET system changed as it was developed. However, the basic functional elements remained the same throughout, and are shown in Figure 3.9. An example of the real hardware used in the system is shown in Figure 3.10. What follows is a generalized description of the experimental system used for actuation and motion capture.

The experimental actuation and image capture system performed two major functions, each controlled by separate computers. A 'control' computer was used for actuator control, motion feedback, and lighting tasks, while 'imaging' computers were used for motion capture from each of the cameras. A dSPACE^{TM} modular hardware control

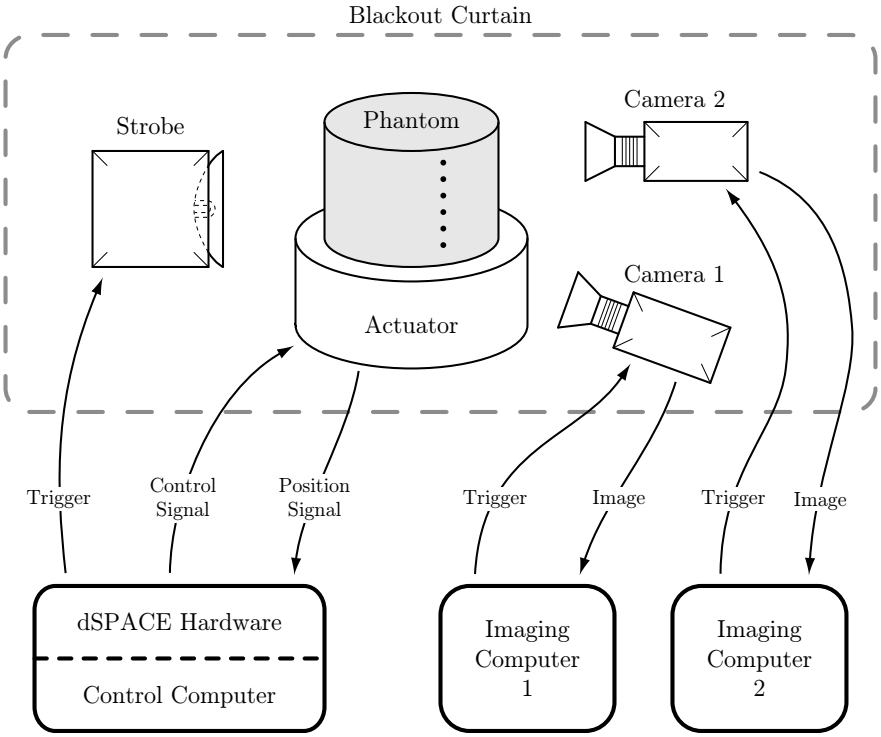

Figure 3.9 The experimental setup for phantom motion capture.

Figure 3.10 A photo of the typical setup for phantom displacement imaging.

system (dSPACE GmbH, Germany) attached to the control computer allowed accurate control of the actuator and stroboscope [96]. This system comprised a MATLAB^{TM} and Simulink^{TM} model incorporating specific dSPACE hardware control blocks. Once compiled, the control system code was downloaded from the control computer to the dSPACE hardware. An analog output port on the dSPACE unit provided a trigger signal to a stroboscope used for scene illumination. The dSPACE unit also provided frequency and amplitude control signals for the actuator. These signals were amplified to drive the electromagnets within the voice coil actuator. A velocity signal returned from the actuator provided the feedback path to complete a closed loop actuator control system. Control software and hardware was run in real time, allowing visualization of all input and output signals using the dSPACE Control Desk environment shown in Figure 3.11.

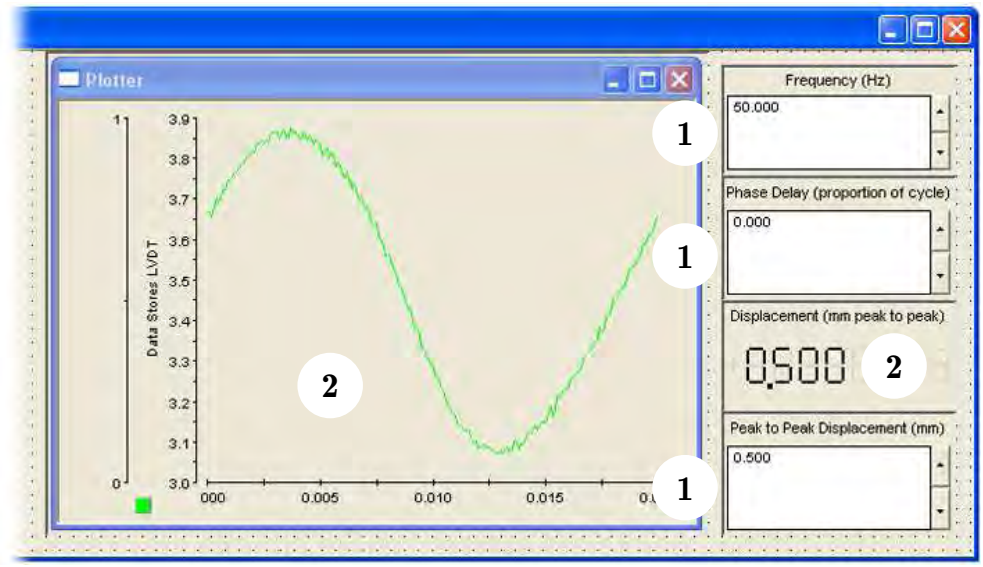

Figure 3.11 The dSPACE Control Desk software interface, where actuation parameters and strobe phase are set manually (1), and the displacement response of the actuator is displayed for the user (2).

Proprietary software limitations preventing simultaneous image capture required two separate computer workstations to control the image capture cameras. Each imaging computer was connected to a digital camera using a USB interface, and ran remote image capture software provided by the camera manufacturer. The image capture process for each camera was manually triggered using the software interface on the respective host computer.

All experimentally tested phantoms were placed on a flat circular surface on top of the actuator, which was configured to provide vertical sinusoidal motion. Both imaging cameras were set up with a field of view including the all reference points on

the phantom surface. The stroboscope was situated to give clear and even illumination of the reference points from the perspective of both cameras. As any ambient light would upset the imaging process, the actuator, strobe and cameras were covered with a blackout curtain for the duration of the imaging process.

Figure 3.12 is a schematic showing how controlled strobe lighting was used to capture the full range of phantom motion, despite the high speed of actuation relative to the longer shutter speed and exposure time required to generate each digital image. Each row of the figure demonstrates the capture of an individual frame, with time the horizontal co-ordinate. The sinusoidal line represents the steady state oscillation of a reference point on the phantom surface.

The time between strobe illumination was constant, and matched the period of the actuator. This synchronization meant that at each strobe offset, the reference point appeared at a single, static location, allowing camera exposures longer than one motion cycle. After both cameras had downloaded their respective images, the phase offset between the strobe and actuation signals was adjusted. In the actual experimental motion capture, the phase increment was in the range 10–20°.

After shifting the strobe phase, the phantom was illuminated at a different position in its motion cycle. This process allowed the motion of any reference point to be tracked across the full range of its steady-state motion. Experimental motion capture was typically performed until at least one complete motion cycle had been captured.

A total of seven motion data sets were obtained from the experimental setup during its development. These data sets fell into two main stages, based on the components used in the system at the time. The first motion data sets were obtained from the homogeneous gelatine phantoms described in Section 3.1.1. An improved motion capture system was used to measure surface motions on all of the silicone phantoms described in Section 3.1.2. Both systems use the same fundamental hardware and software approach.

3.3.1 Motion Capture from Gelatine Phantoms

The first attempt at experimental motion capture used a soft homogeneous gelatine phantom that was 70 mm in diameter and 50 mm in height. The actuation system used for this experiment comprised a linear voice coil actuator (VP5M, Derritron Electronics Ltd) driven by a 300 W amplifier (DCP3, Derritron). Actuation was at a frequency of 50 Hz, with an amplitude of 0.6 mm. Two consumer-level digital cameras (Olympus C-4040 Zoom and Canon PowerShot G6) were used for image acquisition. A Dawe Transistor Stroboflash (Type 1209C) provided the illumination required for motion capture. Actuation plate motion was measured using a Helium-Neon laser and an interferometer (Model OFV-512, Polytec) coupled to a vibrometer controller (Model

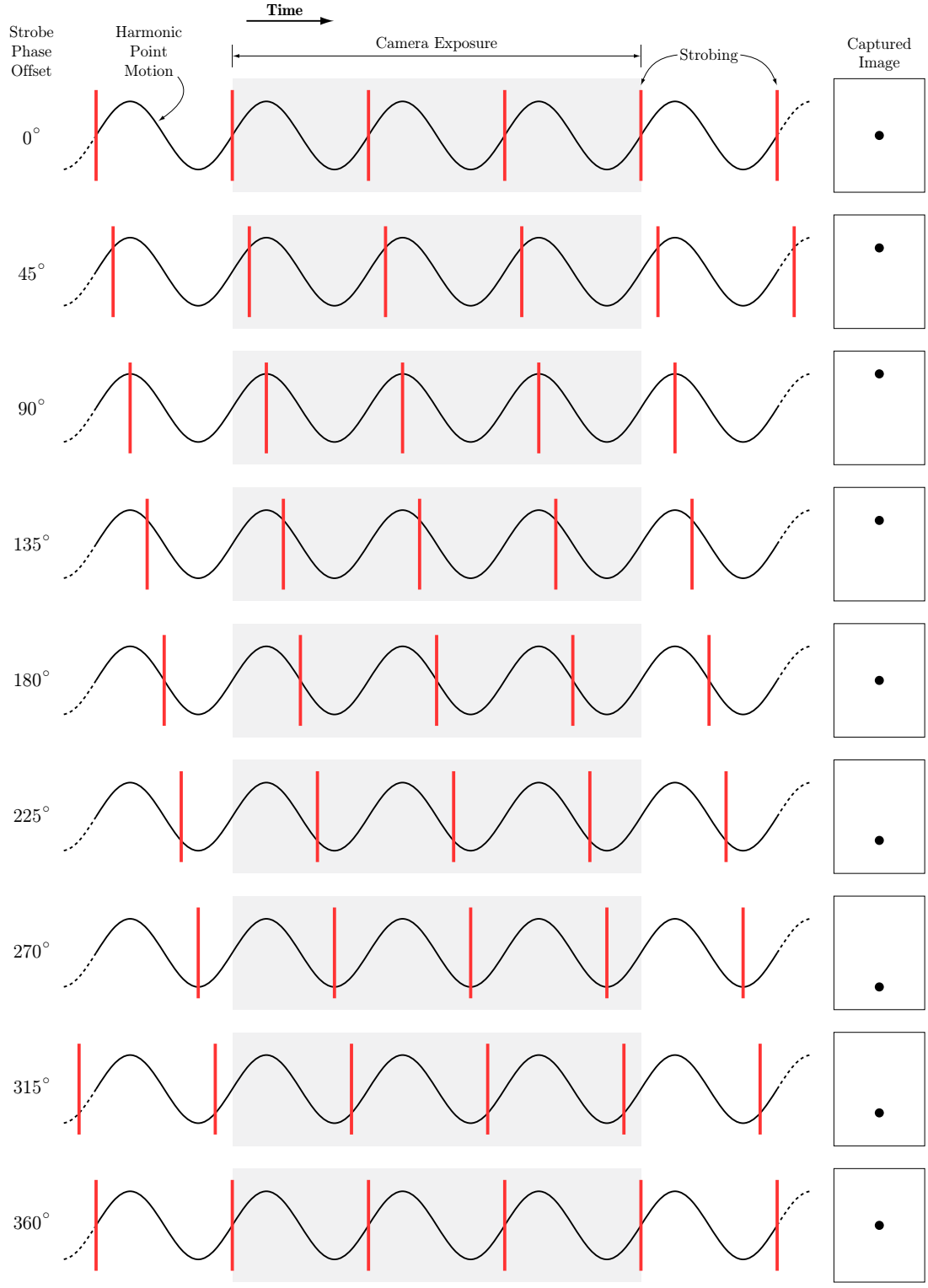

Figure 3.12 A schematic detailing the timing of the image capture process, where in this example the strobe offset between consecutive frames is 45°.

OFV-5000, Polytec). The actuation plate velocity values provided by the interferometer were converted into a real-time position within the dSPACE control system.

Two columns of black dots on the surface of the soft gelatine phantom formed the fourteen reference points that were motion tracked with the camera system. Simultaneous left and right images were captured at 20° phase offsets throughout the sinusoidal motion cycle. The process was repeated until two complete cycles of motion had been captured. The still frames captured by the right camera across one steady state motion cycle are shown in Figure 3.13.

The second round of gelatine phantom imaging was performed using the homogeneous phantom created using the hard gelatine ingredients in Table 3.1. This phantom had a diameter of 75 mm and a height of 70 mm. A single column of fifteen black dots formed the surface reference point locations for motion tracking. Actuation was at a frequency of 50 Hz, with an amplitude of 0.975 mm. The actuation and control system used was identical to the previous soft gelatine phantom testing. However, both cameras used for displacement imaging were Canon PowerShot G5 models, allowing a more consistent approach to camera setup and image capture. The phase offset between sequential still images was 18°, giving a total of 20 images across one steady-state motion cycle.

3.3.2 Motion Capture from Silicone Phantoms

The third stage of experimental data collection was from the silicone phantoms described in Section 3.1.2, and using a new actuation system designed specifically for the DIET phantom testing [101]. This actuator incorporated a Linear Velocity Displacement Transducer (LVDT) that simplified the actuation system by circumventing the requirement for the laser interferometer system used in prior tests. Initial testing indicated the new actuator was accurately controllable to within 0.05 mm. Both cameras used for motion capture were the same Canon Powershot G5 models used for the hard gelatine phantom experiments.

Prior to motion imaging, all silicone phantoms had a single column of fifteen dots applied to the surface, such that they were equally visible to both cameras. The color of these reference markers was chosen to give the greatest possible contrast with the underlying silicone material. Thus, black markers were used for the homogeneous phantoms, and white markers for the heterogeneous phantoms. All silicone phantoms were actuated at 100 Hz, with an amplitude of 0.5 mm. A total of twenty frames were captured across one steady-state motion cycle from each phantom.

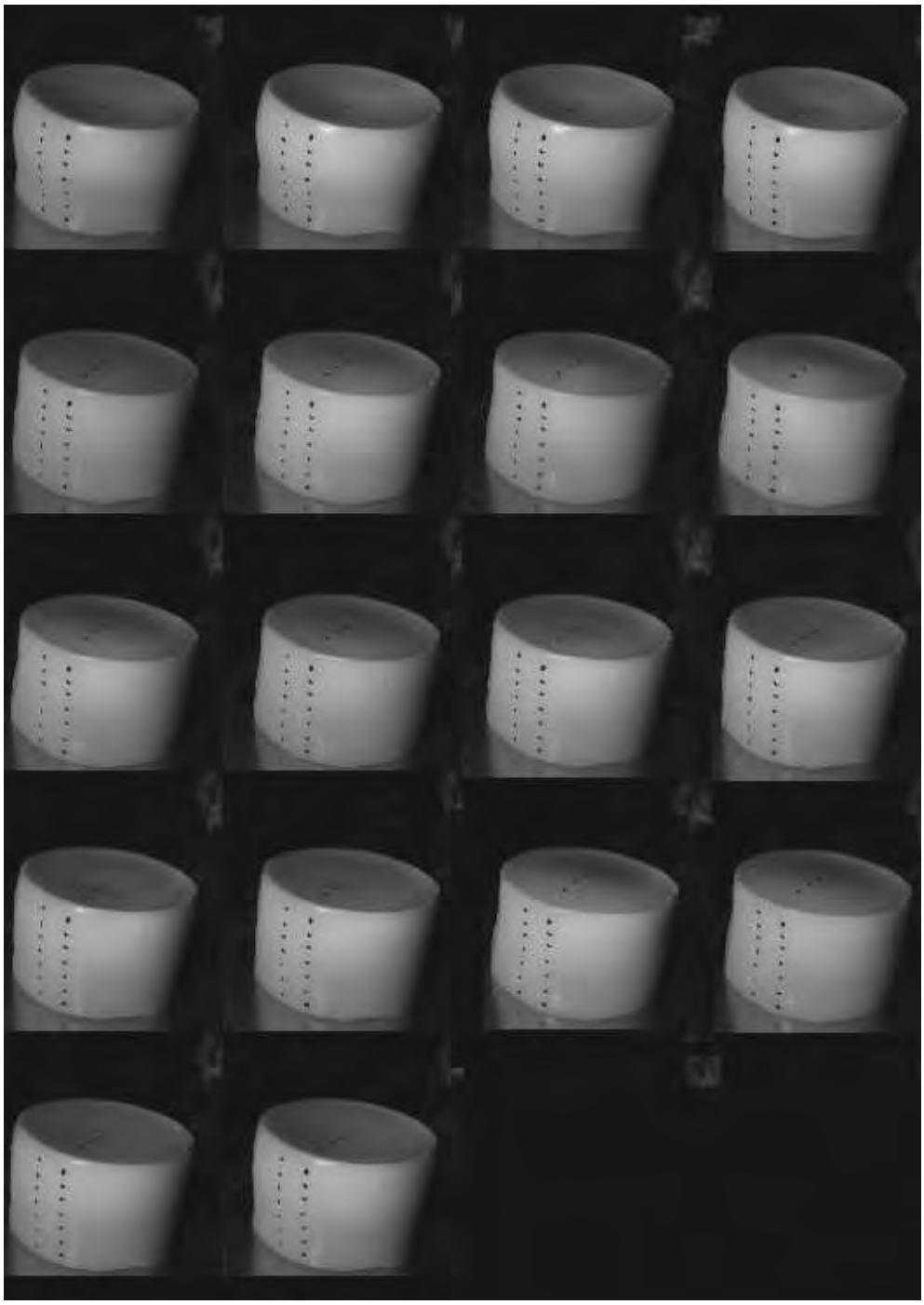

Figure 3.13 Motion frames from the right camera during actuation of the soft gelatine phantom.

3.4 Photogrammetry

Experimental motion capture results in sequential still images of all surface reference points across the complete phantom motion cycle. Because the DIET reconstruction approach is based on three dimensional surface motion information, a conversion of reference point position from the two dimensional image co-ordinate system into a three dimensional, 'world space', co-ordinate system was required. The mathematics used for this conversion are beyond the scope of this work, but are covered in detail in a number of texts, including those by Klette, and Trucco [102, 103].

Calibration of the camera system was performed prior to actuation and motion capture, using a specifically developed calibration object [104]. Images of the calibration cube from the right and left cameras are shown in Figure 3.14. Between calibration and phantom imaging, it is imperative that the camera setup is not altered. The output from the calibration process was a set of camera specific parameters that were used to calculate a three dimensional position in world space for every reference point over every frame i, termed $\bar{\mathbf{P}}^i$.

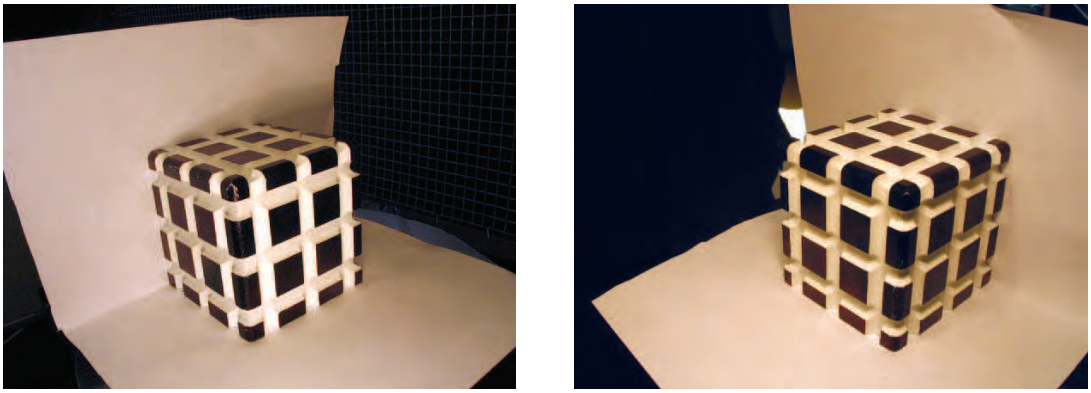

(a) Left camera. (b) Right camera.

Figure 3.14 Left and right camera views of the object used for calibration of the imaging system.

Figure 3.15 demonstrates the result of the conversion process, where left and right images of a reference point motion track are converted into a single three dimensional point path. The upper panels in this figure are based on experimental data from a silicone phantom, where the ellipsoidal shape of each point location is due to the angle between the reference point and the camera lens. The output from experimental motion capture was a vector for each reference point, $\bar{\mathbf{P}}$, describing its three dimensional location across all frames.

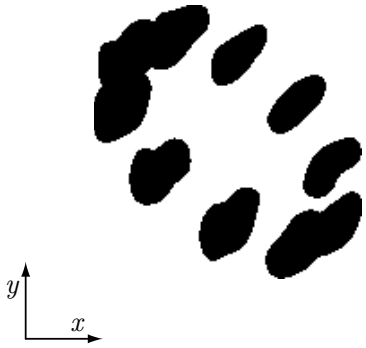

(a) Two-dimensional reference point positions as viewed from the left camera.

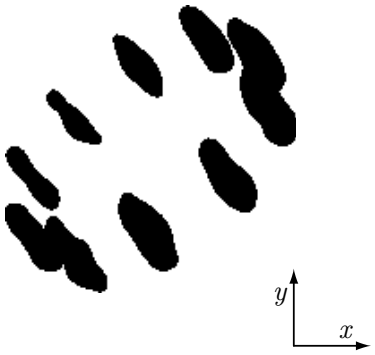

(b) Two-dimensional reference point positions as viewed from the right camera.

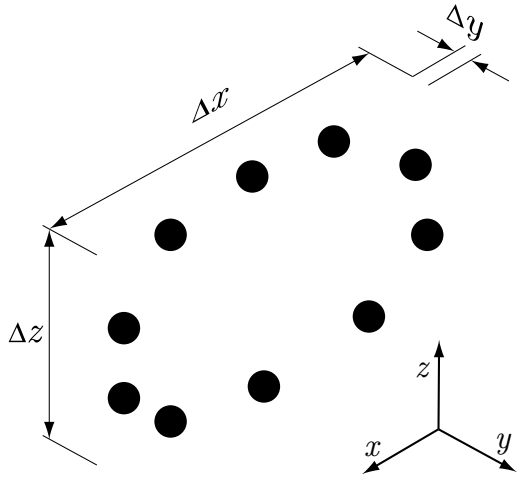

(c) Calculated reference point positions in world space, with the dimensions of the point path bounding box shown.

Figure 3.15 An example of reference point position conversion from two dimensional image co-ordinates to the three dimensional world space coordinate system.

3.5 Displacement Data Correlation

A fundamental principle of the DIET system is the observed correlation between a measured set of displacements and a displacement field simulated using FE analysis. To calculate an error metric value quantifying this displacement correlation, a relationship between the reference point locations and the FE mesh used for displacement simulation is required. The range of solutions developed to provide this relationship evolved alongside developments in the underlying modelling strategy, and are described in this section.

3.5.1 Mesh Alignment

During the initial experimental work, measured surface motions were compared to FE-simulated displacements at surface nodes on the FE mesh. This approach required that the FE mesh had nodal positions matching the world space locations of the reference points used for experimental motion capture. The advantage of the mesh alignment approach was that the measured motion data could be directly compared with the output from FE simulation, providing a rapid method for evaluating the correlation between the two. However, mesh matching required a separate FE mesh, with custom surface node locations, for every experimental data set. An enlargement of a FE mesh created using this technique is shown in Figure 3.16, where the fourteen reference points from the soft gelatine phantom (red) all correspond to unique nodes on the surface of the mesh.

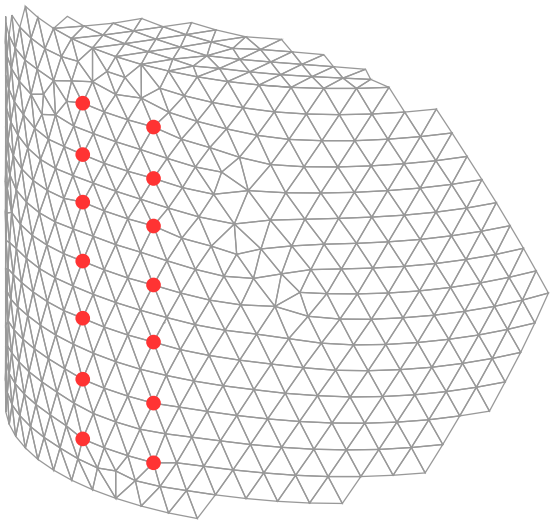

Figure 3.16 An example of the mesh alignment technique, where surface nodes are manipulated so their position corresponds to the dots located at the reference point locations (red).

3.5.2 Surface Projection

A point projection and interpolation scheme was developed to allow an accurate and flexible approach to relating reference point locations to FE mesh geometry. FE meshes were, in general, created using the same dimensions as the phantom being studied. However, it was not possible to obtain an exact match between the surface of a FE mesh and the surface of the phantom. In particular, the phantom size and geometry could not be exactly determined due to small measurement errors. Additionally, geometry discretization into linear tetrahedral mesh elements introduces small errors by representing curved model surfaces as small straight lines, as illustrated in Figure 3.17.

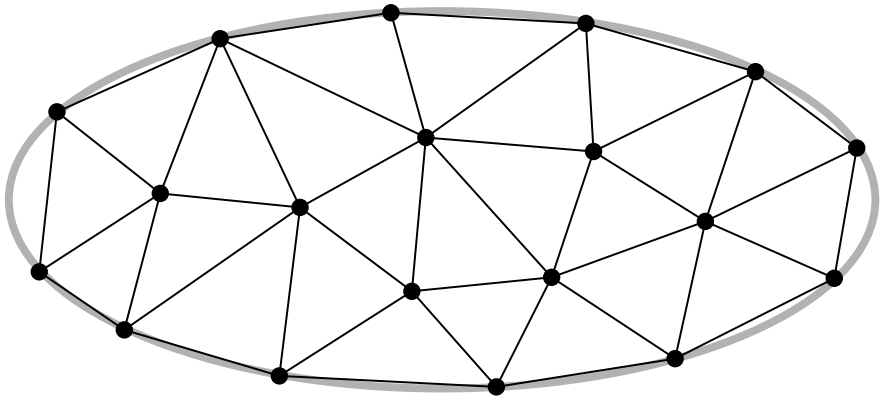

Figure 3.17 An example of the error introduced when a curved surface (grey) is discretized with linear elements (black), where the error is particularly pronounced for curves of small radius.

To allow multiple phantoms with the same external geometry to be represented with a single mesh, a point projection algorithm was developed in MATLAB. Inputs to this algorithm were a node location index, and element incidence lists defining both the tetrahedral mesh elements, and the triangular surface elements on the exterior surface of the mesh. The experimentally measured motion data calculated in Section 3.4 was loaded from a text file. Figure 3.18 is a pictorial representation of the major steps in the surface projection algorithm, where a reference point in three dimensional space (red) is projected to the surface of a FE mesh. Additionally, Figure 3.19 introduces the co-ordinate system and terminology used within the algorithm.

3.5.2.1 Reference Point Centroid

Surface projection of a reference point position involves first identifying the centroid of the reference point's motion path, defined $\mathbf{P}^{\Delta}$. The extent of the motion path in this work was determined by enclosing the measured point position over all frames, $\bar{\mathbf{P}}$,

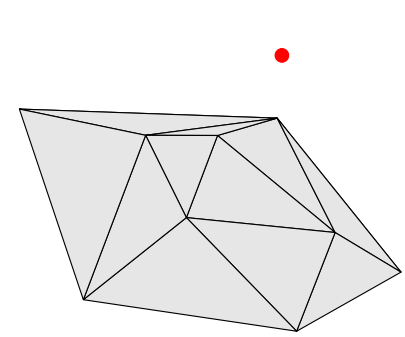

(a) Elevated reference point location.

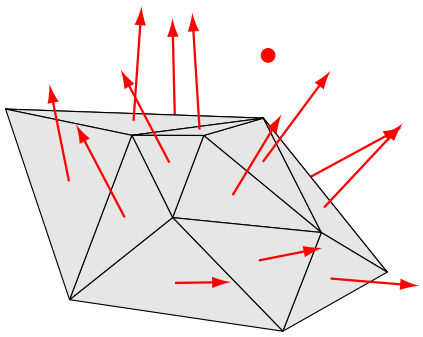

(b) Surface element normal vectors.

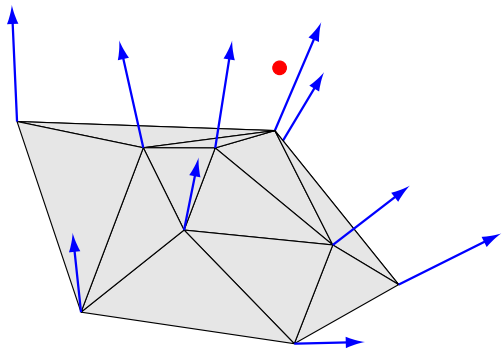

(c) Surface node normal vectors.

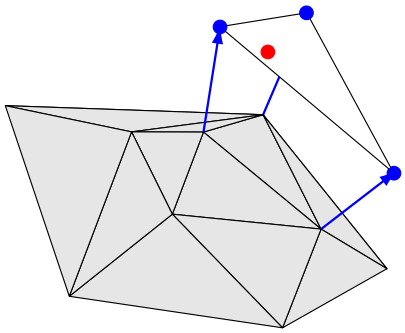

(d) Projected surface element.

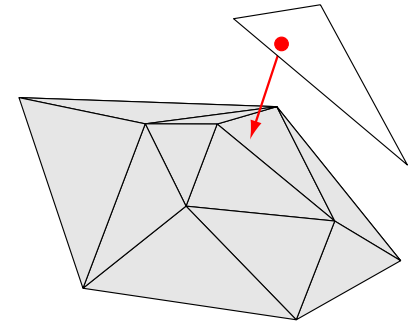

(e) Reference point projection.

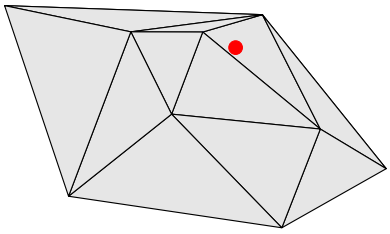

(f) Projected reference point location.

Figure 3.18 A graphical representation of the steps in the surface projection process.

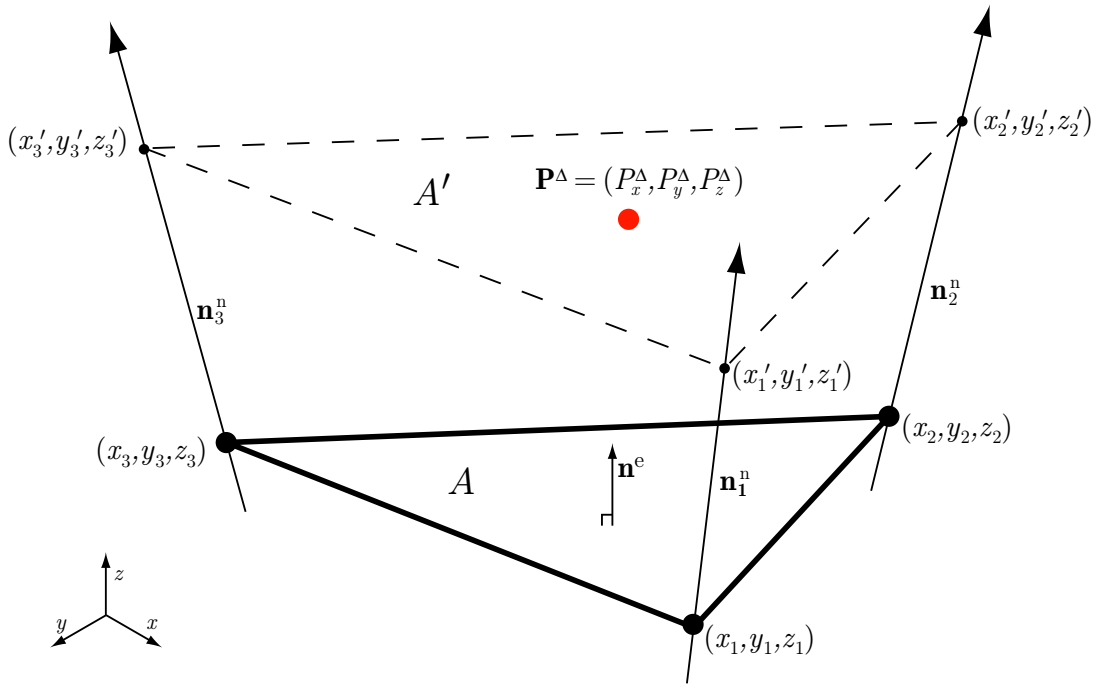

Figure 3.19 A reference point (red) and a triangular surface element (bold) in a three dimensional coordinate system, where the three element vertices lie on the x-y plane.

within a rectangular volume. The side lengths of this volume, Δx, Δy and Δz, are shown in Figure 3.15(c), and were used to calculate the path centroid,

$$\mathbf{P}^\Delta = \begin{pmatrix} \Delta x/2 \\ \Delta y/2 \\ \Delta z/2 \end{pmatrix}, \tag{3.2}$$

where $\mathbf{P}^\Delta$ is assumed to be the neutral position of the reference point motion in world space.

3.5.2.2 Surface Element Normal Vectors

Projecting a reference point centroid, $\mathbf{P}^\Delta$, to the underlying surface mesh, first involves the calculation of a surface element normal vector, $\mathbf{n}^{\mathbf{e}}$, for all surface elements in the mesh. This vector can be calculated for any surface element as the cross product of any two vectors that lie on the plane of the element. For the element shown in Figure 3.19,

$$\mathbf{n}^{\mathbf{e}} = \left\{ \begin{array}{c} x_2 - x_1 \\ y_2 - y_1 \\ z_2 - z_1 \end{array} \right\} \times \left\{ \begin{array}{c} x_3 - x_1 \\ y_3 - y_1 \\ z_3 - z_1 \end{array} \right\}. \tag{3.3}$$

where the x, y and z indices refer to the surface node locations indicated in the figure. Calculated values for $\mathbf{n^e}$ for all surface elements were normalized by vector length, and are shown in Figure 3.18(b) as red arrows.

3.5.2.3 Surface Node Normal Vectors

Following the calculation of surface element normal vectors, a nodal normal vector, $\mathbf{n^n}$, is calculated for all surface nodes. For any surface node i, this process first uses the surface element incidence list to identify the k surface elements in the mesh that contained the node. The surface node's normal vector, $\mathbf{n}_i^\mathbf{n}$, is then defined as the mean of the k connected surface element normal vectors, so that

$$\mathbf{n}_i^\mathbf{n} = \frac{1}{k}\sum_{j=1}^{k}\left(\mathbf{n}_j^\mathbf{e}\right), \tag{3.4}$$

Surface node normal vectors were also normalized by length, and are shown in Figure 3.18(c) as blue arrows.

3.5.2.4 Linear Basis Function Values

After the calculation of surface node normals, $\mathbf{n^n}$, for all surface nodes, all surface elements were projected along their constituent nodal normals until the element plane passed through the reference point centroid, $\mathbf{P}^\Delta$. The surface element with a projection bounding $\mathbf{P}^\Delta$ was then identified, and is shown in Figure 3.18(d). Values from interpolating polynomials within the projected element containing $\mathbf{P}^\Delta$ were used to convert the reference point location back to the surface of the mesh, shown pictorially in Figures 3.18(e)-(f). The relationship between the projected surface element vertices and $\mathbf{P}^\Delta$ was calculated using linear basis functions ϕ, where

$$\begin{aligned}
\phi_1 &= \left[\left(x_2'y_3 - x_3'y_2'\right) + \mathbf{P}_x^\Delta(y_2' - y_3') - \mathbf{P}_y^\Delta(x_2' - x_3')\right]/2A' \\
\phi_2 &= \left[\left(x_3'y_1 - x_1'y_3'\right) + \mathbf{P}_x^\Delta(y_3' - y_1') - \mathbf{P}_y^\Delta(x_3' - x_1')\right]/2A' \\
\phi_2 &= \left[\left(x_1'y_2 - x_2'y_1'\right) + \mathbf{P}_x^\Delta(y_1' - y_2') - \mathbf{P}_y^\Delta(x_1' - x_2')\right]/2A'
\end{aligned}, \tag{3.5}$$

for the projected surface element shown in Figure 3.19. The calculated ϕ values could then be used to interpolate any FE-simulated displacement field to the point on the surface of the mesh that best matched the reference point location. This corresponding surface location is shown in Figure 3.18(f).

3.6 Measured Data Fitting

To make a meaningful comparison between the discrete experimentally measured motion at a reference point, $\bar{\mathbf{P}}$, and a FE-simulated displacement field interpolated to the

surface location matching $\mathbf{P}^{\Delta}$, the experimental data must be expressed as orthogonal components of a steady state harmonic displacement vector. Figure 3.20(a) shows an experimentally measured reference point motion track in a world space co-ordinate system, including noise and any computational error. The approximations to this motion from the range of fitting methods developed are shown in Figure 3.20(b)-(d).

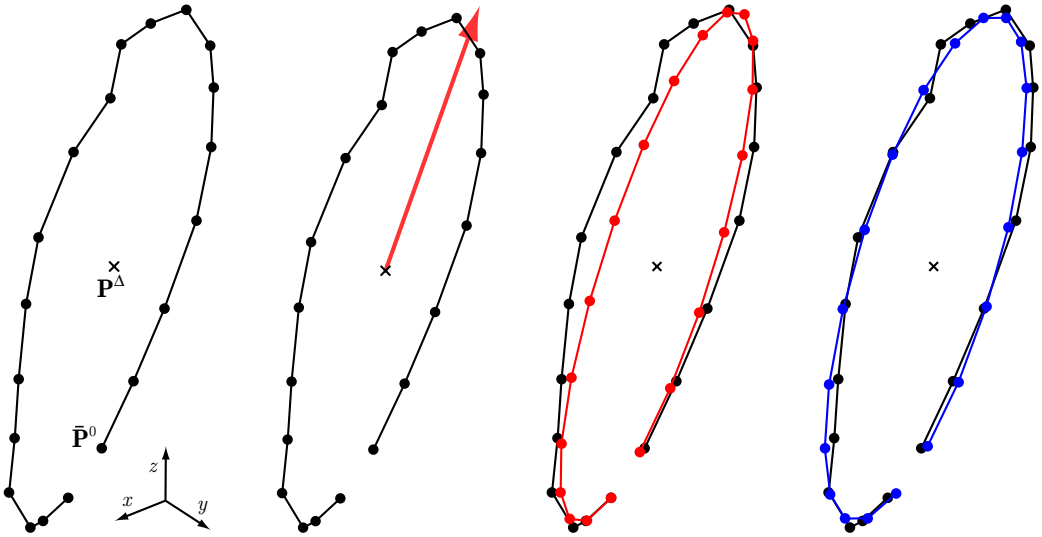

(a) Measured motion. (b) Simple vector. (c) Basic ellipse. (d) Refined ellipse.

Figure 3.20 The evolution of measured motion fitting techniques.

3.6.1 Steady State Measured Motion

The steady state oscillation of a point about an origin can be expressed using a time-harmonic displacement vector, defined at any time t as

$$\bar{\mathbf{u}}(t) = \Re\Big\{\mathbf{u}e^{i\omega t}\Big\}, \tag{3.6}$$

where ω is the frequency of the system, and the amplitude term contains both real and imaginary components, $\mathbf{u} = \mathbf{u_R} - i\mathbf{u_I}$. The measured position of a reference point at time t_i, $\bar{\mathbf{P}}^i$, can be approximated as the addition of a harmonic displacement, $\bar{\mathbf{u}}(t_i)$, to the reference point centroid, $\mathbf{P}^{\Delta}$, as

$$\bar{\mathbf{P}}^i = \bar{\mathbf{u}}(t_i) + \mathbf{P}^{\Delta}. \tag{3.7}$$

Alternatively, reference point motion can be described using a real-valued amplitude, $\tilde{\mathbf{u}}$, and a phase, φ, yielding

$$\bar{\mathbf{u}}(t) = \Re\Big\{\tilde{\mathbf{u}}e^{i(\omega t+\varphi)}\Big\}. \tag{3.8}$$

The motion description in Equation 3.8 can be converted to the form of Equation 3.6 by relating the real-valued damped amplitude, $\tilde{\mathbf{u}}$, and phase, φ, to a complex amplitude, $\mathbf{u} = \mathbf{u_R} - i\mathbf{u_I}$, as follows:

$$\begin{aligned} \Re\left\{\mathbf{u}e^{i\omega t}\right\} &= \Re\left\{\tilde{\mathbf{u}}e^{i(\omega t+\varphi)}\right\} \\ \Re\left\{\mathbf{u}e^{i\omega t}\right\} &= \Re\left\{\tilde{\mathbf{u}}e^{i\omega t}e^{i\varphi}\right\} \\ \mathbf{u} &= \tilde{\mathbf{u}}e^{i\varphi} \\ \mathbf{u_R} - i\mathbf{u_I} &= \tilde{\mathbf{u}}\cos(\varphi) - i\tilde{\mathbf{u}}\sin(\varphi). \end{aligned} \tag{3.9}$$

Experimentally measured damped motion behavior can be approximated by obtaining an undamped motion amplitude, $\mathbf{u}$, from the real component of the expression in Equation 3.9, so that

$$\mathbf{u} \approx \mathbf{u_R} = \tilde{\mathbf{u}}\cos(\varphi). \tag{3.10}$$

3.6.2 Undamped Fitting

When assuming that the measured reference point motion path, $\bar{\mathbf{P}}$, is generated by an undamped material, this motion can be described by Equation 3.6, where imaginary displacement components were ignored, allowing $\mathbf{u}$ to be approximated by $\mathbf{u_R}$. The components of this real-valued amplitude vector were estimated using the bounding box method described in Section 3.5.2.1, where

$$\mathbf{u} = \begin{pmatrix} \Delta x/2 \\ \Delta y/2 \\ \Delta z/2 \end{pmatrix}. \tag{3.11}$$

An example of the estimated motion vector generated by this undamped assumption is shown in Figure 3.20(b).

3.6.3 Damped Fitting

When assuming the measured motion track, $\bar{\mathbf{P}}$, is generated by a material that has some internal damping, Equation 3.8 can be used to generate a motion fit defined using a damped amplitude, $\tilde{\mathbf{u}}$, and phase, φ. A two stage algorithm was developed to optimize the amplitude and phase values, where the first stage created initial estimates, and a second stage refined the estimates using non-linear squared error optimization.

Equation 3.11 can be used to generate a basic estimate of damped amplitude, $\tilde{\mathbf{u}}$, using an undamped assumption. A three-element vector containing an initial phase

estimate for each orthogonal direction, φ, can then be made using the measured reference point location at time $t = 0$, $\bar{\mathbf{P}}^0$, and the centroid of the bounding rectangle, $\mathbf{P}^{\Delta}$,

$$\begin{aligned} \varphi_x &= \sin^{-1}\left(\left| \bar{\mathbf{P}}_x^0 - \mathbf{P}_x^{\Delta} \right| / \tilde{\mathbf{u}}_x \right) \\ \varphi_y &= \sin^{-1}\left(\left| \bar{\mathbf{P}}_y^0 - \mathbf{P}_y^{\Delta} \right| / \tilde{\mathbf{u}}_y \right) . \\ \varphi_z &= \sin^{-1}\left(\left| \bar{\mathbf{P}}_z^0 - \mathbf{P}_z^{\Delta} \right| / \tilde{\mathbf{u}}_z \right) \end{aligned} \tag{3.12}$$

Here, the translation $\bar{\mathbf{P}}^0 - \mathbf{P}^{\Delta}$ allows the measured point location to be related to the origin.

The sign of each component in the estimated phase value, φ, can not be determined based on $\bar{\mathbf{P}}^0$ alone, as the velocity of the reference point at this location is unknown. Therefore, the evaluation of eight possible combinations of $\pm\varphi_x$, $\pm\varphi_y$ and $\pm\varphi_z$ is required before an initial phase estimate φ can be found. Each phase combination was considered by first generating an estimated point path at the discrete time intervals used for motion capture t_i using Equation 3.8. The disagreement between this estimated path, $\bar{\mathbf{u}}(t_i)$, and the measured motion track for the point, $\bar{\mathbf{P}}$, was measured by the error term

$$\Gamma = \sum_i \sqrt{\left\| \bar{\mathbf{u}}(t_i) - \left(\bar{\mathbf{P}}^{\mathbf{i}} - \mathbf{P}^{\mathbf{\Delta}} \right) \right\|^2}, \tag{3.13}$$

where the translation $\bar{\mathbf{P}}^{\mathbf{i}} - \mathbf{P}^{\mathbf{\Delta}}$ expressed the measured point positions relative to the world space origin. The phase combination with the lowest value of Γ provided the initial estimates of φ_x, φ_y and φ_z. An estimated motion track generated using these initial damped amplitude and phase values is shown as a blue ellipse in Figure 3.20(c).

The second stage of the damped motion estimation refined the initial estimates of damped amplitude and phase with a simple least-squares optimization, where the objective function for minimization was taken from Equation 3.13. The result of this optimization was a closely fitted motion estimate containing damped amplitude, $\tilde{\mathbf{u}}$, and phase, φ, for each reference point, expressed as orthogonal components. The red motion track in Figure 3.20(d) was generated using these optimized values.

3.7 Surface Error Calculation

Once the measured motion data was represented in the same coordinate space as the FE model, the quantitative match between the simulated and measured motions could be evaluated. The error metric used varied depending on the assumed FE material model and the methods used for reference point projection and motion fitting.

3.7.1 Soft Gelatine Phantom Surface Error

The undamped FE model used for soft gelatine phantom simulations calculated the time-harmonic reference point motions in the form

$$\bar{\mathbf{u}}(t) = \Re\Big\{ \mathbf{u}^{\mathbf{c}}_{\mathbf{R}} e^{i\omega t} \Big\}, \tag{3.14}$$

where $\mathbf{u}^{\mathbf{c}}_{\mathbf{R}}$ represents a calculated, real-valued displacement amplitude that may be negative. The undamped real motion fitting described in Section 3.6.2 allowed the measured motion to be expressed as a corresponding real displacement amplitude, $\mathbf{u}^{\mathbf{m}}_{\mathbf{R}}$. Using the mesh alignment method described in Section 3.5.1, the measured real amplitude values at each reference point, $\mathbf{u}^{\mathbf{m}}_{\mathbf{R}}$, could be directly compared with the real amplitude values output from FE simulation, $\mathbf{u}^{\mathbf{c}}_{\mathbf{R}}$. In this case, the error metric, Ω_1, was calculated at all N reference points as the error between the measured and simulated motion amplitudes,

$$\Omega_1 = \frac{1}{N} \sum_{i=1}^{N} \Big| \, |\mathbf{u}^{\mathbf{m}}_{\mathbf{R}}| - |\mathbf{u}^{\mathbf{c}}_{\mathbf{R}}| \, \Big|_i. \tag{3.15}$$

By only comparing the magnitude of the displacement vectors, this error calculation avoids any possible errors due to the lack of phase information.

3.7.2 Hard Gelatine Phantom Surface Error

A second variant of the surface error metric was used for the hard gelatine experimental data set described in Section 3.3.1. In this case, FE simulation again assumed an undamped model, and provided real amplitude $\mathbf{u}^{\mathbf{c}}_{\mathbf{R}}$. However, the measured motion was fitted using the damped vectors for amplitude, $\tilde{\mathbf{u}}$, and phase, φ, described in Section 3.6.3. Here, the surface error metric Ω_2 was defined

$$\Omega_2 = \frac{1}{3N} \sum_{i=1}^{N} \left(\sqrt{\left\| \mathbf{u}^{\mathbf{m}}_{\mathbf{R}} - \mathbf{u}^{\mathbf{c}}_{\mathbf{R}} \right\|^2} \right)_i \tag{3.16}$$

where the equivalent undamped measured motion, $\mathbf{u}^{\mathbf{m}}_{\mathbf{R}}$, was approximated from $\tilde{\mathbf{u}}$ and φ using Equation 3.10 before the error metric was calculated.

3.7.3 Silicone Phantom Surface Motion Error

A final motion error metric value was used for the motion data sets obtained from the silicone phantoms described in Section 3.3.2. For these simulations, the FE model included damping, and provided calculated displacement amplitudes containing both real and imaginary components, $\mathbf{u}^{\mathbf{c}} = \mathbf{u}^{\mathbf{c}}_{\mathbf{R}} + i\mathbf{u}^{\mathbf{c}}_{\mathbf{I}}$. The measured motion, $\mathbf{u}^{\mathbf{m}}$, was fitted using damped amplitude, $\tilde{\mathbf{u}}$, and phase, φ, and was expressed as real and imaginary

components, $\mathbf{u^m} = \mathbf{u^m_R} + i\mathbf{u^m_I}$, using Equation 3.9. In this case, the simulated displacement amplitude, $\mathbf{u^c}$, was compared to the measured displacement amplitude, $\mathbf{u^m}$, at all N reference points, using

$$\Omega_3 = \frac{1}{3N} \sum_{i=1}^{N} \left(\left| \mathbf{u^m_R} - \mathbf{u^c_R} \right| + \left| \mathbf{u^m_I} - \mathbf{u^c_I} \right| \right)_i . \tag{3.17}$$

3.8 Summary

The experimental methods described in this chapter provide both real experimental data, and the methods required to compare this data to corresponding FE-simulated displacements. As each experimental data set was obtained, a series of further experiments were performed in an attempt to estimate or reconstruct the material properties of the phantoms. These experiments are described in the following chapters.

Chapter 4

Phantom Surface Motion Error Studies

The experimental methods described in Chapter 3 provided surface motion data from a range of both homogeneous and heterogeneous soft tissue approximating phantoms. To further understand the relationship between internal material properties and experimentally observed motion, an error study was performed on the experimental phantom displacement sets to investigate the suitability of surface motion error as an indicator of internal stiffness distribution. This work involved comparing the measured phantom motion data collected in Chapter 3 with large sets of FE-simulated displacements for a variety of property distributions. The distribution with the lowest resulting surface motion metric could then be compared with the known properties of the phantom to determine the potential effectiveness of the DIET system and method. The experiments performed in this chapter represent an evaluation of surface motion error as an indicator of internal stiffness. Should such an approach give favorable results, an optimization algorithm will be required to automate the process of finding the minimum error value.

The surface error studies involved FE simulation of phantom displacement using a mesh based on the measured phantom geometry. The internal stiffness distribution of the FE model was described using a number of different parameters. All FE simulation used computer code written in a combination of Fortran and Linux shell scripting, with code compiled and executed on Linux workstations. The matrix inversion required during FE simulation was performed using routines from LAPACK, and the matrix solver MUMPS, a direct sparse matrix inversion software package written in Fortran 90 [105, 106]. In addition, the BLAS library developed by Kazushige Goto allowed matrix algebra to be performed in parallel where the workstation had multiple processors available for computation [107].

4.1 Homogeneous Gelatine Phantoms

Experimental data sets were collected from homogeneous gelatine phantoms created during the work described in Section 3.1.1. These experimentally measured motion sets represented the first successful data collection using the DIET actuation and motion measurement system. The surface error studies performed on this experimental motion data aimed to estimate a value for Young's Modulus, E, for the gelatine used to create each phantom. Error studies for the soft and hard gelatine phantoms were performed sequentially, but shared a common objective and approach, and are described simultaneously in this section.

4.1.1 Measured Phantom Displacement

The actuation and surface motion capture of both gelatine phantoms was performed using the experimental setup described in Section 3.3.1. Figure 4.1 shows the surface deformation of both hard and soft gelatine phantoms during actuation, along with the location of each reference point centroid across the motion cycle. The tracked position of all reference points on the soft gelatine phantom was fitted using the undamped motion assumption described in Section 3.6.2, resulting in real amplitude components at each reference point centroid.

Reference point motion on the surface of the hard gelatine phantom was estimated using the more accurate fitting algorithm described in Section 3.6.3, where point motion was described about the motion centroid using damped amplitude and phase values. A selection of measured reference point locations over time, $\bar{\mathbf{P}}$, on both phantoms, are compared with the corresponding fitted motion estimates, $\bar{\mathbf{u}}(t)$, in Figure 4.2.

4.1.2 Finite Element Simulation

The assumed homogeneity of the gelatine phantoms allows a single value for each material property to be assigned across the entire model when simulating displacements using FE methods. Computational limitations constrained the gelatine phantom surface error investigations to variations in Young's Modulus, E. Both hard and soft phantom models had material density, ρ, set at $1{,}000\,\mathrm{kg/m^3}$, and Poisson's Ratio $\nu = 0.49$, representing a close approximation to water, the main ingredient used in gelatine manufacture.

Computer models of both cylindrical phantom geometries were created and meshed using the software program Gambit$^{\mathrm{TM}}$ (Version 2.2.30, Fluent Inc.), where key model dimensions were taken from physical measurement of the actual phantoms. The resulting soft phantom model had a diameter of 70 mm, and a height of 50 mm, while the hard phantom was 75 mm diameter, and 69 mm tall. The FE meshes for the soft and

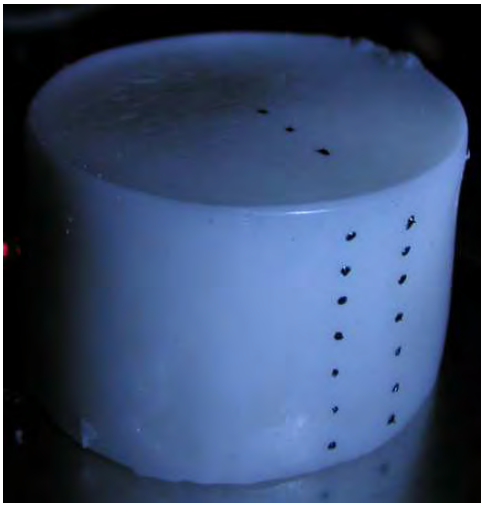

(a) Soft gelatine motion capture.

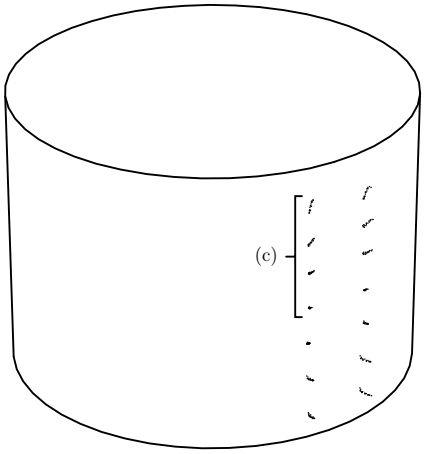

(b) Tracked reference point locations.

(c)

(d) Hard gelatine motion capture.

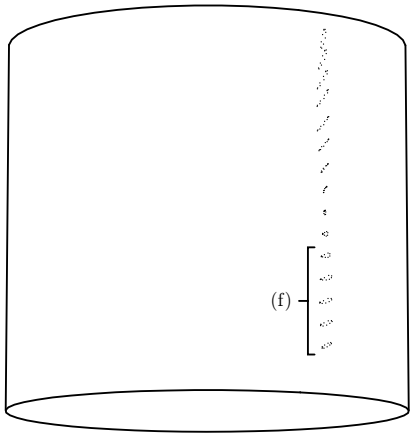

(e) Tracked reference point locations.

(f)

Figure 4.1 The experimentally observed motion of the homogeneous gelatine phantoms.

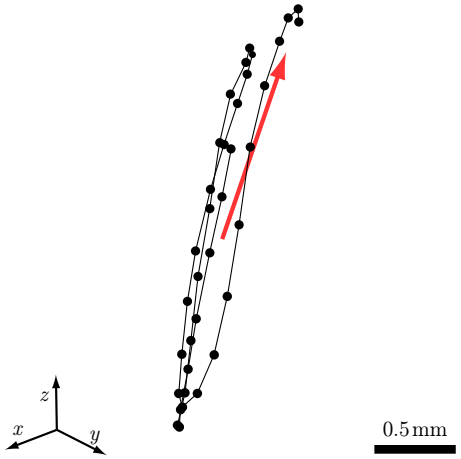

(a) Soft phantom, surface reference point 1.

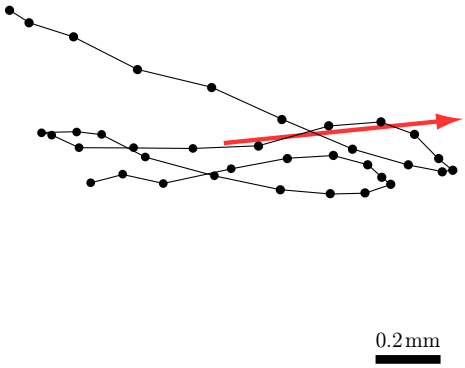

(b) Soft phantom, point 6.

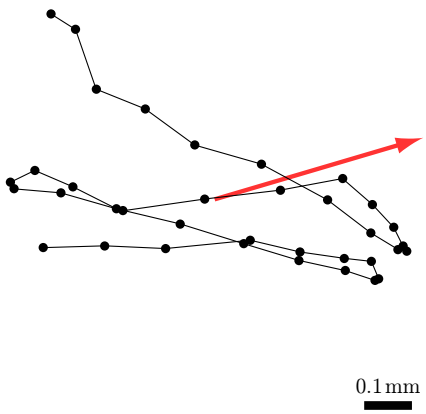

(c) Soft phantom, point 12.

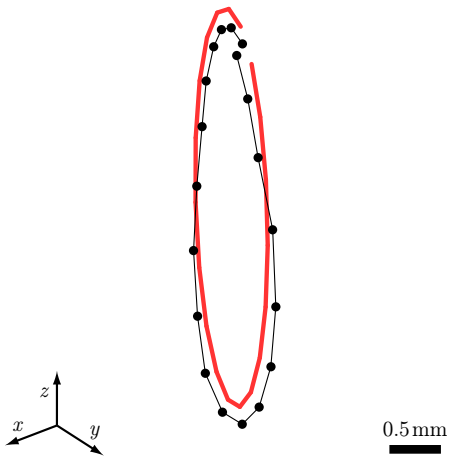

(d) Hard phantom, surface reference point 1.

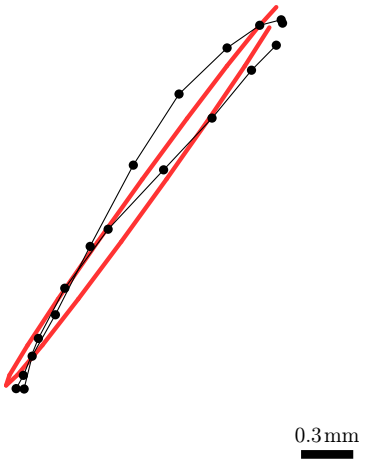

(e) Hard phantom, point 7.

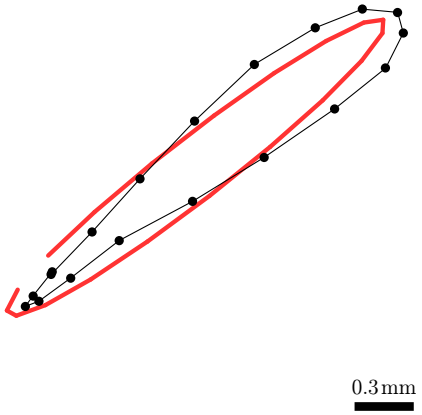

(f) Hard phantom, point 14.

Figure 4.2 A selection of measured (black) and fitted (red) reference point motion from the soft and hard homogenous gelatine phantoms.

hard models contained approximately 37,000 and 120,000 linear tetrahedral elements respectively, and are shown in Figure 4.3.

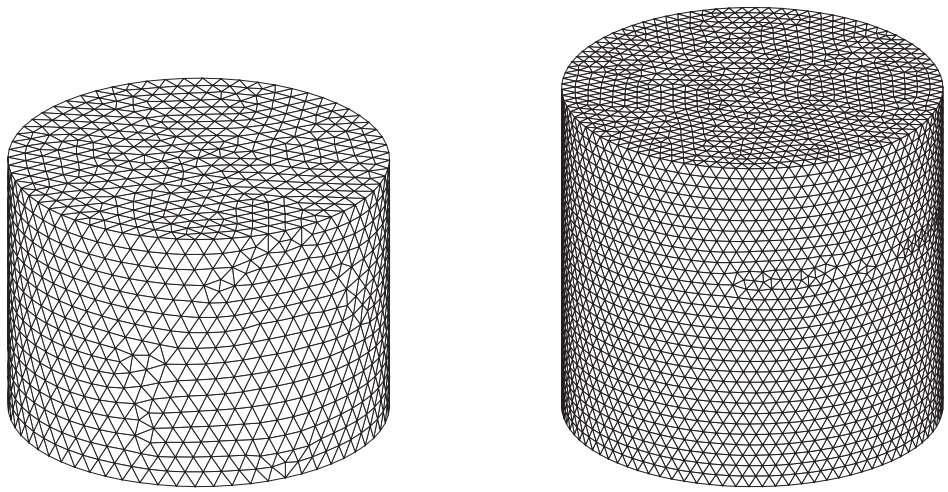

(a) Soft phantom mesh. (b) Hard phantom mesh

Figure 4.3 The FE meshes used to simulate soft and hard gelatine phantom motion.

The increase in mesh density for the hard model was made possible by an increase in computational resources. Surface node locations on the soft phantom mesh were manipulated to match the reference point locations on the phantom surface according to the mesh alignment process outlined in Section 3.5.1. The hard gelatine phantom model did not require any data-specific mesh manipulation due to the subsequent development of the surface projection algorithm described in Section 3.5.2.

Boundary conditions were applied to both FE models that closely matched the experimental conditions. The bottom face of the mesh was displacement-constrained in the horizontal x-y plane, based on the assumption of no slip between the base of the phantom and the actuation plate. In addition, the bottom surface of each model was harmonically displaced in the z direction at frequency and amplitude values corresponding with the experimental data collection. The soft phantom actuation was at an amplitude of 0.6 mm, and frequency 50 Hz, while the hard phantom had an amplitude of 0.975 mm, and a frequency of 50 Hz. All other external faces on both models had free surface boundary conditions, where displacements were not specified, and boundary forces were set to zero in all orthogonal directions. Table 4.1 lists the FE model specifications used when simulating the motions of both the soft and hard gelatine phantoms.

A 'sweep' of FE simulations was performed on both the soft and hard computational models, where full volume displacements were simulated at a range of Young's Modulus values. The modulus range for each model was chosen based on the expected material properties from the mechanical testing in Section 3.2 and Table 3.3. Soft

Table 4.1 Specifications of the hard and soft gelatine models used for FE simulation.

	FE Model	
Specification	**Soft**	**Hard**
Height (mm)	50	69
Diameter (mm)	70	75
Elements (approx.)	37,000	120,000
Frequency (Hz)	50	50
Amplitude (mm)	0.6	0.975
Density (kg/m^2)	1,000	1,000
Poisson's Ratio	0.49	0.49

model simulations were performed between $E = 5$–$20\,\text{kPa}$, and hard model simulations between $E = 5$–$40\,\text{kPa}$. Both sets of simulations were performed at stiffness increments of $100\,\text{Pa}$, providing a good balance between resolution and overall simulation time. The resulting sets of motion data characterized the simulated surface deformation over the prescribed stiffness range, where the surface deformation at a selection of Young's Modulus values is shown for both phantoms in Figure 4.4.

4.1.3 Stiffness Estimation

The displacement fields generated using FE simulation formed a database of solutions that were used to evaluate surface motion error over the range of stiffness values considered. Surface motion error metrics from Section 3.7 were used to compare each simulated displacement field to the corresponding measured motion. An estimate of the phantom stiffness value was taken from the Young's Modulus value corresponding with the lowest error metric, and could be compared with the measured gelatine stiffness values described in Section 3.2.

The surface error metric Ω_1 defined in Equation 3.15 was used to evaluate the surface displacement error for the soft gelatine phantom. Use of the mesh alignment technique from Section 3.5.1 in conjunction with the undamped FE solution allowed measured reference point amplitudes to be directly compared to simulated amplitudes at the corresponding mesh nodes. A plot of the surface error metric over the 5–20 kPa stiffness range is shown in Figure 4.5.

Areas of high motion error on the plot correspond to resonant stiffness values in the FE model where simulated displacements were large and did not match the measured motion. The lowest motion error metric on the figure corresponds to a Young's Modulus value of $E = 12.5\,\text{kPa}$, though the stiffness corresponding to global minimum error is not clearly defined, with other significant local minima at $6.1\,\text{kPa}$ and $9.5\,\text{kPa}$. The

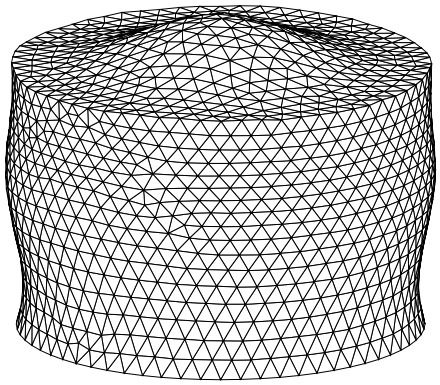

(a) Soft phantom model, $E = 8.5\,\text{kPa}$.

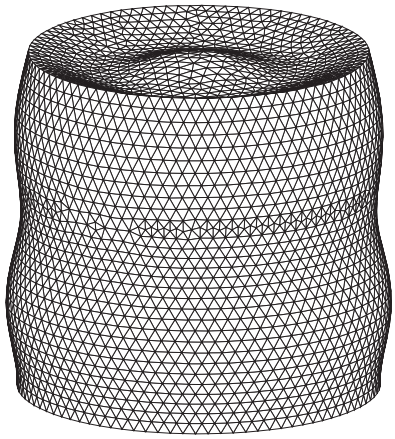

(d) Hard phantom model, $E = 10\,\text{kPa}$.

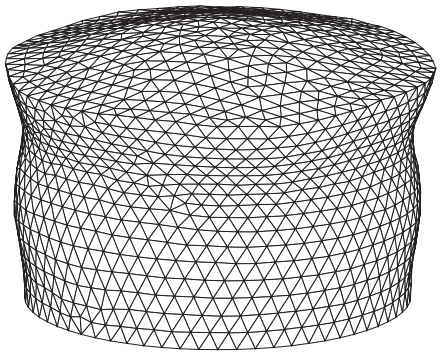

(b) Soft model, $E = 9.5\,\text{kPa}$.

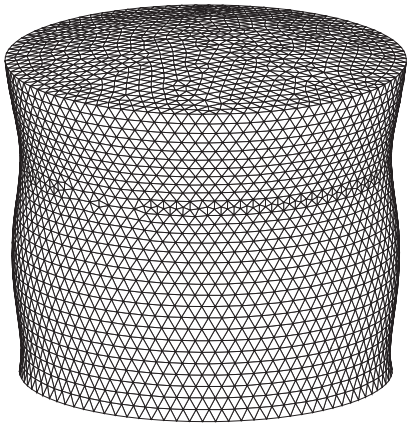

(e) Hard model, $E = 17.5\,\text{kPa}$.

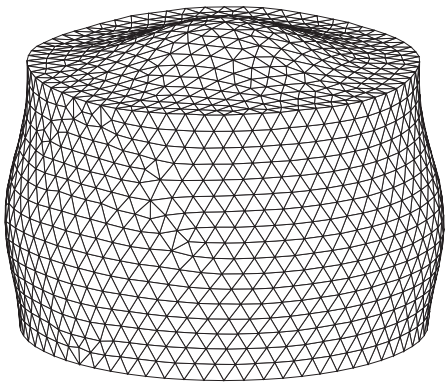

(c) Soft model, $E = 12.5\,\text{kPa}$.

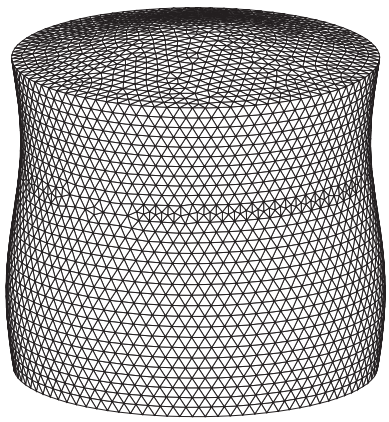

(f) Hard model, $E = 27.5\,\text{kPa}$.

Figure 4.4 FE-simulated displacement for the soft and hard gelatine phantom models across a range of Young's Modulus values.

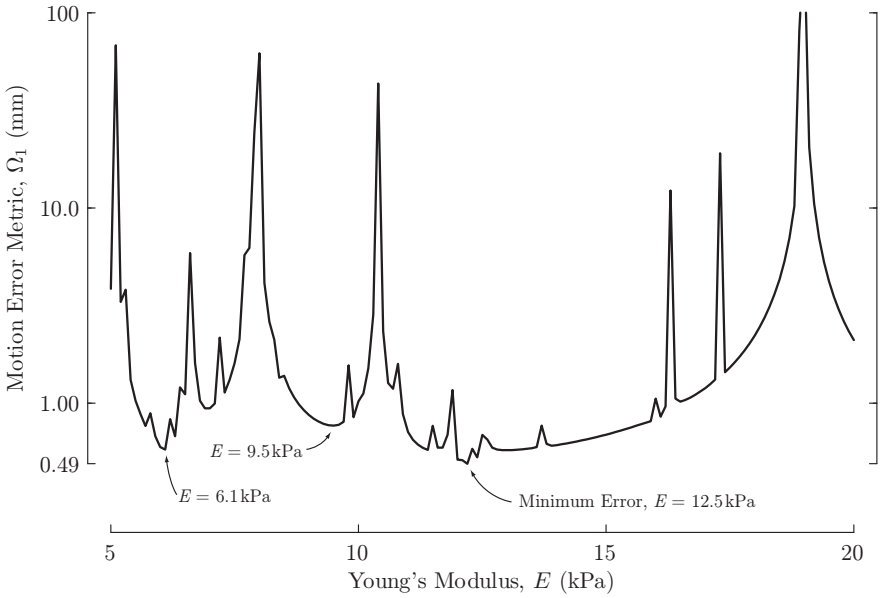

Figure 4.5 Motion error metric (on a logarithmic scale) across a range of homogenous stiffness values for the soft gelatine phantom, where the location of minimum error is indicated.

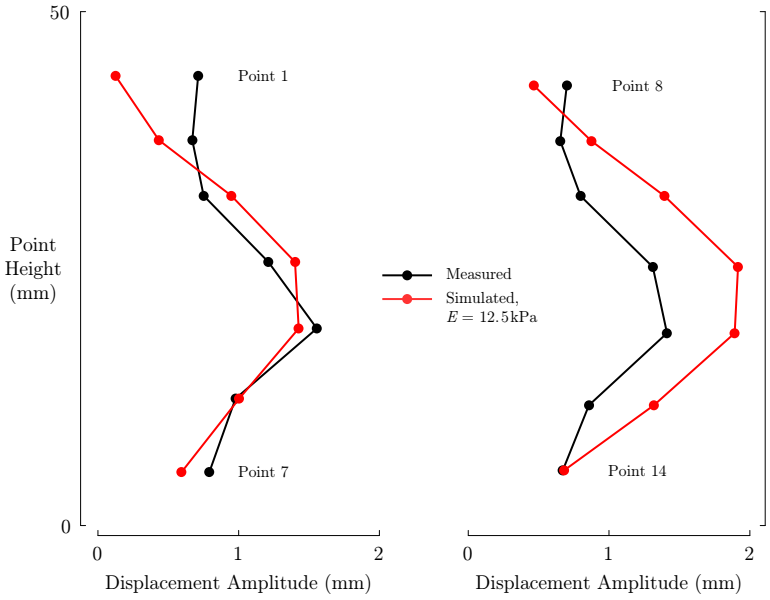

Figure 4.6 A comparison of reference point displacement amplitudes between the experimental soft gelatine phantom and FE-simulated motion at $E = 12.5$ kPa.

simulated displacement amplitudes at $E = 12.5$ kPa are compared with the measured amplitudes at all fourteen reference points in Figure 4.6, where the reference point heights are plotted to scale.

FE simulation of the hard gelatine phantom model generated undamped displacement amplitudes at Young's Modulus values in the range 5–40 kPa. The error between the simulated and measured displacements was defined by the metric Ω_2 in Equation 3.16, where the measured motion's fitted estimates of damped amplitude and phase were converted to an estimated undamped amplitude prior to error calculation. Values for Ω_2 across the stiffness range simulated are shown in Figure 4.7, where the minimum motion error corresponds to a Young's Modulus value of $E = 27.1$ kPa. Here, the stiffness corresponding to global error minimum has increased definition versus the local minima when compared to the soft gelatine case. The match between the components of simulated displacement at $E = 27.1$ kPa and the measured displacement is shown for all reference points in Figure 4.8.

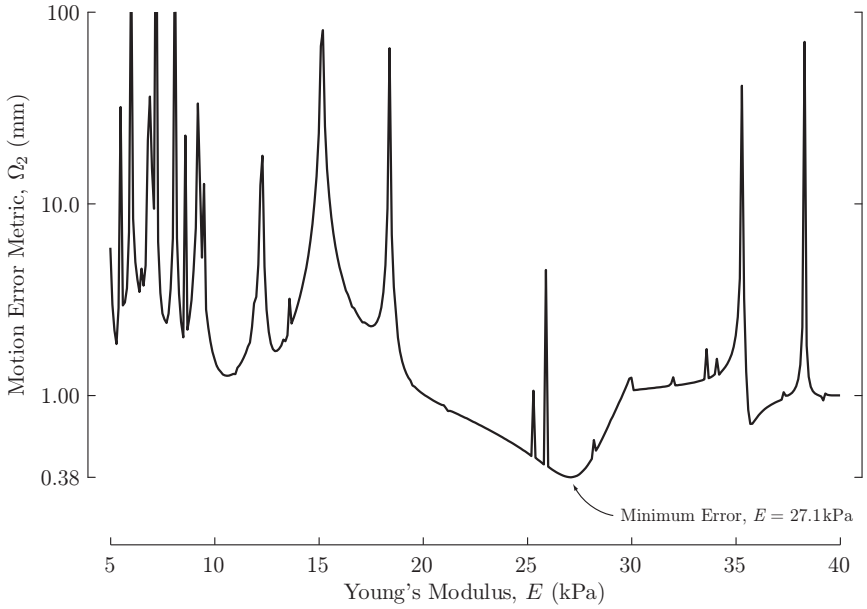

Figure 4.7 Motion error metric across a range of homogenous stiffness values for the hard gelatine phantom, where the location of minimum error is indicated.

4.1.4 Discussion

The Young's Modulus values estimated using the stiffness sweep method showed promising correlation with the mechanically measured stiffness values obtained in Section 3.2. Measured and estimated Young's Modulus values are summarized in Table 4.2, where the estimated modulus value was within 40% of the measured modulus value for the soft phantom, and within 10% for the hard phantom.

The experimentally measured motion from the soft phantom was highly erratic, and often not a good representation of the expected smooth reference point motion path. This irregular motion can be seen in Figure 4.2, particularly for points 6 and 12.

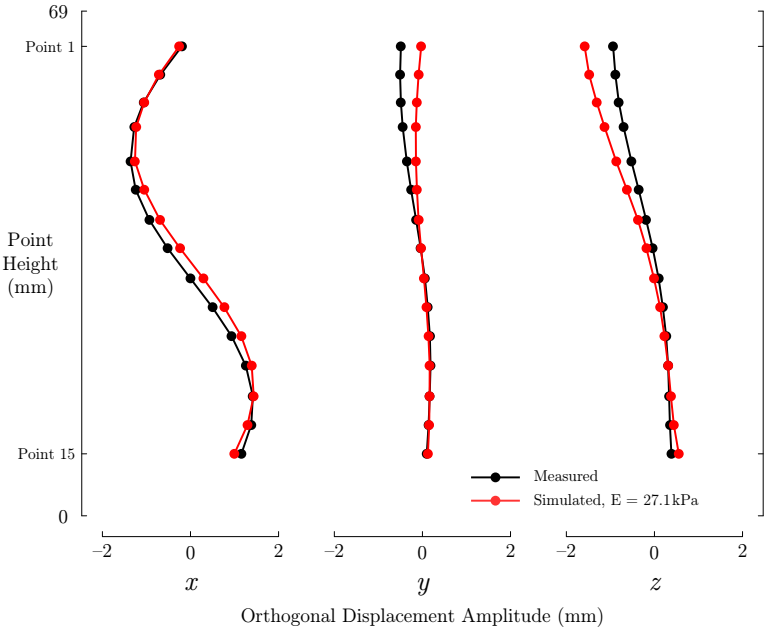

Figure 4.8 The match between FE-simulated displacements at $E = 27.1\,\text{kPa}$ and experimental displacements for the hard gelatine phantom.

Table 4.2 A comparison of surface error estimated and measured Young's Modulus values for the soft and hard gelatine.

	Young's Modulus, E	
Material	**Measured**	**Estimated**
Soft Gelatine	12.5 kPa	9 kPa
Hard Gelatine	27.1 kPa	26 kPa

Obtaining accurate positions for the reference points on the soft phantom was made difficult by a combination of noise within the actuation and strobing system, and the large, non-uniform appearance of the reference points on the phantom surface. Additional error was introduced after motion capture through the use of an undamped amplitude vector to approximate the reference point motion path, where no phase information was considered.

The observed surface motion of the hard gelatine phantom in Figures 4.1 and 4.2 demonstrates the improvement in the motion capture system subsequent to the soft gelatine phantom experiments. These improvements in the experimental setup, in conjunction with the damped motion path fitting algorithm, led to the much closer match between measured and estimated reference point paths visible in Figure 4.2. Here, the clearly ellipsoidal nature of the measured motion indicated that the gelatine ma-

terial was damped, and therefore not ideally suited to simulations using an undamped material model.

FE simulation results from both phantom models indicated resonance issues at a large number of simulated stiffness values. Calculated surface motions at these resonant stiffness values were unrealistically large and would prevent a close match between the measured and simulated motion should the phantom's actual Young's Modulus lie at or near a resonant peak. The reduction in observed resonance around the minimum error location for the hard gelatine phantom was partly attributable to the longer surface wavelengths resulting from higher model stiffness values. Circumventing these resonance issues would require the incorporation of material non-linearity and/or damping into the FE model, but at the cost of added material parameters for material property reconstruction.

The aim of the gelatine phantom surface error study was to investigate the behavior of the linear FE model over a range of stiffness values, and evaluate the potential of the DIET method as a stiffness estimation tool when used with real data. The sweeps performed indicated that limited surface motion error measurements have the potential to be used as an indicator of stiffness in a realistic experimental situation, validating the potential of the overall DIET approach.

The clear identification of a best-fit stiffness value was found to be dependent to a large extent on the accuracy of the experimental motion capture and fitting algorithms. This effect is particularly evident when considering the improvement in both the appearance of the error domain and the minimum error value for the hard gelatine simulations. Resonant behavior was identified as a major obstacle to more generalized reconstruction, requiring special attention if robust methods in elasticity imaging using DIET are to be achieved. Despite the issues identified, this straightforward approach to estimating elasticity was able to clearly differentiate between soft and hard material with a contrast as low as 3x, indicating the potential of a surface error based system to be clinically useful after appropriate refinements.

4.2 Homogeneous Silicone Phantoms

The stiffness sweeps and resulting modulus estimations performed in Section 4.1 used an undamped FE model, where all simulated motions were treated as being in phase. While the stiffness estimations made using this undamped model showed good agreement with independent mechanical property testing, the ellipsoidal reference point motion observed experimentally indicated that the real phantom displacements were generated by a viscoelastic material. Including these viscoelastic effects in a damped FE material model would allow a more thorough consideration of the underlying me-

chanical properties, with the added benefit of reducing the resonance issues observed when performing the gelatine model simulations.

The decision to use silicone phantoms for this study arose from the difficulties encountered using gelatine for phantom manufacture, as outlined in Section 3.1.1. The new silicone material was expected to have similar viscoelastic properties as the gelatine material used previously, confirming the need for a damped material model when simulating displacements. The first silicone surface error studies were performed on data from both soft and hard homogeneous phantoms, with ingredients and measured material properties identified in Sections 3.1.2 and 3.2.

The homogenous silicone error studies focused on optimizing a total of three independent material parameters, where each parameter was assumed to be constant over the entire model. The stiffness of a viscoelastic material undergoing steady-state harmonic displacement can be described by a complex modulus,

$$E^* = E' + iE'', \tag{4.1}$$

where the storage modulus E' relates strains to stored elastic energy, and the loss modulus, E'', describes energy lost to internal attenuation during vibration. The derivation of this complex-valued elastic modulus description is included in Appendix A. This stiffness description was parameterized for the damped material model so that the loss modulus was calculated as the product of a storage modulus E' and a damping parameter ζ, such that

$$E'' = \zeta E'. \tag{4.2}$$

In addition to the viscoelastic material modulus represented by E' and ζ, Poisson's ratio, ν, was also included as an independent parameter as the actual value of ν for the silicone was unknown. Variations in all three material parameters were used to estimate property values for the soft and hard silicone material using the same parameter sweeping method used for the gelatine phantoms in Section 4.1.

4.2.1 Measured Phantom Displacement

Experimental motion was captured from both hard and soft homogeneous silicone phantoms using the system described in Section 3.3, where an improved actuation system had been implemented following the experimental work with gelatine phantoms. Figure 4.9 shows single frames from the motion capture of both hard and soft silicone phantoms, along with the tracked reference point motion across the steady state motion cycle for each phantom. All reference point motion was observed to be continuous and steady-state, confirming the accuracy of the enhanced actuation and motion capture system. Using the damped motion estimation algorithm from Section 3.6.3, a best

fit estimate of the amplitude and phase values was calculated for each of the observed ellipsoidal reference point positions across all frames.

(a) Soft silicone motion capture.

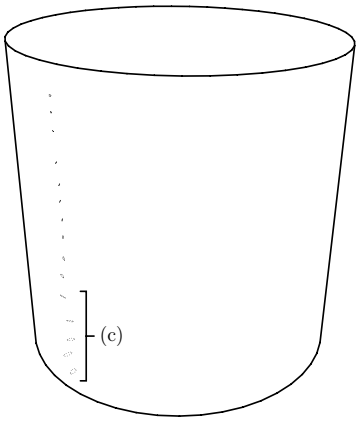

(b) Tracked reference point locations.

(c)

(d) Hard silicone motion capture.

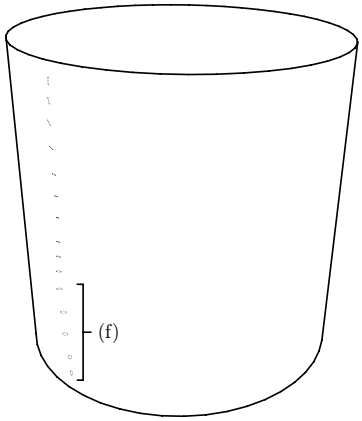

(e) Tracked reference point locations.

(f)

Figure 4.9 The experimentally observed motion of the homogeneous silicone phantoms.

4.2.2 Finite Element Simulation

A FE model matching the cylindrical phantom geometry was generated and meshed using Gambit. The surface projection technique described in Section 3.5.2 allowed a single FE mesh to represent both silicone phantom models, as both phantoms had the

same external dimensions of 74 mm diameter, 74 mm height. The final model contained approximately 92,000 linear tetrahedral elements, with an average element edge length of 3 mm, and is shown in Figure 4.10. The complex-valued stiffness matrix terms in a damped FE simulation required twice as much computer memory as an undamped model, leading to the element size increase when compared to the undamped hard gelatine mesh used in Section 4.1.

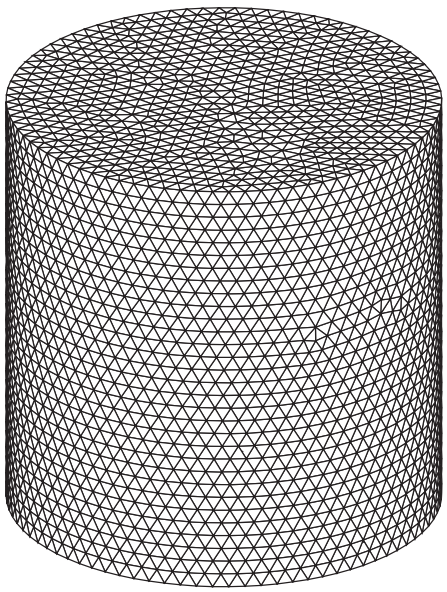

Figure 4.10 The FE mesh used for all silicone phantom simulations.

To match the experimental setup, the FE model was displacement constrained in all three axes on the lower face, with x and y displacements set to zero, and the z direction displacement described by an 0.5 mm amplitude, 100 Hz sinusoid. The model density was set at 1,000 kg/m^3 as an approximation to the measured density values for both phantoms. The single density value used was within five percent of the measured values for these phantoms, and avoided the need for an additional independent material parameter.

Storage modulus ranges of $E' = 10$–50 kPa for the soft model and $E' = 80$–150 kPa for the hard model were covered in a grid search using modulus increments of 2 kPa. The damping ratio, ζ, ranged from 0.1–0.3 in steps of 0.02 for both models. Simulation sets were generated for each model at Poisson's ratio values between $\nu = 0.40$–0.49, the estimated range for the silicone material. The match between a FE-simulated data set interpolated onto the reference points and the measured motion data at the same reference points was represented by the error term Ω_3 previously defined in Equation 3.17. In this case, the metric compared both real and imaginary displacement components of the damped motions.

4.2.3 Mechanical Property Estimation

Following FE simulation, the error metric Ω_3 was calculated for both hard and soft silicone phantom simulations across the ranges of storage modulus E', damping ratio ζ and Poisson's ratio ν considered. Surface error results for the soft phantom simulations are shown in Figure 4.11(a), where a plane of constant ν passing through the location of global minimum error is plotted. Motion error varies from blue (low) to red (high) on the plot, where the minimum error metric corresponds to a storage modulus value $E' = 28\,\text{kPa}$, damping ratio $\zeta = 0.22$, and Poisson's ratio $\nu = 0.48$. Variation in the error metric with changes in Poisson's ratio at constant E' and ζ are shown in Figure 4.11(b).

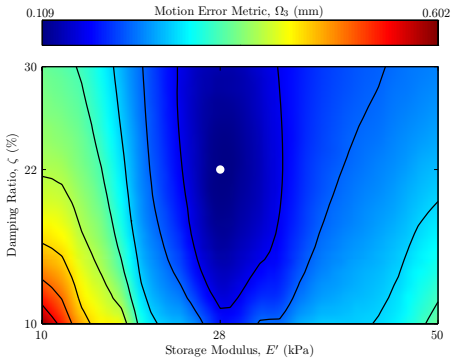

(a) Parameter sweep results at $\nu = 0.48$, where the location of global minimum error is indicated (○).

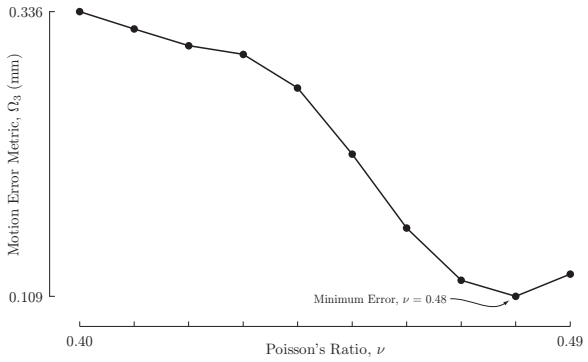

(b) Variations in Ω_3 with ν, where $E' = 28\,\text{kPa}$, and $\zeta = 0.22$.

Figure 4.11 Displacement sweep surface error results for the soft homogeneous silicone phantom.

Displacement error results for the hard silicone phantom are shown in Figure 4.12, where the global error minimum corresponds to parameter values $E' = 103\,\text{kPa}$, $\zeta = 0.20$, and $\nu = 0.41$. Figure 4.12(b) shows variations in Ω_3 with Poisson's ratio at constant E' and ζ. All motion components from the closest simulated matches to the measured motion from the soft and hard phantoms are shown in Figure 4.13, where the vertical location of each reference point is plotted to scale.

4.2.3.1 Storage Modulus Frequency Dependence

Assuming the material storage modulus, E', is independent of actuation frequency assumes that it is comparable to the static measurement of Young's Modulus, E. Therefore, estimated values for E' should not vary when performing an error analysis at varying frequency values. To test the frequency dependence of the estimated value for E', an additional experimental data set collected from the soft silicone phantom at a frequency of 50 Hz was considered. A parameter sweep was performed where the

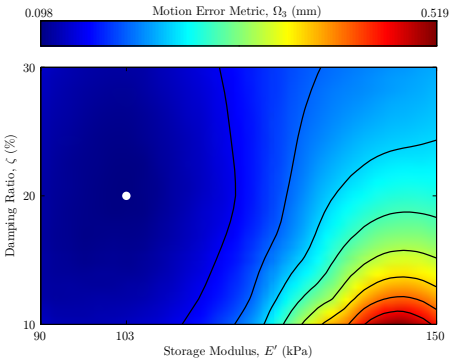

(a) Parameter sweep results at $\nu = 0.41$, where the location of global minimum error is indicated ($\circ$).

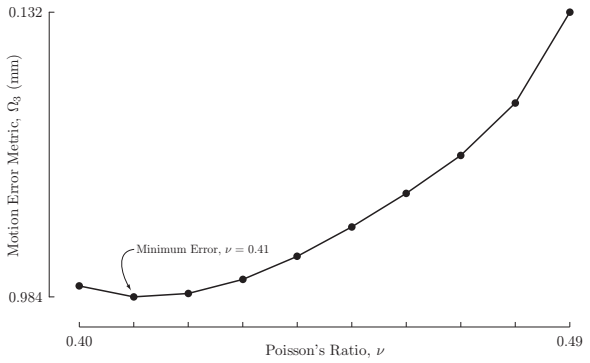

(b) Variations in Ω_3 with Poisson's Ratio, where $E' = 103\,\text{kPa}$, and $\zeta = 0.20$.

Figure 4.12 Displacement sweep surface error results for the hard homogeneous silicone phantom.

FE-simulated amplitude and frequency matched the 50 Hz experimental data, and E' was varied from 10–50 kPa. Values for damping and Poisson's ratios were held constant for these simulations at the previously estimated values of $\zeta = 0.22$ and $\nu = 0.48$ for the soft silicone. The resulting error metric values over the range of E' considered are shown in Figure 4.14. Here, the storage modulus value corresponding to minimum motion error is $E' = 29\,\text{kPa}$, a difference of only 1 kPa from the $E' = 28\,\text{kPa}$ found with 100 Hz actuation.

4.2.4 Discussion

The motion error plots in Figures 4.11–4.12 provide important information about the sensitivity of the motion error metric Ω_3 to variations in the three material parameters considered. The error contours in Figure 4.11(a) indicate the soft phantom motion error has a high sensitivity to storage modulus, while variations in damping ratio have a smaller influence. The wide contour spacing in Figure 4.12(a) indicates that at higher stiffness values, the sensitivity of Ω_3 to variations in E' and ζ is more balanced and less significant. The relatively high error sensitivity to parameter variations in the soft phantom is most likely due to the large proportional change in shear wavelength in the softer material when stiffness is varied. Motion error sensitivity to Poisson's ratio followed a similar trend, where variations in Ω_3 with ν were much more significant in the soft model than in the hard model.

The addition of damping to the material model significantly reduced the effects of resonance that were readily visible in the previous undamped studies, particularly at low stiffness values. Resonant behavior was almost completely eliminated with the addition of a viscoelastic damping effect for the silicone simulations, resulting in continuous error domains where the parameter values corresponding to the location of global

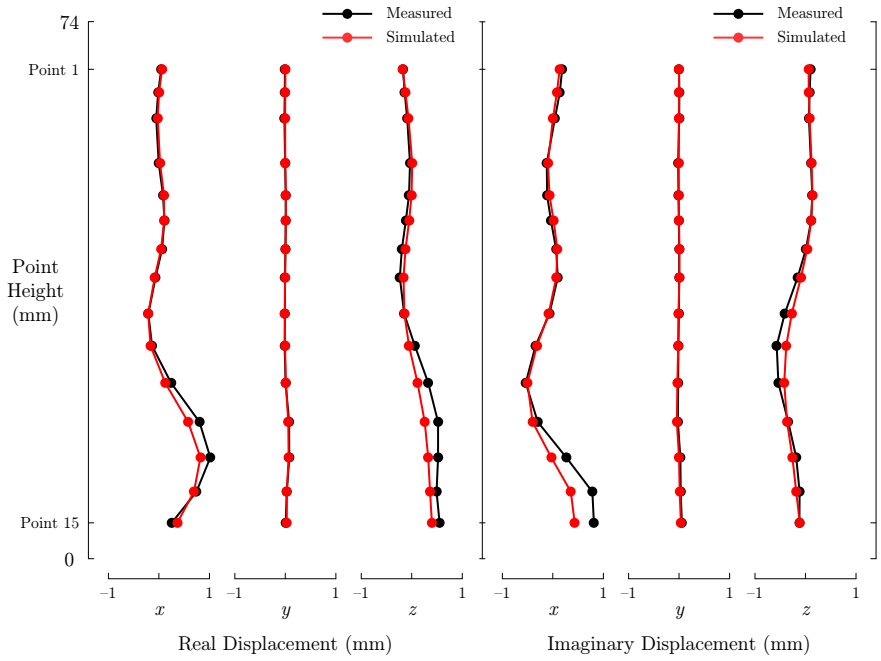

(a) Soft phantom, simulated displacement at $E' = 28\,\text{kPa}$, $\zeta = 0.22$, $\nu = 0.48$.

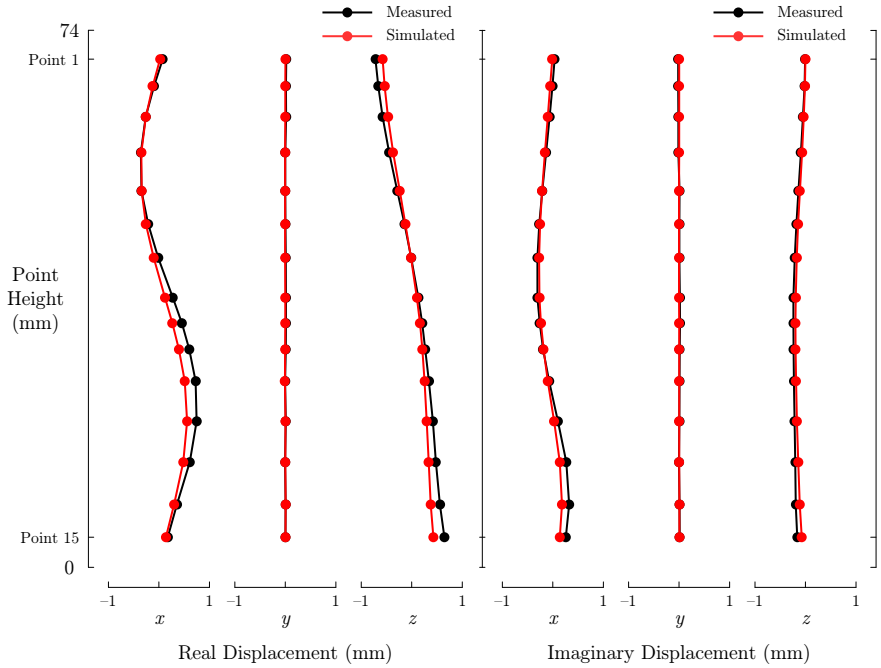

(b) Hard phantom, simulated displacement at $E' = 103\,\text{kPa}$, $\zeta = 0.20$, $\nu = 0.41$.

Figure 4.13 The best fitting FE-simulated cases compared with measured motions for both soft and hard silicone phantoms.

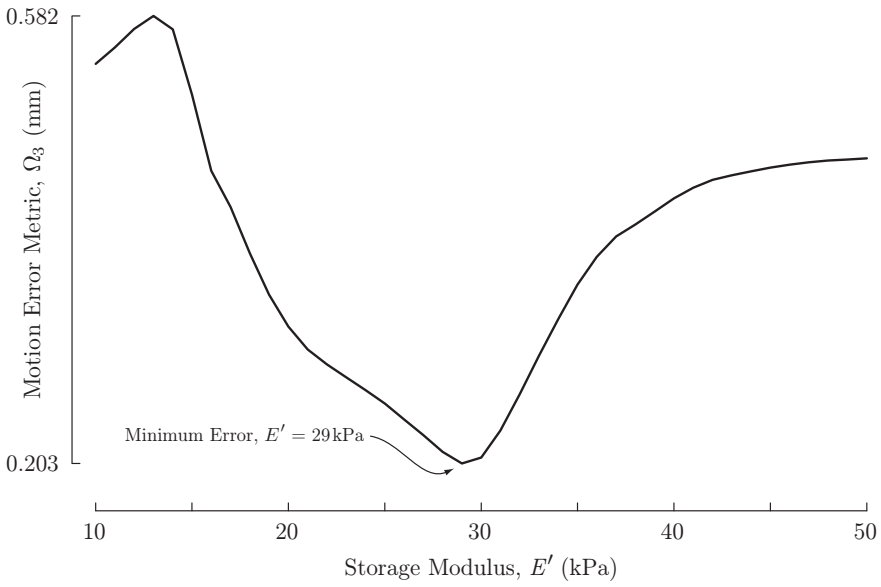

Figure 4.14 Motion error plotted against stiffness for the soft silicone phantom actuated at 50 Hz.

error minimum had clearer definition than in the undamped results from the gelatine phantoms. The distinctness of this global minimum error location is important when considering the ability of reconstruction algorithms to prefer global optimal parameter values over values representing local minima.

The static mechanical testing results from Section 3.2 were a close match to the estimated modulus values based on Ω_3 for the soft silicone, with the estimated value for E' within 15% of the measured static modulus value shown in Table 4.2. The stiffness of the hard phantom was under-estimated by approximately 30 kPa, or 25%, when compared with the mechanical test result. One possible source of this error was a reduction in observed stiffness due to viscoelastic heating of the phantom during the relatively high frequency actuation. Such heating would be more prevalent in the hard silicone, assuming a constant damping ratio. In addition, the static testing boundary conditions discussed in Section 3.2 were found to overestimate the material stiffness measurement by up to 10%. Despite the hard modulus discrepancy, the error sweeps were clearly able to differentiate silicone material stiffness values with a contrast as low as 400–500%. This latter result is more important for the DIET system concept than the exact characterization of material parameter values in hard material, given clinically reported contrasts of up to 1,200% [54–58].

The modulus values in Table 4.3 show that the estimated storage modulus value did not significantly change when the error study was performed on soft phantom experimental data at 50 Hz. This result provides evidence that the estimated storage modulus of the silicone was not strongly dependent on frequency, validating the use

of a static mechanical test as an independent measurement of the silicone stiffness. Due to a similar chemical composition, the hard silicone was be expected to display comparable behavior.

Table 4.3 Elastic modulus values for the soft and hard silicone phantoms, where modulus values estimated using a surface error metric are compared to the measured values from independent static testing.

		Elastic Modulus	
Method	**Frequency**	**Soft Silicone**	**Hard Silicone**
Surface Error	100 Hz	28 kPa	103 kPa
Surface Error	50 Hz	29 kPa	-
Measured (DMA)	static	32 kPa	135 kPa

Geometric non-linearity is one possible explanation for the trend of slightly underestimated displacement amplitudes observed in Figure 4.13. Large measured displacements lead to an increased mismatch with the small strain linear elastic assumption which underpins the FE simulations. That the match between measured and simulated motions is closer toward the top of the phantoms, as evident in Figure 4.13, where vibration amplitudes are lower is further evidence of this effect. Another possible cause of the small displacement mismatch is drive miscalibration, where the actuator displacement may have had a slightly greater amplitude than the prescribed waveform.

The error study performed on the homogeneous silicone data showed that stiffness estimation using the DIET system is possible using a damped material model, with good agreement to mechanical testing results, particularly at lower stiffness values. The method was able to accurately characterize damped material motion on the surface of silicone phantoms to create fitted displacement estimates. Material parameter estimations made for both hard and soft silicone phantoms showed clear differentiation between the storage modulus of hard and soft materials, where optimal parameter values were clearly identified, and resonance was not observed to be a significant issue.

4.3 Heterogeneous Silicone Phantoms

Following the successful estimation of silicone material properties using homogeneous phantoms and a damped material model, a surface error study was performed using the experimental data captured from the two heterogeneous silicone phantoms described in Section 3.3.2. Here, the aim was to evaluate the ability of a surface error metric to estimate a discrete variation in the internal material properties of heterogeneous phantoms. The simple phantom geometries allowed the internal stiffness distribution

to be described by a limited number of shape-based parameters, facilitating the use of the same parameter sweep techniques applied to the homogenous phantoms.

The material properties estimated for both the hard and soft silicone during the heterogeneous surface error study in Section 4.2 are summarized in Table 4.4. The best estimates of damping ratio, ζ, and ν, for the soft and hard silicone were fixed for all heterogeneous simulations, allowing the study to focus on storage modulus values. Clinically, such a simple approach would occur when seeking a tumor at a fixed, large stiffness contrast to healthy tissue values around 20–30 kPa.

Table 4.4 Silicone material properties estimated from the homogenous silicone phantoms using surface error.

Material	E'	ζ	ν
Soft Silicone	28 kPa	0.22	0.48
Hard Silicone	103 kPa	0.20	0.41

4.3.1 Measured Phantom Displacement

Motion capture from the heterogeneous silicone phantoms was performed using the same experimental setup as the homogeneous silicone phantoms, where the components used are described in Section 3.3.2. The tracked reference point positions in three dimensional world space were estimated using the damped fitting algorithm from Section 3.6.3. The observed surface motion for the fifteen reference points on the surface of each heterogeneous phantom are shown in Figure 4.15.

4.3.2 Finite Element Simulation

With material property estimates for the soft and hard silicone in hand, a range of simulations were performed on FE models of the stacked and concentric geometries. The identical size and shape of all silicone phantoms allowed the mesh used for the homogenous silicone phantoms in Section 4.2 to be used for all heterogeneous model simulations. All boundary conditions applied to the models matched the experimental testing conditions, where the actuation was from below in the vertical direction, at 0.5 mm amplitude, 100 Hz frequency.

A two-parameter, shape-based property distribution was used for the heterogeneous phantom error study, where the stiffness distribution within each phantom was defined by independent parameters representing the interface position, P, and stiffness contrast, C, between the soft and hard silicone regions. For the stacked geometry, the interface position, P_s, characterized the ratio of the hard/soft interface height to

the total phantom height. For the concentric geometry, the interface position, P_c, was defined as the ratio of the hard inclusion diameter to the total phantom diameter. The measured values of P_s and P_c for both silicone phantoms manufactured are shown in Table 4.5.

(a) Stacked phantom motion capture.

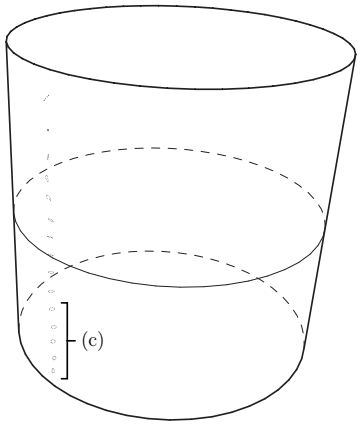

(b) Tracked reference point locations.

(c)

(d) Concentric phantom motion capture.

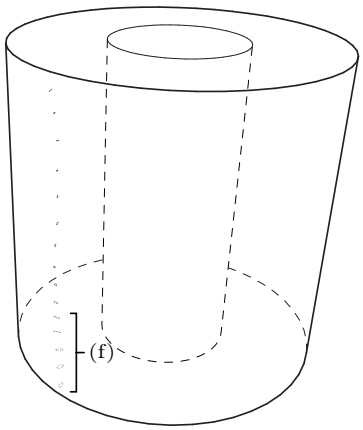

(e) Tracked reference point locations.

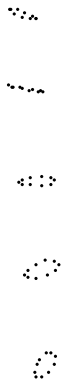

(f)

Figure 4.15 The experimentally observed motion of the stacked and concentric heterogeneous silicone phantoms.

Surface error sweeps in this study thus considered variations in both shape-based parameters P and C. Performing FE simulations over a wide range of both parameters allowed surface error values to be correlated to phantom material property distribu-

Table 4.5 The measured interface position parameter, P, for both heterogeneous silicone phantom geometries.

Geometry	P
Stacked	$P_s = 47\%$
Concentric	$P_c = 42\%$

tions. In line with previous silicone phantom error studies, the experimental evidence for or against a particular property distribution was calculated over all reference points using the surface error metric Ω_3 from Equation 3.17.

4.3.3 Model Parameter Estimation

The heterogeneous study considered two fundamentally different approaches to estimating the phantom stiffness distributions. These two methods are referred to as *corroborative* and *contradictive* methods. Both methods are referenced to a null stiffness distribution, representing the case where the phantom being tested is entirely comprised of soft material.

The *corroborative* method assumes that this soft material modulus is known, and seeks experimental evidence in the form of matching displacement data that confirms the presence of any hard region. If the experimental evidence corroborates this presence, a region of hard material can subsequently be added with an estimated interface position and hard stiffness described by P and C. Conversely, the *contradictive* method assumes that the hard material modulus is known, and seeks to estimate a soft modulus and interface position supported by the experimental evidence. Should the experimental evidence refute any distribution including a high stiffness region, the null result of entirely soft stiffness can still be returned by setting the size of the hard region to zero, $P = 0\%$, and estimating the soft stiffness value alone using the parameter C.

Two stiffness contrast parameters, C, were used during the course of the study. For the corroborative method, where the soft silicone storage modulus, E'_s, was assumed to be known, the focus was on optimizing the stiffness contrast parameter $C_1 = E'_h/E'_s$, where E'_h represents the hard silicone storage modulus. For the contradictive method, where the hard modulus was assumed known, the contrast parameter was defined as $C_2 = E'_s/E'_h$. The definition of these contrast parameters was consistent across both geometries.

4.3.3.1 Corroborative Method

To test the ability of the corroborative method to estimate a heterogeneous phantom stiffness distribution, a set of FE simulations were performed assuming a constant soft silicone modulus value, previously estimated as $E'_s = 28\,\text{kPa}$. For both models, the interface position parameter, P, was varied from 0–100%, and the stiffness contrast parameter, C_1, was varied to generate a range of hard modulus values in the range $E'_h \approx 80\text{–}200\,\text{kPa}$. The resulting values of the error metric Ω_3 from the parameter sweep performed on each geometry are shown in Figure 4.16.

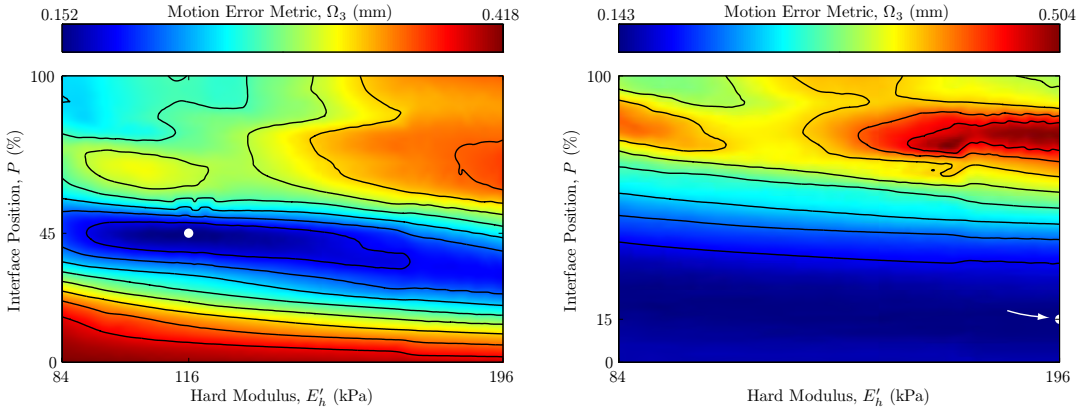

(a) Stacked phantom.

(b) Concentric phantom.

Figure 4.16 Parameter sweep results for the heterogeneous silicone phantoms, using the corroborative method with $E'_s = 28\,\text{kPa}$, where the location of minimum error on each plot is indicated (○).

The estimated stiffness contrast value in Figure 4.16(a) indicates a hard silicone modulus of $E'_h = 116\,\text{kPa}$ for the stacked geometry. The estimated interface position for this geometry was within 3% (relative) of measured position of 47%. The location of minimum error for the concentric model was along the edge of the parameter domain, with neither P_c nor E'_h successfully estimated. In this case, the parameter combination leading to overall minimum motion error was not bounded by the range of parameters simulated.

The sensitivity of the two-parameter corroborative method to variations in the assumed soft modulus value was tested by modifying E'_s by ±15% to 24 kPa and 32 kPa, and repeating the range of simulations. Results from these sweeps are shown in Figure 4.17. The estimated value for P_s for the stacked geometry varied by only 3% (absolute) across the stiffness range, with both estimates of P_s within 10% (relative) of the measured value. Stiffness contrast values corresponding to minimum Ω_3 indicated a hard storage modulus of $E'_h = 116\text{–}122\,\text{kPa}$ for the stacked model.

Results from the additional concentric model corroborative sweeps had varied success. When $E'_s = 32\,\text{kPa}$, the error metric based approach again failed to identify the

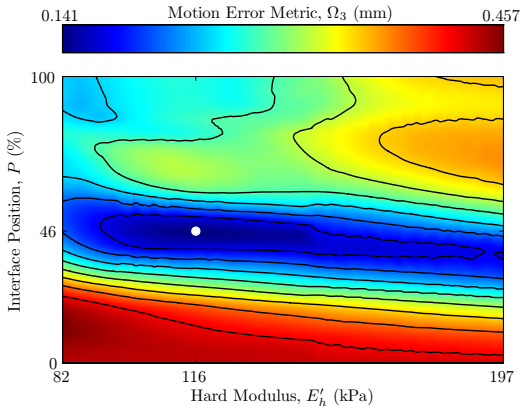

(a) Stacked phantom, $E'_s = 24\,\text{kPa}$.

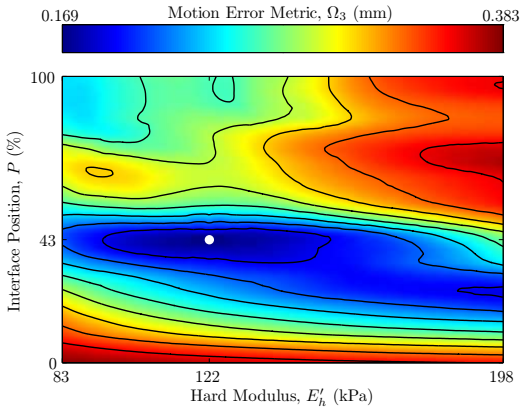

(b) Stacked phantom, $E'_s = 32\,\text{kPa}$.

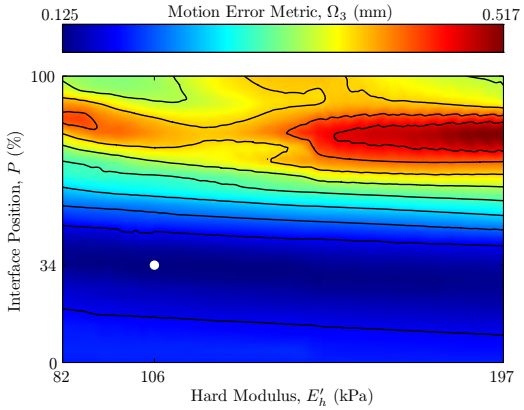

(c) Concentric phantom, $E'_s = 24\,\text{kPa}$.

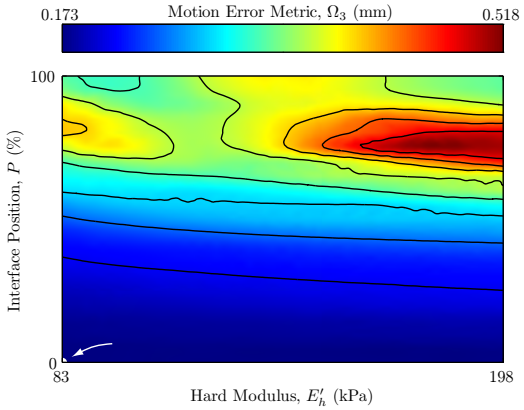

(d) Concentric phantom, $E'_s = 32\,\text{kPa}$.

Figure 4.17 Corroborative method sensitivity analysis results for the heterogeneous phantom data, where the location of minimum error on each plot is indicated (∘).

presence and location of the hard inclusion, with minimum motion error corresponding to an interface position of $P = 0\%$. However, in the case where $E'_s = 24\,\text{kPa}$, the interface position was estimated to within 20% (relative) of the measured value, with the hard modulus estimated at $E'_h = 106\,\text{kPa}$.

4.3.3.2 Contradictive Method

Parameter estimation using a contradictive method was tested by analyzing parameter sweeps based on the previously estimated hard silicone modulus, $E'_h = 103\,\text{kPa}$. Stiffness contrast values, C_2, were varied to cover a soft silicone storage modulus range of approximately $E'_s = 10\text{–}50\,\text{kPa}$, and the interface position, P, was varied from 0–100%. The resulting motion error from these parameter sweeps is shown in Figure 4.18 for both geometries considered.

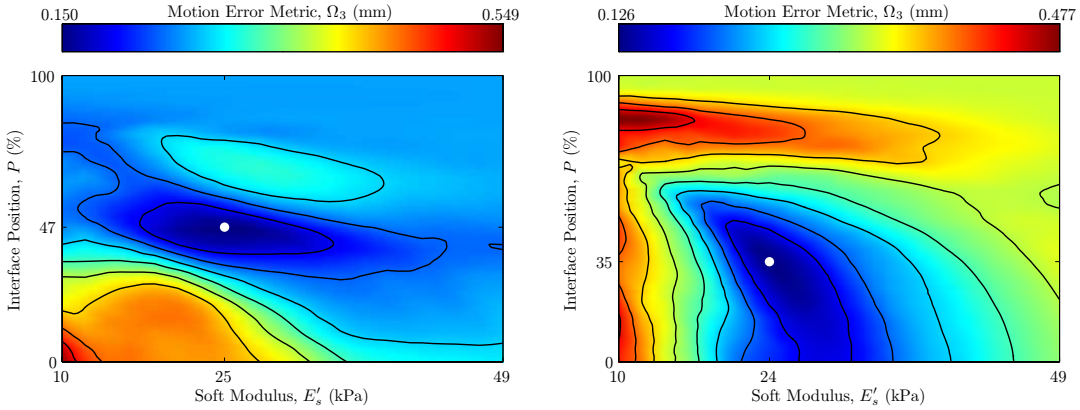

(a) Stacked phantom. (b) Concentric phantom.

Figure 4.18 Parameter sweep results for the heterogeneous silicone phantoms, using the contradictive method with $E'_h = 103\,\text{kPa}$, where the location of minimum error on each plot is indicated (○).

Stacked and concentric motion error plots indicate a soft silicone storage modulus of $E'_s = 24\text{–}25\,\text{kPa}$. The estimated interface position for the stacked geometry was an exact match to the measured value of 47%, while the concentric geometry interface position was estimated as 35%, which is within 20% (relative) of the measured value of $P_c = 42\%$ from Table 4.5. The minimum motion error metric values using the contradictive method were lower for both geometries than in the corroborative case, indicating a closer match to measured displacements using this approach.

The sensitivity of the contradictive method to variations in the assumed hard modulus value was tested by varying E'_h by $\pm 15\%$, to 88 kPa and 118 kPa, and repeating all simulations. Figure 4.19 shows the result of these parameter sweeps. Here, results are consistent with the $E'_h = 103\,\text{kPa}$ case, with all simulations continuing to indicate a soft modulus of $E'_s = 24\text{–}25\,\text{kPa}$. The interface position for the stacked geometry was

estimated within 7% (relative) of the measured value in both cases, while the concentric interface position was estimated to within 20% (relative) of the measured value.

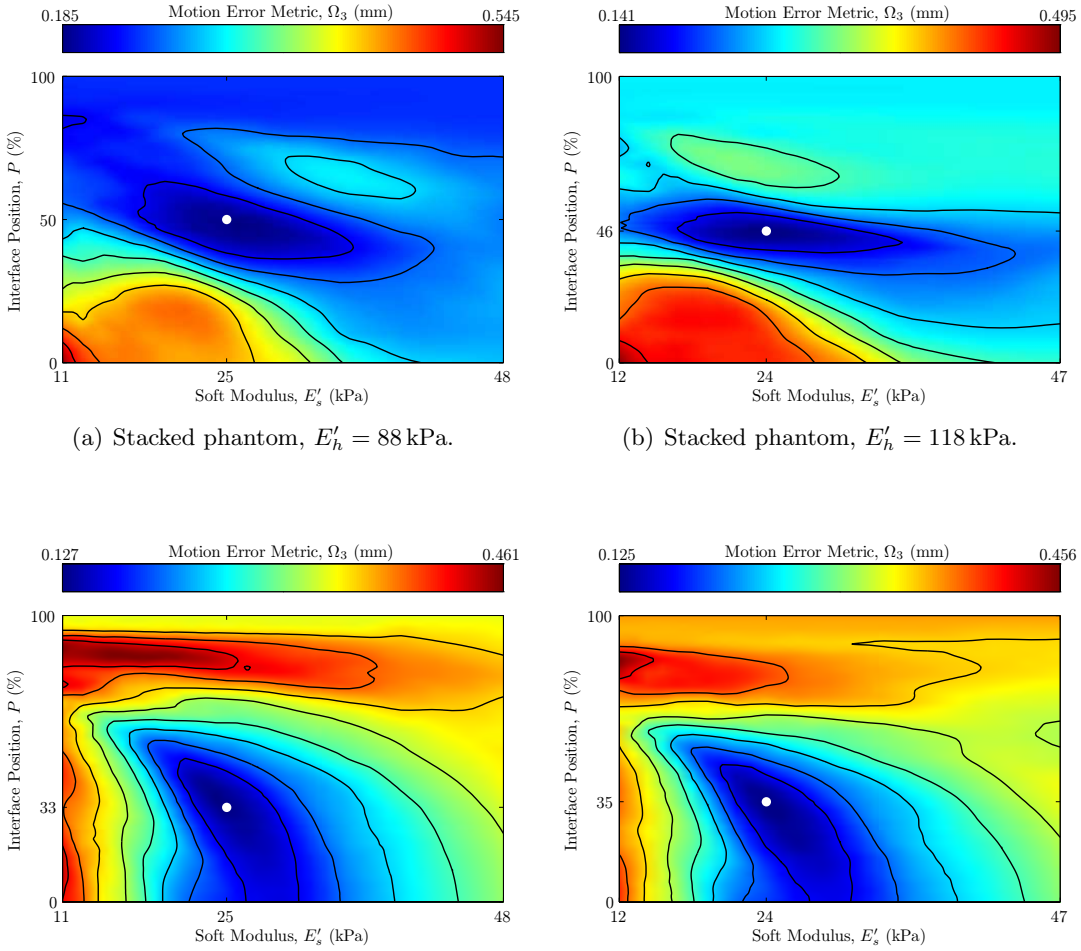

(a) Stacked phantom, $E'_h = 88\,\text{kPa}$.

(b) Stacked phantom, $E'_h = 118\,\text{kPa}$.

(c) Concentric phantom, $E'_h = 88\,\text{kPa}$.

(d) Concentric phantom, $E'_h = 118\,\text{kPa}$.

Figure 4.19 Contradictive method sensitivity analysis results for the heterogeneous silicone phantom data, where the location of minimum error on each plot is indicated (○).

The best match to the experimental data for both geometries was obtained using the contradictive method with $E'_h = 118\,\text{kPa}$. Figure 4.20 is a comparison of the simulated motion at the best fit parameter values when $E'_h = 118\,\text{kPa}$, and the measured motions, for both stacked and concentric geometries. The motion error metric Ω_3 for the stacked and concentric geometries in these cases was 0.141 mm and 0.125 mm respectively. These values represent an average orthogonal amplitude error per reference point of $\frac{\Omega_3}{2} \approx 0.06$–$0.07\,\text{mm}$, which less than 20% of the average surface motion amplitude.

Inherent to the contradictive parameter estimation method is the assumption that if the null stiffness is represented by an entirely soft phantom, the correct stiffness distribution will be returned. To test this hypothesis, measured motion data from the

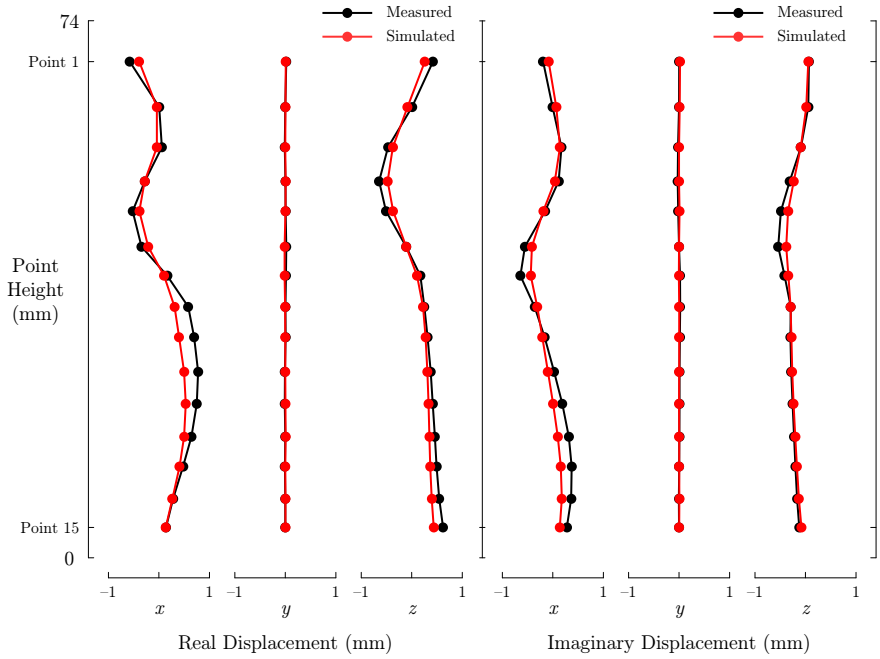

(a) Stacked phantom, simulated displacement at $E'_h = 118\,\text{kPa}$, $E'_s = 24\,\text{kPa}$, $P_s = 46\%$.

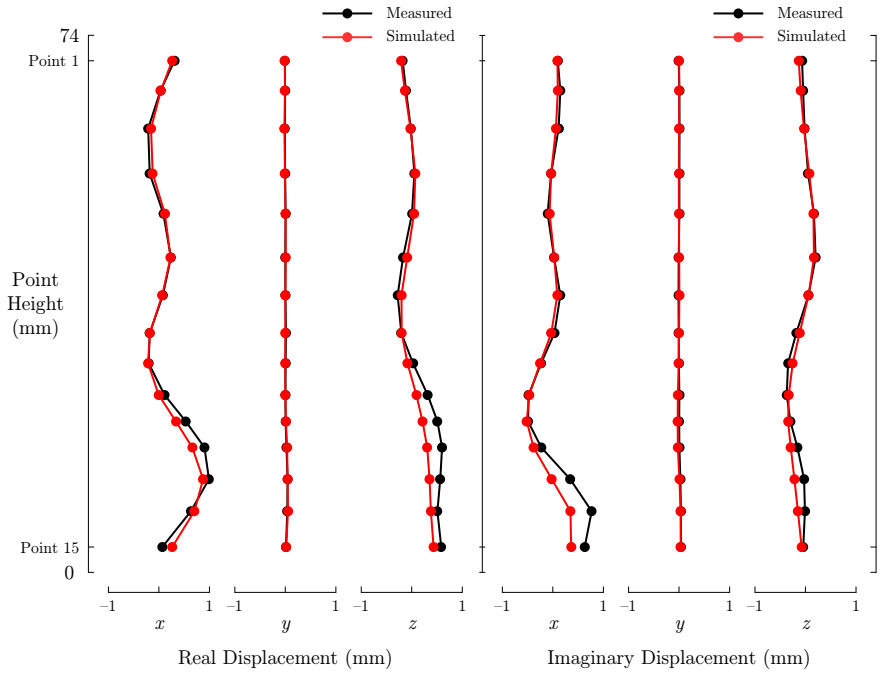

(b) Concentric phantom, simulated displacement at $E'_h = 118\,\text{kPa}$, $E'_s = 24\,\text{kPa}$, $P_c = 35\%$.

Figure 4.20 The best fitting FE-simulated cases compared with experimental motions for both heterogeneous silicone phantoms.

soft homogeneous silicone phantom was used as reference motion data, and compared to sweep displacements using the contradictive method, where $E'_h = 103\,\text{kPa}$. The resulting error domains for the stacked and concentric cases are shown in Figure 4.21. The estimated interface position value for both geometries is $P = 0\%$, corresponding to a homogenous phantom, where estimated E'_s values indicate a soft modulus of 27–28 kPa.

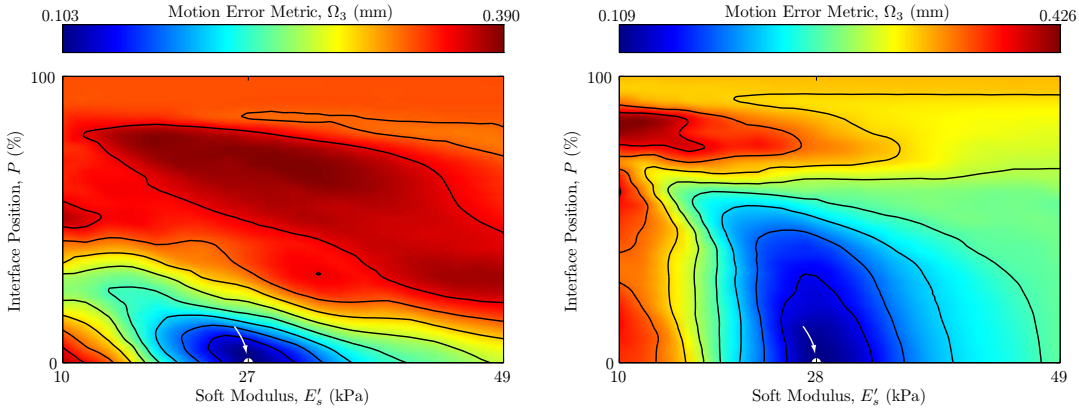

(a) Stacked phantom.

(b) Concentric phantom.

Figure 4.21 Parameter sweep results from the homogenous soft silicone phantom, using the contradictive method with $E'_h = 103\,\text{kPa}$, where the location of minimum error on each plot is indicated (○).

4.3.4 Discussion

The two parameters describing the stiffness distribution of the stacked geometry were consistently estimated correctly using both corroborative and contradictive approaches. Results from the concentric case showed the stiffness distribution can be consistently estimated for this more challenging geometry only when adopting the contradictive approach. The error plots in Figures 4.16 and 4.17 indicate that a corroborative approach to estimation of stiffness distribution is sensitive to any error in the assumed value for E'_s. This sensitivity is more significant in the concentric case, where assumed soft modulus values of $E'_s = 28\,\text{kPa}$ and $E'_s = 32\,\text{kPa}$ led to failed parameter estimation. Because the *a priori* silicone stiffness values were estimated based on phantoms created at a different time, this sensitivity to E'_s renders the corroborative method unsuitable in a clinical sense.

Figures 4.18 and 4.19 provide evidence that parameter estimations using a contradictive approach have very little sensitivity to variations in E'_h, as expected from the relatively long shear wavelength in the harder material. Estimated values for soft modulus and interface position showed relative variation of less than 10% across both geometries over a 30% range in the assumed value of E'_h, indicating a sensitivity of ap-

proximately 33%, or a robust result. All six instances of the contradictive estimations indicated a consistent soft modulus value of 24–25 kPa.

The estimated silicone stiffness values using both corroborative and contradictive estimations did not agree with the previously estimated homogeneous silicone modulus values. In comparison with $E' = 28\,\text{kPa}$ estimated from the homogeneous studies, all contradictive estimations indicated a soft modulus value of $E'_s = 24\text{–}25\,\text{kPa}$, and the lowest motion error values using the corroborative method came when assuming $E'_s = 24\,\text{kPa}$. Similarly, the lowest error metric values when using the contradictive method came when $E'_h = 118\,\text{kPa}$, and all corroborative estimations indicated a value for E'_h above the previously estimated value of $E' = 103\,\text{kPa}$.

The range of values estimated for silicone stiffness indicates that the modulus values for the soft and hard silicone varied between homogeneous and heterogeneous phantoms, most likely due to the different batches of silicone used when preparing these phantoms. Figure 4.22 presents a summary of the range of silicone modulus values estimated and measured during the study, where the different colors indicate batches of silicone prepared at different times. The clustering of results visible in this graphic indicates that there is a degree of variability in the modulus value of the silicone based in part on the experimental uncertainties when preparing the silicone material. Additionally, the values from DMA testing were overestimated by up to 10% due to the boundary condition effects discussed in Section 3.2.

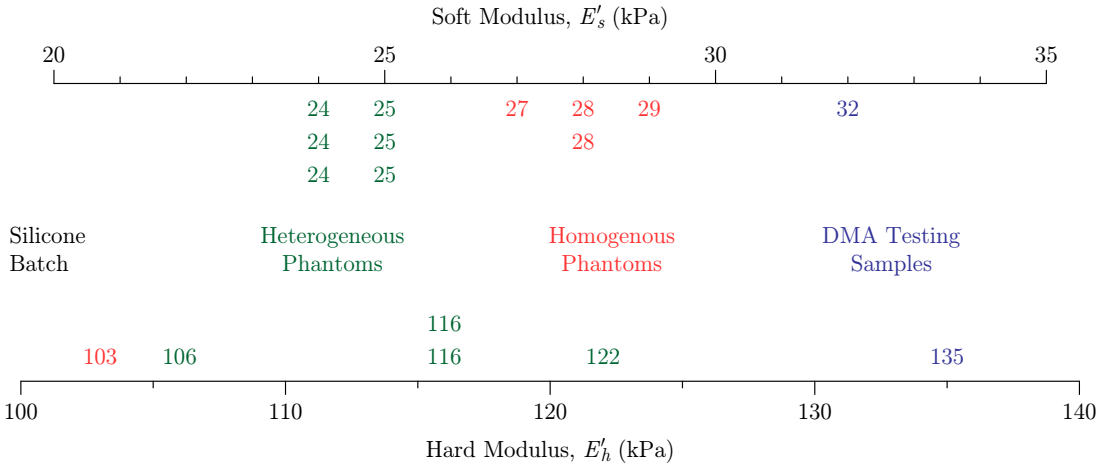

Figure 4.22 The range of modulus values estimated and measured for both soft and hard silicones, where color is used to differentiate batches of silicone prepared at different times.

In general terms, the error metric for the stacked geometry had a higher sensitivity to variations in the interface position parameter than for the concentric case, as evidenced by highly ellipsoidal motion error contours, for example in Figure 4.16(a). This heightened sensitivity is expected as the stacked geometry has reference motion

measurement located directly on the hard and soft silicone regions, allowing the interface position to be accurately identified due to the step change in shear wavelength across the two materials. The wavelength change between the lower and upper portions of the stacked phantom is visible in Figure 4.20(a). The concentric geometry had a significantly lower error sensitivity to interface position, and consequently less accurate interface position estimates. The physical separation of the measurement locations from the stiffness interface provides evidence as to why this loss of accuracy occurs.

The success of the contradictive estimation approach when applied to the soft homogenous silicone phantom data shown in Figure 4.21, confirmed that this method was able to successfully return the null distribution when applied to a phantom with constant stiffness. The estimated value for the soft silicone modulus across both geometries of 27–28 kPa matched the corresponding value estimated from the soft phantom in Section 4.2, while the interface position value of 0% confirmed the absence of any hard inclusion in both cases.

The comparison between the best-fit displacements and the measured motion shown in Figure 4.20 indicates that when measured displacements are large, the equivalent simulated motion is of a smaller amplitude. This result is consistent with the homogeneous silicone phantom study, where the largest differences in amplitude were observed to occur close to the actuation plate, where amplitudes are large. It is possible that geometric non-linearity causes displacements to be under-estimated by FE simulation, an effect that could be minimized by reducing the actuation amplitude.

Though the shape based approach to property distribution estimation involved very simple geometry in this study, the underlying principles allow such a method to be extended to more clinically relevant scenarios. In such cases, an increase in the number of parameters would allow the identification of irregular shaped inclusions using a more sophisticated geometry description. Such an increase in parameters would require non-linear methods for parameter reconstruction, as the problem domain becomes too large for exhaustive exploration using FE simulation. An extension to the heterogeneous study where E'_s, E'_h, and P are estimated independently may provide a more complete method for reconstructing the elasticity distribution of the concentric phantom, which returned less accurate interface position results in this experiment.

The heterogeneous surface error study performed demonstrated that the DIET method can estimate the elasticity distribution of heterogeneous phantoms using a simple two parameter, shape-based approach with limited surface motion data as input. Trials of both corroborative and contradictive techniques indicated that the contradictive method is more robust in the presence of error in any *a priori* stiffness assumptions. Adopting a contradictive approach to estimating elasticity distribution has the potential to reduce the number of parameters required to perform shape-based elasticity reconstructions. In such a method, the stiffness of any inclusion is fixed, as the exact

stiffness used has very little effect on the observed surface motion. Such an approach represents a potentially new avenue to inclusion imaging in elastography, as it is also applicable to problems characterized by a larger number of parameters, allowing more complicated geometries to be reconstructed with less computational effort.

Chapter 5

Non-Linear Reconstruction Algorithms

The studies performed in Chapter 4 provide important information about how experimentally observed and FE-simulated phantom surface motions related to the internal distribution of material properties. In addition, the error sweeps performed also allowed estimates of the phantom material properties to be made using a limited number of material parameters. Performing these error sweeps required an assumed *a priori* knowledge of the material property distribution and computational resources sufficient to perform FE simulations across the entire range of independent, unknown parameters.

While limited *a priori* knowledge may be available in a more realistic clinical scenario, an exhaustive evaluation of the parameter space is not likely to be possible given the time and computational constraints that would be applied to any clinical application of a DIET system. Computational considerations will become more significant as the number of unknown parameters is increased to evaluate more realistic geometries. The work described in this chapter aimed to reconstruct the material property distribution of simulated and experimental phantoms using a range of non-linear reconstruction algorithms.

Inverse problems in the field of elastography are highly non-linear, as the observed displacement field of a solid body, and therefore any error function based on this displacement, has a complex, high order differential relationship to the underlying mechanical properties of the object. A range of strategies have been developed to solve the elastic inverse problem, the majority of which apply an iterative approach based on a gradient descent strategy to minimize the error between a set of model-simulated measurements and corresponding experimental observations. Though novel reconstruction techniques based on a stochastic approach, such as Genetic Algorithms (GAs), have been applied to inverse problems where the FE method is used for system simulation, the application of such stochastic methods to the tomographic elastography problem, particularly when using only exterior surface motion measurements from experimental phantoms, has not been considered. In this study, both deterministic and stochastic

classes of reconstruction algorithm are considered with regards to their suitability for inclusion as a reconstruction algorithm in a DIET system.

The investigation of reconstruction algorithms in this chapter was performed concurrently with the surface error studies presented in Chapter 4. Therefore, the inverse algorithms were tested on a range of phantom data in conjunction with the development of the experimental and FE simulation techniques. Surface error domains similar to those used in Chapter 3 were often developed prior to the evaluation of reconstruction algorithms in this work. This detailed error information provided an additional tool used to allow a more thorough investigation of algorithm performance. However, it is not required for practical, clinical implementation of any of the algorithms considered.

5.1 Gradient Descent Optimization

The minimization of a non-linear error function, Ω, using the gradient descent method, is a deterministic process where an iterative approach is used to optimize a parameter combination, θ. A gradient descent algorithm aims to determine a best fit parameter combination by calculating the gradient of the error function at the current parameter estimate, $\frac{\partial \Omega}{\partial \theta}$, and updating the estimate by moving along this direction towards decreasing error.

To perform gradient descent reconstruction, the gradient of the error function at any parameter combination must be obtainable, requiring that the error function $\Omega(\theta)$ be continuous. This gradient calculation can be made using either analytic or finite-difference methods. For the tomographic reconstruction problem, the error function Ω must be calculated from available experimental and/or simulated data each iteration.

Figure 5.1 is a basic example of gradient descent reconstruction in a two-parameter case, where optimal values for the independent parameters $\theta = (x, y)$ are $\hat{\theta} = (\hat{x}, \hat{y})$. The colored contours on the plot define constant values of the error function $\Omega(\theta)$. Over a number of iterations, the algorithm's estimates of x and y are updated towards the combination that minimizes Ω.

Non-linear elastic property optimization aims to reconstruct any number of parameters, represented by θ, that describe the internal stiffness distribution of a model. Gradient descent optimization in this case involves the minimization of an error function, Ω, that compares a set of measured displacements, $\mathbf{u^m}$, to FE calculated displacements based on the current estimate of the model stiffness parameters, $\mathbf{u^c}(\theta)$. The range of motion error metrics developed for the DIET system are described in Section 3.7, and are represented here in general terms as a squared vector error,

$$\Omega = \|\mathbf{u^m} - \mathbf{u^c}(\theta)\|^2. \tag{5.1}$$

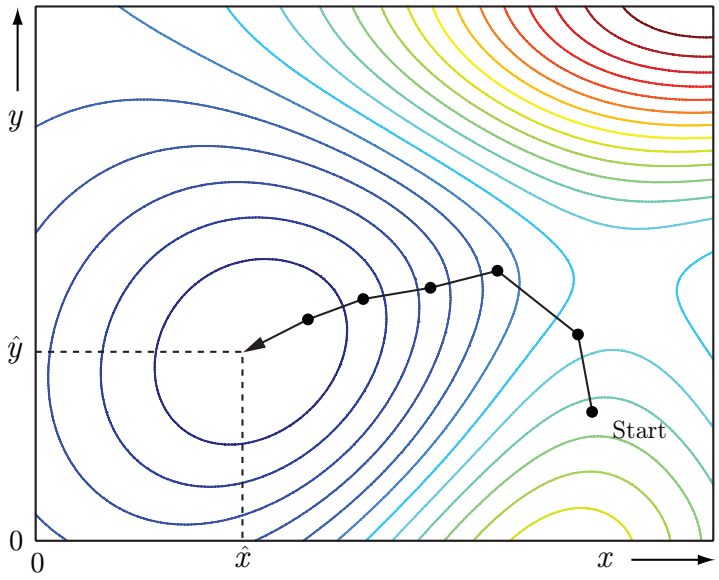

Figure 5.1 An example of a gradient descent algorithm, where successive iterations minimize the value of a two-dimensional error function $\Omega(x, y)$.

The gradient of the error function with respect to θ will be zero at the parameter combination corresponding to a minimum error value. Setting $\frac{\partial \Omega}{\partial \theta} = 0$ generates a non-linear system of equations,

$$\frac{\partial \Omega}{\partial \theta} = -2 \left(\frac{\partial \mathbf{u^c}}{\partial \theta} \right)^T \left(\mathbf{u^m} - \mathbf{u^c}\left(\theta\right) \right) = 0, \tag{5.2}$$

where the operator ^{T} denotes the matrix transpose. Equation 5.2 can be solved iteratively using the Gauss-Newton method. In this case, the formulation is written

$$\theta_{r+1} = \theta_r - \delta_r \left(\frac{\partial^2 \Omega}{\partial \theta^2} \right)^{-1} \left(\frac{\partial \Omega}{\partial \theta} \right) \tag{5.3}$$

for iteration $r + 1$, where δ_r is chosen to influence the step size of the algorithm. Development of the Hessian matrix term, $H = \frac{\partial^2 \Omega}{\partial \theta^2}$, leads to

$$\frac{\partial^2 \Omega}{\partial \theta^2} = 2 \left(\frac{\partial \mathbf{u^c}}{\partial \theta} \right)^T \left(\frac{\partial \mathbf{u^c}}{\partial \theta} \right) - 2 \left(\frac{\partial \mathbf{u^c}}{\partial \theta} \right)^T \left(\mathbf{u^m} - \mathbf{u^c}\left(\theta\right) \right), \tag{5.4}$$

where the term $2 \left(\frac{\partial \mathbf{u^c}}{\partial \theta} \right)^T \left(\mathbf{u^m} - \mathbf{u^c}\left(\theta\right) \right)$ is assumed to be negligible, as $\mathbf{u^m} - \mathbf{u^c}\left(\theta\right)$ is small when θ is close to the actual parameter distribution of the medium being imaged. The full iterative formulation for the problem can thus be written by expanding the form of Equation 5.3,

$$\theta_{r+1} = \theta_r - \delta_r \left(2 \left(\frac{\partial \mathbf{u^c}}{\partial \theta} \right)^T \left(\frac{\partial \mathbf{u^c}}{\partial \theta} \right) + \gamma \mathbf{I} \right)^{-1} \left[-2 \left(\frac{\partial \mathbf{u^c}}{\partial \theta} \right)^T \left(\mathbf{u^m} - \mathbf{u^c}\left(\theta\right) \right) \right], \quad (5.5)$$

where γ is a regularization term added to the Hessian matrix for numerical stability.

5.1.1 Reconstruction Algorithm Structure

Mechanical property reconstruction using a gradient descent algorithm was first performed on the hard gelatine phantom. The surface error study performed on this phantom in Section 4.1 indicated that the gelatine material used in the phantom had a Young's Modulus value of $E = 27.1\,\text{kPa}$. This estimate was also corroborated by independent mechanical testing.

When formulating the inverse problem for this study, a homogeneous, isotropic case was assumed, where ν and ρ were assumed known at 0.49 and $1{,}000\,\text{kg/m}^3$ respectively. These assumptions limited the reconstruction to a single parameter representing Young's Modulus, E. The undamped material model used for FE simulation in Section 4.1 was used for all displacement simulations. A flow chart showing the basic structure of the gradient descent algorithm developed to perform the one parameter reconstruction is shown in Figure 5.2, and is described in the following.

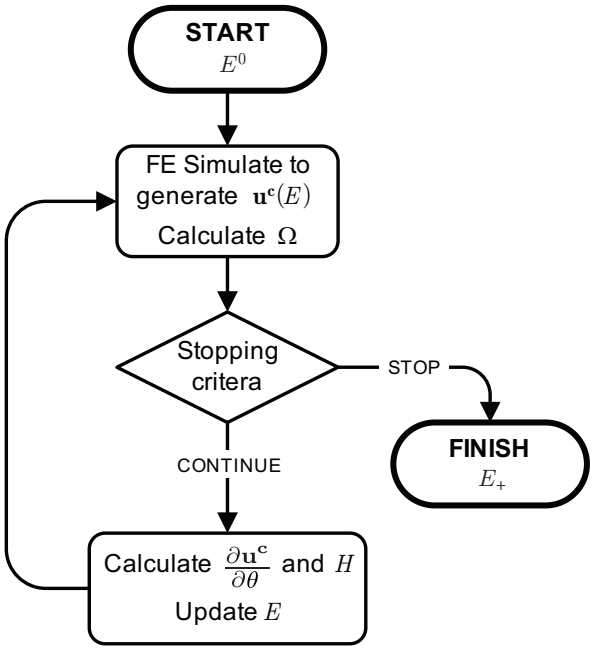

Figure 5.2 A schematic of the gradient descent algorithm used for elastic reconstruction.

The reconstruction of E using the gradient descent algorithm began with an initial guess for the stiffness parameter at iteration zero, E^0. FE simulation using this value and the constant values of ρ and ν previously assumed gave a vector of calculated displacements at all nodes within the model, $\mathbf{u^c}$. The transformation from these nodal amplitude values to the equivalent reference point displacements was performed according to the point projection and damped fitting techniques described in Sections 3.5.2 and 3.6.3. The error between the FE-simulated displacement field and the measured motion was calculated using the metric Ω_2 previously defined in Equation 3.16, where the damped simulated motion was transformed into an undamped approximation prior to error calculation. Following the calculation of $\frac{\partial \Omega}{\partial \theta}$, and the approximate Hessian matrix, regularization was applied to the Hessian matrix diagonal based on the method described by Marquardt [108].

An updated estimate for E was calculated using Equation 5.5, where the parameter step size, δ_r, increased from 0.1–1.0 over the first ten iterations. The new stiffness value was subsequently used to simulate a new displacement vector $\mathbf{u^c}$. Stopping criteria for the gradient descent algorithm were based on the value of the residual term from Equation 5.5,

$$R = \left(\frac{\partial \mathbf{u^c}}{\partial \theta} \right)^T \left(\mathbf{u^m} - \mathbf{u^c}\left(\theta\right) \right). \tag{5.6}$$

In this study, the reconstruction algorithm was halted when $R < 1 \times 10^{-10}\,\mathrm{m^4N^{-1}}$, indicating a situation where the algorithm step size was sufficiently small to consider the reconstruction as having converged. The output from GD reconstruction was the stiffness value providing the closest match to the experimental data, E_+.

5.1.2 Stiffness Reconstruction Results

Stiffness reconstruction for the hard gelatine phantom using the gradient descent algorithm was split into two stages. The first application of the reconstruction algorithm was to a simulated data set, where FE-simulated motion at the previously estimated phantom stiffness value of 27.1 kPa represented the experimentally measured data. Testing the reconstruction algorithm using this noise free simulated data would confirm the ability of the algorithm to reach a global minimum in an ideal case. Following the simulated data study, the same set of reconstructions were performed using the real experimentally measured motion data from the gelatine phantom.

In both the simulated and experimental data cases, knowledge of the error domain across the stiffness range of interest was obtained prior to reconstruction. While this information was not required to perform the reconstructions, it allowed for a more detailed analysis of the results in each case. The stiffness range selected for the reconstruction study was $E = 20$–$30\,\mathrm{kPa}$, where the surface error study from Section 4.1

was refined so that FE-simulated displacement data was available every 1 Pa over this range.

5.1.2.1 Simulated Data

The error metric Ω_2 resulting from comparison of the FE simulations between $E = 20$–$30\,\text{kPa}$ to the simulated data set at $E = 27.1\,\text{kPa}$ is shown in Figure 5.3(a). Several resonance stiffness values are apparent, where the value for the error metric is highly discontinuous. As expected, the optimal value for Young's Modulus was $\hat{E} = 27.1\,\text{kPa}$, where $\Omega_2 = 0$ in the noise free case considered.

A total of 21 gradient descent reconstructions were performed on the simulated data, with initial guesses E^0 at 500 Pa increments in the range 20–30 kPa. The performance of these reconstructions over the first ten iterations is shown in Figure 5.3(b), where each reconstruction progresses vertically downwards. The shaded upper part of the plot represents the continuity of the error function over the range $E = 20$–$30\,\text{kPa}$ using the gradient term $\frac{\partial\Omega}{\partial E}$, where areas of discontinuity appear as dark vertical bands. Of all the reconstructions performed in the simulated case, a total of 7 failed to indicate stiffness values within 5% of the target modulus. The remaining fourteen successful reconstructions all converged to modulus values within 5% of the target value, $E = 27.1\,\text{kPa}$.

5.1.2.2 Experimental Data

The error metric Ω_2 from comparison of the FE-simulated displacement database to the experimental data from the hard gelatine phantom is shown in Figure 5.4(a). Initial estimates of E^0 for the reconstructions were the same as in the simulated case, where a total of 21 reconstructions were performed. The performance of these reconstructions over the first ten iterations is shown in Figure 5.4(b), where the separate upper section of the plot again represents the error gradient, indicating the continuity of the error function over the stiffness range. Of the 21 initial guesses applied to reconstruction of the experimentally measured data, 5 failed to converge to the correct solution. Similar to the simulated data reconstructions, the remaining reconstructed modulus values converged to within 5% of the target value.

5.1.3 Discussion

Application of a gradient descent reconstruction algorithm to the ideal simulated data highlighted significant limitations in the method. In particular, one third of all reconstructions failed to identify the single stiffness parameter correctly when starting from initial guesses within 8 kPa of the target value. Analysis of Figure 5.3 provides clear evidence as to why this issue occurs, with all failed reconstructions converging

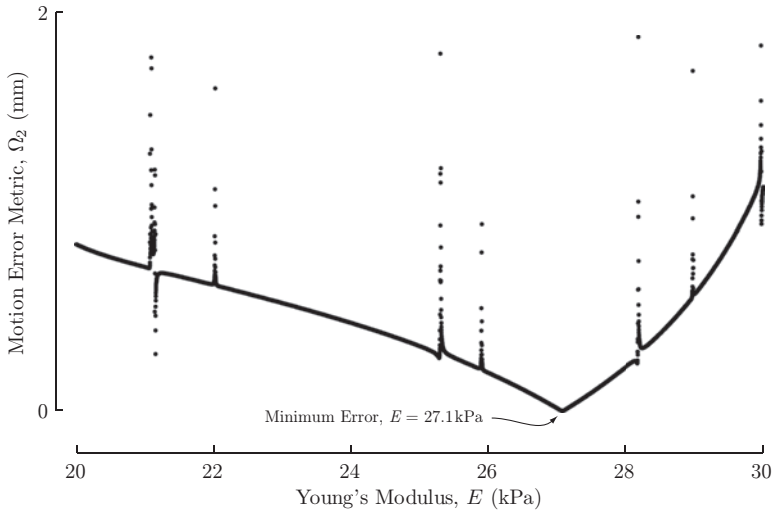

(a) Surface motion error metric variations with stiffness.

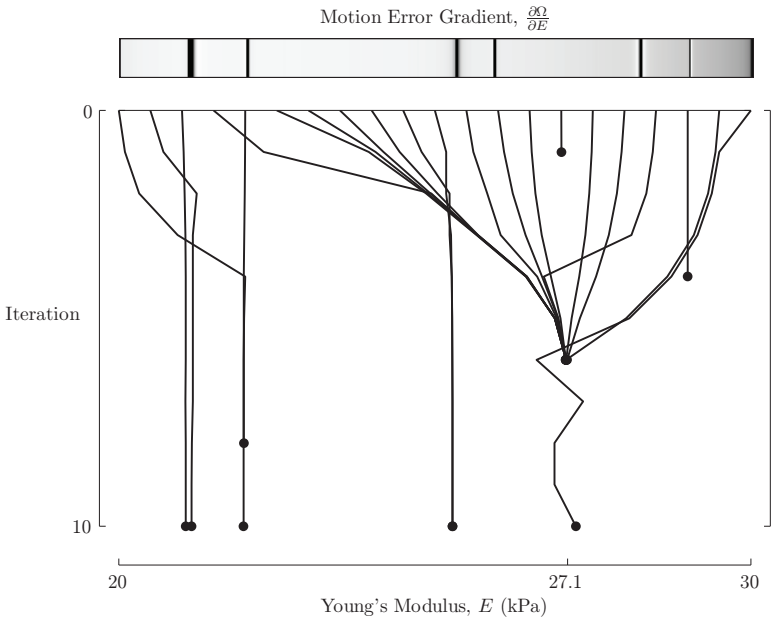

(b) Gradient descent reconstruction results over the first ten iterations, where algorithm convergence is indicated (•).

Figure 5.3 Gradient descent reconstruction results when assuming that simulated motion at $E = 27.1\,\text{kPa}$ represented an experimental data set.

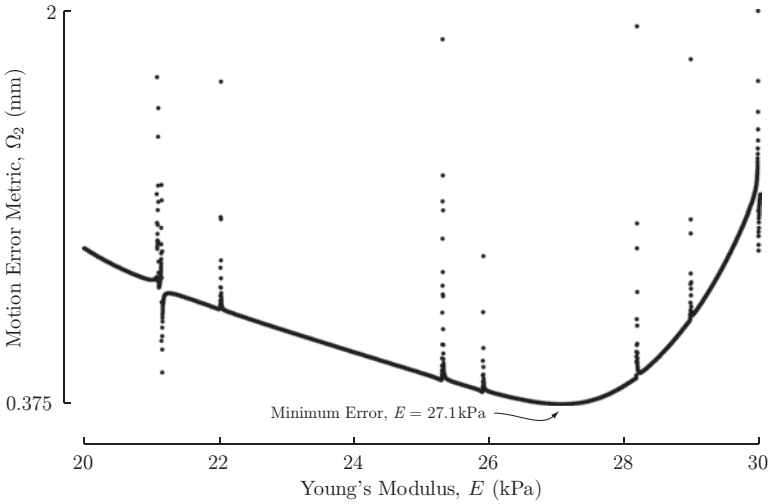

(a) Surface motion error metric variation with stiffness.

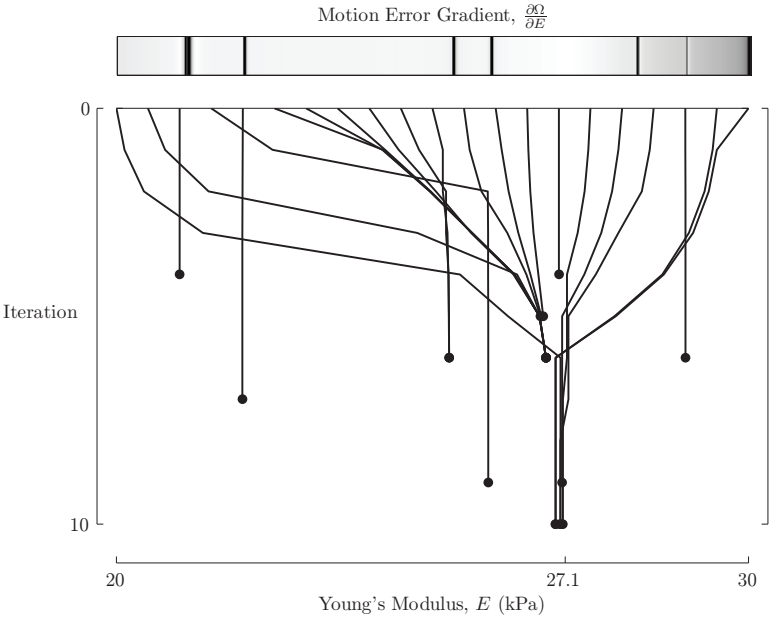

(b) Gradient descent reconstruction results, where algorithm convergence is indicated (•).

Figure 5.4 Gradient descent reconstruction results from the real experimental data captured from the hard gelatine phantom.

on stiffness values at or very near resonant values. These resonance bands are visible as peaks in Figure 5.3(a), and vertical lines of high error gradient in the upper part of Figure 5.3(b). Despite these resonant bands being comparatively narrow, they were sufficient to cause the reconstruction to prematurely converge when evaluating a stiffness value close to a resonance peak.

An example of a local minimum caused by a resonant stiffness value is shown in Figure 5.5. The clear global error minimum in Figure 5.3(a) led to all but one successful reconstruction converging to the correct stiffness value within five iterations. The remaining case showed clear preference for this stiffness value after ten iterations, with its oscillation about the target stiffness value reducing over successive iterations.

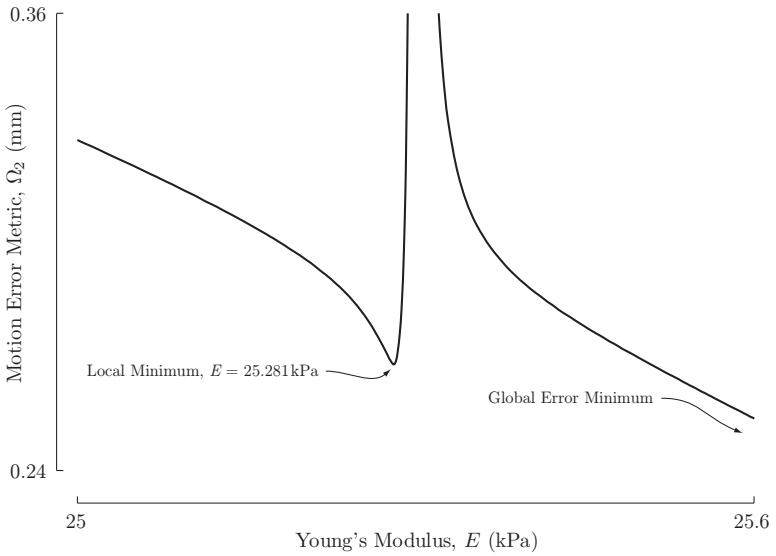

Figure 5.5 An enlarged view of the error domain from Figure 5.3(a), detailing the local minimum caused by a resonant stiffness.

Results from the application of the gradient descent algorithm to the experimentally measured phantom data were very similar to the simulated case, with a slightly higher proportion of reconstructions identifying the 27.1 kPa stiffness value corresponding to minimum motion error. All failed reconstructions again converged to stiffness values corresponding with areas of motion error discontinuity that created local minima. The number of iterations required for convergence in the successful real data reconstructions was greater than in the simulated data reconstructions due to the shallow gradient surrounding the global error minimum visible in Figure 5.4(a).

The high proportion of failed gradient descent reconstructions in this simple one parameter case indicated that even highly localized error minima can cause significant problems for a deterministic reconstruction algorithm based on local gradient calculations. Expanding the stiffness range investigated past the 20–30 kPa considered here would almost certainly increase the number of local error minima, providing a signif-

icant challenge to reconstruction. While adding more sophistication to the gradient descent algorithm to avoid small resonance minima may increase the success rate when applied to the one-dimensional error domain in this study, the expansion of that domain to include multiple parameters introduces additional local minima issues that gradient descent methods would struggle to overcome even if resonance issues could be reduced with a damped material model.

The initial gradient descent study indicated that an investigation into stochastic reconstruction algorithms for the non-linear reconstruction of stiffness was potentially warranted, particularly when considering the more realistic clinical case that will eventually involve multiple independent parameters. The degree of randomness inherent to stochastic algorithms, such as GAs, presents a possible method for overcoming the limitations of the gradient descent approach when dealing with local minima.

In addition, a hybrid combination of deterministic and stochastic reconstruction algorithms for solving the elastic inverse problem also warrants investigation based on these results. When determining the effectiveness and suitability of such alternative methods for use in a DIET system, a comparison to a traditional gradient descent approach should be considered. Performance differences would be measured by the balance of parameter reconstruction effectiveness and computational cost.

5.2 Hybrid Reconstruction Simulation Study

The use of stochastic algorithms for non-linear optimization has increased with the availability of fast and affordable computer hardware that can offset the large computational costs associated with such methods. Stochastic reconstruction methods such as a GAs vary in their application based on simulation techniques, the type and quantity of measured data, and the method used to encode and/or parameterize the optimization problem. Hence, this class of algorithms are highly application specific.

A first study using stochastic algorithms for parameter reconstruction in a DIET system was performed using FE-simulated data to represent experimentally measured motion in a controlled fashion. The intent of this study was to create and evaluate a stochastic algorithm using reference data free from unknown and highly variable experimental error, before performing reconstructions on real phantom data. The algorithm was intended to be a hybrid approach combining both traditional Gradient Descent (GD) methods with novel Combinatorial Optimization (CO) techniques. As part of the algorithm development, the three non-linear reconstruction methods summarized in Table 5.1 were evaluated for their performance when applied to the elastographic inverse problem.

The two shape-based parameters P and C introduced in Section 4.3.2 were used to describe the internal stiffness distribution of the simple heterogeneous model geometries

Table 5.1 The reconstruction algorithms considered during development of the hybrid reconstruction method.

Algorithm	**Identifier**	**Class**
Gradient Descent	GD	Deterministic
Combinatorial Optimization	CO	Stochastic
Hybrid Algorithm	Hybrid	Combination

considered in this study, where both geometries are shown in Figure 5.6. The interface position parameter P_s represented the ratio of the hard/soft interface height to the total model height for the stacked geometry, and P_c the ratio of the hard inclusion diameter to the total diameter in the concentric case. The stiffness contrast parameter C was defined for both geometries as E_h/E_s, representing a corroborative approach according to the definition in Section 4.3.3.

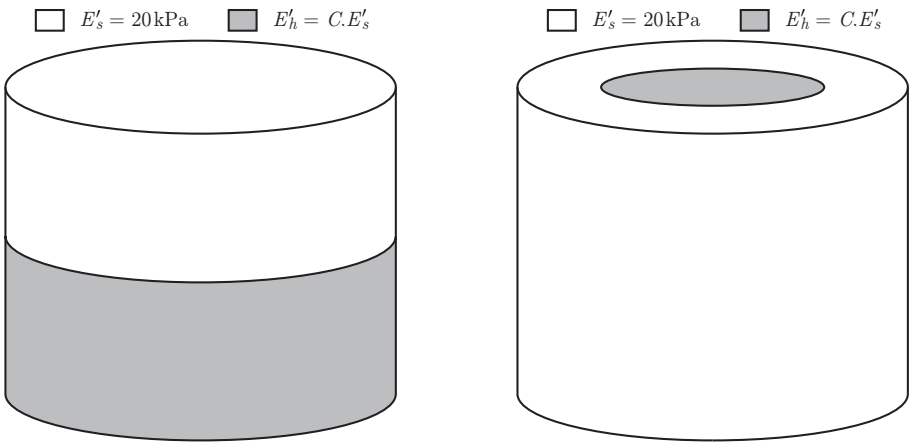

(a) Stacked model geometry. (b) Concentric model geometry.

Figure 5.6 The geometry of both phantom models used in the hybrid algorithm simulation studies.

5.2.1 Finite Element Simulation

Surface motion data sets required for the study were generated by FE simulation, using a mesh containing approximately 169,000 linear tetrahedral elements. The model size of 75 mm diameter and 75 mm height was chosen as a close approximation to the silicone phantoms that were prepared subsequent to this work. The bottom face of the cylinder was constrained in the horizontal plane and actuated vertically with an amplitude of 1 mm at a frequency of 50 Hz. Both geometries were simulated using the

same mesh, with Young's Modulus values assigned nodally based on location relative to the specified values of P and C. An undamped material model was used to simplify the reconstruction problem by reducing the number of parameters required for simulation. While the results from the gelatine phantom gradient descent reconstructions in Section 5.1 indicated an undamped model would not give a close match to experimental phantom displacements, such a model was sufficient in this case for testing reconstruction algorithms where all data was simulated.

The Young's Modulus value for the soft material, E_s, was fixed at 20 kPa, chosen to be of the same order as Young's Modulus measurements of fat and glandular tissue in the human breast, and the soft phantom stiffness values estimated in Chapter 4. Poisson's ratio, ν, and density, ρ, were fixed at 0.45 and 1000 kg/m^3 respectively, approximating the nearly incompressible nature and high water content of human tissue.

The target parameters $\hat{P}$ and $\hat{C}$ that represented the real data set for each geometry are shown in Table 5.2. Also summarized are the relevant material properties required for FE simulation of the experimental motion. All 3,215 nodes on the vertical exterior of the cylinder were chosen as surface motion reference points for the reconstruction problem. This sampling method provided a simple approximation to a more advanced DIET system, where it is hoped motion data from closely spaced points across the entire surface of the breast will be available [109]. Noise added to the two simulated experimental data sets was normally distributed with a mean of zero and a variance of 10% of the average reference point displacement amplitude, giving a controlled approximation of experimental noise.

Table 5.2 The parameter values representing real data for the reconstructions performed using simulated data.

		Geometry	
Model Properties		**Stacked**	**Concentric**
Shape Parameters	$\hat{P}$	40%	50%
	$\hat{C}$	400%	300%
Modulus Values	E_s	20 kPa	20 kPa
	E_h	80 kPa	60 kPa
Material Properties	ν	0.45	0.45
	ρ	1,000 kg/m^3	1,000 kg/m^3

In addition to the target data set, FE simulation was also used to generate a motion database for both geometries across a range of values for P and C. Simulations were performed on both stacked and concentric geometries at interface positions P ranging from 10% to 90% in increments of 1%, and stiffness contrasts C from 100%

to 500% in increments of 5%. These parameter limits defined the problem domain for the reconstruction algorithms, and encompassed a total of 6,561 FE simulations for each geometry. This database of simulations allowed rapid testing of the reconstruction algorithms as well as evaluation of the surface error appearance over the problem domain.

5.2.2 Reconstruction Algorithms

The three non-linear reconstruction algorithms considered all aimed to minimize the squared error between a set of reference displacements, $\mathbf{u^m}$, simulated at the target parameter values $\hat{P}$ and $\hat{C}$, and the corresponding simulated displacements, $\mathbf{u^c}$, calculated using the current estimates of parameters P and C. The error metric that formed the cost function for all reconstructions in this study was a representation of the mean squared motion error across all reference points, and was defined

$$\Omega_4 = \sqrt{\frac{\sum_{i=1}^{N} \|\mathbf{u_i^m} - \mathbf{u_i^c}\|^2}{3N}}, \tag{5.7}$$

where N is the number of reference points. The minimum value of the error metric Ω_4 occurred when simulations were performed at $\hat{P}$ and $\hat{C}$ for a particular geometry, and was defined as $\hat{\Omega}$, representing the lowest possible error metric value any reconstruction could attain.

Figure 5.7 shows the error metric from Equation 5.7 across the entire problem domain for both geometries, where the 'measured' displacements were those simulated at the target parameters from Table 5.2, with the addition of noise. The minimum error value $\hat{\Omega}$ for the stacked geometry was 0.39 mm, and for the concentric geometry 0.24 mm. Indicated on both plots is the target parameter combination corresponding to parameter values $\hat{P}$ and $\hat{C}$. The error information in these plots provided both data and context to the reconstruction algorithms subsequently tested. The three non-linear reconstruction algorithms considered in this study are described in this section in the order in which they were evaluated.

5.2.2.1 Gradient Descent Reconstruction

The GD reconstruction algorithm used in the simulation study was based on the one parameter algorithm developed in Section 5.1. For this study, the algorithm was modified to reconstruct the two independent parameters P and C using the error metric Ω_4 defined in Equation 5.7. For the relatively small number of reconstruction parameters used in this study, the Jacobian matrix, which traditionally relies on parameter values being nodally distributed, is most efficiently calculated through a finite-difference approximation in which terms take the form

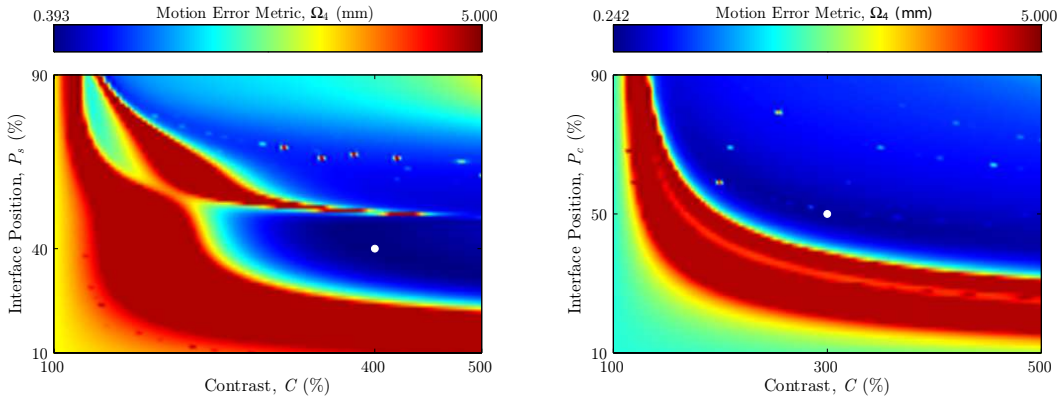

(a) Stacked geometry.

(b) Concentric geometry.

Figure 5.7 The displacement error metric from Equation 5.7 evaluated across the parameter domain for both heterogeneous silicone geometries, where the value of Ω_4 has an upper limit of 5 mm, and the location of minimum error, $\hat{\Omega}$, is indicated ($\circ$).

$$J = \frac{\mathbf{u^c}(\theta + \Delta\theta) - \mathbf{u^c}(\theta)}{\Delta\theta}, \tag{5.8}$$

where θ represents either P or C. As previously described, inversion of the approximate Hessian matrix, $H = J^T J$, allows the calculation of updates applied to both parameters.

Gradient descent reconstructions were performed with a range of initial parameter guesses covering the entire problem domain. Initial parameter guesses were generated for P every 2% between 12% and 88%, and for C every 10% between 110% and 490%, resulting in a total of 1,521 reconstructions for each geometry. A GD reconstruction was stopped when any of the following criteria were satisfied:

1. The surface motion error metric Ω_4 was within 1% of the value for $\hat{\Omega}$ for the geometry considered.

2. The calculated algorithm step size was zero for both P and C parameters for more than 2 consecutive iterations.

3. A total of 100 GD iterations had been performed.

The first criteria represented a definite successful reconstruction. The second was a case where the gradient was either so shallow the algorithm halted, or so steep that the reconstruction continually attempted to step outside the problem domain, and the update was ignored. The third case covers a failure to converge within the allocated number of iterations.

5.2.2.2 Combinatorial Optimization

CO involves efficiently exploring problem search domains to solve large and complex non-linear optimization problems faster than an exhaustive search [84]. The optimization algorithm used in this study combined features of two popular CO techniques – Genetic Algorithms (GAs) and Simulated Annealing (SA).

The CO algorithm shown in Figure 5.8, and described in the following, contains parameter pairs, G_i^j, defined as *genes*, where the subscript refers to the ith gene in the population, $1 \leq i \leq N_G$, and the superscript, j, indicates the gene's *generation*, where $0 \leq j \leq M$. Error metric values, Ω_i^j, are defined using the same convention. Values for both N_G and M can be chosen arbitrarily, with an upper limit usually reflecting increased computational cost. In the CO algorithm used for this study, a total of ten genes were used to define the population, $N_G = 10$, and a maximum of 100 generations was specified, $M = 100$. Within an entire population of genes at a particular generation, termed G^j, the gene providing the closest match to experimental data is described as G_+^j, and has corresponding error metric value, Ω_+^j.

CO begins with a population of N_G genes, each containing an initial value for the two parameters, $G_i^0 = \{P, C\}_i^0$. Initial values for all parameters within all genes are usually randomly assigned within a range based on *a priori* knowledge. Before entering the CO algorithm proper, FE simulations are performed to obtain starting values of the error metric, Ω_i^0, for all genes in the population.

Mating in CO involves interchanging genetic material between genes, with the intent of improving the fitness of the population as a whole [82]. Pairs of genes are identified for mating using roulette wheel selection, where the probability of gene selection is directly proportional to the value of its error metric, Ω_i^j [110]. Genes selected as one of a mating pair have their constituent parameter values modified by swapping a proportion of their binary expression with bits from the corresponding parameter in their mating partner. The chance of the mating operation being performed is set with the probability value Π_{mate}, where for this study $\Pi_{mate} = 0.9$. Parameter values output from the mating process form a new, temporary gene pool.

Random mutation modifies the value of any parameter within any gene by flipping the value of a bit from the parameter's binary expression. This process increases the diversity of the population by introducing new genetic material that is unlikely to be introduced through mating alone. Mutation is potentially performed on every bit within the temporary population after mating, where the likelihood of a bit changing value is governed by the probability Π_{mutate}. In this study $\Pi_{mutate} = 0.02$. The resulting population is defined as $\tilde{G}_i^j$, where the tilde indicates that the mating and mutation operations have taken place. FE simulation at the parameter values provided by these potential genes allows corresponding error metric values, $\tilde{\Omega}_i^j$, to be calculated.

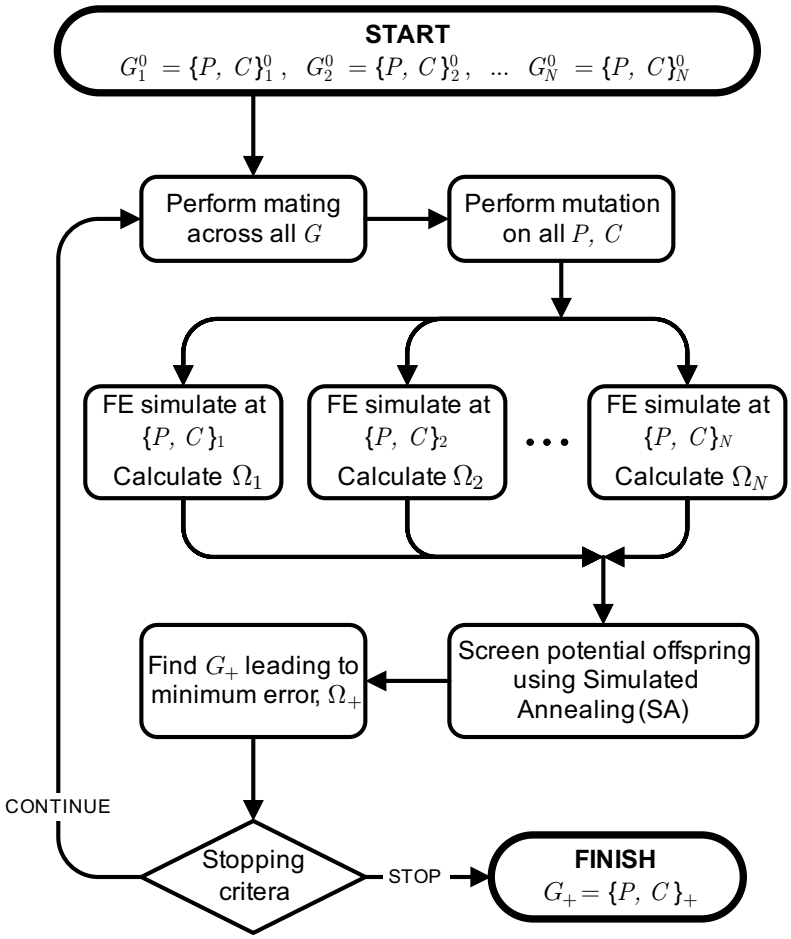

Figure 5.8 A schematic of the CO reconstruction algorithm.

SA takes its theoretical approach from the statistical mechanics of physical annealing, where solutions that decrease the global system 'energy', here the error term Ω, are increasingly preferred as a system-wide temperature variable is decreased over time [87]. In the CO algorithm described here, SA provides a mechanism for determining which genes from the potential offspring population, $\tilde{G}^j$, will become part of the subsequent generation, G^{j+1}. Error values from each potential gene, $\tilde{\Omega}_i^j$, are compared with the corresponding value from the current population, Ω_i^j. The chance of the offspring gene, $\tilde{G}_i^j$, replacing the original gene, G_i^j, in the subsequent population is set by the probability ${}_{SA}\Pi_j^i$, defined

$$ {}_{SA}\Pi_i^j = exp\left(\frac{-\tilde{\Omega}_i^j/\Omega_i^j}{T^j}\right), \tag{5.9} $$

where T^j is the value of the system-wide temperature variable at generation j. Decreasing T each generation means potential genes increasing the population error have a decreasing chance of being selected as generations progress. In this experiment, the temperature was decreased logarithmically between values of 10 and 0.5 over a total of 100 generations. After completing SA screening, parameter values from all genes chosen for the subsequent generation are logged, along with their error values, and the gene displaying the best match to the experimental data, G_+^j, noted.

The CO algorithm in this study had two stopping criteria:

1. The error metric from the best-fitting member of the current population, Ω_+^j, was less than a pre-determined minimum based on the value of $\hat{\Omega}$ for the geometry. This criterion represented a successful reconstruction.

2. The maximum number of generations for the reconstruction, M, was reached. This criterion represented a failed reconstruction.

Upon halting the CO algorithm, the parameter values providing the closest match to the measured motion, $G_+ = \{P, C\}_+$, with corresponding error metric, Ω_+, were output.

5.2.2.3 Hybrid Algorithm

A hybrid algorithm for non-linear reconstruction of shape-based parameters was identified as a possible solution to the DIET elastography problem in Section 5.1. The simple hybrid algorithm investigated in this study involved first running a CO algorithm for a total of 100 generations. The second stage of the algorithm was a GD reconstruction, where the initial guess for the algorithm was taken from the output of the CO reconstruction, $G_+ = \{P_+, C_+\}$. This approach was intended to test the potential of such a method to avoid the issues with local minima previously identified when using GD alone to perform parameter reconstruction.

5.2.3 Parameter Reconstruction Results

The overall success of each type of reconstruction algorithm across all starting values for a particular geometry was represented by a cumulative, normalized parameter error value, defined

$$\Psi_1 = 1 - \left(\frac{\sum_{i=1}^{N} |\hat{P} - (P_+)_i|}{\hat{P}} + \frac{\sum_{i=1}^{N} |\hat{C} - (C_+)_i|}{\hat{C}} \right) / 2N, \tag{5.10}$$

where $\hat{P}$ and $\hat{C}$ are the target parameters from Table 5.2, and N is the total number of reconstructions performed on the geometry in question. Equation 5.10 returns a value

between 0–1, expressed as a percentage, where 100% represents all reconstructions reaching the global optimal solution, where $(P_+)_i = \hat{P}$, and $(C_+)_i = \hat{C}$, for all i. Hence, the metric provides an easy to understand measure of how close a particular set of reconstruction results are to the target parameter combination.

The distribution of the 1,521 GD reconstructed solutions is shown in Figure 5.9. The success metric for the GD algorithm when applied to the stacked and concentric geometries was $\Psi_1 = 71.2\%$ and $\Psi_1 = 78.2\%$, respectively. In both cases, the majority of failed reconstructions were those that attempted to step to parameter values outside the problem domain. These reconstructions can be seen at lower left of Figure 5.9(a), and upper left of Figure 5.9(b), where the imposed limits on parameter values direct the algorithm to a corner of the domain.

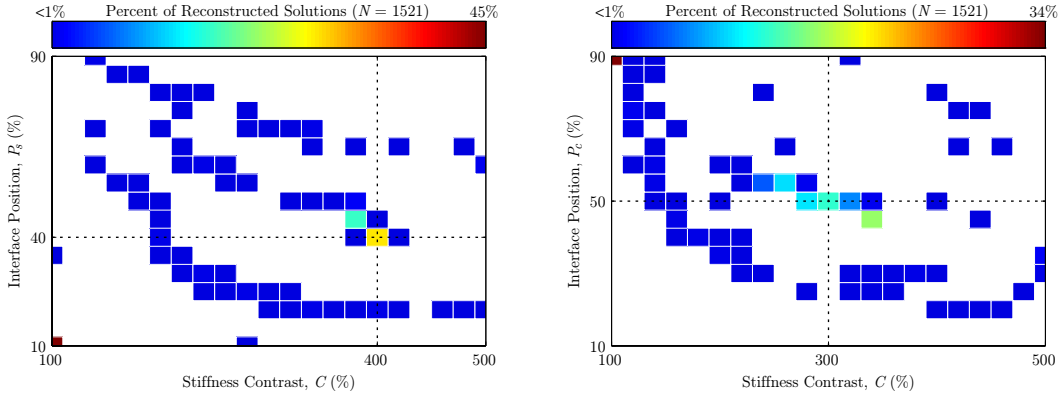

(a) Stacked geometry.

(b) Concentric geometry.

Figure 5.9 The distribution of results from 1,521 GD reconstructions performed on both heterogeneous geometries, where the intersection of the dashed lines indicates the target parameter combination.

To allow statistical comparison with the GD algorithm, the same number of CO reconstructions were performed on each geometry, beginning with random parameter guesses within the problem domain. Figure 5.10 shows the distribution of these 1521 reconstructed solutions for both geometries considered. The success metric Ψ_1 for the stacked and concentric geometries when using CO was 97.8% and 91.2%, respectively. Here the reconstructed solutions are observed to be largely confined to a smaller area or band adjacent to the target parameter combination.

The final reconstruction testing performed the same 1,521 instances using the hybrid reconstruction method, where the results from the previously performed CO were used as the first phase of the algorithm. The reconstructed solution density plots for both geometries are given in Figure 5.11, where success metrics for the stacked and concentric geometries were $\Psi_1 = 98.9\%$ and $\Psi_1 = 94.2\%$, respectively. A clear reduction in solution spread is apparent when comparing Figure 5.11 with Figures 5.9

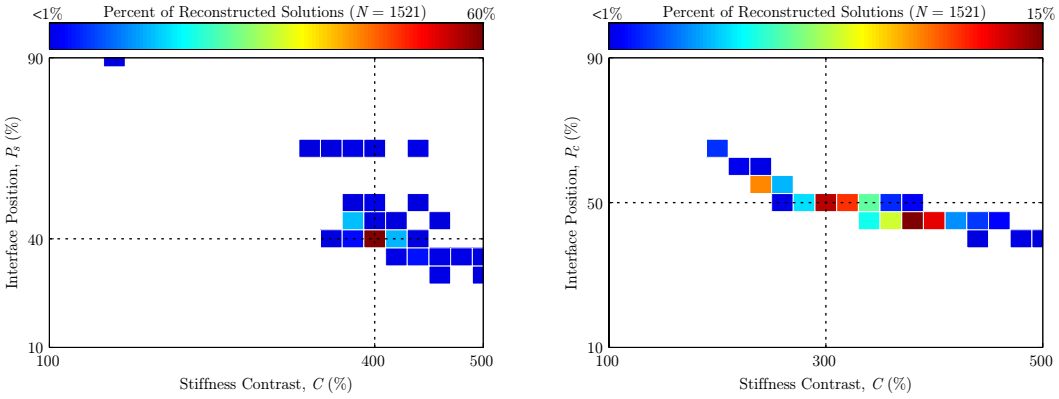

(a) Stacked geometry. (b) Concentric geometry.

Figure 5.10 The distribution of results from 1,521 CO reconstructions performed on both heterogeneous geometries, where the intersection of the dashed lines indicates the target parameter combination.

and 5.10. The success metric Ψ_1 for all three reconstruction algorithms across both heterogeneous phantom geometries considered is summarized in Table 5.3.

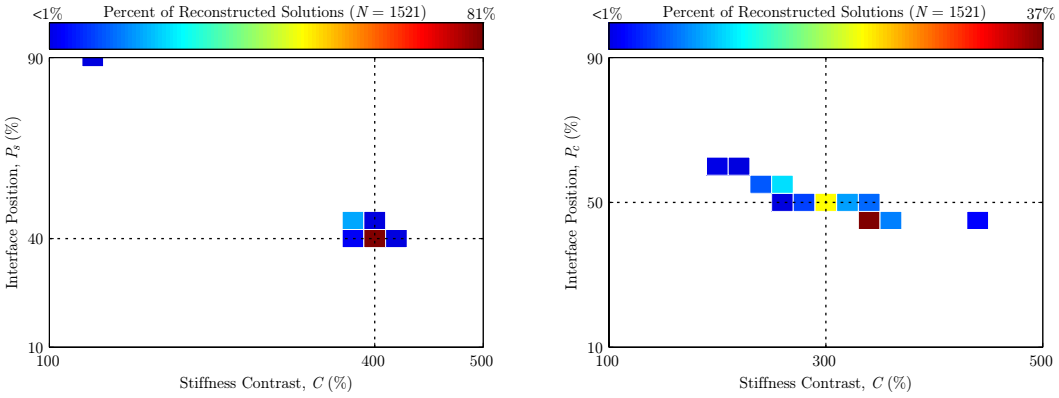

(a) Stacked geometry. (b) Concentric geometry.

Figure 5.11 The distribution of results from 1,521 instances of the hybrid algorithm performed on both heterogeneous geometries, where the intersection of the dashed lines indicates the target parameter combination.

5.2.4 Discussion

The plots in Figure 5.7 provide a clear indication of the error metric trends across the problem domain for each geometry, where the large areas of resonance observed are a result of the undamped linear model used for FE simulations. The stacked model had a more complicated resonance pattern, as the geometry places the interface between hard and soft material perpendicular to the mechanical waves generated by actuation of the model.

Table 5.3 The reconstruction algorithm success metric, Ψ_1, across both stacked and concentric geometries.

	Geometry	
Algorithm	**Stacked**	**Concentric**
GD	71.2%	78.2%
CO	97.8%	91.2%
Hybrid	98.9%	94.2%

While the areas of resonance indicate simulated displacements becoming unrealistically large, they also provide an challenging problem domain with clear local minima, ideal for reconstruction algorithm evaluation. The large area of low error surrounding the target parameter combination for the concentric geometry was due to the low sensitivity of Ω_4 to P or C in this region, and makes accurate elastographic reconstruction of this geometry especially challenging.

The large spread of solutions for the GD reconstructions shown in Figure 5.9 indicate a high probability that a randomly-selected starting position within the parameter domain will not lead to a successful reconstruction. Analysis of failed reconstructions showed that reconstructions initiated on the opposite side of a resonance band from the target solution were not able to reach the correct solution. This result confirms the behavior identified in Section 5.1 when reconstructing in a one parameter scenario, where a GD method converges prematurely at a local minimum. However, the GD solver performed very well when initiated within the vicinity of the global solution, supporting its inclusion in a hybrid algorithm with a good initial value, given the small number of FE simulations required for convergence.

The results in Figure 5.10 demonstrate that CO has a greater ability to avoid local minima and reach solutions surrounding the globally optimal parameter combination. However, the CO approach had a limited ability to differentiate between the globally optimum solution and one nearby, resulting in a spread of solutions at low error metric values. This limitation constrained the effectiveness of the algorithm when applied to parameter domains where the error metric has low sensitivity to the parameters used, such as the concentric geometry in this case. However, a qualitative comparison of Figures 5.9(b) and 5.10(b) clearly shows an obvious clustering about the correct solution for the CO reconstruction that is reinforced by the significant increase in the Ψ_1 metric values in Table 5.3.

The hybrid algorithm was clearly the most accurate and consistent of the three approaches considered, with success metrics above 94% for both geometries. The reduction in solution spread visible in Figure 5.11 demonstrates the potential for a re-

construction algorithm combining the advantageous aspects of GD and CO to have markedly greater success than either algorithm in isolation. Reconstructed solutions from both CO and hybrid algorithms were, in general terms, clustered about the minimum error solution, potentially allowing the use of statistical methods to characterize not only reconstructed parameter values, but also confidence metrics for these reconstructions.

The number of forward FE simulations required for each reconstruction algorithm is shown in Table 5.4, and provides an estimate of the computational cost of each method given the serial computation approach used in this study. While the CO and hybrid methods require a significantly higher numbers of simulations, a large number of these simulations are independent, and could be performed in parallel across multiple processors. For the CO algorithm, which also formed the first 100 iterations of the hybrid method, this would reduce the time taken to complete FE simulations by a factor of ten, as each generation contained ten independent chromosomes. The finite difference approach to Jacobian calculation in the GD algorithm was also able to be parallelized, but to a lesser extent given the limited number independent parameters in this study. However, more advanced gradient calculation methods, such as the adjoint method, have the potential to reduce or eliminate this cost scaling for the GD algorithm as the number of parameters is increased [111]. The theoretical reduction in the number of consecutive FE simulations required if performing reconstructions in a parallel computing environment is also quantified in Table 5.4.

Table 5.4 The total number of FE simulations required for each reconstruction algorithm in the two-parameter simulated case.

FE Solutions	**GD**	**CO**	**Hybrid**
Serial system (actual)	60	1000	1060
Parallel system (theoretical)	20	100	120

Improvements in the sophistication of both the GD and CO algorithms should lead to improved reconstruction success rates. Both algorithms were very simple implementations of these techniques, and could possibly benefit from added features, such as GD regularization, and more sophisticated CO evolution strategies. Efficiency improvements in the hybrid algorithm could be made by an investigation into the best combination of constituent CO and GD algorithms, where the potential exists for the crossover point between the two algorithms to be made dynamically as the reconstruction progresses.

The hybrid algorithm simulation study demonstrated that shape-based reconstruction was able to identify both a positional and stiffness contrast parameter for varying

physical geometries in the presence of noise. Of the three reconstruction algorithms tested, a hybrid algorithm combining aspects of GD and CO was clearly the most successful at avoiding local minima and reaching the global optimal solution. Significant potential exists to refine and improve this form of algorithm when applying such a method to experimental data sets, which are the next logical target for testing.

5.3 Hybrid Reconstruction Optimization

The promising results obtained from noisy simulated data in Section 5.2 indicated the hybrid reconstruction method had significant potential for use in a DIET system. The subsequent study described in this section focuses on optimizing the performance of the hybrid algorithm as applied to the concentric silicone phantom data presented in Section 4.3. A sensitivity analysis is performed in order to determine the influence of different algorithm settings on the reconstruction performance, with regards both to solution accuracy and computational efficiency. In addition, a statistical measure of reconstruction certainty is developed to allow the combination of multiple reconstructions into a single result.

Estimated values for the material properties of the hard and soft silicone material were provided by the surface error studies in Section 4.2. The two-parameter sweeps performed on the heterogeneous silicone phantoms in Section 4.3.3 using both corroborative and contradictive *a priori* stiffness assumptions indicated that surface error metric values had high sensitivity to any assumed soft modulus value. This study considered independent variation in three parameters for the concentric geometry, representing soft modulus, E'_s, hard modulus, E'_h, and interface position, P_c. The use of three parameters provided a larger and more complicated error domain likely to contain multiple local minima.

5.3.1 Sensitivity Analysis

The hybrid reconstruction algorithm introduced in Section 5.2 was modified for this study to allow reconstruction of three independent parameters. A block diagram of the three parameter hybrid algorithm is shown in Figure 5.12, where the optimization involves the three example parameters A, B, and C. All reconstructions performed during this sensitivity study used the experimentally measured concentric motion data as the reference displacement set, and calculated the surface error metric Ω_3 according to Equation 3.17.

The hybrid reconstruction algorithm sensitivity analysis and optimization was performed by varying several key settings controlling both CO and GD stages. As both phases were performed separately in the hybrid method, this optimization was performed on each component individually, before combining both parts. As this form of

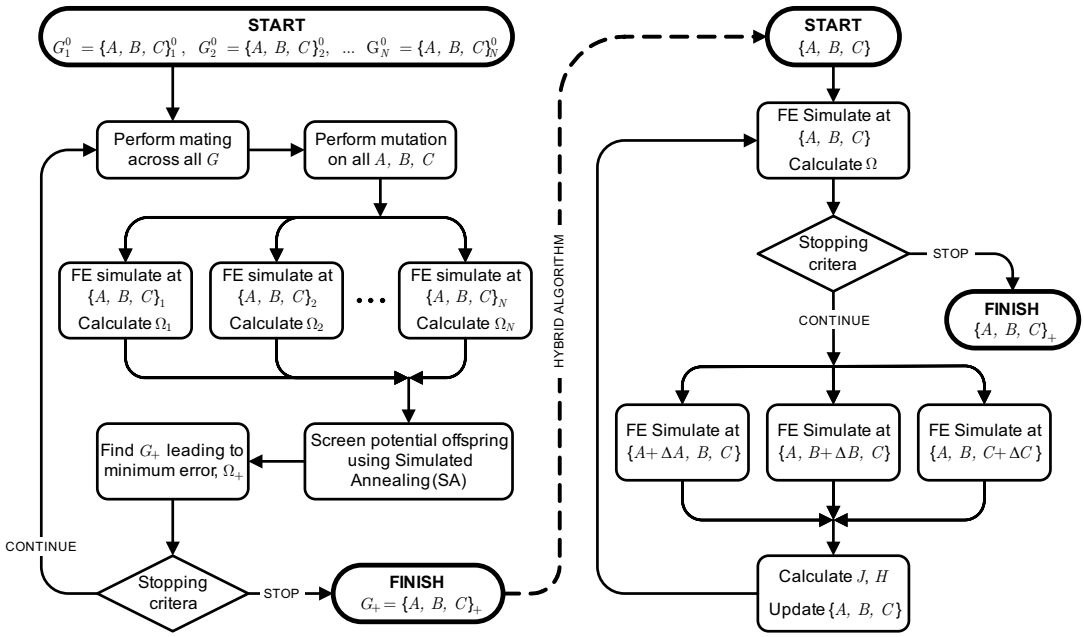

(a) Combinatorial Optimization algorithm (b) Gradient descent algorithm

Figure 5.12 A schematic of the hybrid reconstruction algorithm.

reconstruction algorithm is highly application specific, the optimized algorithm settings chosen would represent the ideal case for the specific shape-based parameter reconstruction considered. To avoid initial bias in the CO sensitivity study, all reconstructions started from the same initial population set.

5.3.1.1 Combinatorial Optimization

The investigation of algorithm settings for the CO optimization involved the results of 100 reconstructions, each based on a different initial population, ${}^{l}G^{0}$, and generating output ${}^{l}G_{+}$, where $1 \leq l \leq 100$. These results were normalized to give a measure of reconstruction performance between 1.0 and 0.0, where 1.0 represented the mean error at generation zero,

$$\bar{\Omega}_{+}^{0} = \frac{1}{100} \sum_{l=1}^{100} \left({}^{l}\Omega_{+}^{0} \right), \tag{5.11}$$

and 0.0 indicated the minimum error value within the domain, $\hat{\Omega}$. To allow performance characterization, the best-fit parameter values leading to $\hat{\Omega}$, termed $\{\hat{A},\ \hat{B},\ \hat{C}\}$, were determined prior to the study.

The first phase of CO optimization varied the value of Π_{mate} from 0.2 to 0.8 in increments of 0.2. For these reconstructions, Π_{mutate} was set to zero to eliminate the influence of random mutation on the reconstruction results, and the number of genes was fixed, $N_G = 10$. The resulting CO algorithm performance across 100 generations is shown in Figure 5.13(a), where each line represents the mean of 100 individual reconstructions performed at a combination of settings. Optimal reconstruction performance was seen when $\Pi_{mate} = 0.6$, where the normalized algorithm performance value was 0.18 after 100 generations.

CO sensitivity to mutation was tested by fixing Π_{mate} at the optimized value of 0.6, and varying Π_{mutate} from 0.0 to 0.2. The resulting normalized CO algorithm performance across 100 generations is shown in Figure 5.13(b). In this plot, the solid line corresponds to the $\Pi_{mate} = 0.6$ result in Figure 5.13(a). No significant improvement in performance was noted at Π_{mutate} values greater than 0.1, where the normalized performance value was 0.05 after 100 generations.

Finally, the number of genes in the population, N_G, was varied, with $\Pi_{mate} = 0.6$, and $\Pi_{mutate} = 0.1$. CO reconstructions containing 5, 10, 20 and 40 genes were performed, with results shown in Figure 5.13(c). In this plot the starting values for the performance metric varied in each case, as the different values for N_G led to a range of values for $\bar{\Omega}_+^0$. To normalize for the increased computational cost of updating additional genes through each generation, the horizontal axis of this figure indicates the total number of FE simulations performed. Regardless of this additional normalization, adding genes to the population continued to improve algorithm performance. A value of $N_G = 10$ was selected as being optimal for this problem, given the physical number of computer workstations available, and the absence of significant performance improvement between 10 and 20 genes. The optimized CO algorithm settings used for subsequent parameter reconstruction are summarized in Table 5.5.

Table 5.5 Optimal settings for the CO algorithm determined via sensitivity analysis.

Setting	**Value**
Π_{mate}	0.6
Π_{mutate}	0.1
N_G	10

5.3.1.2 Gradient Descent Optimization

Experiments with the simple GD algorithm introduced in Section 5.1 indicated that when reconstructing the limited number of parameters in this study, regularization of the approximate Hessian matrix was not required for numerical stability. This inherent

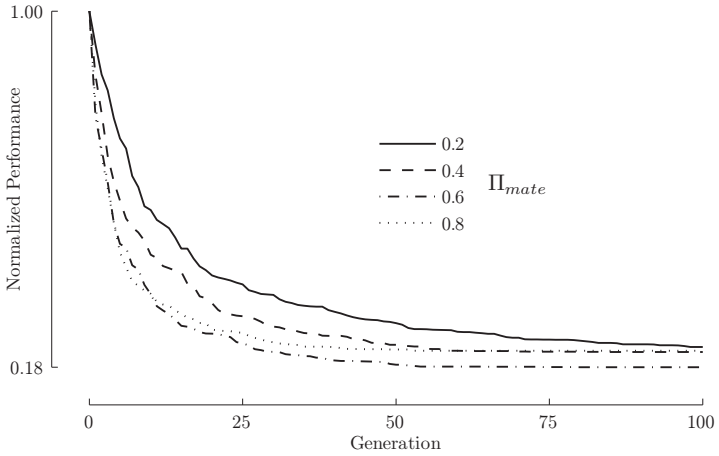

(a) CO algorithm sensitivity to the probability of mating.

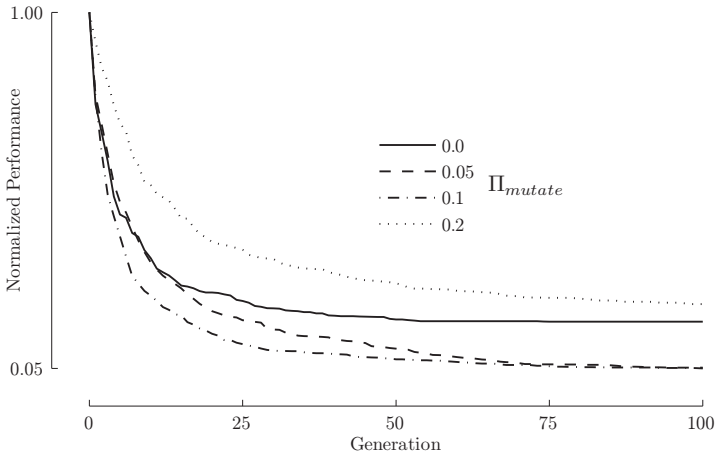

(b) CO algorithm sensitivity to the probability of mutation.

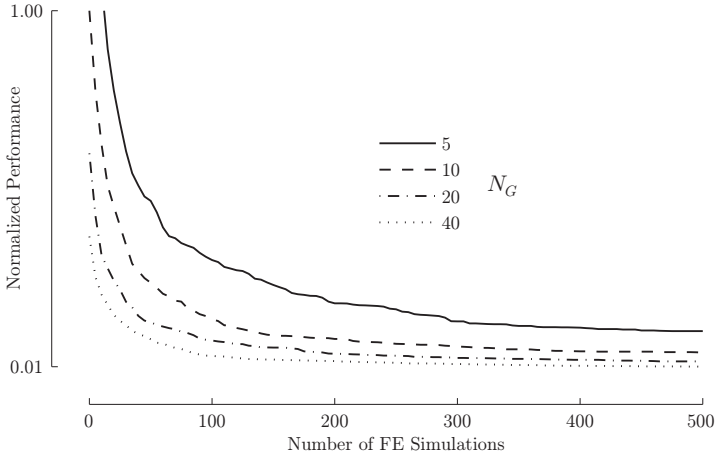

(c) CO algorithm sensitivity to the number of genes in the population.

Figure 5.13 Results from the sensitivity analysis performed on the CO reconstruction algorithm.

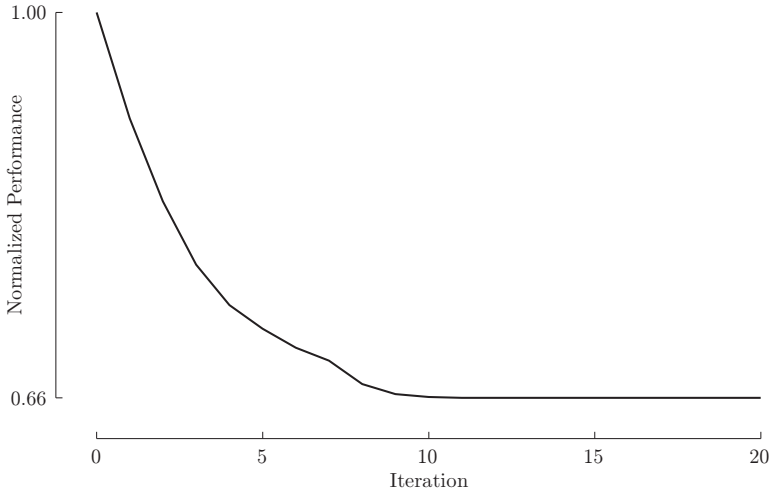

Figure 5.14 The performance of the GD reconstruction algorithm applied to the concentric phantom experimental data.

stability limited the GD algorithm optimization study to the total number of iterations performed. Figure 5.14 shows the normalized performance result from 100 GD reconstructions starting at random parameter values within the domain. The performance metric from all reconstructions was tracked over the total of 20 iterations performed, with no improvement in performance observed beyond 10 iterations. The absence of further improvement in the GD results beyond 10 iterations indicated that all instances of the algorithm had converged prior to this point, where the normalized performance metric was 0.66. The high minimum value of the performance metric in Figure 5.14 indicated that the majority of GD reconstructions converged to a parameter combination representing a local error minimum that was not close to the globally optimum solution.

5.3.2 Heterogeneous Phantom Reconstruction Results

After optimizing the performance of the CO and GD components of the hybrid algorithm, reconstructions were performed on the experimental phantom data using GD and CO separately, followed by the hybrid algorithm that combined both techniques. To evaluate each trial method performed on the experimental data, a total of 100 separate reconstructions were performed. Referring to Figure 5.12, the mean final reconstructed value for each parameter over all 100 reconstructions, $\bar{A}_+$, $\bar{B}_+$, $\bar{C}_+$, was compared to the best-fit value for that parameter, $\hat{A}$, $\hat{B}$, $\hat{C}$, using two metrics. The Ψ_2 metric acts as a measure of the mean normalized parameter error,

$$\Psi_2 = \frac{|\hat{A} - \bar{A}_+|}{|\hat{A}|} + \frac{|\hat{B} - \bar{B}_+|}{|\hat{B}|} + \frac{|\hat{C} - \bar{C}_+|}{|\hat{C}|}. \tag{5.12}$$

Additionally, Σ^2 was used as a measure of the normalized variance of the reconstructed solutions, defined as

$$\Sigma^2 = \sum_{l=1}^{N=100} \frac{\left({}^l\bar{A}_+ - \hat{A}\right)^2}{(N-1)\hat{A}^2} + \frac{\left({}^l\bar{B}_+ - \hat{B}\right)^2}{(N-1)\hat{B}^2} + \frac{\left({}^l\bar{C}_+ - \hat{C}\right)^2}{(N-1)\hat{C}^2}. \tag{5.13}$$

In the following results, the example parameter values $\{A, B, C\}$ are represented by the shape-based parameters relevant to this experiment, $\{E'_s, E'_h, P_c\}$.

Figure 5.15 is the resulting stiffness solution distribution after performing 100 GD reconstructions on the concentric data. Each reconstruction had random starting values and was run for a total of 10 iterations. Reconstruction error metrics Ψ_2 and Σ^2 were 0.79 and 0.55 respectively. The finite-difference method used for the Jacobian matrix calculation meant that a total of 40 FE simulations were required for each reconstruction. The best-fit stiffness profile on the plot represents the parameter values corresponding to $\hat{\Omega}$, while the measured line is based on the mechanical testing performed in Section 3.2, and the measured interface positions previously given in Table 4.5.

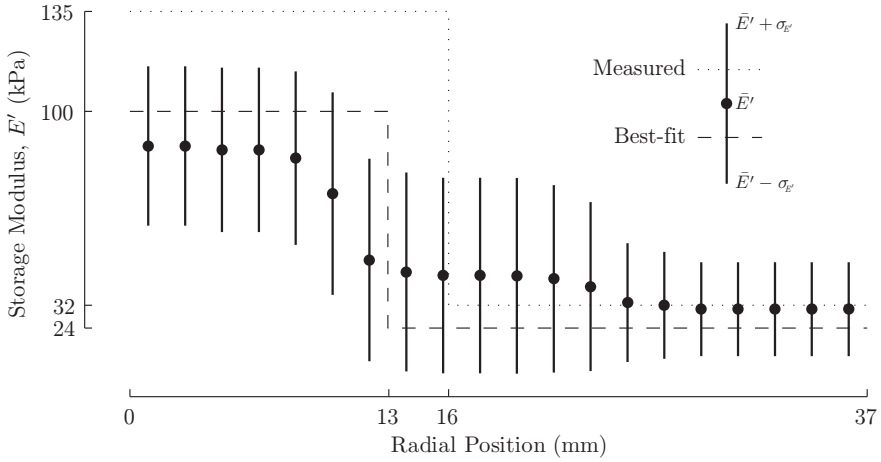

Figure 5.15 The reconstructed stiffness profile distribution from 100 GD reconstructions on concentric phantom data, where the measured stiffness profile, and best-fit profile based on $\hat{\Omega}$, are indicated.

Figure 5.16 shows the result of the optimized CO algorithm applied to the concentric phantom displacements, where results at a range of generations are presented. Figure 5.17 shows results from the hybrid algorithm applied to the same data, where optimized GD reconstruction was performed following CO, using a starting guess for the parameters provided by the best result from the CO reconstructions, G_+. Table 5.6 summarizes the performance metric results across the optimized reconstruction algorithms considered, where the values of Ψ_2 and Σ^2 for the hybrid algorithm are consistently less than the corresponding CO or GD algorithms.

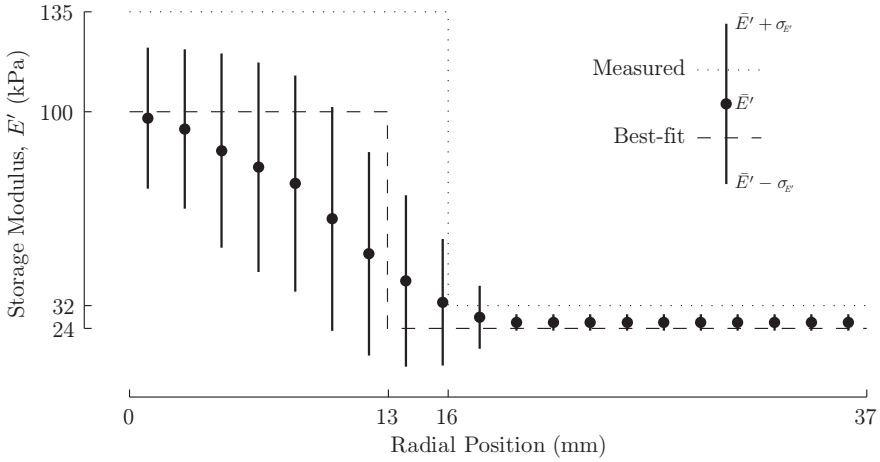

(a) CO algorithm, 1 generation.

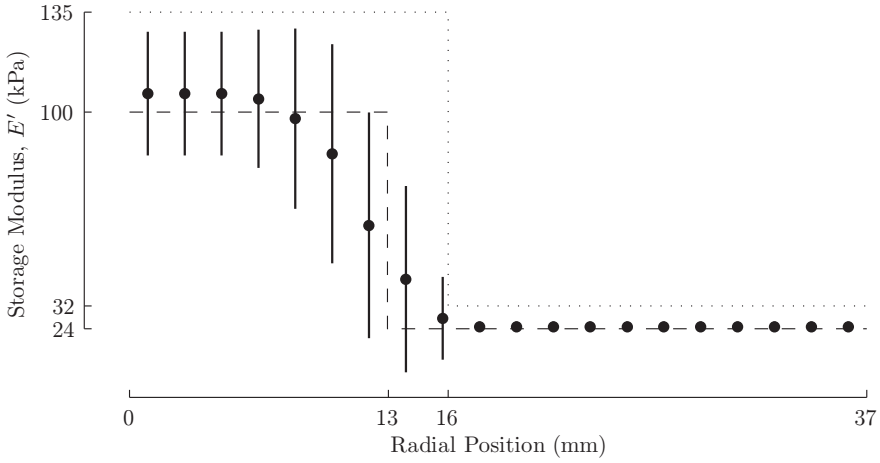

(b) CO algorithm, 10 generations.

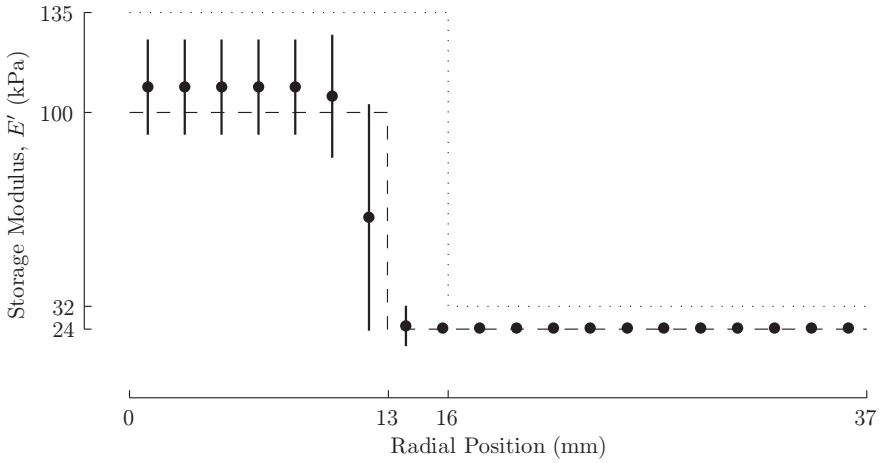

(c) CO algorithm, 100 generations.

Figure 5.16 The stiffness profile distribution from 100 CO reconstructions on concentric phantom data, where the measured stiffness profile, and best-fit profile based on $\hat{\Omega}$, are indicated.

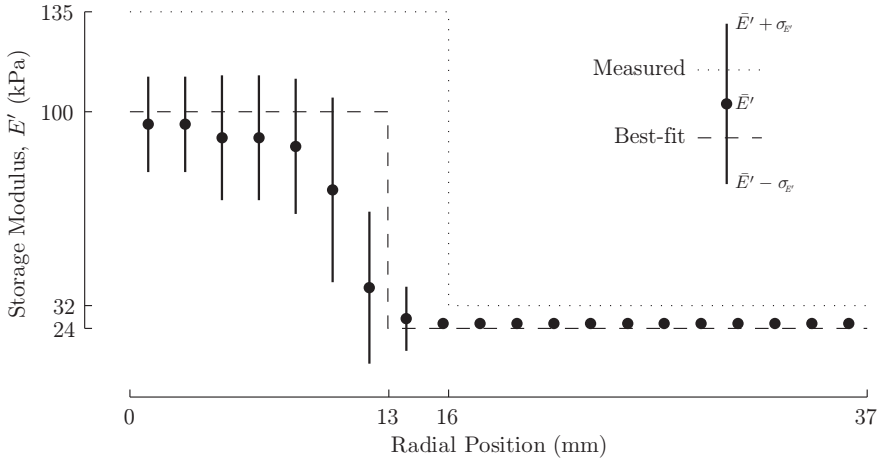

(a) Hybrid algorithm, 1 generation CO, 10 iterations GD.

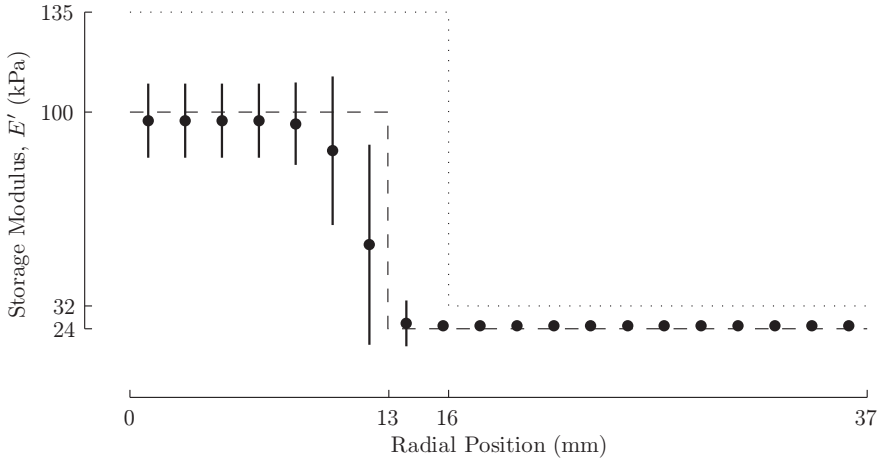

(b) Hybrid algorithm, 10 generations CO, 10 iterations GD.

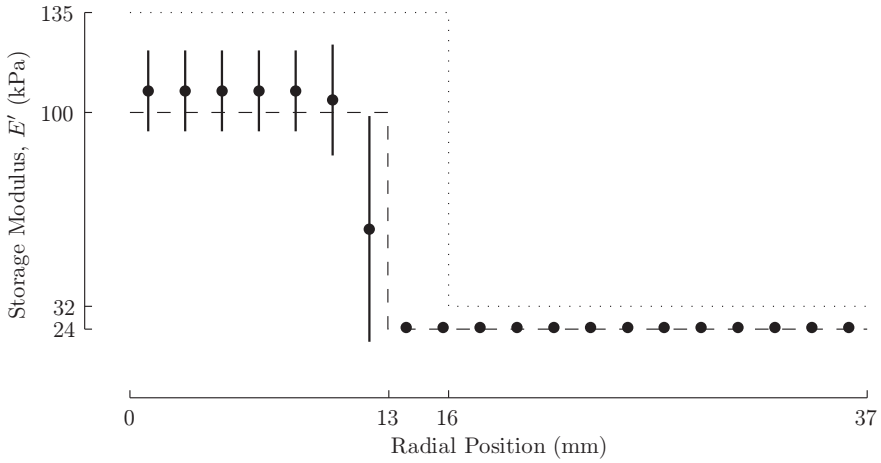

(c) Hybrid algorithm, 100 generations CO, 10 iterations GD.

Figure 5.17 The stiffness profile distribution from 100 hybrid reconstructions on concentric phantom data, where the measured stiffness profile, and best-fit profile based on $\hat{\Omega}$, are indicated.

To confirm the ability of the hybrid algorithm to return the correct stiffness distribution when given a motion data set from a homogenous phantom, the algorithm was additionally performed 100 times on the soft homogeneous silicone phantom data set previously studied in Section 4.2. The hybrid algorithm in this case comprised 10 CO generations followed by 10 GD iterations, a combination found to give the best performance when considering computational cost, based on the results in Table 5.6.

Table 5.6 Results from the hybrid algorithm optimization.

	Iterations		**Metric**		**Consecutive Solves**	
					Serial	**Parallel**
Algorithm	**CO**	**GD**	Ψ_2	Σ^2	**(actual)**	**(theory)**
GD	-	10	0.79	0.55	40	10
CO	1	-	0.64	0.19	10	1
	10	-	0.41	0.09	100	10
	100	-	0.25	0.04	1,000	100
Hybrid	1	10	0.39	0.07	50	11
	10	10	0.25	0.03	140	20
	100	10	0.23	0.03	1,040	110

The distribution of stiffness profiles from these 100 results is shown in Figure 5.18, along with the corresponding measured, and minimum error profiles. Near constant soft stiffness is clearly indicated in the result, with increased uncertainty towards the center of the phantom as a result of the distance from the measured displacements on the surface. The reconstruction metrics Ψ_2 and Σ^2 are not relevant in the homogenous case, where the only independent parameter is E'_s. The best-fit storage modulus value of 28 kPa in Figure 5.18, representing the value of E'_s corresponding to $\hat{\Omega}$ for this error domain, is in agreement with the estimated value of $E' = 28\,\text{kPa}$ for the soft silicone phantom in Section 4.2.

5.3.3 Discussion

The results shown in Figures 5.15–5.17 are the distribution of the spatially interpreted stiffness solutions resulting from performing 100 of the respective reconstructions. As such, they should not be interpreted as the 'result' of a reconstruction, but rather a distribution drawn from several reconstruction results. Reduced values of Ψ and Σ^2 are desirable, as they indicate both reduced mean error and reduced uncertainty, which is important when performing a limited number of reconstructions on a real data set.

The distribution of GD reconstruction results shown in Figure 5.15 do not give a close match to the best-fit phantom stiffness distribution, with reconstruction metrics

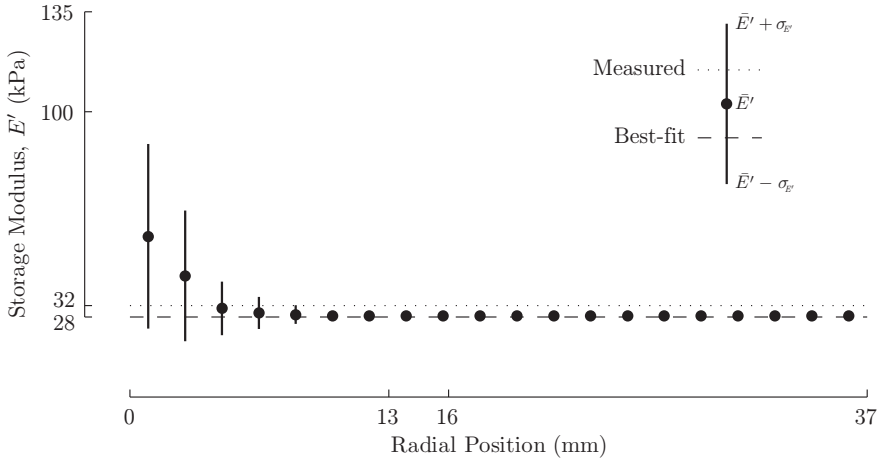

Figure 5.18 The reconstructed stiffness profile distribution from 100 hybrid reconstructions performed on the soft homogenous silicone phantom data, where the measured stiffness profile, and best-fit profile based on $\hat{\Omega}$, are indicated.

of $\Psi_2 = 0.79$, $\Sigma^2 = 0.55$. The large variance visible in the plot at all radial positions indicates that the GD reconstructions failed to converge consistently for the parameters E'_s, E'_h and P_c. Even using a damped material model, it is apparent that local minima severely hamper the algorithm performance, a result consistent with previous studies applying the GD method to reconstructions with fewer parameters in Sections 5.1 and 5.2.

The accuracy of reconstructed solutions showed a marked improvement when using an optimized CO approach. Mean error and variance in the stiffness profile distributions in Figure 5.16 are significantly lower than the GD case, particularly in the estimation of the soft modulus value, E'_s. Improvement is also visible in the definition of the step stiffness change between hard and soft regions. Performance metrics of $\Psi = 0.25$ and $\Sigma^2 = 0.04$ were achieved after 100 generations, where a total of 1000 FE simulations were required for each reconstruction.

Adding GD reconstruction to CO to form a hybrid method led to further improvements in the distribution of results in all cases shown in Figure 5.17. Significantly, the total number of FE solves required to obtain the hybrid result in Figure 5.17(b) is only 14% of the number of solves required to achieve the CO result shown in Figure 5.16(c). This result demonstrates that a hybrid approach can achieve equivalent performance to CO performed alone, while requiring markedly fewer computational resources.

Table 5.6 summarizes the number of FE simulations required for each instance of the three algorithms considered. The results from this study using a serial computation approach show that performing fewer than 100 CO generations can significantly reduce computational cost, while retaining a significant reconstruction performance advan-

tage in relation to the GD algorithm. When considering a parallel implementation of the hybrid algorithm, where independent FE solves are performed concurrently across multiple processors, the total number of consecutive FE solves reduces to 20 for an algorithm comprising 10 generations of CO and 10 iterations of GD reconstruction.

Considering the time required to perform one FE simulation on a modern desktop computer, a single instance of a hybrid reconstruction algorithm could be performed in as little as fifteen minutes on a cluster of such machines. Even considering the additional time required to build up the database of reconstructed solutions used to generate the plots in Figures 5.16 and 5.17, this result is encouraging when considering the exponential increase in the complexity of computer hardware originally predicted by Moore, where such complexity and performance increases are continuing in the present day [112–114].

A reasonable match was obtained between the reconstructed concentric phantom stiffness profile using the hybrid algorithm, and the measured stiffness profile based on static test results from Section 3.2. As the measured modulus values were from samples produced at a different time, they were not expected to provide exact target values for reconstruction, given the number of experimental uncertainties. The smaller inclusion diameter indicated by the best-fit case may be a result of the stiffness interpolation required when solving a FE problem with nodally-based material properties. The effects of this property interpolation should be reduced with the finer nodal spacing in the FE mesh used for simulations.

The hybrid algorithm optimization study described in this section demonstrated the ability of a three parameter approach to reconstruct heterogeneous phantom stiffness using experimentally measured displacements. Though the computational cost was high, the CO method obtained significantly better reconstruction results than a GD approach, confirming the findings of the previous simulation study. The optimized hybrid reconstruction method demonstrated an ability to better the performance of CO performed alone, with almost an order of magnitude reduction in computational cost. When the promising results from the contradictive approach to parameter estimation in Section 4.3 are considered, a hybrid approach to inclusion imaging has the potential to solve problems with increased complexity. Here, more realistic internal geometries can be described without increasing the total number of parameters required, by fixing the modulus value of any predicted hard inclusion.

5.4 Spherical Phantom Reconstructions

The final elastographic reconstruction study performed considered a more complicated and clinically-relevant heterogeneous phantom geometry. In this experiment, a combination of the optimized hybrid algorithm from Section 5.3 and the contradictive a

priori stiffness assumption described in Section 4.3.3 are used to add an additional shape parameter to the reconstruction problem. The new geometry used for this study was a hard inclusion completely contained within a soft body, representing the closest experimental approximation to a clinical scenario considered to this point.

5.4.1 Spherical Silicone Phantom

A 'spherical' heterogeneous silicone phantom was created using the same methods and materials as the stacked and concentric silicone phantoms described in Chapter 3. The phantom comprised a 40 mm diameter sphere of hard silicone suspended within a soft silicone cylinder of the same external geometry as previous silicone phantoms. Creating the phantom involved first casting the spherical inclusion from hard silicone, then suspending this sphere within the cylindrical mold phantom mold while pouring soft silicone to the desired level.

Experimental motion capture from the spherical phantom used the same hardware and settings as described in Section 3.3.2, where mechanical actuation was at a frequency of 100 Hz, with a 0.5 mm amplitude. Figure 5.19 contains an image of the phantom during actuation, along with the tracked reference points on the phantom surface across one steady state motion cycle. The motion fitting performed on this experimental data used the same damped assumption as all previous silicone phantom studies.

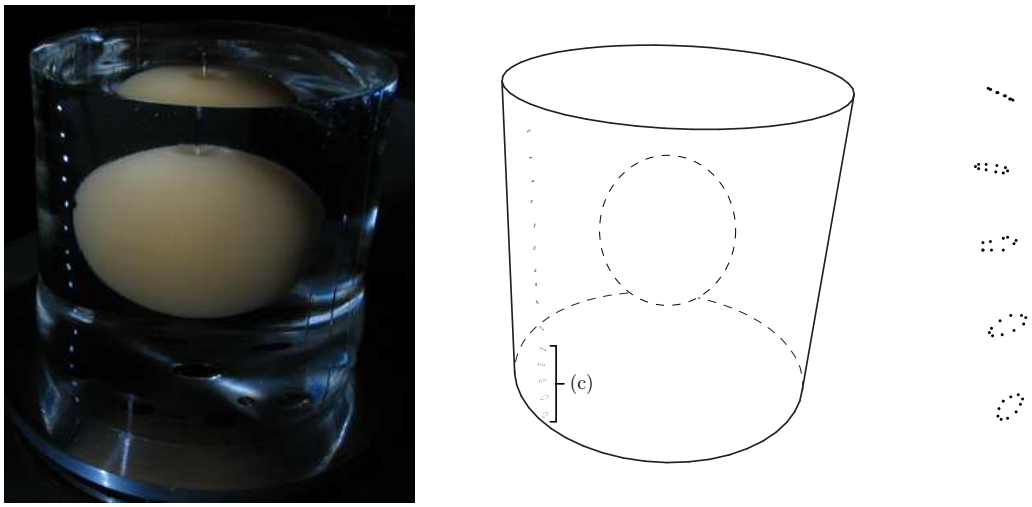

(a) Motion capture. (b) Tracked reference point locations. (c)

Figure 5.19 The experimentally observed motion of the spherical silicone phantom.

5.4.2 Parameter Reconstruction

The elastic reconstruction of the spherical phantom considered a total of three parameters, allowing the hybrid algorithm applied in Section 5.3 to be used in this study with minimal modification. The contradictive approach to internal stiffness estimation introduced in Section 4.3.2 required any hard inclusion to have a constant stiffness value, meaning the value of E'_h was fixed, and hence no longer a reconstructed parameter. The loss of this second stiffness parameter allowed the more complicated spherical phantom geometry to be described using an additional positional value without increasing the total number of independent parameters. Here, the ratio of the inclusion diameter to the overall phantom diameter was described by the parameter P_d. Physical measurements of the phantom gave an actual value for this parameter of $\hat{P}_d = 57\%$. The vertical position of the spherical inclusion, which was assumed to always lie along the central axis of the cylinder, was described by the height parameter P_h, where $\hat{P}_h = 50\%$. During all reconstructions, the soft modulus value, E'_s, was expressed to the nearest 1 kPa, while the values for the positional parameters P_d and P_h were calculated to the nearest 5 %.

5.4.2.1 Spherical Inclusion Phantom

A first attempt at three parameter reconstruction of the spherical phantom was made using the hybrid algorithm settings obtained in Section 5.3, where $\Pi_{mate} = 0.6$, $\Pi_{mutate} = 0.2$, and the number of genes was set at $N_G = 10$. Both CO and GD phases of the hybrid algorithm were run for 10 iterations. Figure 5.20(a) shows the mean stiffness distribution resulting from 100 hybrid reconstructions performed on the spherical geometry. The plane of the figure passes through the center of the cylindrical phantom, and the stiffness value at each point within the image is calculated as the mean indicated stiffness value over all reconstruction results. The measured position and size of the actual phantom inclusion is indicated as a dashed circle. Two distinct regions of high stiffness are visible, where an area of high stiffness near the top of the phantom is indicated in addition to the expected centrally located hard region.

The inconclusive result in Figure 5.20(a) led to an adjustment in the hybrid algorithm settings, based on the results from the optimization study performed in Section 5.3. The previous study found that increasing the number of genes in the CO phase of the hybrid algorithm had a significant performance benefit, even when considering the increased computational cost associated with the larger population. With this result in mind, reconstructions were performed on the spherical geometry using greater values for N_G, where the stiffness distribution resulting from hybrid reconstructions performed with $N_G = 50$ is shown in Figure 5.20(b). Here, improvement can be seen in the spatial modulus distribution, where the presence of the large inclusion near the top of the phantom is somewhat diminished.

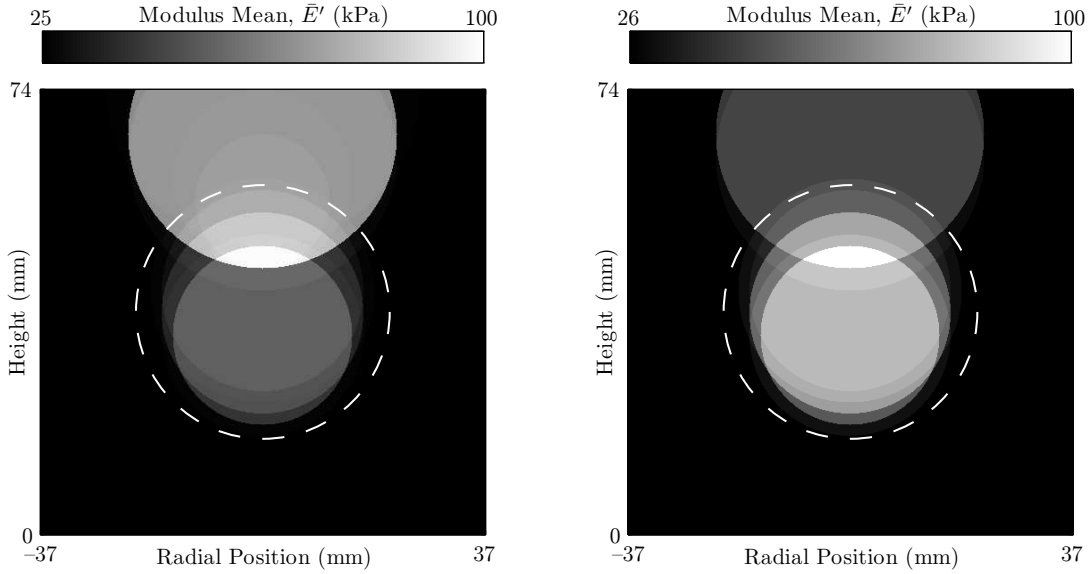

(a) Hybrid algorithm, $N_G = 10$.

(b) Hybrid algorithm, $N_G = 50$.

Figure 5.20 A spatial representation of the spherical phantom modulus reconstructed using the hybrid algorithm with varying numbers of genes.

Further testing led to satisfactory reconstruction performance with a value of $N_G = 100$. Figure 5.21(a) shows the resulting spatial modulus distribution at this value. In this case, the result strongly indicated a preference for the central inclusion location at the measured height, with a slightly smaller diameter. The reconstructed soft modulus value was approximately $E'_s = 26\,\text{kPa}$. The variance of the reconstructed modulus within the phantom is shown in Figure 5.21(b). Figure 5.21(c) indicates the reconstructed phantom stiffness variation with height, where the horizontal axis of the plot corresponds to the dashed red transect in Figure 5.21(a). The dashed line in Figure 5.21(c) represents the best-fit modulus profile that is the target of the reconstruction in this case. Figures 5.21(b) and (c) indicate that the highest variance values occurs near the edges of the central inclusion.

5.4.2.2 Homogeneous Phantom Reconstruction

The specificity of the hybrid algorithm applied to the spherical geometry was evaluated by reconstructing internal stiffness using the spherical model and the experimental motion data obtained from the soft homogeneous silicone phantom. In this case, the expected result was an entirely soft distribution free from significant hard inclusions. The actual reconstructed stiffness distribution obtained is shown in Figure 5.22, where all reconstructions used the same algorithm settings as those used when generating Figure 5.21.

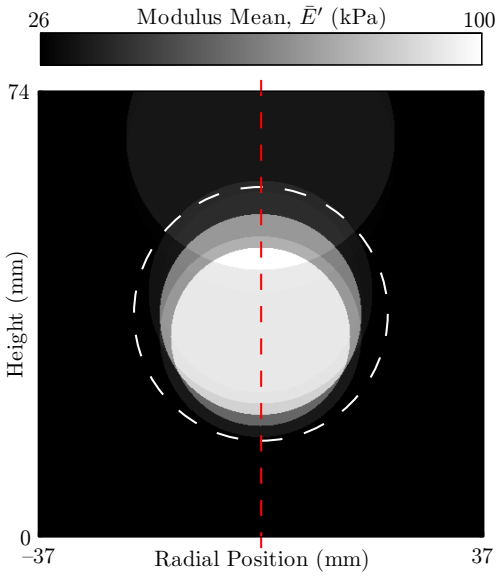

(a) Mean reconstructed modulus.

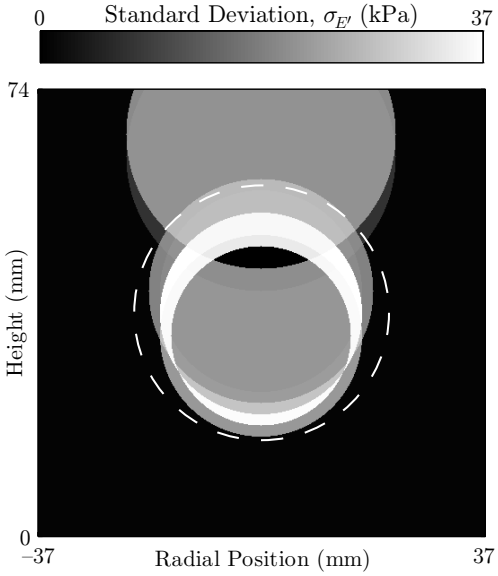

(b) Reconstructed modulus variance.

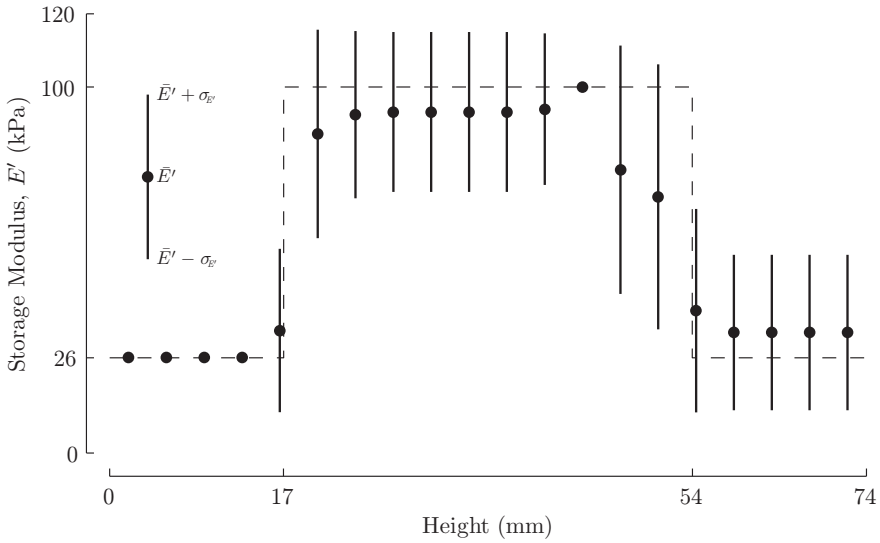

(c) Modulus variation along the dashed vertical transect in (a), where the target profile is indicated.

Figure 5.21 The spherical silicone phantom modulus distribution reconstructed using a contradictive hybrid algorithm with 100 genes.

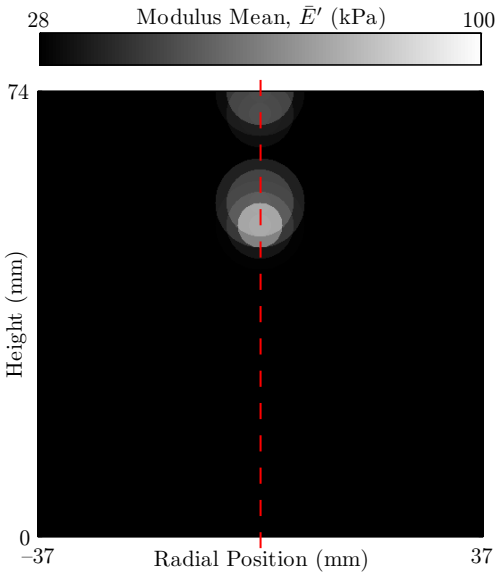

(a) Mean reconstructed modulus.

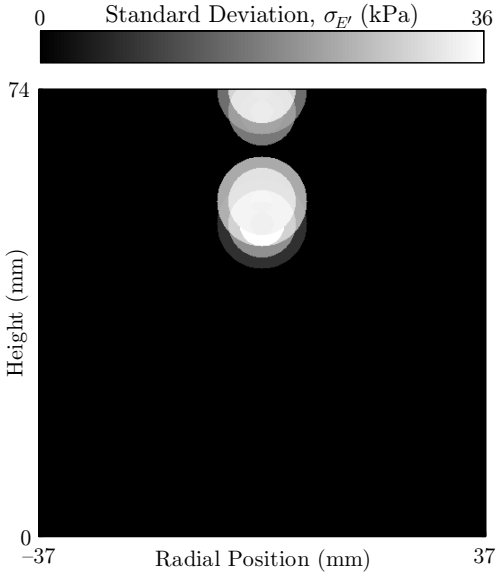

(b) Reconstructed modulus variance.

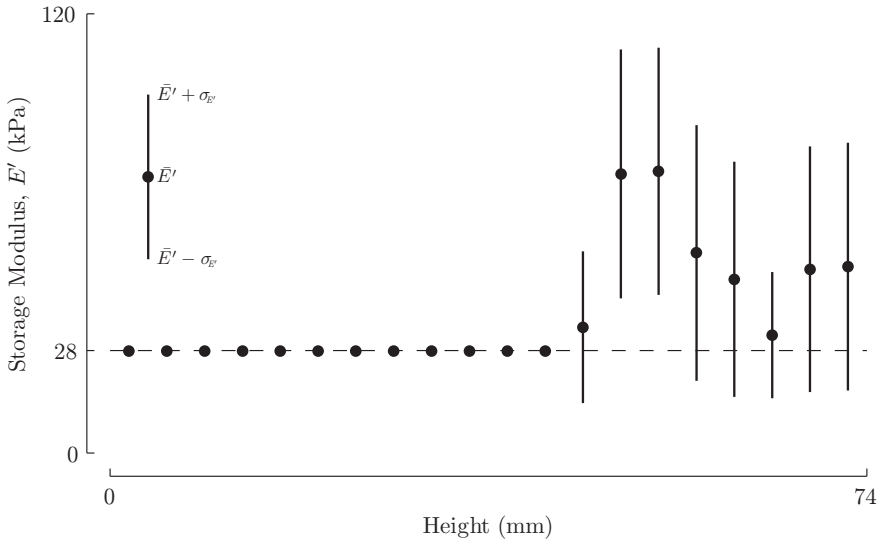

(c) Modulus variation along the dashed vertical transect in (a), where the target profile is indicated.

Figure 5.22 The soft homogenous silicone phantom modulus distribution reconstructed using a contradictive hybrid algorithm with 100 genes.

Two small areas of moderate stiffness are visible in the resulting plots at positions near the top of the model. In both cases, the modulus variance in the vicinity of the areas of increased stiffness is correspondingly high. The estimated value for the soft modulus was $E'_s = 28\,\text{kPa}$.

5.5 Discussion

The reconstructed results in Figure 5.20 indicate that the three dimensional error domain for the spherical reconstruction problem does not contain an obvious single minimum value. A bi-modal distribution is apparent, with Figure 5.20(a) indicating that approximately half of all reconstructions predicted a large inclusion located near the top of the phantom model that would be visible on the upper phantom surface. While the use of CO in previous reconstructions allowed the hybrid algorithm to avoid such local minima, the presence of two potential solutions with very similar surface error metric values presents a significant challenge to the hybrid algorithm when using a population comprising 10 genes.

The improvement in reconstructed modulus distribution when adding genes to the CO phase of the hybrid reconstruction indicates that while the presence of the upper inclusion was the result of a local error minimum, the global error minimum $\hat{\Omega}$ closely corresponds to parameters describing the actual phantom geometry. Additional genes increase the diversity of the CO population, meaning that mating and mutation have a greater chance of creating an offspring gene closer to the globally optimal parameter combination. The population diversity when $N_G = 100$ reached a level at which the globally optimum solution was preferred by almost all reconstructions.

Figure 5.23 shows a plane through the error domain for the spherical case at $E'_s = 27\,\text{kPa}$, containing the global minimum error value $\hat{\Omega}$. This plot confirms that the strongly bi-modal distribution observed during the initial reconstructions is the result of a local error minimum within the parameter domain. A region of low motion error is visible at inclusion diameter and height values greater than the globally optimal solution. The large three-dimensional size of this region means that a large number of solutions converge here, despite the region not containing $\hat{\Omega}$. However, the positive result obtained following an increase in the size of the CO population to $N_G = 100$ indicates that significant local minimum can be overcome with prudent modification of the hybrid algorithm settings.

The existence of substantial local error minimum in the spherical case is likely due to a lack of motion data from the upper surface of the phantom. The surface error studies performed on the stacked phantom in Section 4.3 indicate that when surface reference points are located across an external boundary between soft and hard material, the existence and position of such an interface can be clearly determined.

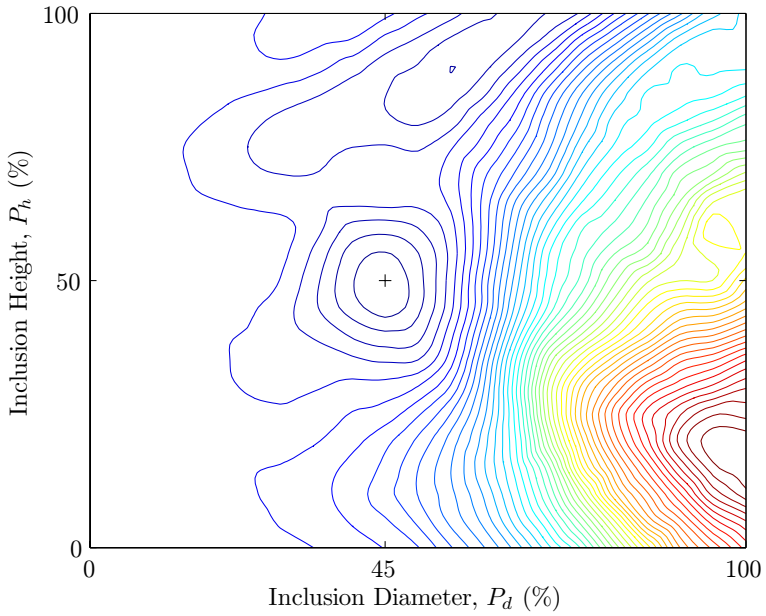

Figure 5.23 A plane at $E'_s = 27\,\text{kPa}$ through the spherical phantom error domain, where the location of global minimum error, $\hat{\Omega}$, is indicated (+).

Additional reference points on the top surface of the phantom should allow the motion error metric to clearly identify the presence or absence of inclusions near or at the top surface of the model based on their surface displacement values.

The slight underestimation of the size of the spherical inclusion in Figure 5.21 is likely a result of the nodal stiffness interpolation used in the FE model, and is in line with the results from the concentric phantom in Section 5.3. Additionally, the rounding of P_d during the reconstructions may have led to a small underestimation of the predicted inclusion diameter.

The specificity analysis of the hybrid reconstruction algorithm using the homogeneous phantom experimental data indicated the presence of small, moderate stiffness regions near the top of the phantom. While the soft modulus value reconstructed across the majority of the phantom was in good agreement with the 28 kPa value obtained from the soft homogeneous silicone phantom in Section 4.2, the small areas of elevated stiffness are undesirable, as the ability of any screening system to minimize the occurrence of false positive results is important. Consideration of the error domain for the homogeneous phantom reconstruction, shown in Figure 5.24, reveals that the presence of the small inclusions near the top of the model are due to inaccuracies in the error domain. Here, the global error metric minimum $\hat{\Omega}$ occurs at $P_d = 20\%$, $P_h = 75\%$, conflicting with the expected location of this minimum, along the left edge of the figure at $P_d = 0\%$. While the difference in motion error metric between these

two locations is very small, the increased performance of the hybrid algorithm with 100 genes meant that a large number of solutions converged to this globally optimal combination of parameters. This result is further evidence that motion data at the upper phantom surface may improve the ability of the surface error metric to correctly eliminate geometries that predict inclusions near the top of the model.

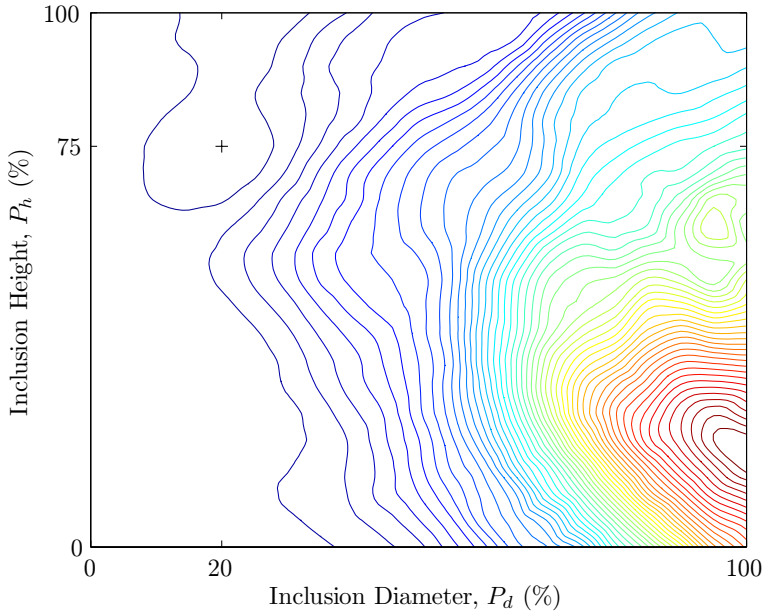

Figure 5.24 A plane at $E'_s = 26\,\text{kPa}$ through the soft homogeneous phantom error domain, where the location of minimum error within the plane is indicated (+).

Despite the challenges presented by both error domains, the presence of a hard inclusion in the spherical case was more strongly suggested than the presence of any hard area in the homogeneous phantom. All areas of elevated stiffness corresponded to the highest observed values for modulus variance in the homogeneous phantom reconstructions. This result differs from the spherical case, where variance values within the interior of the hard inclusion were lower, and the highest variance values were around the edge of the inclusion, as expected.

Increasing the number of genes in the CO stage of the hybrid reconstruction gives a subsequent increase in computational cost, summarized in Table 5.7. Here, the hybrid reconstructions with $N_G = 100$ require 10 times the number of FE solves as the baseline case where $N_G = 10$, when performed on a serial system. However, the inherent suitability of CO to parallel computation means that if performed on a large parallel system of processors, an increase in genes would not increase the overall time required for computation, as each gene would be simulated on a dedicated processor. Additionally, it should be noted that all the hybrid reconstructions required significantly less computational effort than an exhaustive search within the problem domain.

For the spherical geometry considered in this case, with a total of three independent parameters, an exhaustive search would involve a total of 4,851 FE simulations.

Table 5.7 Computational cost considerations for the hybrid algorithm applied to the spherical silicone phantom.

		Consecutive Solves	
		Serial	**Parallel**
Algorithm	N_G	**(actual)**	**(theory)**
Hybrid	10	140	20
	50	540	20
	100	1,040	20

The final reconstruction study indicated that the hybrid reconstruction method had the ability to reconstruct the internal stiffness distribution of a more realistic geometry containing a spherical inclusion. While the algorithm required additional tuning to achieve a positive result in this case, the additional computational cost could be offset with the use of parallel computation. The continued presence of local error minima in this study highlighted the requirement of a DIET system to have accurate motion data from as much of the exposed object surface as possible, if reconstruction results are to return the expected stiffness distribution.

Chapter 6

Conclusions

The research presented in this thesis has shown the DIET approach to stiffness reconstruction to be both technically and clinically realistic. The feasibility of the system has been evaluated and proven with a range of analytical and experimental testing. Promising results have been obtained that warrant further system development towards the eventual goal of a clinical trial. This chapter presents the technical and clinical conclusions that can be drawn from the research performed to this point.

6.1 Technical Outcomes

A number of strategies for fitting experimentally observed phantom displacements to a well defined motion path were developed and implemented. Each approach was based on the modelling assumptions used for the relevant FE simulation. These fitting algorithms allowed experimentally measured motion to be directly compared with computer model displacement output from FE simulation, and form an important link between observed and simulated behavior.

The methods devised for experimental motion capture and processing were validated by a testing phase using tissue-approximating phantoms. The surface motion error metrics developed allowed quantitative comparison of measured and simulated motions. Implementation of these metrics in conjunction with the motion fitting algorithms confirmed that experimentally observed motion can be accurately compared with simulated displacements. These techniques were developed using simulated and phantom data, however they are directly applicable to experimental data from any source.

The motion studies completed on experimental data indicated that surface motion measurements alone are sufficient to estimate an internal stiffness distribution using a limited number of independent parameters. The Young's Modulus values estimated using surface error were a good match to independent mechanical test results when

considering the experimental uncertainties present. This result is the first of its kind in the field, and indicates a major milestone in the technical validation of the DIET approach to stiffness reconstruction.

A number of techniques for mechanical property estimation and reconstruction were developed and tested. The reconstruction methods included both traditional deterministic approaches and novel methods involving stochastic components. The initial validation of each technique used simulated data, providing an environment where noise levels and other uncertainties were controllable. Following validation, the estimation and reconstruction methods were successfully applied to experimental data from tissue-approximating phantoms, showing that identifying a minimum-error solution and automating the search for it is feasible.

Metrics to measure both the accuracy of a reconstruction method and its computational cost were developed and implemented. These metrics allowed the evaluation of each reconstruction algorithm to include performance aspects from both a technical and practical standpoint. In addition, the computational cost metrics give a useful indication of the time required to perform the reconstruction on modern, parallel computer systems.

A novel hybrid reconstruction algorithm was implemented and was able to successfully reconstruct internal stiffness based on minimal surface motion measurements. While this method was identified as having a greater computational cost than a gradient-descent method performed in isolation, the performance of the hybrid approach far outweighed the extra computation required. In addition, the success of the DIET reconstructions with such a limited set of input data gives this method a distinct advantage over alternative modalities such as MRE, where the full-volume data sets involved require significant resources and computation at the data acquisition stage.

During both analytical and experimental stages of the research, sources of modelling and experimental error were identified. The magnitude and consequences of these errors were considered when evaluating the accuracy of the results obtained. When necessary and practical, advances in experimental technique and modelling strategy allowed these sources of error to be minimized or eliminated, giving greater confidence in the subsequent outcomes.

When considered from a technical standpoint, the DIET approach to stiffness reconstruction provides an output that is comparable to similar elastographic techniques. That these results are obtained with significantly less input data presents a significant advantage when considering the practicalities of experimental data collection. In addition, the effective computational cost of DIET reconstruction is rapidly diminishing as parallel computing becomes more mainstream.

6.2 Clinical Outcomes

Analytical pre-cursor studies were completed as a proof of concept for the DIET system. The result of this work indicated that the concept of stiffness reconstruction using DIET may have clinical applicability, and warranted further investigation. While the geometry used in these studies was not an exact match to clinical reality, it was shown that the observed surface motions from an object the same size as a human breast could be used to differentiate between internal stiffness configurations.

The experimental results from gelatine and silicone phantoms indicated that the DIET method can reconstruct elastic properties in an experimental situation. Here, stiffness identification of homogeneous phantoms was performed with good agreement to independent test results. Significantly, the difference in observed surface motion between homogeneous phantoms with a stiffness contrast less than independently-measured tumor contrast values was clearly evident.

Further experiments using silicone phantoms indicated that in addition to homogeneous phantoms, heterogeneous stiffness distributions could be identified using only surface measurements. These experiments provided a further step towards clinical reality, where the identification of areas of different stiffness within a single object is a key objective. Results from the concentric and spherical silicone phantoms were obtained with measurements made entirely on the soft region of the phantom, in a similar manner to the envisaged experimental data collection from a human breast.

The contradictive approach to inclusion imaging was found to give more accurate results than the traditional corroborative approach. The contradictive approach places more emphasis on correctly identifying parameters that have the greatest affect on the observed motion in an attempt to increase the efficiency of the reconstruction process. In a clinical scenario, any loss of accuracy when assuming an inclusion stiffness value would not present a significant disadvantage, as the DIET system is intended as a screening test focused on the presence of inclusions, rather than their exact stiffness.

The final evaluation of the DIET system used a phantom with a spherical inclusion, and showed that reconstruction of simple geometry resembling the configuration of a breast tumor is possible. While the exact stiffness was not characterized, the high stiffness of the inclusion was identified to within accuracy limits acceptable for a screening test. In addition, the specificity of the system was demonstrated, along with clear indications of how this metric could be improved. These encouraging results suggest that further system development should be pursued, with the medium-term aim of obtaining experimental data from a human subject.

Chapter 7

Future Work

The work presented in this thesis developed a number of aspects of the DIET system from a theoretical proof of concept experiment through to a successful elastic property reconstruction on heterogeneous, tissue-approximating phantoms. Although the more complicated geometries that will be present in a clinical scenario may require a more sophisticated approach to the description of the shape of an inclusion, the framework developed during this research should allow advances in actuation, data capture, and model simulation to be incorporated without significant effort. This chapter includes thoughts on the development required to improve the DIET system towards its application in a clinical scenario.

7.1 Short-Term Development Goals

Accurate stiffness reconstruction based on surface motion requires a comprehensive and exact experimental measurement of surface displacements. Issues with surface motion error metric identified during the reconstruction of the spherical phantom confirmed the importance of having complete surface motion data available for the reconstruction problem. In this case, additional reference points across the top of the phantom should improve the reconstruction solution distribution and eliminate the spurious areas of high stiffness visible in the results. Confirming this improvement would require the collection of an additional data set with an increased reference point density, including the continuation of the vertical line of reference points across the top of the phantom.

While the range of reconstructions performed were able to clearly indicate the presence of an inclusion, the limits of this reconstruction have not been explored. Such a study would involve creating a range of phantoms with spherical inclusions of varying size. In conjunction with an increased reference point coverage, this experiment should provide an indication of the minimum size inclusion the DIET system can ac-

curately detect. In addition to inclusion size, variations in inclusion stiffness provide an additional avenue for investigation.

Reducing the amplitude of actuation for subsequent phantom testing may help to reduce the observed under-estimation of experimental displacement by the linear FE model. Recent results from the motion tracking system have indicated that reduced point motion amplitude would not present a significant problem when tracking points, removing the requirement for the larger amplitudes used for the experimental work in this thesis. While the addition of material non-linearity to the FE model provides an alternative approach to improving the displacement match, such a change would add significant complexity to any reconstruction problem that is undesirable at this stage.

Further increases in computational capacity will allow more refined meshes to be used for FE simulation. Mesh refinement will help to reduce the diffusive effect of nodally-distributed material properties on the interface between hard and soft material in the FE model. It is hoped that greater definition between adjacent material regions of different properties will improve the slight under-estimation of inclusion size observed in both the concentric and spherical reconstructed results.

Varying the frequency of actuation has the potential to provide additional experimental information useful for the reconstruction problem. Here, a range of data sets taken across different frequencies would allow the phantom motion at a range of mode shapes to be characterized. The presence of an inclusion may be more obvious in a specific mode of vibration, allowing a reconstruction performed using data at more than one actuation frequency to identify inclusions not visible at a single frequency alone. Clinically, such an approach should not present a significant challenge, allowing motion at a range of frequencies to be obtained from a patient in a matter of minutes.

Shape functions, such as radial-basis functions, may provide an alternative approach to describing the geometry of an inclusion. Such functions have the ability to define inclusions of a more complicated nature that cannot be accurately approximated by the spherical model currently used. In addition, such shape functions may be differentiable with respect to surface displacements, allowing an analytic calculation of the Jacobian matrix for gradient-descent reconstructions, which would be advantageous as the number of shape parameters is increased.

The scenario of multiple inclusions has not been addressed in research to this point. This situation presents an additional experimental scenario relevant to DIET system development, particularly as the case of multiple tumors within a single breast is clinically relevant. The description of internal geometry in such cases may benefit from the use of the shape functions previously described, and is likely to require an increase in the number of reconstructed parameters. The current phantom manufacturing process would not require significant modification in order to create phantoms with multiple

inclusions, and reconstruction of internal geometry will prove a significant challenge to an advanced version of the current reconstruction algorithm.

Further studies using silicone for phantom manufacture should include an in-depth study of the silicone material properties. While the static tests performed in the current work provided a useful benchmark for reconstruction performance, there was an obvious variation in silicone properties across the different batches used for homogeneous phantoms, heterogeneous phantoms, and material testing. Material property variations with temperature should be included in this work, as the notable warming of the silicone phantoms during actuation may lead to variations in the observed stiffness value.

Significant potential was identified for a reduction in computational time through the use of parallel methods for reconstruction algorithm FE simulations. This parallelization should be straightforward through the use of protocols such as the Message Passing Interface (MPI) libraries. Parallelization using MPI has not been required up to this point due to the small number of parameters reconstructed, but will become inevitable as the complexity of the reconstruction problem increases.

7.2 Long-Term DIET System Development

Development of a DIET system capable of performing a clinical trial involves a number of important milestones outside the scope of work presented in this thesis. Concurrent research is investigating a technique where colored glitter can be used to significantly improve the reference point density of the surface of the phantoms [109]. This technique should provide a large increase in the amount of surface motion data available to the reconstruction problem, while presenting a clinically attractive method for obtaining a high point density on the breast surface.

An alternative to manually applied surface features is the use of the natural variation in skin appearance to form reference points for motion tracking. Such points can be identified from image cross-correlation and speckle patterns, and have the ability to provide a high point density from moving skin [95]. This technique may be useful for motion tracking in a clinical scenario, as it would avoid any requirement for artificial reference points that may be inconvenient or impractical to apply to the breast of a patient.

Adding more cameras to the current imaging setup will allow displacements to be tracked over the entire surface of a phantom, an improvement on the single line of dots currently used. This improved surface coverage would release the current constraint that requires all phantoms to be symmetric. Asymmetry would allow more realistic phantoms to be developed, where the inclusion position can vary radially as well as vertically. In addition, phantoms with asymmetric external geometry that closely re-

semble breast geometry can be tested, providing more clinically relevant data for the reconstruction problem.

Boundary Element Methods (BEM) are being investigated as an alternative to the current FE method used for simulating model displacements using a computer [115]. By formulating the forward problem in terms of boundary integral equations, surface displacements can be obtained using a mesh that only describes the external and internal boundaries between discrete regions. While currently limited to a two-dimensional case, BEM is showing promise for incorporation into the DIET system, allowing model simulation using only the relevant surface geometry information.

A major goal for the DIET system is a clinical test that would provide a set of surface displacements from a real breast. Such a test requires the development of a patient positioning device, and refinement of the actuation and motion capture system. While these developments will present a range of significant challenges, having experimental data from a real breast will allow reconstruction algorithms to be refined for use with clinically relevant data.

Appendix A

The Finite Element Method

The finite element (FE) method is a powerful tool that allows computers to simulate a large range of physical scenarios. When used to solve problems in computational solid mechanics, FE methods can generate transient and steady-state solutions in both static and time-harmonic scenarios. The material in this appendix is intended to give a brief overview of the FE approach used to solve steady-state, time-harmonic solid mechanics problems for three-dimensional models.

Weighted Residuals

The equilibrium conditions for a solid body in a static system can be expressed as a null divergence of the stress tensor,

$$\sigma_{ij,j} = 0. \tag{A.1}$$

When considering the inertial forces present in an undamped, steady-state, time-harmonic system, Equation A.1 becomes

$$\bar{\sigma}_{ij,j} + \rho\omega^2\bar{u}_i = 0, \tag{A.2}$$

where ρ represents the material density, ω the system frequency, and $\bar{u}_i$ motion amplitude, and $\bar{\sigma}$ the corresponding time-harmonic stress tensor. In the case where the exact displacement solution within the body is not known, and approximated as $\hat{u}$, Equation A.2 will have a non-zero residual term,

$$R = \hat{\sigma}_{ij,j} + \rho\omega^2\hat{u}_i, \tag{A.3}$$

where $\hat{\sigma}$ are the stresses given by the approximate displacement solution $\hat{u}$. In the ideal case this residual term will be zero over the entire domain, meaning any weighted integration of R should also be zero,

$$\left\langle W^k \left(\hat{\sigma}_{ij,j} + \rho\omega^2 \hat{u}_i \right) \right\rangle = 0, \tag{A.4}$$

where the angled brackets indicate integration over the three-dimensional domain, and W^k is an arbitrarily-chosen weighting function. As the number of weighting functions, N_k, increases, the match between the approximate and exact stress solutions improves towards the limit,

$$\lim_{N_k \to \infty} \hat{u} = \bar{u}. \tag{A.5}$$

Interpolating Polynomials

The FE method makes use of interpolating functions, ϕ^k, to describe the value of field variables at any position within the domain. It is the local influence of these interpolating polynomials that leads to the quantification 'finite' in 'finite element methods'. The shape functions used for field interpolation can take a variety of forms, including simple linear functions, and any number of higher-order descriptions. While higher-order functions, such as cubic polynomials, allow a more accurate description of field variables within a discretized element, the integration performed on these elements has added complexity. Given limited computational resources, a choice must be made between using high-order polynomials on larger elements, or smaller elements with simpler interpolating functions. Linear interpolating functions were used in this work, allowing a fine discretization of the domain while reducing integration times. An example of the linear tetrahedral element used in all three-dimensional FE code is shown in Figure A.1, where the four nodes are numbered according to a right-handed convention.

When considering the case where the interpolating polynomial is linear, field variable interpolation within a four-noded tetrahedral element takes the form

$$\hat{u}_e = \sum_{k=1}^{4} \hat{u}_k \phi^k(x, y, z), \tag{A.6}$$

where in this example $\hat{u}_e$ indicates an approximation to the displacement solution $\bar{u}$ at the position (x, y, z).

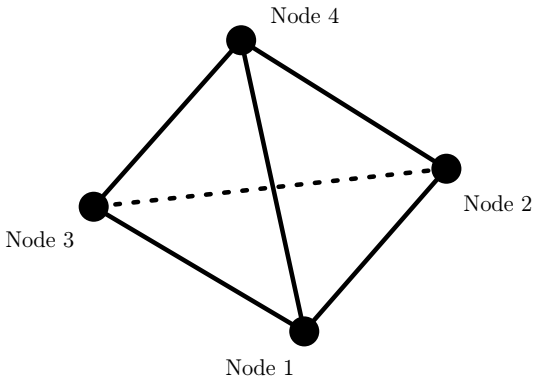

Figure A.1 A three-dimensional linear tetrahedral element with nodes numbered according to a right-handed convention.

The Galerkin Method

The Galerkin method refers to a technique where the weighting functions described in relation to the method of weighted residuals additionally form the basis functions for the interpolating polynomials,

$$W^k = \phi^k \tag{A.7}$$

This approach is widely popular in FE techniques due to its simplicity and effectiveness.

It is standard practice in FE methods to perform the integration of the weighted residual statement in Equation A.4 using Green's theorem,

$$\begin{aligned} \left\langle \phi_i^k \left(\hat{\sigma}_{ij,j} + \rho\omega^2 \hat{u}_i \right) \right\rangle &= 0 \\ \left\langle -\phi_{i,j}^k \hat{\sigma}_{ij} + \phi_i^k \rho\omega^2 \hat{u}_i \right\rangle + \oiint \phi_i^k \hat{\sigma}_{ij} n_j \, dS &= 0, \end{aligned} \tag{A.8}$$

where n_j is a surface outward normal unit vector. Equation A.8 is termed the 'weak' formulation of the weighted residual statement, as stress boundary conditions are only required to match an integration over the surface upon which they are applied.

Stiffness Matrix Terms

Expressing the differential system provided by Equation A.2 in terms of displacements requires a conversion from stress to strain terms. The relationship between displacements, u, and strains, ϵ, for a linear elastic material can be expressed in tensor form as

$$\bar{\epsilon}_{ij} = \tfrac{1}{2}\left(\bar{u}_{i,j} + \bar{u}_{j,i}\right), \tag{A.9}$$

while the corresponding relationship between strains and stresses can be described as

$$\bar{\sigma}_{ij} = \lambda \delta_{ij} \bar{\epsilon}_{kk} + 2\mu \bar{\epsilon}_{ij}, \tag{A.10}$$

where λ and μ are Lamé's constants, and δ_{ij} is the Kronecker delta function. Substituting the relationships defined in Equations A.9 and A.10 into the weak form, given in Equation A.8 for the time-harmonic case, and writing out terms in full for the x-direction gives

$$\left\langle 2\mu \frac{\partial \hat{u}_x}{\partial x} + \lambda \left(\frac{\partial \hat{u}_x}{\partial x} + \frac{\partial \hat{u}_y}{\partial y} + \frac{\partial \hat{u}_z}{\partial z} \right) \frac{\partial \phi_i}{\partial x} \right\rangle + \dots$$
$$\left\langle \mu \left(\frac{\partial \hat{u}_x}{\partial y} + \frac{\partial \hat{u}_y}{\partial x} \right) \frac{\partial \phi_i}{\partial x} \right\rangle + \left\langle \mu \left(\frac{\partial \hat{u}_x}{\partial y} + \frac{\partial \hat{u}_y}{\partial x} \right) \frac{\partial \phi_i}{\partial x} \right\rangle = -\rho \omega^2 \hat{u}_x. \tag{A.11}$$

In order to solve differential equations using FE methods, it is desirable to form a system of equations

$$\left[\, k \,\right] \{u\} = \{b\}, \tag{A.12}$$

where the stiffness matrix $[k]$ contains the material property terms, and $\{b\}$ represents forcing terms arising from inertial forces or externally-applied constraints. For the three-dimensional case, each node has three degrees of freedom representing orthogonal displacement components, and local stiffness matrix terms are defined

$$
\begin{aligned}
k_{11} &= \left\langle (2\mu+\lambda)\,\frac{\partial\phi_i}{\partial x}\frac{\partial\phi_j}{\partial x} + \mu\frac{\partial\phi_i}{\partial y}\frac{\partial\phi_j}{\partial y} + \mu\frac{\partial\phi_i}{\partial z}\frac{\partial\phi_j}{\partial z} \right\rangle \\
k_{12} &= \left\langle \lambda\frac{\partial\phi_i}{\partial x}\frac{\partial\phi_j}{\partial y} + \mu\frac{\partial\phi_i}{\partial y}\frac{\partial\phi_j}{\partial x} \right\rangle \\
k_{13} &= \left\langle \lambda\frac{\partial\phi_i}{\partial x}\frac{\partial\phi_j}{\partial z} + \mu\frac{\partial\phi_i}{\partial z}\frac{\partial\phi_j}{\partial x} \right\rangle \\
k_{21} &= \left\langle \lambda\frac{\partial\phi_i}{\partial y}\frac{\partial\phi_j}{\partial x} + \mu\frac{\partial\phi_i}{\partial x}\frac{\partial\phi_j}{\partial y} \right\rangle \\
k_{22} &= \left\langle \mu\frac{\partial\phi_i}{\partial x}\frac{\partial\phi_j}{\partial x} + (2\mu+\lambda)\,\frac{\partial\phi_i}{\partial y}\frac{\partial\phi_j}{\partial y} + \mu\frac{\partial\phi_i}{\partial z}\frac{\partial\phi_j}{\partial z} \right\rangle \\
k_{23} &= \left\langle \lambda\frac{\partial\phi_i}{\partial y}\frac{\partial\phi_j}{\partial z} + \mu\frac{\partial\phi_i}{\partial z}\frac{\partial\phi_j}{\partial y} \right\rangle \\
k_{31} &= \left\langle \lambda\frac{\partial\phi_i}{\partial z}\frac{\partial\phi_j}{\partial x} + \mu\frac{\partial\phi_i}{\partial x}\frac{\partial\phi_j}{\partial z} \right\rangle \\
k_{32} &= \left\langle \lambda\frac{\partial\phi_i}{\partial z}\frac{\partial\phi_j}{\partial y} + \mu\frac{\partial\phi_i}{\partial y}\frac{\partial\phi_j}{\partial z} \right\rangle \\
k_{33} &= \left\langle \mu\frac{\partial\phi_i}{\partial x}\frac{\partial\phi_j}{\partial x} + \mu\frac{\partial\phi_i}{\partial y}\frac{\partial\phi_j}{\partial y} + (2\mu+\lambda)\,\frac{\partial\phi_i}{\partial z}\frac{\partial\phi_j}{\partial z} \right\rangle.
\end{aligned}
\tag{A.13}
$$

Following the assembly of these local element matrices into a global stiffness matrix, which is sparse, symmetric, and positive definite, the global displacement field $\hat{u}$ can be calculated via matrix inversion.

Viscoelasticity

The response of viscoelastic materials to time-harmonic loading can be simplified by representing the material as a combination of connected springs and dashpots that model stiffness and damping behavior. While a number of complicated rheological models have been proposed to approximate the observed response of different viscoelastic materials, this section will limit consideration to the commonly-used Voigt element shown in Figure A.2 for simplicity. Here, a linear spring with stiffness E, and a dashpot with damping parameter η, are configured in parallel.

The parallel spring and dashpot within the Voigt element require that strains are equivalent in both components,

$$\epsilon = \epsilon_1 = \epsilon_2. \tag{A.14}$$

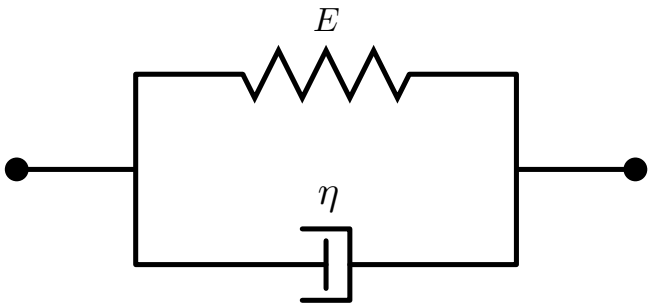

Figure A.2 A Voigt element, where a spring and dashpot are connected in parallel.

In addition, the total stress within the element can be expressed as the sum of the individual component stresses,

$$\sigma = \sigma_1 + \sigma_2 \tag{A.15}$$

Utilizing the stress-strain relationships for a linear spring and a dashpot, this combined element stress can be expressed as

$$\sigma = E\epsilon + \eta\dot{\epsilon}, \tag{A.16}$$

where E has units of Nm^{-2}, η has units of $\mathrm{Nm}^{-2}\mathrm{s}$, and $\dot{\epsilon}$ indicates the time-derivative of strain. Substituting a time-harmonic stress and strain variation into the stress definition provided by Equation A.16 and simplifying,

$$\bar{\sigma} = (E + i\omega\eta)\,\bar{\epsilon}, \tag{A.17}$$

where the overbar indicates the amplitude of the stress and strain terms. In this case, the equivalent elastic modulus of the element is a complex term with both real and imaginary components,

$$E^* = E' + iE'', \tag{A.18}$$

where $E' = E$, and $E'' = \omega\eta$.

While the modulus components derived here are accurate only for a Voigt element, a complex-valued elastic modulus can be developed from many combinations of springs and dashpots. When simulating damped model displacements using FE methods in this work, the generalized description of this complex modulus provided by Equation A.18 was used, and no direct comparison to a specific rheological model was made.

Model Performance Near the Incompressible Limit

A simple experiment was designed to characterize the accuracy of compressible elasticity FE simulations as the value of Poisson's ratio, ν, approaches the incompressible limit. A simple three-dimensional model was created by extruding a square cross-section with side lengths of 38 mm to a height of 200 mm. Boundary conditions constrained the lower face of the block in all three orthogonal directions, with a 0.5 mm, 100 Hz sinusoidal displacement prescribed in one horizontal plane. This actuation induced regular mechanical shear waves throughout the model volume. A damped material model was used for all simulations, with the material storage modulus $E' = 20\,\text{kPa}$, and damping ratio $\zeta = 0.1$. Material density was fixed at $\rho = 1000\,\text{kg/m}^3$, and Poisson's ratio was varied from 0.45 to 0.499 in six increments.

The reference solution for this situation was obtained via FE simulation using an incompressible material model. For the incompressible simulations, the model was meshed using 27-noded quadratic elements, with an average element edge length of 4.7 mm, giving a total of 11,000 nodes, and 1,200 elements. The observed displacement fields for this model over the range of values for Poisson's ratio are shown in Figure A.3.

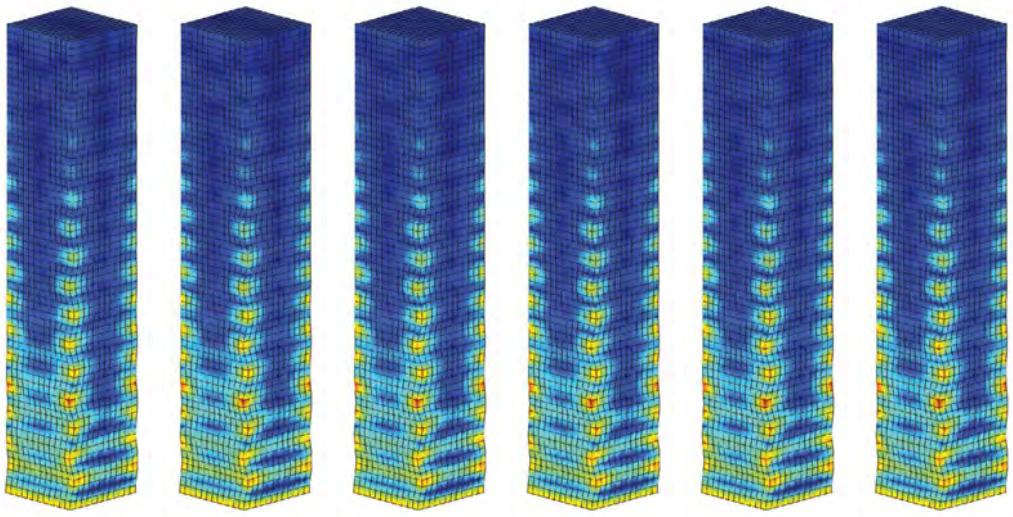

(a) $\nu = 0.45$. (b) $\nu = 0.47$. (c) $\nu = 0.48$. (d) $\nu = 0.49$. (e) $\nu = 0.495$. (f) $\nu = 0.499$.

Figure A.3 Incompressible FE model displacement fields at a range of Poisson's ratio values.

As expected, the observed displacement fields for the incompressible simulations remain consistent as Poisson's ratio approaches the incompressible limit at $\nu = 0.5$. Minor changes in the displacement field are due to the influence of the changing Poisson's ratio value on the material shear modulus. The effect of material damping can be seen in the reduction in shear wave amplitude towards the top of the model.

The FE mesh for compressible elasticity simulations was composed of linear tetrahedral elements. The average element edge length was approximately 2.5 mm, giving a total of 27,000 nodes, and 146,000 elements. Displacement fields from FE simulation using the compressible FE model are shown in Figure A.4 for the range of Poisson's ratio values considered.

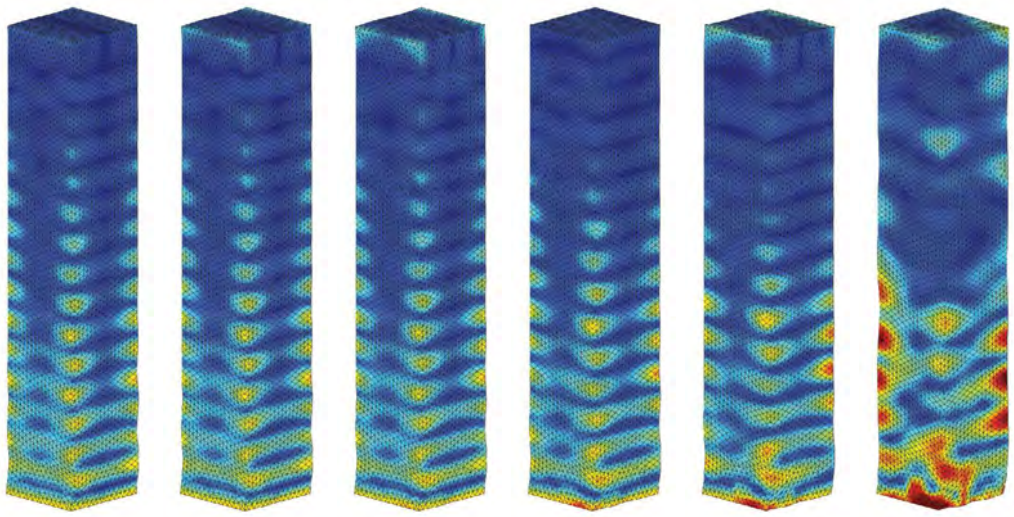

(a) $\nu = 0.45$. (b) $\nu = 0.47$. (c) $\nu = 0.48$. (d) $\nu = 0.49$. (e) $\nu = 0.495$. (f) $\nu = 0.499$.

Figure A.4 Compressible FE model displacement fields at a range of Poisson's ratio values.

The displacement fields from the compressible simulations show good agreement with the reference solution at values of Poisson's ratio up to and including $\nu = 0.49$. Below this value, the observed wavelength and motion field are very similar to the reference case in Figure A.3. At $\nu = 0.49$, small inconsistencies are visible, but the overall motion field is still regular, and generally consistent with the reference solution.

Simulated displacement fields in Figure A.4 at Poisson's ratio values above $\nu = 0.49$ indicate that FE simulations in this region begin to lose accuracy when compared to the reference results. At $\nu = 0.495$, clear variation is apparent, and at $\nu = 0.499$, the standing wave pattern has been significantly disrupted, and can not be relied on as an accurate approximation to real-world behavior.

The simulations performed using a compressible elasticity FE model show good agreement to a reference solution generated using an incompressible material model for values of Poisson's ratio up to and including $\nu = 0.49$. The appearance of slight deviation from the reference solution at $\nu = 0.49$ means that this value should represent the upper limit for simulations if the compressible FE model is expected to be free from significant numerical inaccuracies.

Appendix B

Silicone Material Data

This appendix contains Material Safety Data Sheets (MSDS) for the two types of silicone used during phantom manufacture.

Factor II, Incorporated

P.O. Box 1339
Lakeside, AZ 85929

Phone:(928) 537-8387
Fax: (928) 537-0893

MATERIAL SAFETY DATA SHEET
A-341 Part A
Soft Gel

In Case of Emergency Contact Factor II, Inc. 928-537-8387

Factor II Technology urges each customer or recipient of this MSDS to study it carefully to become aware of and understand the hazards associated with the product. The reader should consider consulting reference works or individuals who are experts in ventilation, toxicology, and fire prevention, as necessary or appropriate to the use and understanding of the data contained in this MSDS.

To promote safe handling each customer or recipient should: (1) notify and furnish its employees, agents, contractors, customers, and others whom it knows or believes will use this material of the information regarding hazards or safety; (2) request its customers to notify their employees, customers and other users of the product of this information.

1. CHEMICAL PRODUCT
PRODUCT NAME: RTV Heat Cure Silicone
CHEMICAL NAME: Organopolysiloxane Mixture

2. PRODUCT COMPOSITION

MATERIAL	CAS#	
POLYMER-ORGANOPOLYSILOXANE	68083192	<60
MIXTURE	13983170/131	<20
MINERAL FILLERS	4234	<20
SILICA FILLER	67762907	

3. HAZARDS and PROTECTION IDENTIFICATION
Personal Protection Recommended: Use local exhaust. Ventilation is required. Use a NIOSH approved respirator to prevent overexposure. Reference 29CFR 1910.134 for Federal standards concerning respiratory protection. Wear impervious gloves and protective clothing as required to prevent skin contact. Wear protective goggles to prevent eye contact. An eyewash and safety shower should be nearby and ready for use.

4. FIRST AID MEASURES
EMERGENCY AND FIRST AID PROCEDURES:
SWALLOWING:
Induce Vomiting
SKIN:
Wash with soap and water.
INHALATION:
Remove to fresh air..
EYES:
Immediately flush eyes with water and continue washing for at least 15 minutes. If irritation persists seek medical attention.
NOTES TO PHYSICIAN:
There is no specific antidote. Treatment of overexposure should be directed at the control of symptoms and the clinical condition of the patient.

Factor II, Incorporated

P.O. Box 1339
Lakeside, AZ 85929

Phone:(928) 537-8387
Fax: (928) 537-0893

5. FIRE FIGHTING MEASURES
FLASH POINT: (TCC) N/A

FLAMMABLE LIMITS IN AIR (by volume): Not Applicable N/A

EXTINGUISHING MEDIA: Dry Chemical ,Foam or Carbon Dioxide

SPECIAL FIREFIGHTING PROCEDURES: None known.

UNUSUAL FIRE AND EXPLOXION HAZARDS: None Known

6. ACCIDENTAL RELEASE MEASURES
STEPS TO BE TAKEN IF MATERIAL IS RELEASED OR SPILLED:
Contain the spill or leak, scrape up with cardboard or a ra and place in a container.
WASTE DISPOSAL METHOD: Dispose of in accordance with all Federal, State, and local regulations.

7. HANDLING AND STORAGE
PRECAUTIONS TO BE TAKEN IN HANDLING AND STORAGE:
Keep container tightly closed. Store in cool place and keep away from Heat or Flame.
Don't lay container on its side.

8. PHYSICAL AND CHEMICAL PROPERTIES (based on typical material)
APPEARANCE & ODOR: Clear odorless paste
BOILING POINT: 500°F
VAPOR PRESSURE at 77°Fmm Hg
VAPOR DENSITY (air=1) N/A
SOLUBILITY IN WATER (By wt): Insoluble
SPECIFIC GRAVITY (water=1) 1.23

Note: The above information is not intended for use in preparing product specifications.

9. STABILITY AND REACTIVITY DATA
STABILITY: Stable. Hazardous polymerization will not occur.
INCOMPATIBILITY: None known
HAZARDOUS COMBUSTION OR DECOMPOSITION PRODUCTS: Carbon Monoxide, Carbon Dioxide, Silicon Dioxide

10. TOXICOLOGICAL INFORMATION
Not available

11. ECOLOGICAL INFORMATION
ECOTOXICOLOGICAL INFORMATION: Keep out of sewage system.

12. DISPOSAL CONSIDERATIONS
Use proper landfill disposal or incineration.

Factor II, Incorporated

P.O. Box 1339
Lakeside, AZ 85929

Phone:(928) 537-8387
Fax: (928) 537-0893

Dispose of in accordance with all Federal, State, and local regulations.

C H I P REGULATIONS

Chemicals (Hazards Information and Packaging) Regulations 1993 requires physico-chemical and health hazard determination of all substances and preparations manufactured, transported, stored, modified, or consumed within the EEC. Components present in this product at a level which could require reporting under the statute are:
****NONE ****

FEDERAL EPA

Comprehensive Environniental Response Compensation and Liability Act of 1980 (CERCLA) requires notification of the National Response Center of release of quantities of Hazardous Substances equal to or greater than the reportable quantities (RQ's) in 40 CFR 302.4. Components present in this product at a level which could require reporting under the statute are: ****NONE ****

Superfund Amendments and Reauthorization Act of 1986 (SARA) Title III requires emergency planning based on Threshold Planning Quantities (TPQ's) and release reporting based on Reportable Quantities (RQ's) in 40 CFR 355 (used for SARA 302, 304, 3 1, and 312). Components present in this product at a level which could require reporting under the statute are: **** NONE ****

Superfund Amendments and Reauthorization Act of 1986 (SARA) Title III requires submission of annual reports of release of toxic chemicals that appear in 40 CFR 372 (for SARA 3 ~ 3). This information must be included in all MSD S's that are copied and distributed for this material. Components present in this product at a level which could require reporting under this statute are: *** NONE****

INVENTORY STATUS
The ingredients of this product are listed on, or are exempt from listing on, the TSCA inventory.

13. OTHER INFORMATION
HMIS FORMAT:
Health: 0 Flammability: 0 Reactivity: 0

We believe that the information contained herein is current as of the date of this Material Safety Data Sheet, and is offered in good faith. Since the use of this information and of these opinions and the conditions of the use of the product are not within the control of Factor II Technology, it is the user's obligation to determine the conditions of safe use of the product.
Factor II Technology Regulatory Compliance Department

Factor II, Incorporated

P.O. Box 1339
Lakeside, AZ 85929

Phone:(928) 537-8387
Fax: (928) 537-0893

MATERIAL SAFETY DATA SHEET
A-341 Part B
Soft Gel

Factor II Technology urges each customer or recipient of this MSDS to study it carefully to become aware of and understand the hazards associated with the product. The reader should consider consulting reference works or individuals who are experts in ventilation, toxicology, and fire prevention, as necessary or appropriate to the use and understanding of the data contained in this MSDS.

To promote safe handling each customer or recipient should: (1) notify and furnish its employees, agents, contractors, customers, and others whom it knows or believes will use this material of the information regarding hazards or safety; (2) request its customers to notify their employees, customers and other users of the product of this information.

1. CHEMICAL PRODUCT
PRODUCT NAME: Catalyst for RTV Heat Cure Silicone
CHEMICAL NAME: Organopolysiloxane Mixture

2. PRODUCT COMPOSITION

MATERIAL	CAS#	
PROPRITARY-ORGANOPOLYSILOXANE	63148607/471	>90
MIXTURE	341	<10
METHYL HYDROGEN SILOXANE	68037592	

3. HAZARDS and PROTECTION IDENTIFICATION
Personal Protection Recommended: Use local exhaust. Ventilation is required. Use a NIOSH approved respirator to prevent overexposure. Reference 29CFR 1910.134 for Federal standards concerning respiratory protection. Wear impervious gloves and protective clothing as required to prevent skin contact. Wear protective goggles to prevent eye contact. An eyewash and safety shower should be nearby and ready for use.

4. FIRST AID MEASURES
EMERGENCY AND FIRST AID PROCEDURES:
SKIN:
Wash with soap and water.
INHALATION:
Remove to fresh air.
EYES:
Immediately flush eyes with water and continue washing for at least 15 minutes. If irritation persists seek medical attention.
NOTES TO PHYSICIAN:
There is no specific antidote. Treatment of overexposure should be directed at the control of symptoms and the clinical condition of the patient.

Factor II, Incorporated

P.O. Box 1339
Lakeside, AZ 85929

Phone:(928) 537-8387
Fax: (928) 537-0893

5. FIRE FIGHTING MEASURES
FLASH POINT: (TCC) N/A

FLAMMABLE LIMITS IN AIR (by volume): Not Applicable N/A

EXTINGUISHING MEDIA: Dry Chemical ,Foam or Carbon Dioxide

SPECIAL FIREFIGHTING PROCEDURES: None known.

UNUSUAL FIRE AND EXPLOXION HAZARDS: None Known

6. ACCIDENTAL RELEASE MEASURES
STEPS TO BE TAKEN IF MATERIAL IS RELEASED OR SPILLED:
Contain the spill or leak, scrape up with cardboard or a ra and place in a container.
WASTE DISPOSAL METHOD: Dispose of in accordance with all Federal, State, and local regulations.

7. HANDLING AND STORAGE
PRECAUTIONS TO BE TAKEN IN HANDLING AND STORAGE:
Keep container tightly closed. Store in cool place and keep away from Heat or Flame.

8. PHYSICAL AND CHEMICAL PROPERTIES (based on typical material)
APPEARANCE & ODOR: Slight solvent odor
BOILING POINT: 500°F
VAPOR PRESSURE at 77°Fmm Hg
VAPOR DENSITY (air=1) N/A
SOLUBILITY IN WATER (By wt): Insoluble
SPECIFIC GRAVITY (water=1) 1.00

Note: The above information is not intended for use in preparing product specifications.

9. STABILITY AND REACTIVITY DATASTABILITY: Stable. Hazardous polymerization will not occur.
INCOMPATIBILITY: None known
HAZARDOUS COMBUSTION OR DECOMPOSITION PRODUCTS: Carbon Monoxide, Carbon Dioxide, Silicon Dioxide, hYDROGEN
INCOMPATIBILITY: avoid contact with acidic bases and oxidizing agents
CONDITIONS TO AVOID: product generates flammable gas on contact with acidic, basic and oxidizing material.

10. TOXICOLOGICAL INFORMATION
Not available

11. ECOLOGICAL INFORMATION
ECOTOXICOLOGICAL INFORMATION: Keep out of sewage system.

12. DISPOSAL CONSIDERATIONS
Use proper landfill disposal or incineration.
Dispose of in accordance with all Federal, State, and local regulations.

Factor II, Incorporated

P.O. Box 1339
Lakeside, AZ 85929

Phone:(928) 537-8387
Fax: (928) 537-0893

C H I P REGULATIONS

Chemicals (Hazards Information and Packaging) Regulations 1993 requires physico-chemical and health hazard determination of all substances and preparations manufactured, transported, stored, modified, or consumed within the EEC. Components present in this product at a level which could require reporting under the statute are:
****NONE ****

FEDERAL EPA

Comprehensive Environniental Response Compensation and Liability Act of 1980 (CERCLA) requires notification of the National Response Center of release of quantities of Hazardous Substances equal to or greater than the reportable quantities (RQ's) in 40 CFR 302.4. Components present in this product at a level which could require reporting under the statute are: ****NONE ****

Superfund Amendments and Reauthorization Act of 1986 (SARA) Title III requires emergency planning based on Threshold Planning Quantities (TPQ's) and release reporting based on Reportable Quantities (RQ's) in 40 CFR 355 (used for SARA 302, 304, 3 1, and 312). Components present in this product at a level which could require reporting under the statute are: **** NONE ****

Superfund Amendments and Reauthorization Act of 1986 (SARA) Title III requires submission of annual reports of release of toxic chemicals that appear in 40 CFR 372 (for SARA 3 ~ 3). This information must be included in all MSD S's that are copied and distributed for this material. Components present in this product at a level which could require reporting under this statute are: *** NONE****
INVENTORY STATUS
The ingredients of this product are listed on, or are exempt from listing on, the TSCA inventory.

13. OTHER INFORMATION
HMIS FORMAT:
Health: 0 Flammability: 0 Reactivity: 0

We believe that the information contained herein is current as of the date of this Material Safety Data Sheet, and is offered in good faith. Since the use of this information and of these opinions and the conditions of the use of the product are not within the control of Factor II Technology, it is the user's obligation to determine the conditions of safe use of the product.
Factor II Technology Regulatory Compliance Department

QA-MSDS-07
Revised 3/27/2007

Factor II, Incorporated

Inventing and Innovating…
(Information: 1.928.537.8387)
In case of emergency call number above

MATERIAL SAFETY DATA SHEET

LSR 05,40,50,60,70 PART A

RHODIA'S V50054, 50007,50008,50009,50010

1. PRODUCT AND COMPANY DESCRIPTION

RHODIA INC.
SILICONES
320 West Stanley Avenue
Ventura CA 93001

Emergency Phone Numbers:
FOR EMERGENCIES INVOLVING A SPILL, LEAK, FIRE, EXPOSURE OR ACCIDENT CONTACT: CHEMTREC (800-424-9300 within the United States or 703-527-3887 for international collect calls) or Rhodia CAERS (Communication and Emergency Response System) at 800-916-3232.

For Product Information: (805) 653-5638

Product Status: FDA regulated use only.

Chemical Name or Synonym: REINFORCED DIMETHYL METHYLVINYL SILOXANES

2. COMPOSITION/INFORMATION ON INGREDIENTS

Component	CAS Reg Number	OSHA Hazard	Percentage
DIMETHYL SILICONE ELASTOMER BASE	**********	N	100

3. HAZARDS IDENTIFICATION

A. EMERGENCY OVERVIEW:
Physical Appearance and Odor: clear paste-like liquid, odorless.

Warning Statements:
Based on currently available data, this product does not meet the regulatory definition of a hazardous substance. However, good industrial hygiene practices should be used in handling it.

B. POTENTIAL HEALTH EFFECTS:
Acute Eye: Slightly irritating. May cause redness, irritation.
Acute Skin: Non-irritating.
Acute Inhalation: Inhalation not likely.
Acute Ingestion: Practically non-toxic.

Factor II, Incorporated
Inventing and Innovating…
(Information: 1.928.537.8387)
In case of emergency call number above

Chronic Effects: This product does not contain any ingredient designated by IARC, NTP, ACGIH or OSHA as probable or suspected human carcinogens.

4. FIRST AID MEASURES

FIRST AID MEASURES FOR ACCIDENTAL:
Eye Exposure:
In case of contact, immediately absorb excess with clean absorbent cloth or cotton. Then, hold eyelids open and flush with a steady, gentle stream of water for at least 15 minutes. Seek medical attention if irritation develops or persists or if visual changes occur.

Skin Exposure:
Immediately wipe excess material off skin with a dry cloth; then wash skin with plenty of soap and water. Seek medical attention if irritation develops or persists.

Inhalation:
Inhalation is not an expected route of exposure. If respiratory irritation or distress occurs remove victim to fresh air. Seek medical attention if respiratory irritation or distress continues.

Ingestion:
If victim is conscious and alert, give 1-2 glasses of water to drink. Do not give anything by mouth to an unconscious person. Seek medical attention. Do not leave victim unattended.

MEDICAL CONDITIONS POSSIBLY AGGRAVATED BY EXPOSURE:
No specific information found.

NOTES TO PHYSICIAN:
All treatments should be based on observed signs and symptoms of distress in the patient. Consideration should be given to the possibility that overexposure to materials other than this product may have occurred.

Treat symptomatically. No specific antidote available.

5. FIRE FIGHTING MEASURES

FIRE HAZARD DATA:

Flash Point: 190 C (374 F). Flammability Class: WILL BURN.

Method Used: Cleveland Open Cup

Flammability Limits (vol/vol%):	Lower:	Upper:
	4	75

Extinguishing Media: Recommended: dry chemical, foam, carbon dioxide, water fog.

Special Fire Fighting Procedures:
Firefighters should wear NIOSH/MSHA approved self-contained breathing apparatus and full protective clothing. Cool containers exposed to fire with water.

Unusual Fire and Explosion Hazards:
Product will burn under fire conditions.

Hazardous Decomposition Materials (Under Fire Conditions):
formaldehyde
oxides of carbon
silica (crystalline)

Autoignition Temperature: > 300 C (572 F)

6. ACCIDENTAL RELEASE MEASURES

Evacuation Procedures and Safety:
Wear appropriate protective gear for the situation. See Personal Protection information in Section 8. CAUTION: Spilled material may make the floor slippery. Do not leave traces of product on floors, ladders, etc., as this may present a slipping hazard.

Containment of Spill:
Follow procedure described below under Cleanup and Disposal of Spill.

Cleanup and Disposal of Spill:
Absorb with an inert absorbent. Scrape up and place in appropriate closed container (see Section 7: Handling and Storage). Clean up residual material with an appropriate solvent like paint thinner or mineral spirits, provided that there is good ventilation and no sources of ignition.

Environmental and Regulatory Reporting:
Do not flush to drain.

7. HANDLING AND STORAGE

Minimum/Maximum Storage Temperatures:
< 0 C (32 F)

Handling:
Avoid breathing vapors and mists. Avoid direct or prolonged contact with skin and eyes.
Storage:

Factor II, Incorporated
Inventing and Innovating…
(Information: 1.928.537.8387)
In case of emergency call number above

Store in tightly closed containers. Store in an area that is clean, well-ventilated, away from ignition sources, away from incompatible materials (see Section 10. Stability and Reactivity).

8. EXPOSURE CONTROLS/PERSONAL PROTECTION

Introductory Remarks:
These recommendations provide general guidance for handling this product. Because specific work environments and material handling practices vary, safety procedures should be developed for each intended application. While developing safe handling procedures, do not overlook the need to clean equipment and piping systems for maintenance and repairs. Waste resulting from these procedures should be handled in accordance with Section 13: Disposal Considerations. Assistance with selection, use and maintenance of worker protection equipment is generally available from equipment manufacturers.
This product can form formaldehyde vapors when heated to temperatures above 150 degrees C in the presence of air. Formaldehyde is a potential cancer hazard, a known skin and respiratory sensitizer, and an irritant to the eyes, nose, throat, skin, and digestive system. Safe handling conditions may be maintained by keeping vapor concentrations within the OSHA Permissible Exposure Limit for formaldehyde.

Exposure Guidelines:
No exposure limits were found for this product or any of its ingredients.

Engineering Controls:
Where engineering controls are indicated by use conditions or a potential for excessive exposure exists, the following traditional exposure control techniques may be used to effectively minimize employee exposures: general area dilution/exhaust ventilation.

Respiratory Protection:
When respirators are required, select NIOSH/MSHA approved equipment based on actual or potential airborne concentrations and in accordance with the appropriate regulatory standards and/or industrial recommendations.
For reasonably foreseeable industrial end uses of this material, respiratory protection should not be necessary.

Eye/Face Protection:
Eye and face protection requirements will vary dependent upon work environment conditions and material handling practices. Appropriate ANSI Z87 approved equipment should be selected for the particular use intended for this material. It is generally regarded as good practice to wear a minimum of safety glasses with side shields when working in industrial environments.

Skin Protection:
Skin contact should be minimized through use of gloves and suitable long-sleeved clothing (i.e., shirts and pants). Consideration must be given both to durability as well as permeation resistance.

Work Practice Controls:
Personal hygiene is an important work practice exposure control measure and the following general measures should be taken when working with or handling this material:
(1) Do not store, use, and/or consume foods, beverages, tobacco products, or cosmetics in areas where this material is stored.
(2) Wash hands and face carefully before eating, drinking, using tobacco, applying cosmetics, or using the toilet.
(3) Wash exposed skin promptly to remove accidental splashes or contact with this material.

9. PHYSICAL AND CHEMICAL PROPERTIES

Physical and Chemical properties here represent typical properties of this product. Contact the business area using the Product Information phone number in Section 1 for its exact specifications.

Physical Appearance: clear paste-like liquid.
Odor: odorless.
pH: Not Applicable
Specific Gravity: 1.1 at 25 C (77 F).
Water Solubility: insoluble
Melting Point Range: Not Available
Freezing Point Range: < 0 C (32 F)
Boiling Point Range: > 260 C (500 F) at 760 mmHg
Vapor Pressure: < 0.1 mmHg at 25 C (77 F)
Vapor Density: Not Available
Viscosity: viscosity (centipoises) : 3000 to 4000 cps at 25 C (77 F).

10. STABILITY AND REACTIVITY

Chemical Stability:
This material is stable under normal handling and storage conditions described in Section 7.

Conditions To Be Avoided:
heat
open flame
spark

Materials/Chemicals To Be Avoided:
strong bases
strong acids
strong oxidizing agents

The Following Hazardous Decomposition Products Might Be Expected:

Decomposition Type: thermal
dimethylcyclosiloxanes
methylphenylcyclosiloxanes

Decomposition Type: oxidative/thermal formaldehyde

Hazardous Polymerization Will Not Occur.

Factor II, Incorporated
Inventing and Innovating…
(Information: 1.928.537.8387)
In case of emergency call number above

Avoid The Following To Inhibit Hazardous Polymerization:
not applicable

11. TOXICOLOGICAL INFORMATION

Acute Eye Irritation:
No test data found for product.

Acute Skin Irritation:
No test data found for product.

Acute Dermal Toxicity:
The following data is for the specified ingredients.

Acute Respiratory Irritation:
No test data found for product.

Acute Inhalation Toxicity:
No test data found for product.

Acute Oral Toxicity:
The following data is for the specified ingredients.

Chronic Toxicity:
This product does not contain any substances that are considered by OSHA, NTP, IARC or ACGIH to be "probable" or "suspected" human carcinogens.

12. ECOLOGICAL INFORMATION

Ecotoxicological Information: No data found for product.
Chemical Fate Information: No data found for product.

13. DISPOSAL CONSIDERATIONS

Waste Disposal Method:
Chemical additions, processing or otherwise altering this material may make the waste management information presented in this MSDS incomplete, inaccurate or otherwise inappropriate. Please be advised that state and local requirements for waste disposal may be more restrictive or otherwise different from federal laws and regulations. Consult state and local regulations regarding the proper disposal of this material.

Container Handling and Disposal:
Any containers or equipment used should be decontaminated immediately after use.

EPA Hazardous Waste - NO

14. TRANSPORTATION INFORMATION

Transportation Status: IMPORTANT! Statements below provide additional data on listed DOT classification.
The listed Transportation Classification does not address regulatory variations due to changes in package size, mode of shipment or other regulatory descriptors.

US Department of Transportation
Shipping Name: NOT REGULATED

15. REGULATORY INFORMATION

Inventory Status

Inventory	Status
UNITED STATES (TSCA)	Y
CANADA (DSL)	Y
EUROPE (EINECS/ELINCS)	P
AUSTRALIA (AICS)	Y
JAPAN (MITI)	N
SOUTH KOREA (KECL)	Y

Y = All ingredients are on the inventory.
E = All ingredients are on the inventory or exempt from listing.
P = One or more ingredients fall under the polymer exemption or are on the no longer polymer list. All other ingredients are on the inventory or exempt from listing.
N = Not determined or one or more ingredients are not on the inventory and are not exempt from listing.

FEDERAL REGULATIONS
Inventory Issues:
All functional components of this product are listed on the TSCA Inventory.

SARA Title III Hazard Classes:

Fire Hazard	- NO
Reactive Hazard	- NO
Release of Pressure	- NO
Acute Health Hazard	- NO
Chronic Health Hazard	- NO

STATE REGULATIONS:
This product does not contain any components that are regulated under California Proposition 65.

16. OTHER INFORMATION

Factor II, Incorporated

Inventing and Innovating…
(Information: 1.928.537.8387)
In case of emergency call number above

National Fire Protection Association Hazard Ratings--NFPA(R):
1 Health Hazard Rating--Slight
1 Flammability Rating--Slight
0 Instability Rating--Minimal

National Paint & Coating Hazardous Materials Identification System--HMIS(R):
1 Health Hazard Rating--Slight
1 Flammability Rating--Slight
0 Reactivity Rating--Minimal

Reason for Revisions:
Change and/or addition made to Section 3, Section 8.

Key Legend Information:
ACGIH - American Conference of Governmental Industrial Hygienists
OSHA - Occupational Safety and Health Administration
TLV - Threshold Limit Value
PEL - Permissable Exposure Limit
TWA - Time Weighted Average
STEL - Short Term Exposure Limit
NTP - National Toxicology Program
IARC - International Agency for Research on Cancer
ND - Not determined
RPI - Rhodia Established Exposure Limits

Disclaimer: The information herein is given in good faith but no warranty, expressed or implied, is made.

QA-MSDS-07

Revised 12/14/2006

Factor II, Incorporated

Inventing and Innovating…
(Information: 1.928.537.8387)
In case of emergency call number above

MATERIAL SAFETY DATA SHEET

LSR 05,40,50,& 60,70 PART B

RHODIA'S V50054, 50007,50008,50009,50010

1. PRODUCT AND COMPANY DESCRIPTION

RHODIA INC.
SILICONES
320 West Stanley Avenue
Ventura CA 93001

Emergency Phone Numbers:
FOR EMERGENCIES INVOLVING A SPILL, LEAK, FIRE, EXPOSURE OR ACCIDENT CONTACT: CHEMTREC (800-424-9300 within the United States or 703-527-3887 for international collect calls) or Rhodia CAERS (Communication and Emergency Response System) at 800-916-3232.

For Product Information: (805) 653-5638

Product Status: FDA regulated use only.

Chemical Name or Synonym: REINFORCED DIMETHYL METHYLVINYL SILOXANES

2. COMPOSITION/INFORMATION ON INGREDIENTS

Component	CAS Reg Number	OSHA Hazard	Percentage
DIMETHYL SILICONE ELASTOMER BASE	**********	N	100

3. HAZARDS IDENTIFICATION

A. EMERGENCY OVERVIEW:
Physical Appearance and Odor: clear paste-like liquid, odorless.

Warning Statements:
Based on currently available data, this product does not meet the regulatory definition of a hazardous substance. However, good industrial hygiene practices should be used in handling it.

B. POTENTIAL HEALTH EFFECTS:
Acute Eye: Slightly irritating. May cause redness, irritation.
Acute Skin: Non-irritating.
Acute Inhalation: Inhalation not likely.
Acute Ingestion: Practically non-toxic.

Factor II, Incorporated
Inventing and Innovating…
(Information: 1.928.537.8387)
In case of emergency call number above

Chronic Effects: This product does not contain any ingredient designated by IARC, NTP, ACGIH or OSHA as probable or suspected human carcinogens.

4. FIRST AID MEASURES

FIRST AID MEASURES FOR ACCIDENTAL:
Eye Exposure:
In case of contact, immediately absorb excess with clean absorbent cloth or cotton. Then, hold eyelids open and flush with a steady, gentle stream of water for at least 15 minutes. Seek medical attention if irritation develops or persists or if visual changes occur.

Skin Exposure:
Immediately wipe excess material off skin with a dry cloth; then wash skin with plenty of soap and water. Seek medical attention if irritation develops or persists.

Inhalation:
Inhalation is not an expected route of exposure. If respiratory irritation or distress occurs remove victim to fresh air. Seek medical attention if respiratory irritation or distress continues.

Ingestion:
If victim is conscious and alert, give 1-2 glasses of water to drink. Do not give anything by mouth to an unconscious person. Seek medical attention. Do not leave victim unattended.

MEDICAL CONDITIONS POSSIBLY AGGRAVATED BY EXPOSURE:
No specific information found.

NOTES TO PHYSICIAN:
All treatments should be based on observed signs and symptoms of distress in the patient. Consideration should be given to the possibility that overexposure to materials other than this product may have occurred.

Treat symptomatically. No specific antidote available.

5. FIRE FIGHTING MEASURES

FIRE HAZARD DATA:

Flash Point: 190 C (374 F). Flammability Class: WILL BURN.

Method Used: Cleveland Open Cup

Flammability Limits (vol/vol%):	Lower:	Upper:
	4	75

Extinguishing Media: Recommended: dry chemical, foam, carbon dioxide, water fog.

Special Fire Fighting Procedures:
Firefighters should wear NIOSH/MSHA approved self-contained breathing apparatus and full protective clothing. Cool containers exposed to fire with water.

Unusual Fire and Explosion Hazards:
Product will burn under fire conditions.

Hazardous Decomposition Materials (Under Fire Conditions):
formaldehyde
oxides of carbon
silica (crystalline)

Autoignition Temperature: > 300 C (572 F)

6. ACCIDENTAL RELEASE MEASURES

Evacuation Procedures and Safety:
Wear appropriate protective gear for the situation. See Personal Protection information in Section 8. CAUTION: Spilled material may make the floor slippery. Do not leave traces of product on floors, ladders, etc., as this may present a slipping hazard.

Containment of Spill:
Follow procedure described below under Cleanup and Disposal of Spill.

Cleanup and Disposal of Spill:
Absorb with an inert absorbent. Scrape up and place in appropriate closed container (see Section 7: Handling and Storage). Clean up residual material with an appropriate solvent like paint thinner or mineral spirits, provided that there is good ventilation and no sources of ignition.

Environmental and Regulatory Reporting:
Do not flush to drain.

7. HANDLING AND STORAGE

Minimum/Maximum Storage Temperatures:
< 0 C (32 F)

Handling:
Avoid breathing vapors and mists. Avoid direct or prolonged contact with skin and eyes.
Storage:

Factor II, Incorporated
Inventing and Innovating…
(Information: 1.928.537.8387)
In case of emergency call number above

Store in tightly closed containers. Store in an area that is clean, well-ventilated, away from ignition sources, away from incompatible materials (see Section 10. Stability and Reactivity).

8. EXPOSURE CONTROLS/PERSONAL PROTECTION

Introductory Remarks:
These recommendations provide general guidance for handling this product. Because specific work environments and material handling practices vary, safety procedures should be developed for each intended application. While developing safe handling procedures, do not overlook the need to clean equipment and piping systems for maintenance and repairs. Waste resulting from these procedures should be handled in accordance with Section 13: Disposal Considerations. Assistance with selection, use and maintenance of worker protection equipment is generally available from equipment manufacturers.
This product can form formaldehyde vapors when heated to temperatures above 150 degrees C in the presence of air. Formaldehyde is a potential cancer hazard, a known skin and respiratory sensitizer, and an irritant to the eyes, nose, throat, skin, and digestive system. Safe handling conditions may be maintained by keeping vapor concentrations within the OSHA Permissible Exposure Limit for formaldehyde.

Exposure Guidelines:
No exposure limits were found for this product or any of its ingredients.

Engineering Controls:
Where engineering controls are indicated by use conditions or a potential for excessive exposure exists, the following traditional exposure control techniques may be used to effectively minimize employee exposures: general area dilution/exhaust ventilation.

Respiratory Protection:
When respirators are required, select NIOSH/MSHA approved equipment based on actual or potential airborne concentrations and in accordance with the appropriate regulatory standards and/or industrial recommendations.
For reasonably foreseeable industrial end uses of this material, respiratory protection should not be necessary.

Eye/Face Protection:
Eye and face protection requirements will vary dependent upon work environment conditions and material handling practices. Appropriate ANSI Z87 approved equipment should be selected for the particular use intended for this material. It is generally regarded as good practice to wear a minimum of safety glasses with side shields when working in industrial environments.

Skin Protection:
Skin contact should be minimized through use of gloves and suitable long-sleeved clothing (i.e., shirts and pants). Consideration must be given both to durability as well as permeation resistance.

Work Practice Controls:
Personal hygiene is an important work practice exposure control measure and the following general measures should be taken when working with or handling this material:
(1) Do not store, use, and/or consume foods, beverages, tobacco products, or cosmetics in areas where this material is stored.
(2) Wash hands and face carefully before eating, drinking, using tobacco, applying cosmetics, or using the toilet.
(3) Wash exposed skin promptly to remove accidental splashes or contact with this material.

9. PHYSICAL AND CHEMICAL PROPERTIES

Physical and Chemical properties here represent typical properties of this product. Contact the business area using the Product Information phone number in Section 1 for its exact specifications.

Physical Appearance: clear paste-like liquid.
Odor: odorless.
pH: Not Applicable
Specific Gravity: 1.1 at 25 C (77 F).
Water Solubility: insoluble
Melting Point Range: Not Available
Freezing Point Range: < 0 C (32 F)
Boiling Point Range: > 260 C (500 F) at 760 mmHg
Vapor Pressure: < 0.1 mmHg at 25 C (77 F)
Vapor Density: Not Available
Viscosity: viscosity (centipoises) : 3000 to 4000 cps at 25 C (77 F).

10. STABILITY AND REACTIVITY

Chemical Stability:
This material is stable under normal handling and storage conditions described in Section 7.

Conditions To Be Avoided:
heat
open flame
spark

Materials/Chemicals To Be Avoided:
strong bases
strong acids
strong oxidizing agents

The Following Hazardous Decomposition Products Might Be Expected:

Decomposition Type: thermal
dimethylcyclosiloxanes
methylphenylcyclosiloxanes

Decomposition Type: oxidative/thermal formaldehyde

Hazardous Polymerization Will Not Occur.

Factor II, Incorporated
Inventing and Innovating…
(Information: 1.928.537.8387)
In case of emergency call number above

Avoid The Following To Inhibit Hazardous Polymerization:
not applicable

11. TOXICOLOGICAL INFORMATION

Acute Eye Irritation:
No test data found for product.

Acute Skin Irritation:
No test data found for product.

Acute Dermal Toxicity:
The following data is for the specified ingredients.

Acute Respiratory Irritation:
No test data found for product.

Acute Inhalation Toxicity:
No test data found for product.

Acute Oral Toxicity:
The following data is for the specified ingredients.

Chronic Toxicity:
This product does not contain any substances that are considered by OSHA, NTP, IARC or ACGIH to be "probable" or "suspected" human carcinogens.

12. ECOLOGICAL INFORMATION

Ecotoxicological Information: No data found for product.
Chemical Fate Information: No data found for product.

13. DISPOSAL CONSIDERATIONS

Waste Disposal Method:
Chemical additions, processing or otherwise altering this material may make the waste management information presented in this MSDS incomplete, inaccurate or otherwise inappropriate. Please be advised that state and local requirements for waste disposal may be more restrictive or otherwise different from federal laws and regulations. Consult state and local regulations regarding the proper disposal of this material.

Container Handling and Disposal:
Any containers or equipment used should be decontaminated immediately after use.

EPA Hazardous Waste - NO

14. TRANSPORTATION INFORMATION

Transportation Status: IMPORTANT! Statements below provide additional data on listed DOT classification.
The listed Transportation Classification does not address regulatory variations due to changes in package size, mode of shipment or other regulatory descriptors.

US Department of Transportation
Shipping Name: NOT REGULATED

15. REGULATORY INFORMATION

Inventory Status

Inventory	Status
UNITED STATES (TSCA)	Y
CANADA (DSL)	Y
EUROPE (EINECS/ELINCS)	P
AUSTRALIA (AICS)	Y
JAPAN (MITI)	N
SOUTH KOREA (KECL)	Y

Y = All ingredients are on the inventory.
E = All ingredients are on the inventory or exempt from listing.
P = One or more ingredients fall under the polymer exemption or are on the no longer polymer list. All other ingredients are on the inventory or exempt from listing.
N = Not determined or one or more ingredients are not on the inventory and are not exempt from listing.

FEDERAL REGULATIONS
Inventory Issues:
All functional components of this product are listed on the TSCA Inventory.

SARA Title III Hazard Classes:

Fire Hazard	- NO
Reactive Hazard	- NO
Release of Pressure	- NO
Acute Health Hazard	- NO
Chronic Health Hazard	- NO

STATE REGULATIONS:
This product does not contain any components that are regulated under California Proposition 65.

16. OTHER INFORMATION

Factor II, Incorporated
Inventing and Innovating…
(Information: 1.928.537.8387)
In case of emergency call number above

National Fire Protection Association Hazard Ratings--NFPA(R):
1 Health Hazard Rating--Slight
1 Flammability Rating--Slight
0 Instability Rating--Minimal

National Paint & Coating Hazardous Materials Identification System--HMIS(R):
1 Health Hazard Rating--Slight
1 Flammability Rating--Slight
0 Reactivity Rating--Minimal

Reason for Revisions:
Change and/or addition made to Section 3, Section 8.

Key Legend Information:
ACGIH - American Conference of Governmental Industrial Hygienists
OSHA - Occupational Safety and Health Administration
TLV - Threshold Limit Value
PEL - Permissable Exposure Limit
TWA - Time Weighted Average
STEL - Short Term Exposure Limit
NTP - National Toxicology Program
IARC - International Agency for Research on Cancer
ND - Not determined
RPI - Rhodia Established Exposure Limits

Disclaimer: The information herein is given in good faith but no warranty, expressed or implied, is made.

QA-MSDS-07
Revised 12/14/2006

References

[1] A. Jemal, R. Seigel, E. Ward, T. Murray, J. Xu, and M.J. Thun. Cancer statistics 2007. *CA: A Cancer Journal for Clinicians*, 57:43–66, 2007.

[2] New Zealand Health Information Service. *Cancer: New Registrations and Deaths 1999*. New Zealand Ministry of Health, 2002.

[3] New Zealand Health Information Service. *Cancer Patient Survival Covering the Period 1994 to 2003*. New Zealand Ministry of Health, 2006.

[4] D. Hanahan and R.A. Weinberg. The hallmarks of cancer. *Cell*, 100:57–70, 2000.

[5] D.B. Kopans. *Breast Imaging*. Lippincott-Ravens, 1998.

[6] R.R. Seeley, T.D. Stephens, and P. Tate. *Anatomy & Physiology*. McGraw-Hill, 2003.

[7] S.Z. Ali. An atlas of breast images. `www.hopkinsbreastcenter.org/library/educational_information/mal.shtml`, 2007.

[8] V.L. Ernster and J. Barclay. Increases in ductal carcinoma in situ (DCIS) of the breast in relation to mammography: a dilemma. *Journal of the National Cancer Institute*, 22:151–156, 1997.

[9] F.L. Greene, D.L. Page, I.D Fleming, A. Fritz, C.M. Balch, D.G. Haller, and M. Morrow, editors. *AJCC Cancer Staging Manual*. Lippincott Raven, 1997.

[10] National Comprehensive Cancer Network. *Breast Cancer: Treatment Guidelines for Patients*. 2005.

[11] Canadian Cancer Society. *Breast self-examination: What you can do*. 2005.

[12] M.A.J. Chaplain, L. Graziano, and L. Preziosi. Mathematical modelling of the loss of tissue compression responsiveness and its role in solid tumour development. *Mathematical Medicine and Biology*, 23:197–229, 2006.

[13] P.A. Newcomb, N.S. Weiss, B.E. Storer, D. Scholes, B.E. Young, and L.F. Voigt. Breast self-examination in relation to the occurrence of advanced breast cancer. *Journal of the National Cancer Institute*, 83:260–265, 1991.

[14] L. Holmberg, A. Ekbom, E. Calle, A. Mokdad, and T. Byers. Breast cancer mortality in relation to self-reported use of breast self-examination: A cohort study of 450,000 women. *Breast Cancer Research and Treatment*, 43:137–140, 1997.

[15] D.B. Thomas, D.L. Gao, S.G. Self, C.J. Allison, Y. Tao, J. Mahloch, R. Ray, Q. Qin, R. Presley, and P. Porter. Randomized trial of breast self-examination in Shanghai: methodology and preliminary results. *Journal of the National Cancer Institute*, 89:355–365, 1997.

[16] R. Herdman and L. Norton, editors. *Saving Women's Lives: Strategies for Improving Breast Cancer Detection and Diagnosis*, Washington DC, 2005. The National Academies Press.

[17] V.C. Cokkinides, A. Samuels, E.M. Ward, and M.J. Thun. *Cancer Prevention & Early Detection Facts & Figures*. American Cancer Society, 2004.

[18] National Screening Unit. *BreastScreen Aotearoa National Policy and Quality Standards*. New Zealand Ministry of Health, 2004.

[19] BreastScreen Aoteoroa. *An update on the free national screening program*. New Zealand Ministry of Health, 2004.

[20] L. Tabar, M. Yen, B. Vitak, H.T. Chen, R.A. Smith, and S.W. Duffy. Mammography service screening and mortality in breast cancer patients: 20-year follow-up before and after introduction of screening. *The Lancet*, 361:1405–1410, 2003.

[21] O. Olsen and P.C. Gtzsche. Cochrane review on screening for breast cancer with mammography. *The Lancet*, 358:1340–1342, 2001. Research letter.

[22] S.K. Moore. Better breast cancer detection. *IEEE Spectrum*, 38:50–54, 2001.

[23] C.T. Derk. Systemic sclerosis and cancer. `www.scleroderma.org/medical/other_articles/derk_2004_3.shtm`, 2004.

[24] Partnership for Breast Care. Mammograms. `www.partnershipforbreastcare.org/PBC/problems/ways/mammogram.aspx`, 2002.

[25] M.J. Yaffe. What should the burden of proof be for acceptance of a new breast-cancer screening technique? *The Lancet*, 364:1111–1112, 2004. Comment.

[26] M. Kriege, C.T.M. Brekelmans, C. Boetes, P.E. Besnard, H.M. Zonderland, I.M. Obdeijn, R.A. Manoliu, T. Kok, H. Peterse, M.M.A. Tilanus-Linthorst, S.H. Muller, S. Meijer, J.C. Oosterwijk, L.V.A.M. Beex, R.A.E.M. Tollenaar, H.J. de Koning, E.J.T. Rutgers, and J.G.M Klijn. Effacy of MRI and mammography for breast cancer screening in women with familial or genetic disposition. *New England Journal of Medicine*, 351:427–437, 2004.

[27] C.A. Beam, P.M. Layde, and D.C. Sullivan. Variability in the interpretation of screening mammograms by US radiologists. *Archives of Internal Medicine*, 156:209–213, 1996.

[28] S. Ciatto, M.R. Del Turco, G. Risso, S. Catarzi, R. Bonardi, V. Viterbo, P. Gnutti, B. Guglielmoni, L. Pinelli, A. Pandiscia, F. Navarra, A. Lauria, R. Palmiero, and P.L. Indovina. Comparison of standard reading and computer aided detection (CAD) on a national proficiency test of screening mammography. *European Journal of Radiology*, 45:135–138, 2003.

[29] H. Jonsson, L-G. Larsson, and P. Lenner. Detection of breast cancer with mammography in the first screening round in relation to expected incidence in different age groups. *Acta Oncologica*, 42:22–29, 2003.

[30] P.R. Snoeren and N. Karssemeijer. Thickness correction of mammographic images by means of a global parameter model of the compressed breast. *IEEE Trans. on Medical Imaging*, 23:799–806, 2004.

[31] R. Sapir, M. Patlas, S.D. Strano, I. Hadas-Halpern, and N.I. Cherny. Does mammography hurt? *Journal of Pain and Symptom Management*, 25:53–63, 2003.

[32] A. Asghari and M.K. Nicholas. Pain during mammography: the role of coping strategies. *Pain*, 108:170–179, 2004.

[33] S. Kashikar-Zuck, F.J. Keefe, P. Kornguth, P. Beaupre, A. Holzberg, and D. Delong. Pain coping and the pain experience during mammography: a preliminary study. *Pain*, 73:165–172, 1997.

[34] P.J. Kornguth, F.J. Keefe, and M.R. Conaway. Pain during mammography: characteristics and relationship to demographic and medical variables. *Pain*, 66:187–194, 1996.

[35] J.P. Hornak. The basics of MRI. `http://www.cis.rit.edu/htbooks/mri`, 1996.

[36] J. Safir, J.L Zito, M.E. Gershwind, D. Faegenburg, C.E. Tobin, P.D. Cayea, W.J. Wortman, L.M. Sclafani, and V.E. Maurer. Contrast-enhanced breast MRI for cancer detection using a commercially available system - a perspective. *Clinical Imaging*, 22:162–179, 1998.

[37] Aurora Imaging Technology. MRI Products. `www.auroramri.com/mri/product/biopsy.shtml`, 2002.

[38] BOCA Radiology Group. Our experience with breast MRI. `www.bocaradiology.com/Procedures/breast_MRI/index.html`, 2007.

[39] E. Warner, D.B. Plewes, R.S. Shumak, G.C. Catzavelos, L.S. Di Prospero, M.J. Yaffe, V. Goel, P.L. Chart E. Ramsay, D.E.C. Cole, G.A. Taylor, M. Cutrara, T.H. Samuels, J.P. Murphy, J.M. Murphy, and S.A. Narod. Comparison of breast magnetic resonance imaging, mammography, and ultrasound for surveillance of women at high risk for hereditary breast cancer. *Journal of Clinical Oncology*, 19:3524–3531, 2001.

[40] L. Liberman. Breast cancer screening with MRI - what are the data for patients at hight risk? *New England Journal of Medicine*, 351:497–500, 2004. Editorial.

[41] Siemens Medical Imaging. Ultrasound systems. `www.siemens.com/medical`, 2006.

[42] D. Lister, A.J. Evans, H.C. Burrell, R.W. Blamey, A.R. Wilson, S.E. Pinder, I.O. Ellis, C.W. Elston, and J. Kollias. The accuracy of breast ultrasound in the evaluation of clinically benign discrete, symptomatic breast lumps. *Clinical Radiology*, 53:490–492, 1998.

[43] R. Lawson. Implications of surface temperatures in the diagnosis of breast cancer. *Canadian Medical Association Journal*, 75:309–311, 1956.

[44] W.C. Amalu, W.B. Hobbins, J.F Head, and R.L Elliot. *Medical Devices and Systems*, chapter 25. Taylor & Francis, 2006.

[45] Y. Zou and Z. Guo. A review of electrical impedance techniques for breast cancer detection. *Medical Engineering and Physics*, 25:79–90, 2003.

[46] V. Cherepenin, A. Karpov, A. Korjenevsky, V. Kornienko, A. Mazaletskaya, D. Mazourov, and D. Meister. A 3D electrical impedance tomography (EIT) system for breast cancer detection. *Physiological Measurement*, 22:9–18, 2001.

[47] N.K. Soni, A. Hartov, C. Kogel, S.P. Poplack, and K.D. Paulsen. Multi-frequency electrical impedance tomography of the breast: new clinical results. *Physiological Measurement*, 25:301–314, 2004.

[48] K.D. Paulsen, P.M. Meaney, and L.C. Gilman, editors. *Alternative Breast Imaging: Four Model-Based Approaches*. Springer, 2005.

[49] G.G. Senaratne, R.B. Keam, W.L. Sweatman, and G.C. Wake. Inverse methods for detection of internal objects using microwave technology: With potential for

breast screening. In *Proceedings of the 5th International Conference on Inverse Problems in Engineering: Theory and Practice*, pages S1–10. Leeds University Press, 2005.

[50] J. Ophir, E.I. Céspedes, H. Ponnekanti, Y. Yazdi, and X. Li. Elastography: a quantitative method for imaging the elasticity of biological tissues. *Ultrasonic Imaging*, 13:111–134, 1991.

[51] L. Gao, K.J. Parker, R.M. Lerner, and S.F. Levinson. Imaging the elastic properties of tissue – a review. *Ultrasound in Medicine and Biology*, 22:959–977, 1996.

[52] A.P. Sarvazyan, A.R Skovoroda, S.Y. Emelianov, J.B. Fowlkes, J.G. Pipe, R.S Adler, R.B. Boxton, and P.L Carson. Biophysical bases of elasticity imaging. *Acoustical Imaging*, 21:223–240, 1995.

[53] A. Sarvazyan. Mechanical imaging: A new technology for medical diagnostics. *International Journal of Medical Informatics*, 49:195–216, 1998.

[54] T.A. Krouskop, T.M. Wheeler, F. Kallel, B.S. Garra, and T. Hall. Elastic moduli of breast and prostate tissues under compression. *Ultrasonic Imaging*, 20:260–274, 1998.

[55] P.S. Wellman, R.D. Howe, E. Dalton, and K.A. Kern. Breast tissue stiffness in compression is correlated to histological diagnosis. Technical report, Harvard BioRobotics Laboratory, 1999.

[56] A. Samani, J. Bishop, C. Luginbuhl, and D.B. Plewes. Measuring the elastic modulus of ex vivo small tissue samples. *Physics in Medicine and Biology*, 48:2183–2198, 2003.

[57] A. Samani and D. Plewes. An inverse problem solution for measuring the elastic modulus of intact ex vivo breast tissue tumours. *Physics in Medicine and Biology*, 52:1247–1260, 2007.

[58] A. Samani, J. Zubovits, and D. Plewes. Elastic moduli of normal and pathological human breast tissues: An inversion technique based investigation of 169 samples. *Physics in Medicine and Biology*, 52:1565–1576, 2007.

[59] R.M. Lerner, S.R Huang, and K.J. Parker. Sonoelasticity images derived from ultrasound signals in mechanically vibrated tissues. *Ultrasound in Medicine and Biology*, 16:231–239, 1990.

[60] K.J. Parker, S.R. Huang, R.A. Musulin, and R.M. Lerner. Tissue response to mechanical vibrations for sonoelasticity imaging. *Ultrasound in Medicine and Biology*, 16:241–246, 1990.

[61] F. Lee, J.P. Bronson, R.M. Lerner, K.J. Parker, S-R. Huang, and J.B. Roach. Sonoelasticity imaging: Results in in vitro tissue specimens. *Radiology*, 181:237–239, 1991.

[62] J. Ophir, F. Kallel, T. Varghese, E. Konofagou, S.K. Alam, T. Krouskop, B. Garra, and R. Righetti. Elastography. *Comptes Rendus de l'Academie des Sciences Series IV Physics*, 2:1193–1212, 2001.

[63] R.G. Barr. Clinical applications of a real-time elastography technique in breast imaging. In *Proceedings of the 5th International Conference on the Ultrasonic Measurement and Imaging of Tissue Elasticity*, page 51, 2006.

[64] P.E. Barbone and J.C. Bamber. Quantitative elasticity imaging: what can and cannot be inferred from strain images. *Physics in Medicine and Biology*, 47:2147–2164, 2002.

[65] P.E. Barbone and N. Gokhale. Elastic modulus imaging: on the uniqueness and nonuniqueness of the elastography inverse problem in two dimensions. *Inverse Problems*, 20:283–296, 2004.

[66] P.E. Barbone and A.A. Oberai. Elastic modulus imaging: some exact solutions of the compressible elastography inverse problem. *Physics in Medicine and Biology*, 52:1577–1593, 2007.

[67] F. Kallel and M. Bertrand. Tissue elasticity reconstruction using linear perturbation method. *IEEE Trans. on Medical Imaging*, 15:299–313, 1996.

[68] M.M. Doyley, S. Srinivasan, S.A. Pendergrass, Z. Wu, and J. Ophir. Comparative evaluation of strain-based and model-based modulus elastography. *Ultrasound in Medicine and Biology*, 31:787–802, 2005.

[69] J. Bercoff, S. Chaffai, M. Tanter, L. Sandrin, S. Catheline, M. Fink, J.L. Gennisson, and M. Meunier. In vivo breast cancer detection using transient elastography. *Ultrasound in Medicine and Biology*, 29:1387–1396, 2003.

[70] D.B. Plewes, J. Bishop, A. Samani, and J. Sciarretta. Visualization and quantification of breast cancer biomechanical properties with magnetic resonance elastography. *Physics in Medicine and Biology*, 45:1591–1610, 2000.

[71] R. Muthupillai, P. J. Rossman, D. J. Lomas, J. F. Greenleaf, S. J. Riederer, and R. L. Ehman. Magnetic resonance elastography by direct visualization of propagating acoustic strain waves. *Science*, 269:1854–1857, 1995.

[72] A. Manduca, T.E. Oliphant, M.A. Dresner, D.S. Lake, J.F. Greenleaf, and R.L. Ehman. Comparitive evaluation of inversion algorithms for magnetic resonance

elastography. In *IEEE International Symposium on Biomedical Imaging*, pages 997–1000. IEEE, 2002.

[73] E.E.W. Van Houten, M.M. Doyley, F.E. Kennedy, J.B. Weaver, and K.D. Paulsen. Initial in vivo experience with steady-state subzone-based MR elastography of the human breast. *Journal of Magnetic Resonance Imaging*, 17:72–85, 2003.

[74] E.E.W. Van Houten. *Mechanical Property Reconstruction from MR Detected Harmonic Displacement Data*. PhD thesis, Thayer School of Engineering at Dartmouth College, 2001.

[75] J.B. Weaver, E.E.W. Van Houten, M.I. Miga, F.E. Kennedy, and K.D. Paulsen. Magnetic resonance elastography using 3D gradient echo measurements of steady state motion. *Medical Physics*, 28:1620–1628, 2001.

[76] M.M. Doyley, J.B. Weaver, E.E.W. Van Houten, F.E. Kennedy, and K.D. Paulsen. Thresholds for detecting and characterizing focal lesions using steady-state MR elastography. *Medical Physics*, 30:495–504, 2003.

[77] S.J. Kirkpatrick and D.D. Duncan. Optical elastography. In *Saratov Fall Meeting 2000 Optical Technologies in Biophysics and Medicine II*, pages 58–68. Society of Photo-Optical Instrumentation Engineers, 2001.

[78] S.J. Kirkpatrick and D.D. Duncan. Acousto-optical elastography. In *Laser-Tissue Interaction XII: Photochemical, Photothermal, and Photomechanical*, pages 426–432. Society of Photo-Optical Instrumentation Engineers, 2001.

[79] M.P. Rothney, C.W. Washington, and M.I. Miga. Evaluation of a similarity-based elastography technique using four similarity metrics. In *IEEE International Symposium on Biomedical Imaging*, pages 696–699. IEEE, 2004.

[80] P. Barbone, N. Gokhale, M. Richards, A. Oberai, and M. Doyley. Simultaneous elastic image registration and elastic modulus reconstruction. In *Proceedings of the 2004 IEEE International Symposium on Biomedical Imaging: From Nano to Macro*, pages 543–546, 2004.

[81] Y. Liu, L.Z. Sun, , and G. Wang. Tomography-based 3D anisotropic elastography using boundary measurements. *IEEE Trans. Medical Imaging*, 24:1323–1333, 2005.

[82] J.H. Holland. *Adaptation in Natural and Artificial Systems*. MIT Press, USA, 1992.

[83] R. Salomon. Evolutionary algorithms and gradient search: Similarities and differences. *IEEE Trans. on Evolutionary Computation*, 2:45–55, 1998.

[84] J. Carnahan and R. Sinha. Nature's algorithms. *IEEE Potentials*, 20:21–24, 2001.

[85] E. Mezura-Montes, C.A. Coello Coello, and R. Landa-Becerra. Engineering optimization using a simple evolutionary algorithm. In *Proc. 15th IEEE Int. Conf. on Tools with Artificial Intelligence*. IEEE, 2003.

[86] A. Konak, D.W. Coit, and A.E. Smith. Multi-objective optimization using genetic algorithms: A tutorial. *Reliability Engineering and System Safety*, 91:992–1007, 2006.

[87] S. Kirkpatrick, D.G. Gelatt Jr., and M.P. Vecchi. Optimization by simulated annealing. *Science*, 220:671–680, 1983.

[88] R.A. Rutenbar. Simulated annealing algorithms: An overview. *Circuits and Devices Magazine*, 5:19–26, 1989.

[89] T. Matsuoka, S. Yamamoto, and M. Takahara. Prediction of structures and mechanical properties of composites using a genetic algorithm and finite element method. *Journal of Materials Science*, 36:27–33, 2001.

[90] R. Olmi, M. Bini, and S. Priori. A genetic algorithm approach to image reconstruction in electrical impedance tomography. *IEEE Trans. on Evolutionary Computation*, 4:83–88, 2000.

[91] Y. Zhang, L.O. Hall, D.B. Goldgof, and S. Sarkar. A constrained genetic approach for computing material property of elastic objects. *IEEE Trans. on Evolutionary Computation*, 10:341–357, 2006.

[92] R. Olmi, M. Bini, and S. Priori. A combined FEM/Genetic algorithm for vascular soft tissue elasticity estimation. *Cardiovascular Engineering*, 6:93–102, 2006.

[93] F.S. Azar, D.N. Metaxas, and M.D. Schnall. A deformable finite element model of the breast for predicting mechanical deformations under external perturbations. *Academic Radiology*, 8:965–975, 2001.

[94] M.M Doyley, P.M. Meaney, and J. Bamber. Evaluation of an iterative reconstruction method for quantitative elastography. *Physics in Medicine and Biology*, 45:1521–1540, 2000.

[95] A.J.H. Hii, C.E. Hann, J.G. Chase, and E.E.W. Van Houten. Fast normalized cross corelation for motion tracking using basis functions. *Computer Methods and Programs in Biomedicine*, 82:144–156, 2006.

[96] S. Wortmann. Soft tissue actuation and imaging-based measurement system. Technical report, University of Canterbury, 2005.

[97] T.J. Hall, M. Bilgen, M.F. Insana, and T.A. Krouskop. Phantom materials for elastography. *IEEE Transactions on Ultrasonics, Ferroelectrics, and Frequency Control*, 44:1355–1365, 1997.

[98] Gelita Group. Gelatin production. `www.gelita.com`, 2004.

[99] J.M. Blackall, D. Rueckert, C.R. Maurer Jr., G.P. Penney, D.L.G. Hill, and D.J. Hawkes. An image registration approach to automated calibration for freehand 3d ultrasound. In *Medical Image Computing and Computer-Assisted Intervention MICCAI 2000*. Springer, 2000.

[100] Dow Corning. The basics of silicon chemistry. `www.dowcorning.com`, 2007.

[101] J. Steel, J. Fincher, C. Murray, and A. Morrison. Diet soft tissue actuator. Technical report, University of Canterbury, 2005.

[102] R. Klette, K. Schlüns, and A. Koschan. *Computer Vision, Three-Dimensional Data from Images*. Springer-Verlag, Singapore, 1998.

[103] E. Trucco and A. Verri. *Introductory Techniques for 3D Computer Vision*. Prentice-Hall, New Jersey, USA, 1998.

[104] A. Milsant and J. Rouzé. Digital image-based elasto-tomography: Motion sensing system. Technical report, University of Canterbury, 2004.

[105] E. Anderson, Z. Bai, C. Bischof, S. Blackford, J. Demmel, J. Dongarra, J. Du Croz, A. Greenbaum, S. Hammarling, A. McKenney, and D. Sorensen. *LAPACK Users' Guide*. Society for Industrial and Applied Mathematics, 1999.

[106] P.R. Amestoy, A. Guermouche, J-Y. L'Excellent, S. Pralet, G. Alessandrini, A. Morassi, and E. Rosset. Hybrid scheduling for the parallel solution of linear systems. *Parallel Computing*, 32:136–156, 2006.

[107] K. Goto and R.A. can de Geijn. Anatomy of high-performance matrix multiplication. *ACM Transactions on Mathematical Software (in Press)*, 2006.

[108] D.W. Marquardt. An algorithm for least-squares estimation of nonlinear parameters. *SIAM Journal of Applied Mathematics*, 11:431–441, 1963.

[109] R.G. Brown, J.G. Chase, and E.E.W Van Houten. Discrete colour-based euclidean-invariant signatures for feature tracking in a diet breast cancer screening system. In *Proc. SPIE Int. Soc. Opt. Eng.* SPIE, February 2007.

[110] J. Zhong, X. Hu, J. Zhang, and M. Gu. Comparison of performance between different selection strategies on simple genetic algorithms. In *Computational Intelligence for Modelling, Control and Automation*, pages 1115–1121. IEEE, 2005.

[111] A. Oberai, N.H. Gokhale, and G.R. Feijóo. Solution of inverse problems in elasticity imaging using the adjoint method. *Inverse Problems*, 19:297–313, 2003.

[112] G.E. Moore. Cramming more components onto integrated circuits. *Electronics*, 38:114–117, 1965.

[113] A. Sarvazyan. Moore's law: past, present and future. *IEEE Spectrum*, 34:52–59, 1997.

[114] M. Lundstrom. Moore's law forever? *Science*, 299:210–211, 2003.

[115] H-U. Berger, C.E. Hann, J.G. Chase, R.L. Broughton, and E.E.W Van Houten. Boundary element methods in elastography – a first exploratory study. In *Proc. SPIE Int. Soc. Opt. Eng.* SPIE, 2007.